



Development of numerical optimization algorithms for power system real-time estimation tools

Author:

Sadinezhad, Iman

Publication Date:

2012

DOI:

<https://doi.org/10.26190/unsworks/15362>

License:

<https://creativecommons.org/licenses/by-nc-nd/3.0/au/>

Link to license to see what you are allowed to do with this resource.

Downloaded from <http://hdl.handle.net/1959.4/51791> in <https://unsworks.unsw.edu.au> on 2024-04-30

Development of Numerical Optimization Algorithms for Power System Real-Time Estimation Tools



UNSW
THE UNIVERSITY OF NEW SOUTH WALES

Iman Sadinezhad

A thesis submitted in fulfilment of the requirements for
the degree of Doctor of Philosophy

School of Electrical Engineering and Telecommunications
The University of New South Wales
NSW, Australia

April 2012

PLEASE TYPE

THE UNIVERSITY OF NEW SOUTH WALES
Thesis/Dissertation Sheet

Surname or Family name: Sadinezhad

First name: Iman

Other name/s:

Abbreviation for degree as given in the University calendar: PhD

School: Electrical Engineering and Telecommunications

Faculty: Engineering

Title: Development of Numerical Optimization Algorithms for
Power System Real-Time Estimation Tools

Abstract 350 words maximum: (PLEASE TYPE)

The estimation of voltage/current phasors and local frequency are key parts to operate and control the ever evolving electricity networks. Phasor and frequency can be estimated by using numerical optimisation techniques. These techniques offer the flexibility to handle frequency variations, disturbances, and fault conditions more effectively when compared with the commonly used digital techniques such as fast Fourier transform (FFT) and discrete Fourier transform (DFT). Although numerical techniques such as Kalman filter (KF), Newton-type algorithm (NTA), recursive least-squares (RLS), and least-squares (LS) rectify the shortcomings of FFT and DFT techniques, their immense computational burden and stability issues impede their real-time application.

The objective of this thesis is to propose the application of new numerical optimisation techniques as real-time estimation tools for power system phasors, harmonics, and frequency. The contributions of this research work are as follows:

- The LS technique is modified to deliver frequency adaptive estimate of voltage envelope.
- A new decoupled recursive-least-squares (DRLS) technique is presented for harmonics and phasor estimation.
- A modified gradient search (MGS) undersampling technique for harmonics/interharmonics and phasor estimation is presented which shows comparable accuracy with that of the recommended technique by IEC Standard 61000-4-7.
- A new Newton-type-algorithm and least-squares (NTA-LS) frequency estimation technique is presented.

MATLAB software has been used to emulate harmonics, frequency variation, and fault conditions in a computer environment.

Programmable power supplies have been used to conduct experiments in the laboratory. Two widely available research & development digital signal processor (DSP) controllers have been used for real-time phasor and frequency estimation in the experiments. Simulation studies and real-time experiments have been performed and results presented in this thesis support the following observations.

- The proposed LS technique shows better performance in tracking voltage envelope and frequency variations when compared with the adaptive notch filter (ANF) and enhanced phase-locked loop (EPLL) techniques. The proposed new least-squares-Kalman (LSK) estimation technique shows better accuracy than the DFT technique in tracking voltage flicker patterns.

- The DRLS technique shows considerable improvement in terms of reducing the computational burden of the conventional RLS technique for real-time implementation on DSPs. The computational efficiency of the DRLS technique is also better than that of the DFT and adaptive linear combiner (ADALINE) techniques for extracting phasors and harmonics under highly harmonic distorted power system environments. The DRLS technique also shows a higher level of accuracy and stability to track synchronized phasors under fault conditions when compared with the EPLL technique.

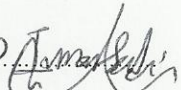
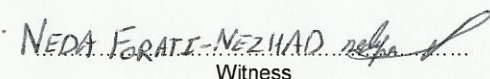
- The simplicity of the proposed undersampling MGS technique is promising for analysing the voltage and current spectra in real-time on the simple hardware platforms at a low sampling frequency. This thesis also proposes an extension of the staggered undersampling to reduce the estimation delays associated with the staggered undersampling. The presented extension on the undersampling concept lays the basis of wide-area-measurement systems (WAMs) implementation at the distribution level based on what the residential area broadband internet services can already offer. The proposed technique of direct transfer of data over the communication network is more reliable than the global positioning system (GPS) based synchrophasor detection and bypasses the DSP clock synchronization errors.

- The NTA-LS technique demonstrates faster estimation pace, higher accuracy and better noise immunity for implementation at low sampling frequency in comparison with the PLL and DFT-based decomposition of single-phase into orthogonal components (DSPOC) techniques. The stability of the proposed modified NTA-LS technique is also superior to that of the conventional NTA. This work lays the basis for using new numerical optimisation techniques for real-time parameter estimation in power systems and studying the electric load based on slow sampling observations.

Declaration relating to disposition of project thesis/dissertation

I hereby grant to the University of New South Wales or its agents the right to archive and to make available my thesis or dissertation in whole or in part in the University libraries in all forms of media, now or here after known, subject to the provisions of the Copyright Act 1968. I retain all property rights, such as patent rights. I also retain the right to use in future works (such as articles or books) all or part of this thesis or dissertation.

I also authorise University Microfilms to use the 350 word abstract of my thesis in Dissertation Abstracts International (this is applicable to doctoral theses only).

IMAN SADINEZHAD  NEDA FORATI-NEZHAD  26/04/2012
Signature Witness Date

The University recognises that there may be exceptional circumstances requiring restrictions on copying or conditions on use. Requests for restriction for a period of up to 2 years must be made in writing. Requests for a longer period of restriction may be considered in exceptional circumstances and require the approval of the Dean of Graduate Research.

FOR OFFICE USE ONLY

Date of completion of requirements for Award:

ORIGINALITY STATEMENT

'I hereby declare that this submission is my own work and to the best of my knowledge it contains no materials previously published or written by another person, or substantial proportions of material which have been accepted for the award of any other degree or diploma at UNSW or any other educational institution, except where due acknowledgement is made in the thesis. Any contribution made to the research by others, with whom I have worked at UNSW or elsewhere, is explicitly acknowledged in the thesis. I also declare that the intellectual content of this thesis is the product of my own work, except to the extent that assistance from others in the project's design and conception or in style, presentation and linguistic expression is acknowledged.'

Signed



Date

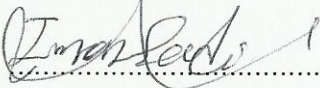
26/04/2012

COPYRIGHT STATEMENT

'I hereby grant the University of New South Wales or its agents the right to archive and to make available my thesis or dissertation in whole or part in the University libraries in all forms of media, now or here after known, subject to the provisions of the Copyright Act 1968. I retain all proprietary rights, such as patent rights. I also retain the right to use in future works (such as articles or books) all or part of this thesis or dissertation.

I also authorise University Microfilms to use the 350 word abstract of my thesis in Dissertation Abstract International (this is applicable to doctoral theses only).

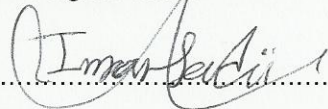
I have either used no substantial portions of copyright material in my thesis or I have obtained permission to use copyright material; where permission has not been granted I have applied/will apply for a partial restriction of the digital copy of my thesis or dissertation.'

Signed 

Date 26/04/2012

AUTHENTICITY STATEMENT

'I certify that the Library deposit digital copy is a direct equivalent of the final officially approved version of my thesis. No emendation of content has occurred and if there are any minor variations in formatting, they are the result of the conversion to digital format.'

Signed 

Date 26/04/2012

To my beautiful wife Neda and my parents

ABSTRACT

The estimation of voltage/current phasors and local frequency are key parts to operate and control the ever evolving electricity networks. Phasor and frequency can be estimated by using numerical optimisation techniques. These techniques offer the flexibility to handle frequency variations, disturbances, and fault conditions more effectively when compared with the commonly used digital techniques such as fast Fourier transform (FFT) and discrete Fourier transform (DFT). Although numerical techniques such as Kalman filter (KF), Newton-type algorithm (NTA), recursive-least-squares (RLS), and least-squares (LS) rectify the shortcomings of FFT and DFT techniques, their immense computational burden and stability issues impede their real-time application. Adaptive notch filter (ANF) and enhanced phase-locked loop (EPLL) benefit from simple structures although their performance degrade under severe unbalance and fault conditions.

The objective of this thesis is to propose the application of new numerical optimisation techniques as real-time estimation tools for power system phasors, harmonics, and frequency. The contributions of this research work are as follows:

- The LS technique is modified to deliver frequency adaptive estimate of voltage envelope.
- A new decoupled recursive-least-squares (DRLS) technique is presented for harmonics and phasor estimation.
- A modified gradient search (MGS) undersampling technique for harmonics/interharmonics and phasor estimation is presented which shows comparable accuracy with that of the recommended technique by IEC Standard 61000-4-7.
- A new Newton-type-algorithm and least-squares (NTA-LS) frequency estimation technique is presented.

MATLAB software has been used to emulate harmonics, frequency variation, and fault conditions in a computer environment. Programmable power supplies have been used to conduct experiments in the laboratory. Two widely available research & development digital signal processor (DSP) controllers have been used for real-time phasor and frequency estimation in the experiments.

Simulation studies and real-time experiments have been performed and results presented in this thesis support the following observations.

- The proposed LS technique shows better performance in tracking voltage

envelope and frequency variations when compared with the ANF and EPLL techniques. The proposed new least-squares-Kalman (LSK) estimation technique shows better accuracy than the DFT technique in tracking voltage flicker patterns.

- The DRLS technique shows considerable improvement in terms of reducing the computational burden of the conventional RLS technique for real-time implementation on DSPs. The computational efficiency of the DRLS technique is also better than that of the DFT and adaptive linear combiner (ADALINE) techniques for extracting phasors and harmonics under highly harmonic distorted power system environments. The DRLS technique also shows a higher level of accuracy and stability to track synchronized phasors under fault conditions when compared with the EPLL technique.
- The simplicity of the proposed undersampling MGS technique is promising for analysing the voltage and current spectra in real-time on the simple hardware platforms at a low sampling frequency. This thesis also proposes an extension of the staggered undersampling to reduce the estimation delays associated with the staggered undersampling. The presented extension on the undersampling concept lays the basis of wide-area-measurement systems (WAMs) implementation at the distribution level based on what the residential area broadband internet services can already offer. The proposed technique of direct transfer of data over the communication network is more reliable than the global positioning system (GPS) based synchrophasor detection and bypasses the DSP clock synchronization errors.
- The NTA-LS technique demonstrates faster estimation pace, higher accuracy and better noise immunity for implementation at low sampling frequency in comparison with the PLL and DFT-based decomposition of single-phase into orthogonal components (DSPOC) techniques. The stability of the proposed modified NTA-LS technique is also superior to that of the conventional NTA.

This work lays the basis for using new numerical optimisation techniques for real-time parameter estimation in power systems and studying the electric load based on slow sampling observations.

ACKNOWLEDGEMENTS

The financial and technical support provided by the School of Electrical Engineering and Telecommunications is gratefully acknowledged.

I would like to express my deepest and sincere gratitude to my supervisor Professor Vassilios G. Agelidis for giving me the rare and precious opportunity to begin my Ph.D. studies under his supervision. It is hard to find any word to express my appreciation for his support and guidance throughout my Ph.D. studies. I wish him the best and hope many more students have the chance to go through such a life-changing experience with him for many years to come.

I am thankful to all my fellow Ph.D. students at Australian Energy Research Institute (AERI) with whom I had the pleasure of companionship. Specifically, I would like to thank Mr. Georgios S. Konstantinou, Dr. Sridhar Reddy Pulikanti, and Mr. Minsoo Jang for having interesting discussions, valuable assistance in the laboratory, and their friendship. I would also like to thank Dr. Mihai Ciobotaru for his valuable guidance and help at AERI.

I would like to express my special thanks to my beautiful wife Neda for her support, patience, and unconditional love during my Ph.D. studies. Last but not least, special thanks go to my parents for their enormous support and encouragement which have kept me going every day.

Table of Contents

ABSTRACT.....	ii
ACKNOWLEDGEMENTS.....	iv
Table of Contents.....	v
List of Figures.....	ix
List of Tables.....	xix
List of Abbreviations	xix
List of Parameters.....	xxiv
List of Greek Symbols	xxxiv
Chapter 1 : Introduction.....	1
1.1. Literature Review	1
1.1.1. Adaptive Notch Filter (ANF)	2
1.1.2. Enhanced Phase-Locked Loop (EPLL)	5
1.1.3. Adaptive Linear Combiner (ADALINE)	7
1.1.4. Recursive Discrete Fourier Transform (RDFT)	10
1.1.5. Least-Squares (LS)	12
1.1.6. Kalman Filter (KF)	16
1.1.7. Newton-Type-Algorithm (NTA)	19
1.1.8. Recursive-Least-Squares (RLS)	21
1.1.9. Summary of the Literature Review.....	24
1.2. Research Motivation	26
1.3. Statement of Originality	27
1.4. List of Publications	29
1.4.1. Journal Papers.....	29
1.4.2. Conference Papers	30
1.5. Thesis Organisation	31
Chapter 2 : Frequency Adaptive Least-Squares-Kalman Technique for Real-Time Voltage Envelope and Flicker Estimation.....	33
2.1. Introduction	33
2.2. Frequency Adaptive Least-Squares Technique for Fundamental Frequency Envelope Estimation.....	36
2.2.1. Frequency Estimation	37

2.2.2. Envelope Estimation	43
2.3. Instantaneous Flicker Level Prediction.....	46
2.4. Real-Time Implementation Experiments	55
2.4.1. Implementation 1: Sampling Frequency of 1 kHz	56
2.4.1.1. Case 1: Phasor Estimation in Presence of Frequency Drift	56
2.4.1.1. Case 2: Phasor Estimation in Presence of Frequency Drift and Harmonics	59
2.4.1.2. Case 3: Voltage Sag and Frequency Step Change.....	61
2.4.2. Implementation 2: Sampling Frequency of 10 kHz.....	63
2.4.2.1. Case 4: Frequency Drift and Harmonics.....	64
2.4.2.2. Case 5: Voltage Sag and Frequency Step Change.....	69
2.4.2.3. Case 6: Triangle-Modulated Voltage Flicker.....	70
2.4.2.4. Case 7: Square-Modulated Voltage Flicker	75
2.4.2.5. Case 8: Flicker and Frequency Drift.....	80
2.4.2.6. Case 9: Noise Immunity.....	83
2.5. Conclusion.....	84
Chapter 3 : Real-Time Power System Phasors and Harmonics Estimation Using a New Decoupled Recursive-Least-Squares Technique.....	85
3.1. Introduction	85
3.2. Recursive-Least-Squares Technique for Harmonics and Phasors Estimation	88
3.3. Decoupled Recursive-Least-Squares Technique	95
3.3.1. Initializing the DRLS Technique.....	100
3.3.2. Comparison between RLS and DRLS Techniques.....	103
3.3.3. Simulation Studies	104
3.3.3.1. Case 1: Fault Simulation in MATLAB-Simulink	104
3.3.3.2. Case 2: Noise Immunity.....	112
3.3.4. Real-Time DSP Implementation	113
3.3.4.1. Investigating Turnaround-Time on Different DSP Platforms.....	113
3.3.4.2. Case 3: Real-Time Harmonics Estimation.....	116
3.4. Synchronized Phasors and Instantaneous Symmetrical Components Extraction by Using the DRLS Technique	119
3.4.1. Simulation Studies	125
3.4.1.1. Case 4: Fault Condition	125

3.4.1.2. Case 5: Frequency Drift in a Balanced Three-Phase System.....	137
3.4.1.3. Case 6: Frequency Drift in an Unbalanced Three-Phase System.....	142
3.4.2. Investigating Turnaround-Time on Different DSP Platforms.....	148
3.5. Conclusion.....	150
Chapter 4 : Real-Time Slow Sampling Estimation of Harmonics/Interharmonics and Phasors	152
4.1. Introduction	152
4.2. Staggered Undersampling Concept	155
4.3. Modified Gradient Search Algorithm for Harmonics/Interharmonics Estimation	157
4.3.1. Harmonics Grouping and Smoothing	162
4.3.2. Simulation Results	163
4.3.2.1. Case 1: Harmonics and Interharmonics	163
4.3.2.2. Case 2: Out-of-Resolution-Step Interharmonic Contamination.....	166
4.3.2.3. Case 3: Non-Stationary Load and Estimation Latency.....	169
4.3.3. Real-Time Implementation	177
4.3.3.1. Case 4: Quasi-Stationary Third Harmonic Variation	181
4.3.3.2. Case 5: Harmonics Estimation	185
4.3.3.3. Case 6: Desktop Personal Computer Load	188
4.4. Extending the Undersampling Concept for Synchrophasor Estimation in Wide-Area Measurement Systems.....	192
4.4.1. Synchrophasor Definition	195
4.4.2. Extended Staggered Undersampling for Synchrophasor Detection	197
4.4.2.1. Effect of Time Reference.....	198
4.4.2.2. Extended Staggered Undersampling.....	200
4.4.2.3. Proposed Synchrophasor Detection Technique.....	205
4.4.3. Simulation Results	207
4.4.3.1. Case 7: Numerical Simulation.....	207
4.4.3.2. Case 8: MATLAB-Simulink Simulation	209
4.5. Conclusion.....	213
Chapter 5 : Slow Sampling Real-time Optimization Approach to Estimate Power System Frequency.....	215
5.1. Introduction	215

5.2. Newton-Type Algorithm and Least Squares Method for Power System Frequency Estimation	218
5.3. Mathematical Development	229
5.3.1. Newton Technique Algorithm Development	229
5.3.2. Least-Squares Technique Development	231
5.4. Methods for Comparison.....	233
5.4.1. DSPOC Algorithm to Estimate Power System Frequency	233
5.4.2. Phase-Locked-Loop Technique.....	234
5.5. Simulation Studies	235
5.5.1. Case 1: Frequency Step Change	236
5.5.2. Case 2: Voltage Step.....	237
5.5.3. Case 3: Harmonic/Interharmonic Contamination.....	238
5.5.4. Case 4: Noise Immunity.....	242
5.5.5. Case 5: Switching Notches and Harmonics	247
5.6. Real-Time Implementation	250
5.6.1. Case 6: Non-Sinusoidal Waveform Frequency Tracking	250
5.6.2. Case 7: Stepwise Dynamic Frequency Change	252
5.6.3. Case 8: Power System Simulator Frequency Monitoring.....	254
5.6.4. Case 9: Harmonic Contamination and Ramp Frequency Variation	261
5.7. Conclusion.....	264
Chapter 6 : Summary and Conclusion	265
6.1. Conclusion.....	267
6.2. Future Research	271
Appendix: Total Vector Error	274
References	276

List of Figures

Figure 1.1. ANF structure [48].	3
Figure 1.2. EPLL structure [52].	6
Figure 2.1. Schematic definition of the moving time slots to collect data and perform frequency estimation.	38
Figure 2.2. RDSPOC frequency estimation algorithm.	42
Figure 2.3. The proposed least-squares-Kalman (LSK) algorithm to predict the instantaneous flicker level (IFL).	54
Figure 2.4. Case 1: ± 0.1 Hz frequency drift in a sinusoidal voltage (a) instantaneous line-to-neutral voltage waveform (b) estimated fundamental frequency voltage amplitude (c) estimated voltage frequency.	57
Figure 2.5. Case 1: 1 Hz frequency drift in a sinusoidal voltage (a) instantaneous line-to-neutral voltage waveform (b) estimated fundamental frequency voltage amplitude (c) estimated voltage frequency.	58
Figure 2.6. Case 2: 3 Hz frequency drift in presence of harmonic contamination (a) instantaneous line-to-neutral voltage waveform (b) estimated fundamental frequency voltage amplitude (c) estimated voltage frequency.	60
Figure 2.7. Case 3: voltage sag and 2 Hz frequency drift (a) instantaneous line-to-neutral voltage waveform (b) estimated fundamental frequency voltage amplitude (c) estimated voltage frequency.	62
Figure 2.8. Case 4: ± 0.1 Hz frequency drift in a sinusoidal voltage (a) instantaneous line-to-neutral voltage waveform (b) estimated fundamental frequency voltage amplitude (c) estimated voltage frequency.	65
Figure 2.9. Case 4: 1 Hz frequency drift in a sinusoidal voltage (a) instantaneous line-to-neutral voltage waveform (b) estimated fundamental frequency voltage amplitude (c) estimated voltage frequency.	66
Figure 2.10. Case 4: 3 Hz frequency drift in presence of harmonic contamination, The harmonic spectrum of voltage waveform for 50 Hz fundamental frequency.	67

Figure 2.11. Case 4: 3 Hz frequency drift in presence of harmonic contamination (a) instantaneous line-to-neutral voltage waveform (b) estimated fundamental frequency voltage amplitude (c) estimated voltage frequency.....	68
Figure 2.12. Case 5: voltage sag and -1 Hz frequency drift (a) instantaneous line-to-neutral voltage waveform (b) estimated voltage envelope (c) estimated voltage frequency.....	69
Figure 2.13. Case 6: 5 Hz triangular flicker with the modulation depth of 2% (a) line-to-neutral instantaneous voltage waveform (b) instantaneous flicker level (IFL) estimation.....	71
Figure 2.14. Case 6: 5 Hz triangular flicker with the modulation depth of 2% (a) estimated voltage envelope before post-filtering (b) estimated voltage envelope after post-filtering (c) estimated voltage frequency.....	72
Figure 2.15. Case 6: 4.167 Hz triangular flicker with the modulation depth of 2% (a) line-to-neutral instantaneous voltage waveform (b) instantaneous flicker level (IFL) estimation.....	73
Figure 2.16. Case 6: 4.167 Hz triangular flicker with the modulation depth of 2% (a) estimated voltage envelope before post-filtering (b) estimated voltage envelope after post-filtering (c) estimated voltage frequency.....	74
Figure 2.17. Case 7: 2% square-wave flicker at the modulation frequency of 5 Hz (a) line-to-neutral instantaneous voltage waveform (b) instantaneous flicker level (IFL) estimation.....	76
Figure 2.18. Case 7: 2% square-wave flicker at the modulation frequency of 5 Hz (a) estimated voltage envelope before post-filtering (b) estimated voltage envelope after post-filtering (c) estimated voltage frequency.....	77
Figure 2.19. Case 4: 2% square-wave flicker at the modulation frequency of 4.167 Hz (a) line-to-neutral instantaneous voltage waveform (b) instantaneous flicker level (IFL) estimation.....	78
Figure 2.20. Case 7: 2% square-wave flicker at the modulation frequency of 4.167 Hz (a) estimated voltage envelope before post-filtering (b) estimated voltage envelope after post-filtering (c) estimated voltage frequency.....	79
Figure 2.21. Case 8: flicker estimation in presence of frequency drift (a) instantaneous line-to-neutral voltage waveform at 49 Hz (b) instantaneous flicker level (IFL) estimation.....	81

Figure 2.22. Case 8: flicker estimation in presence of frequency drift (a) estimated voltage envelope before post-filtering (b) estimated voltage envelope after post-filtering (c) estimated voltage frequency.	82
Figure 3.1. The proposed real-time DRLS technique modular implementation.....	100
Figure 3.2. DRLS initialization from zeros by using 1%, 20%, and 100% of the 2×2 identity matrix for the initial value of input-waveform correlation matrix.	103
Figure 3.3. Case 1: Fault simulation, Simulated power system in the MATLAB-Simulink software.	106
Figure 3.4. Case 1: Fault simulation (a) three-phase line-to-neutral voltage waveforms (b) three-phase line current waveforms.....	106
Figure 3.5. Case 1: Fault simulation (a) phase-A fundamental frequency line current amplitude estimation (b) phase-A fundamental frequency line current phase-angle estimation.....	107
Figure 3.6 Case 1: Fault simulation (a) phase-A-to-neutral fundamental frequency voltage amplitude estimation (b) phase-A-to-neutral fundamental frequency voltage phase-angle estimation.....	108
Figure 3.7. Case 1: Fault simulation (a) phase-B fundamental frequency line current amplitude estimation (b) phase-B fundamental frequency line current phase-angle estimation.....	109
Figure 3.8. Case 1: Fault simulation (a) phase-B-to-neutral fundamental frequency voltage amplitude estimation (b) phase-B-to-neutral fundamental frequency voltage phase-angle estimation.....	110
Figure 3.9. Case 1: Fault simulation (a) phase-C fundamental frequency line current amplitude estimation (b) phase-C fundamental frequency line current phase-angle estimation.....	111
Figure 3.10. Case 1: Fault simulation (a) phase-C-to-neutral fundamental frequency voltage amplitude estimation (b) phase-C-to-neutral fundamental frequency voltage phase-angle estimation.....	112
Figure 3.11. Case 3: Real-time harmonics estimation (a) line-to-neutral voltage waveform (b) fundamental component amplitude estimation (c) 5 th harmonic amplitude estimation.....	117
Figure 3.12. Case 3: Real-time harmonics estimation (a) 7 th harmonic amplitude estimation (b) 11 th harmonic amplitude estimation (c) 13 th harmonic amplitude estimation.....	118
Figure 3.13. Implementation of the modified three-phase RDSPOC frequency estimation technique. ...	123
Figure 3.14. DRLS technique real-time implementation for instantaneous synchronized symmetrical components extraction.	124

Figure 3.15. Case 4: Fault condition, Simulated radial power distribution system in MATLAB-Simulink.	127
Figure 3.16. Case 4: phase-A-to-ground fault simulation (a) three-phase current waveforms (b) three- phase voltage waveforms.	128
Figure 3.17. Case 4: phase-A-to-ground fault simulation (a) estimate of current instantaneous zero sequence (b) estimate of current instantaneous positive sequence (c) estimate of current instantaneous negative sequence.....	129
Figure 3.18. Case 4: phase-A-to-ground fault simulation (a) estimates of voltage instantaneous zero sequence (b) estimates of voltage instantaneous positive sequence (c) estimates of voltage instantaneous negative sequence.....	130
Figure 3.19. Case 4: phase-A-to-ground fault simulation (a) phase-A current estimate of amplitude (b) phase-A current estimate of phase-angle.	131
Figure 3.20. Case 4: phase-A-to-ground fault simulation (a) phase-B current amplitude estimate (b) phase- B current phase-angle estimate.....	132
Figure 3.21. Case 4: phase-A-to-ground fault simulation (a) phase-C current estimate of amplitude (b) phase-C current estimate of phase-angle.	133
Figure 3.22. Case 4: phase-A-to-ground fault simulation (a) phase-A-to-neutral voltage estimate of amplitude (b) phase-A-to-neutral voltage estimate of phase-angle.	134
Figure 3.23. Case 4: phase-A-to-ground fault simulation (a) phase-B-to-neutral voltage estimate of amplitude (b) phase-B-to-neutral voltage estimate of phase-angle.	135
Figure 3.24. Case 4: phase-A-to-ground fault simulation (a) phase-C-to-neutral voltage estimate of amplitude (b) phase-C-to-neutral voltage estimate of phase-angle.	136
Figure 3.25. Case 5: Frequency drift in a balanced three-phase system, Three-phase voltage waveforms.	137
Figure 3.26. Case 5: Frequency drift in a balanced three-phase system (a) estimate of zero sequence (b) estimate of the positive sequence (c) estimate of the negative sequence.	138

Figure 3.27. Case 5: Frequency drift in a balanced three-phase system (a) phase-A-to-neutral amplitude estimate (b) phase-A-to-neutral phase-angle estimate.	139
Figure 3.28. Case 5: Frequency drift in a balanced three-phase system (a) phase-B-to-neutral amplitude estimate (b) phase-B-to-neutral phase-angle estimate.	140
Figure 3.29. Case 5: Frequency drift in a balanced three-phase system (a) phase-C-to-neutral amplitude estimate (b) phase-C-to-neutral phase-angle estimate.	141
Figure 3.30. Case 6: Frequency drift in an unbalanced three-phase system, Three-phase voltage waveforms.	143
Figure 3.31. Case 6: Frequency drift in an unbalanced three-phase system (a) estimate of zero sequence (b) estimate of the positive sequence (c) estimate of the negative sequence.	144
Figure 3.32. Case 6: Frequency drift in an unbalanced three-phase system (a) phase-A-to-neutral amplitude estimate (b) phase-A-to-neutral phase-angle estimate.	145
Figure 3.33. Case 6: Frequency drift in an unbalanced three-phase system (a) phase-B-to-neutral amplitude estimate (b) phase-B-to-neutral phase-angle estimate.	146
Figure 3.34. Case 6: Frequency drift in an unbalanced three-phase system (a) phase-C-to-neutral amplitude estimate (b) phase-C-to-neutral phase-angle estimate.	147
Figure 4.1. Real-time MGS harmonics/interharmonics estimation algorithm.	161
Figure 4.2. Realization of a digital smoothing low-pass filter.	163
Figure 4.3. Case 1: Harmonics and interharmonics, Instantaneous voltage waveform contaminated by harmonics and interharmonics at the sampling frequency of 200 kHz.	164
Figure 4.4. Case 1: Harmonics and interharmonics, Instantaneous voltage waveform contaminated by harmonics and interharmonics at the sampling frequency of 105.2632 Hz.	164
Figure 4.5. Case 1: Harmonics and interharmonics, Harmonics and interharmonics rms estimation (at 105.2632 Hz sampling frequency).	165
Figure 4.6. Case 2: Out-of-resolution-step interharmonic contamination, Voltage waveform contaminated by the 177.5 Hz interharmonic component at the sampling frequency of 200 kHz.	167

Figure 4.7. Case 2: Out-of-resolution-step interharmonic contamination, Voltage waveform contaminated by the 177.5 Hz interharmonic component at the sampling frequency of 105.2632 Hz.	167
Figure 4.8. Case 2: Out-of-resolution-step interharmonic contamination, The fundamental frequency rms voltage estimation in presence of the 177.5 Hz interharmonic (at 105.2632 Hz sampling frequency). ...	168
Figure 4.9. Case 2: Out-of-resolution-step interharmonic contamination, The fundamental frequency phase-angle estimation in presence of the 177.5 Hz interharmonic (at 105.2632 Hz sampling frequency).	168
Figure 4.10. Case 3: Non-stationary load and estimation latency, Non-stationary current waveform.	171
Figure 4.11. Case 3: Non-stationary load and estimation latency, Non-stationary voltage waveform.....	171
Figure 4.12. Case 3: Non-stationary load and estimation latency (a) fundamental frequency voltage amplitude estimations at the downsampling factors of 19 and 3 (b) third harmonic voltage amplitude estimations at the downsampling factors of 19 and 3.....	172
Figure 4.13. Case 3: Non-stationary load and estimation latency (a) fifth harmonic voltage amplitude estimations at the downsampling factors of 19 and 3 (b) seventh harmonic voltage amplitude estimations at the downsampling factors of 19 and 3.....	173
Figure 4.14. Case 3: Non-stationary load and estimation latency (a) fundamental frequency current amplitude estimations at the downsampling factors of 19 and 3 (b) third harmonic current amplitude estimations at the downsampling factors of 19 and 3.....	174
Figure 4.15. Case 3: Non-stationary load and estimation latency (a) fifth harmonic current amplitude estimations at the downsampling factors of 19 and 3 (b) seventh harmonic current amplitude estimations at the downsampling factors of 19 and 3.....	175
Figure 4.16. Case 3: Non-stationary load and estimation latency, Active power estimation at the downsampling factors of 19 and 3.	176
Figure 4.17. Schematic of the laboratory setup for real-time implementation.	180
Figure 4.18. Case 4: Quasi-stationary third harmonic variation, Instantaneous current waveform sensed by a current transducer and captured by DS1104 at the sampling frequency of 20 kHz.....	182

Figure 4.19. Case 4: Quasi-stationary third harmonic variation, Instantaneous current waveform sensed by a current transducer and captured by DS1104 at the sampling frequency of 105.2632 Hz.	183
Figure 4.20. Case 4: Quasi-stationary third harmonic variation, The dc offset estimation from the current transducer output signal (at 105.2632 Hz sampling frequency).	183
Figure 4.21. Case 4: Quasi-stationary third harmonic variation, Third harmonic group rms voltage C_3 estimation (at 105.2632 Hz sampling frequency).	184
Figure 4.22. Case 4: Quasi-stationary third harmonic variation, Spectral estimation (at 105.2632 Hz sampling frequency).	184
Figure 4.23. Case 5: Harmonics estimation, Line-to-neutral instantaneous voltage waveform which is captured by a digital oscilloscope at the sampling frequency of 250 kHz.	186
Figure 4.24. Case 5: Harmonics estimation, Undersampled line-to-neutral instantaneous voltage waveform which is captured by DS1104 at 105.2632 Hz sampling frequency.	186
Figure 4.25. Case 6: Desktop personal computer load (a) current waveform (b) a magnified section of the current waveform.	189
Figure 4.26. Case 6: Desktop personal computer load (a) phase-to-neutral voltage waveform (b) a magnified section of the phase-to-neutral voltage waveform.	190
Figure 4.27. Case 6: Desktop personal computer load, The fundamental frequency current amplitude estimation.	190
Figure 4.28. Case 6: Desktop personal computer load, The fundamental frequency voltage amplitude estimation.	191
Figure 4.29. Case 6: Desktop personal computer load, Active power estimation.	191
Figure 4.30. Case 6: Desktop personal computer load, Reactive power estimation.	192
Figure 4.31. (a) Voltage waveform contaminated with the 3 rd harmonic (b) undersampled unshuffled waveform (c) shuffled map of undersampled waveform.	202
Figure 4.32. (a) Synchrophasor detection IEEE Standard C37.118 (b) Proposed technique to utilize the communication link to transfer samples of \hat{d} to the data centre.	206

Figure 4.33. Case 7: Numerical simulation (a) voltage waveform (b) amplitude estimation (c) phase-angle estimation.	208
Figure 4.34. Case 8: MATLAB-Simulink simulation, IEEE 14-bus test system.	210
Figure 4.35. Case 8: MATLAB-Simulink simulation, Three-phase current waveforms flowing from bus 2 to bus 4.	210
Figure 4.36. Case 8: MATLAB-Simulink simulation (a) voltage rms at bus 5 (b) voltage rms at bus 4 (c) phase-angle of bus 5 voltage with respect to bus 4.	211
Figure 4.37. Case 8: MATLAB-Simulink simulation (a) current rms flowing from bus 3 to bus 4 (b) current rms flowing from bus 4 to bus 5 (c) phase-angle of current flowing from bus 3 to bus 4 with respect to bus 4 (d) phase-angle of current flowing from bus 4 to bus 5 with respect to bus 4.	212
Figure 5.1. Principle of frequency estimation from the phase-angle.	218
Figure 5.2. (a) Magnitude response of the peak notch filter (b) Phase response of the peak notch filter.	220
Figure 5.3. NTA-LS algorithm to estimate power system frequency.	228
Figure 5.4. Recursive implementation of the DSPOC frequency estimation.	234
Figure 5.5. MATLAB-Simulink single-phase PLL [216].	235
Figure 5.6. Case 1: frequency step change, Frequency estimation at 285.71 Hz sampling frequency by the NTA-LS, NTA, DSPOC, and PLL techniques.	236
Figure 5.7. Case 2: voltage step (a) frequency estimation at 285.71 Hz sampling frequency by the NTA-LS, NTA, DSPOC, and PLL techniques (b) voltage waveform.	237
Figure 5.8. Case 3: Harmonic contamination, Instantaneous voltage waveform captured at 10 kHz sampling frequency.	239
Figure 5.9. Case 3: Harmonic contamination, Frequency estimation at 285.71 Hz sampling frequency by the NTA-LS, NTA, DSPOC, and PLL techniques.	240
Figure 5.10. Case 3: Interharmonic contamination, Frequency estimation at 285.71 Hz sampling frequency by the NTA-LS, NTA, DSPOC, and PLL techniques.	241
Figure 5.11. Case 4: Noise immunity, Voltage waveform contaminated with a zeros mean Gaussian noise, SNR=10 dB, captured at 10 kHz.	243

Figure 5.12. Case 4: Noise immunity, The estimated frequency in presence of a Gaussian noise, $SNR=10$ dB, estimation at 285.71 Hz sampling frequency.	244
Figure 5.13. Case 5: Switching notches and harmonics, Simulated dc motor powered by a six-pulse thyristor converter.	248
Figure 5.14. Case 5: Switching notches and harmonics, Phase-A line-to-neutral voltage waveform captured at 10 kHz.	249
Figure 5.15. Case 5: Switching notches and harmonics Frequency estimation at 285.71 Hz sampling frequency by the NTA-LS, NTA, DSPOC, and PLL techniques.	249
Figure 5.16. Case 6: Non-sinusoidal waveform frequency tracking (a) the triangle voltage waveform produced by a function generator captured at 100 kHz by a digital oscilloscope (b) the triangle voltage waveform produced by a function generator captured at 285.71 Hz by the dSPACE.	251
Figure 5.17. Case 6: Non-sinusoidal waveform frequency tracking, Frequency estimation at 285.71 Hz sampling frequency.	252
Figure 5.18. Case 7: Stepwise frequency change between 46.0 Hz and 54.0 Hz (a) the typical sinusoidal voltage waveform produced by a function generator which is captured at 100 kHz sampling frequency by a digital oscilloscope (b) the typical sinusoidal voltage waveform produced by a function generator which is captured at 285.71 Hz sampling frequency by the dSPACE.	253
Figure 5.19. Case 7: Stepwise frequency change between 46.0 Hz and 54.0 Hz, Frequency estimation at 285.71 Hz sampling frequency.	254
Figure 5.20. Case 8: Power system simulator frequency monitoring, Single-line diagram of the power system for the frequency estimation experiment on the PSS1.	256
Figure 5.21. Case 8: Power system simulator frequency monitoring, The power system simulator PSS1 in a laboratory setup for real-time power system frequency measurement experiment.	257
Figure 5.22. Case 8: Power system simulator frequency monitoring (a) the typical phase-A line-to-neutral voltage captured at the sampling frequency of 100 kHz by a digital oscilloscope (b) the typical phase-A line-to-neutral voltage captured at the sampling frequency of 285.71 Hz by the dSPACE.	258

Figure 5.23. Case 8: resistive load switching (a) phase-A line-to-neutral voltage waveform samples at 285.71 Hz sampling frequency (b) frequency estimation at 285.71 Hz sampling frequency.....	259
Figure 5.24. Case 8: step frequency change (a) phase-A line-to-neutral voltage waveform samples at 285.71 Hz sampling frequency (b) frequency estimation at 285.71 Hz sampling frequency.....	260
Figure 5.25. Case 9: Harmonic contamination and ramp frequency variation (a) line-to-neutral voltage waveform captured at 100 kHz sampling frequency by a digital oscilloscope (b) line-to-neutral voltage waveform captured at 285.71 Hz sampling frequency by the dSPACE.....	262
Figure 5.26. Case 9: Harmonic contamination and ramp frequency variation (a) undersampled line-to-neutral voltage waveform samples at 285.71 Hz sampling frequency (b) frequency estimation at 285.71 Hz sampling frequency.....	263

List of Abbreviations

ANF	Adaptive notch filter
ADALINE	Adaptive linear combiner
ANN	Artificial neural network
AMI	Advanced metering infrastructure
A/D	Analogue-to-digital
DFT	Discrete Fourier transform
DSP	Digital signal processor
DG	Distributed generation
DSPOC	Decomposition of single-phase into orthogonal components
DRLS	Decoupled recursive-least-squares
EPLL	Enhanced phase-locked loop
EAF	Electric arc furnaces
FIR	Finite-impulse-response
FDR	Frequency disturbance recorder
GPS	Global positioning system
HT	Hilbert transform
HPF	High-pass filter
IFL	Instantaneous flicker level
IEC	International Electrotechnical Commission
IEEE	Institute of Electrical and Electronics Engineers
IED	Intelligent electronic device

KF	Kalman filter
LS	Least-squares
LSK	Least-squares-Kalman
LMS	least mean square
LR-WPAN	low-speed low-rate wireless personal area network
LPF	Low-pass filter
MGS	Modified gradient search
NBN	National broadband network
NTA	Newton-type algorithm
NASPI	North American Synchrophasor Initiative
NTA-LS	Newton-type algorithm and the least-squares
PMU	Phasor measurement unit
PC	Personal computer
PLL	Phase-locked loop
PEV	Plug-in electric vehicle
PQ	Power quality
QPLL	Quadrature phase-locked loop
RLS	Recursive-least-squares
RDFT	Recursive discrete Fourier transform
R&D	Research and development
RTU	Remote terminal unit
SCADA	Supervisory control and data acquisition

SNR	Signal-to-noise ratio
TVE	Total vector error
UTC	Universal time coordinate
VFD	variable frequency drive
VE	Voltage envelope
WAMS	Wide-area measurement system
WT	Wavelet transform
WSE	Weighted squares error
WAC	Wide-area control

List of Tables

Table 1.1. Summary of ANF and EPLL Techniques: References, Merits, and Demerits.	24
Table 1.2. Summary of ADALINE and DFT/RDFT Techniques: References, Merits, and Demerits.	25
Table 1.3. Summary of LS and KF Techniques: References, Merits, and Demerits.	25
Table 1.4. Summary of NTA and RLS Techniques: References, Merits, and Demerits.	26
Table 2.1. Case 2: Phasor Estimation in Presence of Frequency Drift and Harmonics, Harmonics Component of the Voltage Waveform.	59
Table 2.2. Average Steady State Frequency Estimation Error Absolute Value for Different Levels of SNR and Frequency Drift of -1 Hz, Case 9.	83
Table 2.3. Average Steady State Amplitude Estimation Error Absolute Value for Different Levels of SNR and Frequency Drift of -1 Hz, Case 9.	83
Table 3.1. Case 2: Average Value of Absolute Estimation Error Percentage for Different SNR Levels.	113
Table 3.2. Turnaround-Time on DS1104 R&D Control Board (μ s).	115
Table 3.3. Turnaround-time on DS1103 R&D Control Board (μ s).	116
Table 3.4. Case 6: Frequency Drift in an Unbalanced Three-Phase System, Unbalanced System Information.	143
Table 3.5. Turnaround-time on DS1104 R&D control board (μ s).	149
Table 3.6. Turnaround-time on DS1103 R&D control board (μ s).	150
Table 4.1. Estimation Latency for Different Downsampling Factors (δ) and Spectral Estimation Frequency Resolutions (f_r).	176
Table 4.2. Case 5: Harmonics Estimation.	187
Table 5.1. Case 4: Noise Immunity for Coloured Noise and Compliance Level 0, <i>TVE</i> for Different Levels of Coloured Noise for 0.5 Hz Frequency Drift.	245
Table 5.2. Case 4: Noise Immunity for Coloured Noise and Compliance Level 1, <i>TVE</i> for Different Levels of Coloured Noise for -5.0 Hz Frequency Drift.	245
Table 5.3. Case 4: Noise Immunity for Cyclostationary Noise and Compliance Level 0, <i>TVE</i> for Different Levels of Cyclostationary Noise for -0.5 Hz Frequency Drift.	246

Table 5.4. Case 4: Noise Immunity for Cyclostationary Noise and Compliance Level 1, <i>TVE</i> for Different Levels of Cyclostationary Noise for 5.0 Hz Frequency Drift.....	246
Table 5.5. Case 5: Switching notches and harmonics, Harmonic Content of the Voltage Waveform at B_1	248
Table 5.6. Case 8: Power System Simulator Frequency Monitoring Parameter Values of the Simulated Power System Components for Figure 5.20 at 50.0 Hz.	257

List of Parameters

$A_{dc}(k)$	DC component of the voltage/current waveform
$A_i(k)$	Amplitude of the i^{th} harmonic
$A_1(k)$	Fundamental frequency amplitude
$\bar{A}_1(k+1)$	Predicted value of $A_1(k+1)$ in the flicker model
$\hat{A}_i(k)$	Estimate of $A_i(k)$
$\hat{A}_{dc}(k)$	Estimate of $A_{dc}(k)$
$\bar{\hat{A}}_i$	Average local/global value of $\hat{A}_i(k)$
\hat{A}_{odc}	Estimate of the dc component by the DRLS technique
$B_{IFL}(n)$	Extended Kalman filter gain matrix in the flicker model
B_{KF}	KF Gain matrix
$b_{IFL}(n)$	Measurement of the desired signal in the Kalman model for flicker
$\hat{b}_{IFL}(n)$	Nominal IFL output of the extended KF
C_g	RMS value of the harmonic group g
$d_{KF}(n)$	Kalman filter estimation function
$d(k)$	Measured voltage/current waveform sample
d_{IFL}	Estimation function of Kalman filter for IFL prediction
$\hat{d}(k)$	Estimate of $d(k)$

d^0	Instantaneous zero sequence component of voltage or current estimate by the DRLS technique
d^+	Instantaneous positive sequence component of voltage or current estimate by the DRLS technique
d^-	Instantaneous negative sequence component of voltage or current estimate by the DRLS technique
D_{KF}	KF Estimation matrix
D_{IFL}	Extended Kalman estimation matrix for IFL prediction
$\hat{D}_{LS}(k)$	LS estimation vector
$D_{LS}(k)$	LS input vector
$\hat{d}_{RLS}(k)$	Estimate of $d(k)$ by the RLS algorithm
$D_{KF}(n)$	Extended Kalman estimation matrix
$D_{NTA}(k)$	NTA input vector
$\hat{D}_{NTA}(k)$	NTA estimation vector
$D_{RLS}(k)$	Weighted least-squares input vector for RLS technique
$\hat{D}_{RLS}(k)$	Weighted least-squares estimation vector for RLS technique
$\hat{d}_i(k)$	Estimate of the i^{th} harmonic component in the DRLS technique
$\hat{d}_{dc}(k)$	Estimate of the dc component in the DRLS technique
Det	Determinant
$d_u(k)$	Undersampled waveform

$\hat{d}_u(k)$	Estimate of $d_u(k)$
e_{ANF}	ANF estimation error
$e_{RLS}(k)$	RLS estimation error
$E_{RLS}(k)$	Weighted error vector of RLS
E_{NTA}	NTA estimation error vector
$e_{MGS}(k)$	Estimation error
$e'_{MGS}(k)$	Rate of change in the estimation error of MGS
$e_{NTA}(k)$	NTA estimation error value
$e_{DRLS}(k)$	Estimation error of the DRLS technique
$e_{ADA}(k)$	Estimation error of the ADALINE technique
f_s	Sampling frequency
f_o	Nominal fundamental frequency of power system
f_r	Frequency resolution of MGS algorithm
$F_{LS}(k)$	LS Objective function of NTA-LS algorithm
f_{N_o}	The dense sampling frequency according to the Nyquist-Shannon theorem
f'_{N_o}	The dense sampling frequency for extended staggered undersampling
$f_d(k)$	Frequency drift
$G_{LS}(k)$	LS model goal function

g_1	EPLL amplitude estimation regulation factor
g_2	EPLL phase detection regulation factor
g_3	EPLL frequency tracking regulation factor
$\nabla G_{LS}(k)$	Gradient of the LS algorithm goal function G_k
$G_{WSE}(k)$	WSE goal function
$G_1(k)$	Primary objective function of MGS
$G_2(k)$	Secondary objective function MGS
$\nabla G_1(k)$	Gradient of $G_1(k)$
$\nabla G_2(k)$	Gradient of $G_2(k)$
$G_{NTA}(k)$	Goal function of NTA
$\nabla G_{NTA}(k)$	Gradient of $G_{NTA}(k)$
$\nabla^2 G_{NTA}(k)$	Hessian of $G_{NTA}(k)$
$h_{NTA}(X_{NTA}(k))$	NTA estimation function
$H_{LS}(k)$	LS Jacobian of NTA-LS algorithm
$I_{sl}(k)$	Low frequency component of $I_s(kT_s)$
$I_{cl}(k)$	Low frequency component of $I_c(kT_s)$
i	Harmonic order
$I_s(k)$	In-phase component for RDSPOC frequency estimation
$I_c(k)$	Quadrature-phase component for RDSPOC frequency estimation

$I_{4 \times 4}$	The 4 by 4 identity matrix
I_{rms}	RMS value of current waveform
In_i	In-phase component of the i^{th} harmonic in DFT technique
$J_{LS}(k)$	Jacobian matrix for LS technique
$J_{NTA}(k)$	Jacobian matrix for NTA
k	Sampling instance index
L	Length of LS residual vector
m	LS estimation model order in the NTA-LS algorithm
M	LSK model order for envelope estimation
$v_F(k)$	Flicker source in the flicker model
N	Total number of harmonics
N_G	Model order of MGS algorithm
N_o	Number of samples in one period of the fundamental frequency component waveform
n	State index number of KF
N_{rms}	Number of samples which are used for rms calculation
N_C	KF measurement noise covariance
N_{CIFL}	Extended KF measurement noise covariance for IFL prediction
$O(k, 1: 2N + 1)$	MGS observation vector
\vec{O}_{ANF}	Periodic orbit of ANF

$p_1(k)$	Steepest descent search direction for $G_1(k)$
$p_2(k)$	Steepest descent search direction for $G_2(k)$
$P_{IFL}^-(n)$	Kalman filter predicted error covariance matrix for flicker modelling
$\hat{P}_{IFL}(n)$	Estimated error covariance matrix of the Kalman filter for IFL estimation
P_{KF}^-	KF predicted error covariance matrix
\hat{P}_{KF}	KF estimated error covariance matrix
$P_{RLS}(k)$	Cross-correlation between measurement and input-waveform of the RLS technique
Q_{IFL}	Process noise covariance matrix of the Kalman filter for IFL estimation
Q_{KF}	Process noise covariance matrix of the Kalman filter
q_l	Observation instance of the LS Jacobian matrix
Qd_i	Quadrature-phase component of the i^{th} harmonic in the DFT technique
$R_{LS}(k)$	Vector of residual values for LS technique
$R(k)$	Input-waveform correlation matrix of the RLS technique
$\bar{R}_{i,j}$	Average value of R at the i^{th} row and j^{th} column
$[R_i(k)]$	The i^{th} diagonal matrix in the RLS model
$r_{LS}(k)$	LS estimation residual term

$R_{dc}(k)$	The dc component of the RLS input-waveform correlation matrix
$R_o(k)$	Input-waveform correlation matrix of the DRLS technique
$[R_{oi}(k)]$	Input-waveform correlation matrix for the i^{th} unit in the DRLS technique
$R_{odc}(k)$	Input-waveform correlation matrix for dc component estimation unit in the DRLS technique
$R_{oi}^{-1}(k)$	Inverse of $[R_{oi}(k)]$ in the DRLS technique
$R_{odc}^{-1}(k)$	Inverse matrix of $R_{odc}(k)$ in the DRLS technique
$\nabla r_{LS}(k)$	Gradient of the residual term in the LS technique
$R_{LS}(k)$	LS algorithm residual vector
S_l	Amplitude of the l^{th} spectral component in the MGS algorithm
S_{dc}	DC offset in the MGS algorithm
SP	Solution space for staggered undersampling shuffling map
SP_1	Solution space for extended staggered undersampling shuffling map
t_k	Time of observation
t_q	Observation instance of the LS Jacobian matrix
T_s	Sampling period
T_m	Memory time constant of RLS technique
T_o	Power system fundamental frequency period

T_{ngst}	The sampling period equivalent to the Nyquist rate
t	Continuous value of observation instance
T_o	Nominal fundamental frequency period
T	Indicating transposition of a vector when appears as a superscript
T_d	Difference between the DSP internal clock and UTC
t_c	Communication network time reference
U_c	Fundamental carrier signal in the flicker model
U_A	ADALINE input vector
$v(k)$	Voltage waveform at the k^{th} sample
$\hat{v}(k)$	Estimate of $v(kT_s)$
$v_F(k)$	Instantaneous flicker level
$V_{LS}(k)$	LS algorithm input voltage vector
$v_{AM}(kT_s)$	Amplitude modulated fundamental frequency component in the flicker model
$v(k)$	Voltage waveform
v	The α component of the three-phase-to- $\alpha\beta$ Clarke transformation
v_1	In-phase component of v
v_2	Quadrature-phase component of v
$V_{NTA}(k)$	Amplitude of the fundamental frequency in the NTA
$V_{NTAdc}(k)$	DC offset in the NTA

$W(k)$	Weight vector of the ADALINE technique
$x_{IFL1}(n)$	Estimated IFL at the n^{th} state
$x_{IFL2}(n)$	Estimated quadrature component of IFL at the n^{th} state
$x_{IFL3}(n)$	Estimated IFL total phase-angle at the n^{th} state
$x_{IFL4}(n) _{n=k}$	Estimation of $U_c(k)$ in the IFL estimation
$x_{IFL}(n)$	Kalman state vector for flicker prediction
$\hat{x}_{IFL}(n)$	Estimation of $x_{IFL}(n)$ by the extended Kalman filter
$\bar{x}_{IFL}(n+1)$	Predicted state vector by the Kalman filter for IFL modelling
$\bar{x}_{KF}(n)$	Predicted state vector by the KF
\hat{x}_{KF}	Estimation vector of the KF
$\hat{X}_{RLS}(k)$	The Jacobian matrix of in the RLS estimation model
$\hat{x}(k)$	Gradient vector of the RLS estimation error
$\hat{x}_i(k)$	i^{th} element of $\hat{x}(k)$
$\hat{x}_{oi}(k)$	Gradient vector of the i^{th} harmonic in the DRLS technique
$\hat{x}_{odc}(k)$	Gradient of the dc component estimation unit of the DRLS technique
X_m	Synchrophasor amplitude
X_i	In-phase component of synchrophasor
X_r	Quadrature-phase component of synchrophasor
\hat{X}_i	Estimate of X_i

\hat{X}_r	Estimate of X_r
$X_{NTA}(k)$	Time-varying estimation vector of NTA
$\Delta X_{NTA}(k)$	NTA correction vector
X_s	Synchrophasor
$y(t)$	ANF estimation variable

List of Greek Symbols

ADA	ADALINE Reduction factor
Γ_1	Primary regulating factor of MGS
Γ_2	Secondary regulating factor of MGS
$\dot{\theta}(k)$	Rate of change in the phase-angle estimation of NTA
$\hat{\Gamma}_{LS}$	LS estimation vector
$\Gamma_{RLS}(k)$	Optimal vector of RLS technique
$\hat{\Gamma}_{RLS}(k)$	RLS Estimation vector
$\hat{\Gamma}_{oi}(k)$	Estimation vector of the i^{th} unit in the DRLS technique
$\hat{\Gamma}_{LS}(k)$	Optimal estimation matrix of LS technique
I_n	Measurement noise in the Kalman model
Δ	Downsampling factor
Δ'	Downsampling factor of the extended staggered undersampling
k	Measurement noise
n	Process noise in the Kalman model
	Oscillation rejection parameter of ANF
$\mathcal{Q}(k)$	Phase-angle of the i^{th} harmonic
$\mathcal{Q}_c(k)$	Constant part of the phase-angle estimation in the NTA-

	LS technique
ϑ^G	Phase-angle of the l^{th} component in the MGS
$\vartheta_i(k)$	Phase-angle of the i^{th} harmonic
$\hat{\vartheta}_i(k)$	Estimate of $\vartheta_i(k)$
$\vartheta_{NTA}(k)$	Voltage phase-angle in the NTA
Θ_k	Phase-angle estimation vector in the NTA
ϑ^G	Phase-angle of the l^{th} spectral component in the MGS algorithm
λ	Forgetting factor (either RLS or DRLS)
$\Lambda_k(1:2N+1)$	MGS Estimation vector
	Frequency tracking adaptation parameter of the ANF
(t)	ANF Power system frequency estimate
$Id(k)_i$	RDFT in-phase recursive variable
$Qd(k)_i$	RDFT quadrature-phase recursive variable
$\Phi_{IFL}(n)$	Kalman state transition function for IFL prediction
$\Phi_{IFL}(n)$	Extended Kalman transition matrix for IFL prediction
Φ_{KF}	KF Transition matrix
$\vartheta_i(k)$	Total phase-angle of the i^{th} harmonic
$\vartheta_1(k)$	Total phase-angle of the fundamental frequency

$\hat{i}_i(k)$	Estimate of $i_i(k)$
θ_s	Synchrophasor phase-angle
Ω_o	Nominal voltage angular frequency
$\Omega_u(k)$	Instantaneous angular frequency drift

Chapter 1 : Introduction

This chapter presents a critical review of the technical literature on power system phasor and frequency estimation, the research motivation, the original contributions of this thesis, the thesis organization, and the list of publications derived from this thesis so far. The rest of this chapter is organized as follows. Section 1.1 reviews the power system parameter estimation techniques and the research motivation is presented in Section 1.2. The statement of originality, thesis organization, and list of publications are presented in Sections 1.3, 1.5, and 1.4 respectively.

1.1. Literature Review

Harmonic contamination has become a concern due to the increasing penetration of nonlinear loads, personal computers (PCs), variable frequency drives (VFDs), electric arc furnaces (EAFs), and distributed generation (DG). All of these new loads impose extra losses due to harmonics, communication interferences, low power factor, heating in transformers and cables, and reduction of torque in certain rotating machines [1]-[4]. Estimation of harmonics and phasors is the building block for power quality assessment.

The harmonics and phasor estimation techniques applied to power systems include the discrete Fourier transform (DFT) and the fast Fourier transform (FFT) algorithms [5]-[7], adaptive notch filter (ANF) [8], quadrature phase-locked loop (QPLL) [9], enhanced phase-locked loop (EPLL) [10], adaptive linear combiner (ADALINE) [11], least-squares (LS) technique [12], Kalman filter (KF) [12], [13], recursive-least-squares (RLS) technique [14], finite-impulse-response (FIR) filters [15], and Newton-type

algorithm (NTA) [16].

The power system frequency encompasses information about the system operation and dynamics [17], [18]. It is a universal parameter across the entire interconnected power system [19]. Frequency estimation in power systems has evolved along several paths including zero crossing technique [20], DFT algorithm [21], smart DFT technique [22], ANF [23], demodulation of two complex signals for three-phase power systems [24], decomposition of single-phase into orthogonal components (DSPOC) [25], KF [26], nonlinear least squares method [27], using equidistant samples [28], LS technique [29], Taylor series approximation method [30], artificial neural networks (ANNs) [31], NTA [32]-[34], maximum likelihood method [35], least mean square (LMS) method [36], and phase-locked loop (PLL) [19].

Phasor and frequency estimations are crucial to operate the power system at large and the interconnected power transmission network specifically [36]-[42]. Harmonics estimation is the pivotal part in power distribution systems operation, monitoring, protection, service quality assessment, and optimal planning [43]-[47].

The following subsections critically review the ANF, EPLL, ADALINE, RDFT, LS, KF, NTA, and RLS techniques.

1.1.1. Adaptive Notch Filter (ANF)

The ANF implementation is relatively simple and is capable of extracting harmonics and phasors synchronously. The ANF structure is shown in Figure 1.1. α and β are ANF oscillation rejection parameter and frequency tracking adaptation parameter respectively. The governing differential equations of ANF are described as follows [48]:

$$\frac{d^2 y(t)}{dt^2} + \Omega^2(t) y(t) = 2 \Omega(t) e_{ANF}(t) \quad (1.1)$$

$$\frac{d \Omega(t)}{dt} = - \Omega(t) e_{ANF}(t) \quad (1.2)$$

$$e_{ANF}(t) = d(t) - \frac{dy(t)}{dt} \quad (1.3)$$

where

d is the measured voltage/current waveform

$\Omega(t)$ is ANF Power system frequency estimate.

The fundamental frequency amplitude estimate (\hat{A}_1) and the angular frequency drift estimate (Ω_d) are calculated as follows:

$$\hat{A}_1(t) = \sqrt{\Omega^2(t) y^2(t) + \left(\frac{dy(t)}{dt} \right)^2} \quad (1.4)$$

$$\Omega_d(t) = \Omega(t) - \Omega_o \quad (1.5)$$

where

Ω_o is the power system nominal fundamental angular frequency.

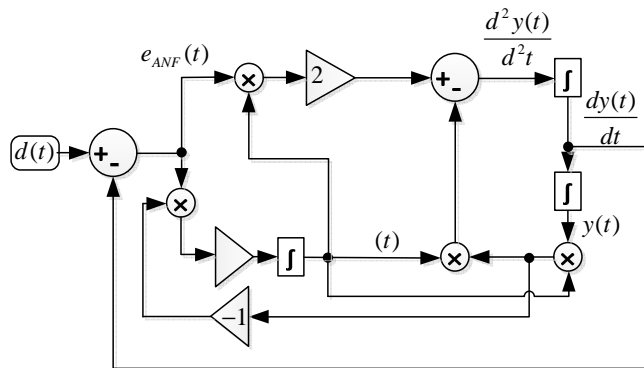


Figure 1.1. ANF structure [48].

The structure of ANF has two independent design parameters, namely, $\hat{\omega}_o$ and \hat{A}_1 . A trade-off between accuracy and convergence speed can be carried out by adjusting the design parameters $\hat{\omega}_o$ and \hat{A}_1 . By increasing $\hat{\omega}_o$, one can achieve a faster convergence. At the same time, \hat{A}_1 should be increased to avoid oscillatory behaviours.

The averaged system of ANF can be presented as [49]:

$$\frac{d}{dt} = -\frac{1}{2} \left(\hat{\omega}_o^2 - \Omega_o^2 \right) \frac{\hat{A}_1}{2\Omega_o^2} \quad (1.6)$$

Therefore, the convergence rate of the ANF technique directly depends on the amplitude of the waveform which however can vary drastically during faults and transients.

On the other hand, the periodic orbit of ANF is defined as [8]:

$$\vec{O}_{ANF} = \begin{bmatrix} \frac{\hat{A}_1}{\hat{\omega}_o} \cos(\hat{\omega}_o t + \hat{\theta}_1) \\ \hat{A}_1 \sin(\hat{\omega}_o t + \hat{\theta}_1) \\ \hat{\omega}_o \end{bmatrix} \quad (1.7)$$

Since the amplitude of the periodic orbit \vec{O}_{ANF} grows unboundedly with $\hat{\omega}_o \rightarrow 0$ and decreases to zero as $\hat{\omega}_o \rightarrow \infty$, two problems may arise. If $\hat{\omega}_o$ is large, the amplitude estimate (\hat{A}_1) may become so small that the convergence becomes very slow [50]. On the other hand, with small $\hat{\omega}_o$, large oscillations may provoke unpredictable behaviours and trigger instability. It is clear from the governing equations that nothing prevents $\hat{\omega}_o$ from taking negative values during the transients. This triggers instability. Even though a simple projection could be added to avoid this, there is no guarantee that

an accumulation point of the algorithm occurs close to zero where the projection will be turning on and off indefinitely. This is a very delicate well-known problem in adaptive systems [50].

There are also two other challenges with real-time application of the ANF for power systems applications which are dealing with the dc component [51] and digitizing the continuous-time domain governing equations of ANF for DSP implementation [23]. The problem of accommodating dc component in the ANF model has recently been addressed in [51]. The other issue is that the ANF governing differential equations are basically continuous-time domain equations which should be digitized in the discrete-time domain for DSP implementation. The sampling rate for the ANF needs to be high as its integrators must operate on the internal parameters which are changing fast for DSP implementation [23]. The performance of ANF can be partially improved by using pre-filtering stages [23], which however leads to the offsets in phase-angle and amplitude estimates.

1.1.2. Enhanced Phase-Locked Loop (EPLL)

The EPLL structure is also a frequency adaptive technique with a simple structure. The EPLL structure is shown in Figure 1.2. g_1 , g_2 , and g_3 are EPLL amplitude estimation regulation factor, phase detection regulation factor, and frequency tracking regulation factor respectively [52]. The EPLL governing differential equations are described as follows [52]:

$$\frac{d\hat{A}_1(t)}{dt} = g_1 \sin(\hat{\theta}_1(t)) \left(d(t) - \hat{A}_1(t) \sin(\hat{\theta}_1(t)) \right) \quad (1.8)$$

$$\frac{d\hat{\theta}_1(t)}{dt} = g_2 \cos(\hat{\theta}_1(t)) \left(d(t) - \hat{A}_1(t) \sin(\hat{\theta}_1(t)) \right) \quad (1.9)$$

$$\frac{d\Omega_d(t)}{dt} = g_3 \cos(\hat{\theta}_1(t)) \left(d(t) - \hat{A}_1(t) \sin(\hat{\theta}_1(t)) \right) \quad (1.10)$$

where

\hat{A}_1 is the fundamental frequency amplitude estimate

$\hat{\theta}_1$ is the phase-angle of the fundamental frequency estimate

$\hat{\theta}_1$ is the total phase-angle of the fundamental frequency estimate

Ω_d is the angular frequency drift estimate.

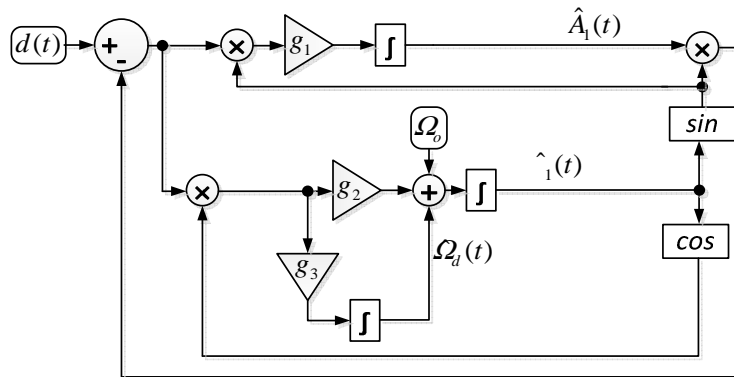


Figure 1.2. EPLL structure [52].

However, PLL-type techniques, including EPLL, are prone to errors where the signal amplitudes vary over a wide range [53], the three-phase power system is severely

unbalanced or distorted by harmonics [54], and dc components appear either caused by a fault or the analogue-to-digital conversion stage [10]. EPLL also relies on the knowledge of amplitude to tune the regulation factors g_1, g_2, g_3 . Although applying the nominal value of amplitude, as discussed in [10], is viable under normal conditions, the rapid and unpredictable changes in the amplitude force the EPLL out of tune. The effect of harmonics can be reduced by applying serial or parallel PLL modules [54]. A new technique recently has been introduced for dc component cancelation for the EPLL structure in [10]. However, the introduced technique of [10] tunes the EPLL regulation factors according to the nominal value of the amplitude which does not remain the optimum value during faults and drastic changes of amplitude [53].

1.1.3. Adaptive Linear Combiner (ADALINE)

The ADALINE technique was introduced for power system phasors and harmonics estimation in [55]. Since then, ADALINE and its different modifications have been widely applied to measurement and control applications because of its simple structure and computational efficiency [14], [56], [11].

The ADALINE input vector is defined as:

$$U_A(k) = [\sin(2 f_o t_k), \cos(2 f_o t_k), \dots, \sin(2 N f_o t_k), \cos(2 N f_o t_k), 1]^T \quad (1.11)$$

where

f_o is the nominal power system fundamental frequency

$t_k = kT_s$ is the time of observation

k is the sampling index

T_s is the sampling period

N is the number of harmonics in the ADALINE model.

The weight vector of ADALINE is defined as:

$$W(k) = [w_1(k), w_2(k), \dots, w_{2N+1}(k)]^T \quad (1.12)$$

The ADALINE estimation of input is calculated as:

$$\hat{d}(k) = W^T(k)U_A(k) \quad (1.13)$$

The ADALINE error is evaluated as:

$$e_{ADA}(k) = d(k) - \hat{d}(k) \quad (1.14)$$

The weight vector of ADALINE is updated as [55]:

$$W(k) = W(k-1) + \frac{ADA e_{ADA}(k-1)U_A(k-1)}{U_A^T(k-1)U_A(k-1)} \quad (1.15)$$

where

ADA is the reduction factor for which the practical range is 0.01-1 [56].

However, the conventional presentation of ADALINE governing equation in (1.15) suffers from unnecessary calculation redundancy which will be explained and addressed hereafter. It is possible to simplify the ADALINE structure for a more efficient DSP implementation. A closer look into the right-hand-side of (1.15) shows that the term $U_A^T(k-1)U_A(k-1)$ in the denominator can be rewritten by using (1.11) as follows:

$$U_A^T(k-1)U_A(k-1) = 1 + \sum_{i=1}^N \left(\sin^2(2 \text{ } if_{\sigma} t_{k-1}) + \cos^2(2 \text{ } if_{\sigma} t_{k-1}) \right) \quad (1.16)$$

The basic property of trigonometric functions is that:

$$\sin^2(2 \text{if}_o t_{k-1}) + \cos^2(2 \text{if}_o t_{k-1}) = 1 \quad (1.17)$$

and the term $U_A^T(k-1)U_A(k-1)$ is rewritten as:

$$U_A^T(k-1)U_A(k-1) = 1 + \sum_{i=1}^N 1 = N+1 \quad (1.18)$$

Eqn. (1.15) is therefore executed as:

$$W(k) = W(k-1) + \frac{ADA^e ADA(k-1)U_A(k-1)}{N+1} \quad (1.19)$$

The presented analysis in (1.16)-(1.19) shows resemblance with the gradient search techniques. This resemblance has also motivated investigating modifying the gradient search technique to introduce a new modified gradient search (MGS) technique which will be presented in Chapter 4.

The amplitude of the i^{th} harmonic (\hat{A}_i) is estimated by using the in-phase and quadrature-phase components as:

$$\hat{A}_i(k) = \sqrt{w_{2i-1}^2(k) + w_{2i}^2(k)} \quad (1.20)$$

The phase-angle of the i^{th} harmonic ($\hat{\Theta}_i$) is calculated by using the inverse tangent function while the sign of the in-phase component should be considered according to IEC Standard 61000-4-7 [57] as:

$$\hat{\Theta}_i(k) = \begin{cases} \arctan(w_{2i}(k)/w_{2i-1}(k)) & w_{2i-1}(k) \geq 0 \\ + \arctan(w_{2i}(k)/w_{2i-1}(k)) & w_{2i-1}(k) < 0 \end{cases} \quad (1.21)$$

The ADALINE technique can be used in two arrangements for DSP implementation:

- 1) ADALINE1: To merely estimate the amplitude of harmonics by executing (1.11)-(1.14), (1.19), and (1.20); or

2) ADALINE2: To estimate both the amplitude and phase-angle of harmonics by using (1.11)-(1.14) and (1.19)-(1.21).

It should be noted that there is no methodological difference between these two arrangements of ADALINE but the number of executed equations and the type of output they provide are different.

However, the ADALINE technique does not produce synchronized estimates of phasors because it is a frequency-domain technique and needs to recover the concept of time for synchronization [58] (e.g. application of a PLL to synchronize the ADALINE technique in [59]). Fine-tuning the ADALINE reduction factor (μ_{ADA}) also needs supervisory procedures such as the genetic algorithm and fuzzy logic controller which create huge computational burden for real-time DSP implementation as well as complications of designing these intelligent systems [11], [60].

1.1.4. Recursive Discrete Fourier Transform (RDFT)

The DFT technique is based on calculating in-phase component (In_i) and quadrature-phase component (Qd_i) of the i^{th} harmonic as follows:

$$In(k)_i = \frac{2}{N_o} \sum_{l=1}^{N_o} \sin(2\pi f_o t_{k-l}) d(k-l) \quad (1.22)$$

$$Qd(k)_i = \frac{2}{N_o} \sum_{l=1}^{N_o} \cos(2 if_o t_{k-l}) d(k-l) \quad (1.23)$$

where

$$N_o = 1/(T_s f_o)$$

f_o is the power system nominal fundamental frequency.

However, the above presentation of DFT loads the DSP with an enormous amount of calculations especially if the option of removing the anti-aliasing filter is considered for real-time applications [61]. The computational efficiency of the DFT can be improved by using the recursive DFT (RDFT) algorithm to calculate In_i and Qd_i as follows [62], [63]:

$$In(k)_i = In(k-1)_i + \frac{2}{N_o} (In(k)_i - In(k-N_o)_i) \quad (1.24)$$

$$Qd(k)_i = Qd(k-1)_i + \frac{2}{N_o} (Qd(k)_i - Qd(k-N_o)_i) \quad (1.25)$$

$$In(k)_i = \sin(2 if_o t_k) d(k) \quad (1.26)$$

$$Qd(k)_i = \cos(2 if_o t_k) d(k) \quad (1.27)$$

The amplitude of the i^{th} harmonic (\hat{A}_i) is estimated as:

$$\hat{A}_i(k) = \sqrt{In(k)_i^2 + Qd(k)_i^2} \quad (1.28)$$

The phase-angle of the i^{th} harmonic ($\hat{\Theta}_i$) is calculated by using the inverse tangent function while the sign of the in-phase component should be considered according to IEC Standard 61000-4-7 [57] as:

$$\hat{\theta}_i(k) = \begin{cases} \arctan(Qd(k)_i / In(k)_i) & In(k)_i \geq 0 \\ + \arctan(Qd(k)_i / In(k)_i) & In(k)_i < 0 \end{cases} \quad (1.29)$$

As seen, the RDFT can be implemented in two arrangements for DSP execution:

- 1) RDFT1: To merely estimate the amplitude of harmonics by executing (1.24)-(1.28); and
- 2) RDFT2: To estimate both the amplitude and phase-angle of harmonics by executing (1.24)-(1.29).

It should be noted that there is no methodological difference between these two arrangements of RDFT but the number of executed equations and the type of output they provide are different.

However, RDFT technique is subjected to instability when implemented on DSPs as discussed in [63]. Moreover, although DFT and RDFT are the most popular techniques for real-time power system phasor and harmonics estimation, they suffer from errors in the presence of non-stationary power quality (PQ) disturbances [1], [64], frequency components which are not integer multiples of the base frequency [65], decaying dc offset [66], limited memory of digital signal processing hardware [67], and unsynchronized sampling which leads to leakage effect and picket-fence effect [68].

1.1.5. Least-Squares (LS)

The LS technique is based on considering the following expansion of the waveform $d(k)$:

$$d(k) = \sum_{i=1}^N A_i(k) \cos(\Theta_i(k)) \sin(i \Omega_o k T_s) + \sum_{i=1}^N A_i(k) \sin(\Theta_i(k)) \cos(i \Omega_o k T_s) + A_{dc}(k) \quad (1.30)$$

where

$T_s = 1/f_s$ is the sampling period

f_s is the sampling frequency

N is the total number of harmonics

i is the harmonic order

Ω_o is the power system nominal fundamental angular frequency

$A_{dc}(k)$ is the dc component

$A_i(k)$ is the amplitude of the i^{th} harmonic

$\Theta_i(k)$ is the phase-angle of the i^{th} harmonic.

The LS estimation technique is based on fitting the waveform $d(k)$ with the estimate $\hat{d}(k)$ as [27], [69], [70]:

$$\hat{d}(k) = \sum_{i=1}^N \hat{A}_i(k) \cos(\hat{\Theta}_i(k)) \sin(i \hat{\Omega}_o k T_s) + \sum_{i=1}^N \hat{A}_i(k) \sin(\hat{\Theta}_i(k)) \cos(i \hat{\Omega}_o k T_s) \quad (1.31)$$

where

$\hat{A}_i(k)$ is the estimate of $A_i(k)$

$\hat{\Theta}_i(k)$ is the estimate of $\Theta_i(k)$

$\hat{\Omega}_o$ is the estimate of Ω_o .

The matrix representation of (1.31) is:

$$\hat{D}_{LS}(k) = J_{LS}(k) \hat{\Gamma}_{LS}^T(k) \quad (1.32)$$

where

$\hat{D}_{LS}(k)$ is the LS estimation vector which is defined as:

$$\hat{D}_{LS}(k) = [\hat{d}(k-L+1) \quad \cdots \quad \hat{d}(k-1) \quad \hat{d}(k)]^T \quad (1.33)$$

where

L is the length of LS input vector technique such as $L \geq 2N$.

The minimum required length is $L = 2N$ while considering an over-determined system with $L > 2N$ will give a better estimation [27].

$J_{LS}(k)$ is the Jacobian matrix of LS which is defined as:

$$J_{LS}(k) = [J_{LS1} \quad J_{LS2}] \quad (1.34)$$

$$J_{LS1}(k) = \begin{bmatrix} \cos(\Omega_o q_1) & \cos(2\Omega_o q_1) & \cdots & \cos(N\Omega_o q_1) \\ \cos(\Omega_o q_2) & \cos(2\Omega_o q_2) & \cdots & \cos(N\Omega_o q_2) \\ \vdots & \vdots & \vdots & \vdots \\ \cos(\Omega_o q_L) & \cos(2\Omega_o q_L) & \cdots & \cos(N\Omega_o q_L) \end{bmatrix} \quad (1.35)$$

$$J_{LS2}(k) = \begin{bmatrix} \sin(\Omega_o q_1) & \sin(2\Omega_o q_1) & \cdots & \sin(N\Omega_o q_1) \\ \sin(\Omega_o q_2) & \sin(2\Omega_o q_2) & \cdots & \sin(N\Omega_o q_2) \\ \vdots & \vdots & \vdots & \vdots \\ \sin(\Omega_o q_L) & \sin(2\Omega_o q_L) & \cdots & \sin(N\Omega_o q_L) \end{bmatrix} \quad (1.36)$$

q_l is defined at the k^{th} sample as:

$$q_l = (k-l+1)T_s \quad (1.37)$$

$\hat{\Gamma}_{LS}(k)$ is the optimal LS estimation matrix which is defined as:

$$\hat{\Gamma}_{LS}(k) = \left[\hat{\Gamma}_{LS1}(k) \quad \hat{\Gamma}_{LS2}(k) \right]^T \quad (1.38)$$

$$\begin{aligned} \hat{\Gamma}_{LS1}(k) = & \\ & \left[\hat{A}_1 \sin(\hat{\Theta}_1(k)) \quad \hat{A}_2 \sin(\hat{\Theta}_2(k)) \quad \cdots \quad \hat{A}_{N-1} \sin(\hat{\Theta}_{N-1}(k)) \quad \hat{A}_N \sin(\hat{\Theta}_N(k)) \right]^T \end{aligned} \quad (1.39)$$

$$\begin{aligned} \hat{\Gamma}_{LS2}(k) = & \\ & \left[\hat{A}_1 \cos(\hat{\Theta}_1(k)) \quad \hat{A}_2 \cos(\hat{\Theta}_2(k)) \quad \cdots \quad \hat{A}_{N-1} \cos(\hat{\Theta}_{N-1}(k)) \quad \hat{A}_N \cos(\hat{\Theta}_N(k)) \right]^T \end{aligned} \quad (1.40)$$

$\hat{\Gamma}_{LS}(k)$ is calculated as:

$$\hat{\Gamma}_{LS}(k) = \left(J_{LS}^T(k) J_{LS}(k) \right)^{-1} J_{LS}^T(k) D_{LS}(k) \quad (1.41)$$

$D_{LS}(k)$ is the LS input vector which is defined as:

$$D_{LS}(k) = [d(k-L+1) \quad \cdots \quad d(k-1) \quad d(k)]^T \quad (1.42)$$

The residual value of LS technique is evaluated as:

$$r_{LS}(k) = J_{LS}(k) \left(J_{LS}^T(k) J_{LS}(k) \right)^{-1} J_{LS}^T(k) D_{LS}(k) - D_{LS}(k) \quad (1.43)$$

The Euclidean norm of residual values is calculated as:

$$\|r_{LS}(k)\|^2 = \sum_{l=1}^L r_{LS}^2(k-l+1) \quad (1.44)$$

The value of Ω_o which minimizes $\|r_{LS}(k)\|^2$ is taken as the optimal estimate of power system angular frequency [27].

The amplitude of the i^{th} harmonics component is estimated as:

$$\hat{A}_1(k) = \sqrt{\left(\hat{\Gamma}_{LS1}(k, i) \right)^2 + \left(\hat{\Gamma}_{LS2}(k, i) \right)^2} \quad (1.45)$$

The phase-angle of the i^{th} harmonic component is estimated as:

$$\hat{\Theta}_i(k) = \begin{cases} \arctan\left(\frac{\hat{\Gamma}_{LS1}(k,i)}{\hat{\Gamma}_{LS2}(k,i)}\right) & , \hat{\Gamma}_{LS2}(k,i) \geq 0 \\ + \arctan\left(\frac{\hat{\Gamma}_{LS1}(k,i)}{\hat{\Gamma}_{LS2}(k,i)}\right) & , \hat{\Gamma}_{LS2}(k,i) < 0 \end{cases} \quad (1.46)$$

The LS technique reduces the leakage effect which however suffers from delays and phase-shifts when a long window of data is required for precise estimation [71], [72]. Moreover, the LS technique performs the estimation task in a quantized neighbourhood of credible frequency. This however subjects the accuracy of LS technique to the quantization errors from the accuracy point of view. From the calculation efficiency point of view, the dimension of matrixes should also increase as the order of harmonics distorting the waveform increases. This creates serious complications if the required resolution on the frequency is high and its domain of creditable values is wide. For example, for the credible neighbourhood of ± 10 Hz and frequency resolution of 0.001 Hz, the LS calculation should be repeated $\frac{10 - (-10)}{0.001} = 20000$ times to calculate only one optimal value at each sampling instance. Chapter 2 presents a solution to reduce the computational burden of LS by breaking it down into two separate stages of frequency estimation and phasor estimation. The proposed technique reduces the quantization error of LS technique by performing frequency estimation task independently from the phasor estimation procedure.

1.1.6. Kalman Filter (KF)

Consider the following deterministic state-variable equation for a periodic signal

having harmonic components up to the N^{th} order:

$$\bar{x}_{KF}(n+1) = \Phi_{KF}(n)\hat{x}_{KF}(n) \quad (1.47)$$

where

n is the state index number

\bar{x}_{KF} is the predicted state vector by the KF

\hat{x}_{KF} is the estimation vector of the KF.

\hat{x}_{KF} is defined as:

$$\hat{x}_{KF}(k) = \begin{bmatrix} \hat{A}_1(k) \sin(\hat{\theta}_1(k)) & \hat{A}_1(k) \cos(\hat{\theta}_1(k)) & \dots \\ \hat{A}_i(k) \sin(\hat{\theta}_i(k)) & \hat{A}_i(k) \cos(\hat{\theta}_i(k)) & \hat{A}_{dc}(k) \end{bmatrix}^T \quad (1.48)$$

where

$\hat{A}_i(k)$ is the estimated amplitude of the i^{th} harmonic.

$\hat{\theta}_i(k)$ is the total phase-angle of the i^{th} harmonic which is calculated as:

$$\hat{\theta}_i(k) = i\Omega_o kT_s + \hat{\Theta}_i(k) \quad (1.49)$$

where

$\hat{\Theta}_i(k)$ is the phase-angle of the i^{th} harmonic.

\hat{x}_{KF} is calculated as follows:

$$\hat{x}_{KF}(n) = \bar{x}_{KF}(n)B_{KF}(n)(d(n) - D_{KF}(n)\bar{x}_{KF}(n)) \quad (1.50)$$

where

B_{KF} is the KF gain matrix which is calculated as:

$$B_{KF}(n) = P_{KF}^-(n)D_{KF}^T(n)\left(D_{KF}(n)P_{KF}^-(n) + N_{CKF}\right)^{-1} \quad (1.51)$$

N_{CKF} is the KF measurement noise covariance.

P_{KF}^- is the KF predicted error covariance matrix which is calculated as:

$$P_{KF}^-(n) = \Phi_{KF}(n)\hat{P}_{KF}^-(n-1)\left(\Phi_{KF}(n)\right)^T + Q_{KF} \quad (1.52)$$

Q_{KF} is the KF process noise covariance.

\hat{P}_{KF} is the KF estimated error covariance matrix which is calculated as

$$\hat{P}_{KF}(n) = P_{KF}^-(n) - B_{KF}(n)D_{KF}(n)P_{KF}^-(n) \quad (1.53)$$

D_{KF} is the KF estimation matrix which is defined as:

$$D_{KF}(n) = [1 \ 0 \ \dots \ 1 \ 0 \ 1] \quad (1.54)$$

Φ_{KF} is the KF transition matrix which is defined as:

$$\Phi_{KF} = \begin{bmatrix} \Phi_{KF}^1 & 0 & \dots & 0 & 0 \\ 0 & \Phi_{KF}^2 & \dots & 0 & 0 \\ \vdots & \vdots & \dots & \vdots & \vdots \\ 0 & 0 & \dots & \Phi_{KF}^N & \vdots \\ 0 & 0 & \dots & 0 & 1 \end{bmatrix} \quad (1.55)$$

$$\Phi_{KF}^i = \begin{bmatrix} \cos(i\Omega_0 T_s) & \sin(i\Omega_0 T_s) \\ -\sin(i\Omega_0 T_s) & \cos(i\Omega_0 T_s) \end{bmatrix} \quad (1.56)$$

The KF is robust against noise [73] and cable of instantaneous amplitude variation detection [74] although the computational complexity of KF technique impedes its practical real-time application [75]. Moreover, applying the KF technique in a harmonics distorted environment requires accounting for all harmonics in the KF governing equations and consequently requires a great deal of matrix calculation and

inversion according to (1.51)-(1.53). This makes the application of KF very hard for real-time DSP implementation [73], [76]. Stability of KF technique is also a big challenge since fine-tuning the values of N_{CKF} and Q_{KF} requires continuous adjustment during abrupt changes [77], [78]. The KF technique also assumes an additive term to accommodate dynamic changes but the assumption of signal dynamic model availability makes it inconvenient for low-frequency oscillation parameter estimation [68].

1.1.7. Newton-Type-Algorithm (NTA)

The NTA is a nonlinear algorithm which was introduced in [16] for power system phasor and frequency estimations. The voltage/current waveforms are considered in the following nonlinear form:

$$d(k) = A_{dc}(k) + \sum_{i=1}^N A_i \sin(ki\Omega_o(k)T_s + \Theta(k)) \quad (1.57)$$

The NTA estimation function is described as [16]:

$$\hat{h}_{NTA}(\hat{X}_{NTA}(k)) = \hat{A}_{dc}(k) + \sum_{i=1}^N \hat{A}_i \sin(ki\Omega_o(k)T_s + \hat{\Theta}(k)) \quad (1.58)$$

where $\hat{X}_{NTA}(k)$ is defined as:

$$\hat{X}_{NTA}(k) = \left[\hat{A}_{dc} \quad \Omega_o(k) \quad \hat{A}_1(k) \quad \dots \quad \hat{A}_N(k) \quad \hat{\Theta}(k) \quad \dots \quad \hat{\Theta}_R(k) \right]^T \quad (1.59)$$

$\hat{X}_{NTA}(k)$ is updated as follows:

$$\hat{X}_{NTA}(k+1) = \hat{X}_{NTA}(k) + \left(J_{NTA}^T(k) J_{NTA}(k) \right)^{-1} J_{NTA}^T(k) \left(D_{NTA}(k) - \hat{D}_{NTA}(\hat{X}_{NTA}(k)) \right) \quad (1.60)$$

$D_{NTA}(k)$ is the NTA input vector which is defined as:

$$D_{NTA}(k) = [d(k-2N-1) \quad \dots \quad d(k)]^T \quad (1.61)$$

$\hat{D}_{NTA}(k)$ is the NTA estimation vector which is defined as:

$$\hat{D}_{NTA}(k) = [\hat{h}_{NTA}(k-2N-1) \quad \dots \quad \hat{h}_{NTA}(k)]^T \quad (1.62)$$

$\hat{J}_{NTA}(k)$ is the $2N+2$ by $2N+2$ Jacobian matrix of NTA such as its a^{th} row, $1 \leq a \leq 2N+2$, is calculated as follows:

$$\hat{J}_{NTA}^a(k) = [\hat{J}_{NTA}^{(a,1)}(k) \quad \dots \quad \hat{J}_{NTA}^{(a,2N+2)}(k)] \quad (1.63)$$

$$\hat{J}_{NTA}^{(a,1)}(k) = 1 \quad (1.64)$$

$$\hat{J}_{NTA}^{(a,2)}(k) = \sum_{i=1}^N i(k-N+a)T_s \hat{A}_i(k-N+a) \cos(i\Omega_o(k-N+a)T_s + \hat{\Theta}_i(k-N+a)) \quad (1.65)$$

$$\hat{J}_{NTA}^{(a,i+2)}(k) = \sin(i\Omega_o(k-N+a)T_s + \hat{\Theta}_i(k-N+a)) \quad 1 \leq i \leq N \quad (1.66)$$

$$\hat{J}_{NTA}^{(a,i+N+2)}(k) = \hat{A}_i(k-N+a) \cos(i\Omega_o(k-N+a)T_s + \hat{\Theta}_i(k-N+a)) \quad 1 \leq i \leq N \quad (1.67)$$

Although NTA provides an adaptive solution to handle frequency changes and decaying dc offset, the immense computational burden of calculating inverse matrix $(J_{NTA}^T(k)J_{NTA}(k))^{-1}$ is a major drawback of this technique [79]-[82]. Another key problem with the NTA is that if the amplitude of the i^{th} harmonic ($\hat{A}_i(k)$) becomes/is zero, the inverse matrix $((J_{NTA}^T(k)J_{NTA}(k))^{-1})$ calculation becomes ill-conditioned.

1.1.8. Recursive-Least-Squares (RLS)

A power system current/voltage waveform d which includes N harmonics can be numerically modelled in the discrete-time domain as:

$$d(k) = A_{dc}(k) + \sum_{i=1}^N A_i(k) \sin(\Omega_o(k)t_k + \Theta_i(k)) \quad (1.68)$$

where

$t_k = kT_s$ is the time of observation

T_s is the sampling period

$\Omega_o(k)$ is the power system angular fundamental frequency

$A_i(k)$ is the amplitude of the i^{th} harmonic

$\Theta_i(k)$ is the phase-angle of the i^{th} harmonic

$A_{dc}(k)$ is the dc component.

Eqn. (1.68) can be rewritten as follows:

$$d(k) = \sum_{i=1}^N A_i(k) \sin(\phi_i(k)) + A_{dc}(k) \quad (1.69)$$

where

$\phi_i(k) = 2\pi f_o kT_s + \Theta_i(k)$ is the total phase-angle of the i^{th} harmonic.

Eqn. (1.69) is a nonlinear equation with respect to the phase-angle $\Theta_i(k)$ and $\Omega_o(k)$.

The RLS technique fits the voltage/current waveform with the curve $\hat{d}_{RLS}(k)$ as [81]:

$$\begin{cases} \hat{d}_{RLS}(k) = \sum_{i=1}^N \hat{A}_i(k) \sin(\hat{\omega}_i(k)) + \hat{A}_{dc}(k) \\ \hat{\omega}_i(k) = ikT_s \hat{\Omega}_o(k) + \hat{\Theta}_i(k) \end{cases} \quad (1.70)$$

in which

$\hat{d}_{RLS}(k)$ is the estimate of $\hat{d}_{RLS}(k)$

$\hat{A}_i(k)$ is the estimate of $A_i(k)$

$\hat{\omega}_i(k)$ is the estimate of $\omega_i(k)$

$\hat{\Theta}_i(k)$ is the estimate of $\Theta_i(k)$

$\hat{\Omega}_o(k)$ is the estimate of $\Omega_o(k)$

$\hat{A}_{dc}(k)$ is the estimate of $A_{dc}(k)$.

The estimation error $e_{RLS}(k)$ is evaluated as:

$$e_{RLS}(k) = \hat{d}_{RLS}(k) - d(k) \quad (1.71)$$

The estimation vector is defined as:

$$\hat{\Gamma}_{RLS}(k) = \left[\hat{A}_1(k) \quad \hat{\Theta}_1(k) \quad \cdots \quad \hat{A}_N(k) \quad \hat{\Theta}_N(k) \quad \hat{A}_{dc}(k) \quad \hat{\Omega}_o(k) \right]^T \quad (1.72)$$

$\hat{\Gamma}_{RLS}(k)$ is recursively calculated as follows:

$$\hat{\Gamma}_{RLS}(k) = \hat{\Gamma}_{RLS}(k-1) - e_{RLS}(k) R^{-1}(k) \hat{x}(k) \quad (1.73)$$

$R(k)$ is called the input-waveform correlation matrix which is defined as:

$$R(k) = \hat{X}_{RLS}^T(k) \hat{X}_{RLS}(k) \quad (1.74)$$

$\hat{X}_{RLS}(k)$ is the Jacobian matrix of the RLS technique which is defined as:

$$\hat{X}_{RLS}(k) = \begin{bmatrix} \hat{x}^T(k) \\ \Lambda^{1/2} \hat{x}^T(k-1) \\ \vdots \\ \Lambda^{(k-1)/2} \hat{x}^T(1) \end{bmatrix} \quad (1.75)$$

$\hat{x}(k)$ is an $(2N+2) \times 1$ vector for which the components are evaluated as follows:

$$\hat{x}(k) = [\hat{x}_1(k), \dots, \hat{x}_{2N+2}(k)]^T \quad (1.76)$$

$$\begin{cases} \hat{x}_{2i-1}(k) = \sin(\hat{\theta}_i(k)) & 1 \leq i \leq N \\ \hat{x}_{2i}(k) = \hat{A}_i(k) \cos(\hat{\theta}_i(k)) & 1 \leq i \leq N \\ \hat{x}_{2N+1}(k) = 1 \\ \hat{x}_{2N+2}(k) = \sum_{i=1}^N ikT_s \hat{A}_i(k) \cos(\hat{\theta}_i(k)) \end{cases} \quad (1.77)$$

$R^{-1}(k)$ is recursively calculated as:

$$R^{-1}(k) = \frac{1}{\Lambda} \left[R^{-1}(k-1) - \frac{R^{-1}(k-1) \hat{x}(k) \hat{x}^T(k) R^{-1}(k-1)}{\Lambda + \hat{x}^T(k) R^{-1}(k-1) \hat{x}(k)} \right] \quad (1.78)$$

The RLS technique can effectively handle the decaying dc offsets, power system frequency variations, and sub-synchronous oscillations [14], [79], [83]-[98]. However, there are two challenges to use the RLS technique for real-time applications which are the computational burden of RLS technique and its stability. The computational burden of RLS technique is of the order of N^2 since the dimension of $R(k)$ is $(2N+2) \times (2N+2)$. This is a real challenge which impedes the real-time application of the RLS technique [84], [85].

Another challenge is to make sure that the determinant of $R(k)$ is not zero to have a well-defined inverse matrix $R^{-1}(k)$ [86]. However, this condition is not always

sustained. If $\hat{A}_i(k)$ becomes zero, the ($2i^{\text{th}}$) row of $R(k)$, $1 \leq i \leq N$, becomes zero according to (1.77). This means that the determinant of $R(k)$ becomes zero. Therefore, matrix $R^{-1}(k)$ principally is ill-defined and the whole system becomes unstable. This happens when the amplitude of the i^{th} harmonic is zero while it has been being accommodated in the estimation model. Moreover, although there have been many efforts to study the nonlinear model of RLS technique recently [87]-[91], the RLS model has not been analysed for the power system harmonics and phasor estimation specifically and thoroughly [84]. Chapter 3 presents a very detailed analysis of RLS technique for the specific application of harmonics and phasor estimation in power systems and proposes a restructured model for real-time DSP implementation.

1.1.9. Summary of the Literature Review

The presented literature review can be summarized in Table 1.1-Table 1.4 as follows.

TABLE 1.1. SUMMARY OF ANF AND EPLL TECHNIQUES: REFERENCES, MERITS, AND DEMERITS.

Technique	ANF	EPLL
References	[8], [23], [48]-[51]	[52]-[54], [9], [10]
Merits	<ul style="list-style-type: none"> • Relatively simple nonlinear structure • Frequency adaptive 	<ul style="list-style-type: none"> • Simple nonlinear structure • Frequency adaptive
Demerits	<ul style="list-style-type: none"> • Dependency of stability on the waveform amplitude and frequency • Dependency of estimation pace on the waveform amplitude and frequency • Errors in presence of dc component • Relatively high sampling frequency required for DSP implementation 	<ul style="list-style-type: none"> • Dependency of stability, estimation pace, and control parameters on the waveform amplitude • Errors in presence of dc component • Errors in severely unbalanced and harmonics distorted environments

TABLE 1.2. SUMMARY OF ADALINE AND DFT/RDFT TECHNIQUES: REFERENCES, MERITS, AND DEMERITS.

Technique	ADALINE	DFT/RDFT
References	[11], [14], [55], [56], [58]-[60]	[1], [57], [61]-[68]
Merits	<ul style="list-style-type: none"> • Simple linear estimation technique • Effective cancelation of the dc component 	<ul style="list-style-type: none"> • Simple linear technique • The most popular technique for DSP implementation
Demerits	<ul style="list-style-type: none"> • Cannot produce synchronous estimates and requires complementary routines to do so • Difficulty of tuning the reduction factor • Computational redundancy in the conventional form of ADALINE 	<ul style="list-style-type: none"> • The RDFT technique is subjected to instability for DSP implementation • Cannot track non-stationary PQ disturbances • Errors in presence of interharmonics and decaying dc offset • DFT stability is outstanding but it suffers from computational redundancy • Leakage effect and picket-fence effect because of unsynchronized sampling

TABLE 1.3. SUMMARY OF LS AND KF TECHNIQUES: REFERENCES, MERITS, AND DEMERITS.

Technique	LS	KF
References	[12], [27], [69]-[72]	[68], [73]-[78]
Merits	<ul style="list-style-type: none"> • Reducing the leakage effect • Linear and stable • Frequency adaptive 	<ul style="list-style-type: none"> • Instantaneous detection of disturbances • Adaptive parameter estimation • Robust noise cancelation
Demerits	<ul style="list-style-type: none"> • Delays and phase-shifts in case of applying a long window • Computational redundancy for high-resolution frequency tracking 	<ul style="list-style-type: none"> • High computational burden • State variable modelling is critical • A priori information of noise and process is needed • Subject to instability during abrupt changes

TABLE 1.4. SUMMARY OF NTA AND RLS TECHNIQUES: REFERENCES, MERITS, AND DEMERITS.

Technique	NTA	RLS
References	[16], [79]-[82]	[14], [79], [83]-[98]
Merits	<ul style="list-style-type: none"> • Frequency adaptive • Effective dc component cancelation 	<ul style="list-style-type: none"> • Frequency adaptive • Effective handling of dc components • Effectively tracks subsynchronous oscillations
Demerits	<ul style="list-style-type: none"> • Immense computational burden • Subject to instability during abrupt changes 	<ul style="list-style-type: none"> • Relatively high computational burden • The stability depends on the amplitude of the waveform

1.2. Research Motivation

The new numerical techniques such as ADALINE, KF, LS, RLS, and NTA have been developed to rectify the abovementioned shortcomings of DFT and FFT algorithms. Although these new methods prove to be efficient in resolving some of these shortcomings, they have not been widely applied for real-time implementation on DSPs. In fact, application of these methods is mostly limited to simulation and offline studies and their reported real-time application is limited in the technical literature of power systems.

The main challenges of applying numerical techniques are:

- A. Concerns over their stability when implemented on DSPs
- B. The inherent heavy computational burden of numerical methods

Therefore, it is required to consider restructuring the numerical methods and investigate new techniques for real-time power system parameters estimation.

Regarding the former challenge, Chapter 2 proposes a new hybrid least-squares-Kalman (LSK) technique which demonstrates high accuracy and outstanding stability for DSP implementation. Regarding the latter challenge, Chapter 3 critically reviews the RLS technique and introduces a new decoupled RLS (DRLS) technique with the prime objective of reducing the RLS computational burden and improving the RLS stability for real-time harmonics estimation on DSPs.

On the other hand, the emerging smart grid paradigm [99], using smart meters as new information gateways [100], [101], and integrating load signature and load composite analysis [102]-[106] into advanced metering infrastructures (AMIs) [99], [107], [108] require efficient estimation tools. Besides, managing vast amount of information that will overwhelm the communication infrastructure and control centres requires solutions that can extract power system characteristics from a few concentrated data [109]. This challenge though offers the research opportunity of investigating new multi-rate algorithms [110] and undersampling techniques [111]-[114] for power system parameters estimation based on low-bandwidth data acquisition techniques which simplify the infrastructure requirements of realizing the smart grid vision. The undersampling real-time optimisation techniques for harmonics/interharmonics and frequency estimation are investigated and implemented in Chapter 4 and Chapter 5 respectively.

1.3. Statement of Originality

The main contributions of this research work can be summarized as follows:

- A new real-time least-squares-Kalman (LSK) technique for voltage envelope and flicker estimation is presented in Chapter 2. The proposed LSK technique reduces the dimension and computational burden of the conventional KF technique, demonstrates outstanding stability, and shows better accuracy to detect voltage flicker than that of the DFT technique.
- A new decoupled recursive-least-squares (DRLS) harmonics and phasors estimation technique is presented in Chapter 3. The proposed DRLS technique considerably reduces the computational burden for DSP implementation in comparison with the conventional RLS technique, demonstrates better stability and estimation speed in comparison with the EPLL method under fault conditions, and is more efficient to extract harmonics in a highly distorted power system.
- A new undersampling technique for power system harmonics and interharmonics estimation is presented in Chapter 4. The proposed modified gradient search (MGS) technique efficiency is better than the DFT technique and its accuracy is comparable with that of the IEC Standard 61000-4-7. The extended staggered undersampling is also presented in Chapter 4 which promises to facilitate synchrophasor detection by using the residential area internet services for distribution level wide-area measurements system (WAMS) applications and increasing the reliability of transmission level WAMSs.
- A slow sampling real-time optimisation approach for power system frequency estimation is presented in Chapter 5. The presented NTA-LS technique shows better accuracy, estimation speed, stability, and noise immunity in comparison

with the PLL and DFT-based methods for slow sampling power system frequency monitoring. The NTA-LS technique also shows superior stability, accuracy, and estimation pace when compared with the conventional NTA.

1.4. List of Publications

This research work has resulted in a number of peer reviewed journal papers and conference publications as follows:

1.4.1. Journal Papers

1. I. Sadinezhad and V.G. Agelidis, "Slow sampling on-line optimization approach to estimate power system frequency," *IEEE Transactions on Smart Grid*, vol. 2, no.2, 2011, pages 265-277.
2. I. Sadinezhad and V.G. Agelidis, "Slow sampling on-line harmonics/interharmonics estimation technique for smart meters," *Electric Power Systems Research Journal*, vol. 81, no. 8, 2011, pages 1643–1653.
3. I. Sadinezhad and V.G. Agelidis, "Frequency adaptive least-squares-Kalman technique for real-time voltage envelope and flicker estimation," *IEEE Transactions on Industrial Electronics*, vol. 59, no. 8, 2012, pages 3330-3341.
4. I. Sadinezhad and V.G. Agelidis, "Real-time power system phasors and harmonics estimation using a new decoupled recursive-least-squares technique for DSP implementation," *IEEE Transactions on Industrial Electronics*, 2012, pages 1-13.

1.4.2. Conference Papers

1. I. Sadinezhad and V.G. Agelidis “A new hybrid complex ADALINE-LES filter for off-nominal frequency symmetrical components extraction,” *IEEE ICIT Conference*, 2009, pages 1-6.
2. I. Sadinezhad and V.G. Agelidis, “Monitoring voltage disturbances based on LES algorithm, wavelet transform and Kalman filter,” *35th Annual Conference of IEEE Industrial Electronics*, 2009, pages 1961-1966.
3. I. Sadinezhad and V.G. Agelidis, “A new quasi Newton filtering technique for power system frequency estimation and harmonics/interharmonics rejection,” *14th International Conference on Harmonics and Quality of Power (ICHQP)*, 2010, pages 1-6.
4. I. Sadinezhad and V.G. Agelidis, “A new optimization technique to measure frequency and harmonics in power systems,” *14th International Conference on Harmonics and Quality of Power (ICHQP)*, 2010, pages 1-8.
5. I. Sadinezhad and V.G. Agelidis, “Undersampled on-line ANN-EKF based estimation of harmonics/interharmonics in power systems,” *IEEE Power and Energy Society General Meeting*, 2010, pages 1-8.
6. I. Sadinezhad and V.G. Agelidis, “Slow sampling on-line optimization approach to estimate power system frequency,” *IEEE Power and Energy Society General Meeting*, 2010, pages 1-7.
7. I. Sadinezhad and V.G. Agelidis, “On optimizing DSP implementation of the recursive-least-squares technique for real-time power system applications,” *37th Annual Conference of IEEE Industrial Electronics*, 2011, pages 640-645.

8. I. Sadinezhad and V.G. Agelidis, "Decoupled recursive-least-squares technique for extraction of instantaneous synchronized symmetrical components under fault conditions," *37th Annual Conference of IEEE Industrial Electronics*, 2011, pages 4672-4678.
9. I. Sadinezhad and V.G. Agelidis, "Extended staggered undersampling synchrophasor estimation technique for wide-area measurement systems," *IEEE ISGT-Asia 2011*, pages 1-6.

1.5. Thesis Organisation

The remaining of this thesis is organised as follows:

- Chapter 2 presents real-time implementation of a new frequency adaptive least-squares-Kalman (LSK) technique for voltage envelope and flicker estimation in power systems. The proposed method is based on a two-stage mathematical model of a voltage waveform and a simple low computation frequency tracking method. The proposed method is evaluated experimentally through real-time implementation on two R&D DSP platforms.
- Chapter 3 lays the mathematical basis to restructure the recursive-least-squares (RLS) technique for real-time implementations on DSPs. The performance of the proposed technique has been evaluated by simulations using MATLAB-Simulink and through real-time DSP experiments.
- Chapter 4 investigates the application of an undersampling strategy to estimate harmonics and interharmonics. A modified gradient search (MGS) technique to estimate harmonics/interharmonics of power system voltages and currents is also

presented. The effects of undersampling on the accuracy and estimation latency have been investigated. Performance of the proposed method is evaluated by simulations in MATLAB-Simulink and confirmed by experimental results. The concept of staggered undersampling is also extended in this chapter and its application for synchrophasor detection in WAMSs is evaluated by simulations in MATLAB-Simulink.

- Chapter 5 investigates frequency estimation from an undersampled waveform. A real-time optimization approach based on the Newton-type algorithm (NTA) and the least-squares (LS) method for power system frequency estimation is presented. The performance of the proposed method is validated by simulations in MATLAB-Simulink and DSP real-time experiments.
- Chapter 6 summarizes this research work and suggests directions for future research.

Chapter 2 : Frequency Adaptive Least-Squares-Kalman Technique for Real-Time Voltage Envelope and Flicker Estimation

2.1. Introduction

The voltage quality is the main focus of power quality assessment as the current disturbances also manifest themselves in voltage by passing through the system impedance [115]. Detection of the waveform instantaneous amplitude called voltage envelope is part of the voltage quality assessment and forms the basis to detect voltage sags, swells, and flickers.

Voltage frequency varies because of disturbances such as the loss of a major tie-line, the loss of a large generating station or a sudden impact of a major overload [116]. Voltage flickers cause annoying variations in the quality of illumination from lamps and drastically decrease the power quality [4], [117]-[121]. Voltage sags are the result of temporary disconnection of supply, the flow of inrush currents associated with the starting of motors and transformers, and the flow of fault currents, or lightning strikes [122], [123]. These voltage sags, in turn, cause under-voltage faults in various sensitive loads and subsequent interruptions to manufacturing processes which lead to massive financial losses [115], [124].

The voltage quality is traditionally monitored with phasor measurement and envelope tracking [119]. The discrete Fourier transform (DFT) and the fast Fourier transform

(FFT) algorithms [5]-[7] have widely been used to estimate phasors. However, the DFT and FFT limitations can be summarised as follows:

- unable to track non-stationary PQ disturbances [1], [64]
- unable to cancel the decaying dc offset [66], and
- being subjected to the errors of leakage and picket-fence effects [68].

To resolve these deficiencies, a number of new algorithms have been proposed in the technical literature, such as: wavelet transform (WT) [125], [1], adaptive notch filter (ANF) [8], quadrature phase-locked loop (QPLL) [9], enhanced phase-locked loop (EPLL) [10], adaptive linear combiner (ADALINE) [11], least-squares (LS) algorithm [12], Hilbert transform (HT), and Kalman filter (KF) [12], [13].

However, the ANF, QPLL, and EPLL techniques are vulnerable to decaying dc offset and digitization errors for implementation on DSPs [23], [51]. Although the WT is capable of localizing transient components of power quality disturbances and providing the time-frequency map of events, it requires a separate FFT or DFT routine and several neural networks along with the wavelet multi-resolution analysis to capture the features of low-frequency and high-frequency power quality disturbances [126]. These complementary techniques, which are required in addition to the WT, create high computational burden [127], [128].

The LS technique reduces the leakage effect but a high precision LS technique requires a long window of data. This lengthy data window creates delays and phase-shifts in the LS phasor estimates [71]. Although the ADALINE technique presents a simple linear solution to deal with the dc offset, it does not produce synchronized estimates of phasors because it is a frequency-domain technique and needs to recover

the concept of time for synchronization [58], [59]. Fine-tuning the ADALINE reduction factor also needs computationally intensive intelligent algorithms such as genetic and fuzzy logic algorithms which demand complicated and stochastic design procedures [11], [60].

Although the HT generates a quadrature signal and thereby an analytical signal from which the instantaneous amplitude and phase can be easily extracted, it gives a correct approximate of a quadrature signal only if the waveform is band-limited [129], [130]. The KF is capable of instantaneous amplitude variation detection [74] although the computational complexity of KF technique impedes its practical real-time application [75], [76].

The objective of this chapter is to propose the application of a frequency adaptive LS optimization technique for the estimation of the voltage envelope at fundamental frequency. The proposed method merges the performance of a relatively simple frequency estimation method and the LS technique to develop a robust fundamental frequency voltage envelope estimation technique. To monitor voltage flickers and predict the instantaneous flicker level (IFL), a combination of the LS method and a Kalman filter to predict the IFL state variables is introduced. As the proposed least-squares-Kalman (LSK) technique eases the heavy computation burden of a full order Kalman filter, which would require accommodating all frequency components, the implementation of the Kalman filter becomes possible in real-time applications. The performance of the proposed technique in the presence of frequency variation, harmonic contamination, and noise is verified and compared with the EPLL, ANF, and DFT techniques through real-time implementation experiments.

This chapter is organised as follows. Section 2.2 presents the proposed frequency adaptive LS optimisation technique for voltage envelope estimation. The proposed LSK technique to estimate instantaneous flicker level is described in Section 2.3. Section 2.4 presents the real-time implementation and comparative study results and Section 2.5 concludes this chapter.

2.2. Frequency Adaptive Least-Squares Technique for Fundamental Frequency Envelope Estimation

A nonstationary, nonsinusoidal voltage waveform at the k^{th} sample is mathematically expressed as follows:

$$v(k) = \sum_{i=1}^N A_i(k) \sin(i(\Omega_o + \Omega_d(k))kT_s + \mathcal{Q}(k)) + A_{dc}(k) \quad (2.1)$$

where

$T_s = 1/f_s$ is the sampling period

f_s is the sampling frequency

N is the total number of harmonics

i is the harmonic order

Ω_o is the nominal voltage angular frequency

$\Omega_d(k)$ is the instantaneous angular frequency drift

$A_{dc}(k)$ is the dc component

$A_i(k)$ is the voltage amplitude of the i^{th} harmonic

$\mathcal{Q}_i(k)$ is the phase-angle of the i^{th} harmonic.

This model is used in a two-level algorithm to estimate the voltage frequency and the fundamental frequency amplitude.

2.2.1. Frequency Estimation

Fast changes in the fundamental frequency phase-angle are rare events in power systems except under fault situations [33]. In addition, the IEC Standard 61000-4-7 considers 10 cycles for 50 Hz power systems to complete the phasor measurement task [57]. Therefore, in this chapter, the problem of frequency estimation is approached by considering moving time slots with a specific fixed length. Within each of these time slots, the i^{th} harmonic voltage amplitude, voltage phase-angle, dc component, and angular frequency drift are considered to be frozen parameters A_i , Θ_i , A_{dc} , and Ω_d respectively. The estimation is updated sample by sample as the window shifts on the time axis. This “*parameter-freezing*” approach is consistent with the asymptotic analysis concept and the averaging theorem [131] which have been used in estimation techniques such as ANF, QPLL, and EPLL [8]-[10].

The length of the time slot is chosen to be one cycle of the voltage nominal frequency which is $T_o = 20$ ms for 50 Hz power systems. Figure 2.1 shows a schematic definition of the moving time slots to collect data and perform the frequency estimation task.

Therefore, within each time slot, the voltage waveform is expressed as:

$$v(k) = \sum_{i=1}^N A_i \sin(i(\Omega_o + \Omega_d)kT_s + \Theta_i) + A_{dc} \quad (2.2)$$

For the nominal fundamental frequency (f_o) of 50 Hz, $\Omega_o = 2f_o = 100$.

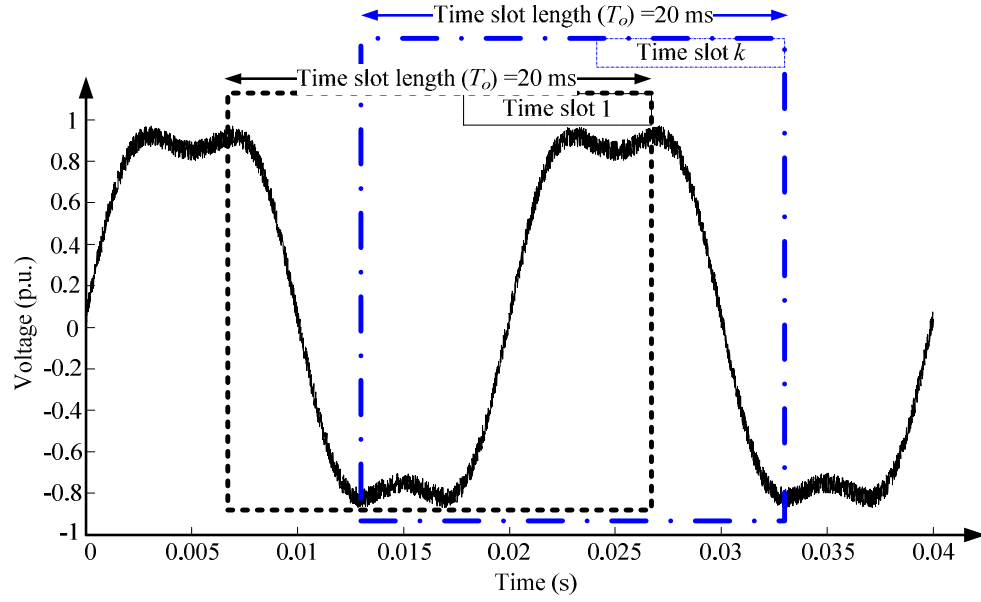


Figure 2.1. Schematic definition of the moving time slots to collect data and perform frequency estimation.

Eqns. (3) and (4) are used to transform the voltage waveform $v(kT_s)$ into two orthogonal components based on the decomposition of a single-phase into orthogonal components (DSPOC) [5], [25] as follows:

$$I_s(kT_s) = T_s \sum_{l=k-N_o+1}^k v(l) \sin(l\Omega_o T_s) \quad (2.3)$$

$$I_c(kT_s) = T_s \sum_{l=k-N_o+1}^k v(l) \cos(l\Omega_o T_s) \quad (2.4)$$

where

$N_o = f_s / f_o$ is the number of samples in one period of the fundamental frequency

component.

These transformations produce two orthogonal waveforms in which their low frequency components are modulated at the frequency drift from the nominal value of f_o . Eqns.

(2.3) and (2.4) can be rewritten by simplifying trigonometric functions as follows:

$$I_s(kT_s) = \frac{A_1}{\Omega_d} \cos(\Omega_d kT_s + \Theta_1 - \Omega_d T_o / 2) \sin(\Omega_d T_o / 2) + \quad (2.5)$$

$$\sum_{i=2}^N \frac{A_i}{\Omega_o(i-1) + i\Omega_d} \cos((i-1)\Omega_o kT_s + i\Omega_d(kT_s - T_o / 2) + \Theta_i) \sin(i\Omega_d T_o / 2) -$$

$$\sum_{i=1}^N \frac{A_i}{\Omega_o(i+1) + i\Omega_d} \cos((i+1)\Omega_o kT_s + i\Omega_d(kT_s - T_o / 2) + \Theta_i) \sin(i\Omega_d T_o / 2)$$

$$I_c(kT_s) = \frac{A_1}{\Omega_d} \sin(\Omega_d kT_s + \Theta_1 - \Omega_d T_o / 2) \sin(\Omega_d T_o / 2) + \quad (2.6)$$

$$\sum_{i=2}^N \frac{A_i}{\Omega_o(i-1) + i\Omega_d} \sin((i-1)\Omega_o kT_s + i\Omega_d(kT_s - T_o / 2) + \Theta_i) \sin(i\Omega_d T_o / 2) +$$

$$\sum_{i=1}^N \frac{A_i}{\Omega_o(i+1) + i\Omega_d} \sin((i+1)\Omega_o kT_s + i\Omega_d(kT_s - T_o / 2) + \Theta_i) \sin(i\Omega_d T_o / 2)$$

On the right hand-side of (2.5) and (2.6), the first terms are sinusoidal functions with an angular frequency of Ω_d and the remaining terms are higher frequency components whose amplitudes are reduced by factors of $\sin(i\Omega_d T_o / 2) / (\Omega_o(i \pm 1) + i\Omega_d)$. If $I_s(kT_s)$ and $I_c(kT_s)$ are passed through a low-pass filter (LPF), the results will respectively be $I_{sl}(kT_s)$ and $I_{cl}(kT_s)$ as follows:

$$I_{sl}(kT_s) = \frac{A_1}{\Omega_d} \cos(\Omega_d kT_s + \Theta_1 - \Omega_d T_o / 2) \sin(\Omega_d T_o / 2) \quad (2.7)$$

$$I_{cl}(kT_s) = \frac{A_1}{\Omega_d} \sin(\Omega_d kT_s + \Theta_1 - \Omega_d T_o / 2) \sin(\Omega_d T_o / 2) \quad (2.8)$$

According to the testing requirements of IEC Standard 61000-4-30 page 18 [176], the power system frequency estimation bandwidth is 42.5-57.5 Hz for 50 Hz power systems and 51-69 Hz for 60 Hz power systems. Therefore, considering the cut-off frequency of 10 Hz for the LPF is in compliance with the IEC Standard 61000-4-30 requirements for both 50 Hz and 60 Hz power systems. This mid-filtering stage practically reduces the energy of higher frequency components to a very low level but does not completely eliminate them, as the real-time implementation shows in Section 2.4. The following derivative relationship holds true between $I_{sl}(kT_s)$ and $I_{cl}(kT_s)$:

$$\left. \frac{\partial I_{cl}(t)}{\partial t} I_{sl}(t) - \frac{\partial I_{sl}(t)}{\partial t} I_{cl}(t) \right|_{t=kT_s} = \Omega_d (I_{sl}^2[t] + I_{cl}^2[t]) \Big|_{t=kT_s} \quad (2.9)$$

Therefore, Ω_d provides an estimation of $\Omega_d(k)$ for the time slot which covers the voltage waveform between $(kT_s - T_o)$ and kT_s . $\Omega_d(k)$ is calculated as:

$$\Omega_d(k) = \left. \frac{H_s(t) (\partial I_{cl}(t) / \partial t) - I_{cl}(t) (\partial I_{sl}(t) / \partial t)}{(I_{sl}^2(t) + I_{cl}^2(t))} \right|_{t=kT_s} \quad (2.10)$$

The above equation is also consistent with the time-frequency representation of a periodic signal. The following recursive relationships hold true between two consecutive values for both $I_{sl}(kT_s)$ and $I_{cl}(kT_s)$ according to the recursive DFT [62] algorithm:

$$I_s(kT_s) = I_s((k-1)T_s) + T_s v(k) \sin(k\Omega_o T_s) - T_s v((k-N_o)) \sin((k-N_o)\Omega_o T_s) \quad (2.11)$$

$$I_c(kT_s) = I_c((k-1)T_s) + T_s v(k) \cos(k\Omega_o T_s) - T_s v((k-N_o)) \cos((k-N_o)\Omega_o T_s) \quad (2.12)$$

As a result, there is no need to use all samples of the voltage waveform in each time

slot to calculate $I_s(kT_s)$ and $I_c(kT_s)$ since two samples at the k^{th} and $(k-N_o)^{\text{th}}$ instances are sufficient if the values of $I_s((k-1)T_s)$ and $I_c((k-1)T_s)$ are recursively updated according to (2.11) and (2.12). Eqns. (2.11) and (2.12) present the recursive DSPOC (RDSPOC) method. The LPF which is used to cut the high frequency components is a Hamming window with the length of $1.25N_o$ and cut-off frequency of 10 Hz. The following approximate equations are used to calculate the derivative terms $\partial I_{sl}(t)/\partial t$ and $\partial I_{cl}(t)/\partial t$ as:

$$\left. \frac{\partial I_{sl}(t)}{\partial t} \right|_{t=kT_s} = \frac{I_{sl}(kT_s) - I_{sl}((k-1)T_s)}{T_s} \quad (2.13)$$

$$\left. \frac{\partial I_{cl}(t)}{\partial t} \right|_{t=kT_s} = \frac{I_{cl}(kT_s) - I_{cl}((k-1)T_s)}{T_s} \quad (2.14)$$

The angular frequency drift $\Omega_d(k)$ is calculated by applying (2.13) and (2.14) into (2.10) for digital implementation as:

$$\Omega_d(k) = \frac{I_{cl}(kT_s)I_{sl}((k-1)T_s) - I_{sl}(kT_s)I_{cl}((k-1)T_s)}{T_s (I_{sl}^2(kT_s) + I_{cl}^2(kT_s))} \quad (2.15)$$

The frequency drift is $f_d(k) = \Omega_d(k)/2$.

Figure 2.2 shows the RDSPOC implementation in the discrete time domain where z^{-1} is the unit delay and z^{-N_o} recalls the value of a parameter at the $(k-N_o)^{\text{th}}$ sample.

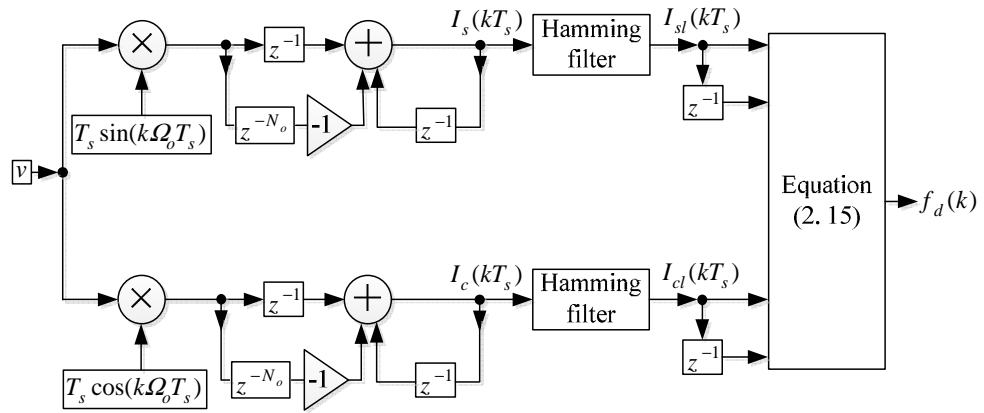


Figure 2.2. RDSPOC frequency estimation algorithm.

2.2.2. Envelope Estimation

Eqn. (2.1) can be expanded as:

$$v(k) = \sum_{i=1}^N A_i(k) \cos(\Theta_i(k)) \sin(i(\Omega_o + \Omega_d(k))kT_s) + \sum_{i=1}^N A_i(k) \sin(\Theta_i(k)) \cos(i(\Omega_o + \Omega_d(k))kT_s) + A_{dc}(k) \quad (2.16)$$

The value of $\Omega_d(k)$ is calculated from the frequency estimation procedure of Figure 2.1. The envelope estimation is performed on the line-to-neutral voltage waveform. In the case of a three-phase power system, the estimation of the envelope is carried out on each phase separately to provide the event detection resolution on each phase.

To estimate the fundamental frequency voltage envelope, a time-varying linear estimation model is considered, which accommodates odd harmonics up to a specific order, while other harmonics and the dc component are projected on the residual term ($r_{LS}(k)$).

The estimation model is defined as:

$$\hat{v}(k) = \sum_{i=1}^M \hat{\Gamma}_{LS}(2i-1, k) \sin((2i-1)(\Omega_o + \Omega_d(k))kT_s) + \sum_{i=1}^M \hat{\Gamma}_{LS}(2i, k) \cos((2i-1)(\Omega_o + \Omega_d(k))kT_s) + r_{LS}(k) \quad (2.17)$$

where

$\hat{v}(kT_s)$ is an estimation of $v(kT_s)$

$r_{LS}(k)$ is the estimation error which is also called the residual value

$\hat{\Gamma}_{LS}(1:2M, k)$ is the estimation vector in which $\hat{\Gamma}_{LS}(2i-1, k)$ estimates the in-phase

component ($A_{2i-1}(k)\cos(\Theta_{2i-1}(k))$)

$\hat{\Gamma}_{LS}(2i, k)$ estimates the quadrature-phase component ($A_{2i-1}(k)\sin(\Theta_{2i-1}(k))$) at the k^{th} sample, and

M is the order of the estimation model which is the defining factor for the accuracy of the estimation and is smaller than or equal to N ($M \leq N$).

The model order is chosen to be $M = 2$, which means including odd harmonic components up to the $2 \times 2 - 1 = 3^{\text{rd}}$ harmonic according to (2.17). Therefore, the even harmonics, along with odd harmonics higher than the 3^{rd} order, and the dc component are projected on the residual term $r_{LS}(k)$. The residual term $r_{LS}(k)$ shows the difference between $v(kT_s)$ and $\hat{v}(kT_s)$ which is:

$$r_{LS}(k) = \hat{v}(k) - v(k) \quad (2.18)$$

To solve (2.17) and find $\hat{\Gamma}_{LS}(k, 1:2M)$, a goal function ($G_{LS}(k)$) is considered based on the least-squares optimization technique in the following form [132]:

$$G_{LS}(k) = 0.5 \|R_{LS}(k)\|^2 \quad (2.19)$$

where

$\| \cdot \|$ is the Euclidean norm [132] and

$R_{LS}(k)$ is the vector of L residual terms, which is defined as:

$$R_{LS}(k) = [r_{LS}(k) \ r_{LS}(k-1) \ \dots \ r_{LS}(k-L+1)]^T \quad (2.20)$$

where

L is the closet integer number to the value of $f_s / (f_o + f_d(k))$ which is rounded toward

positive infinity.

Based on the linear model of (2.17), the residual vector can be written in the following vector format:

$$R_{LS}(k) = J_{LS}(k)\hat{\Gamma}_{LS}(1:2M, k) - V_{LS}(k) \quad (2.21)$$

where

$V_{LS}(k)$ is an $L \times 1$ vector which carries L consecutive samples of the measured voltage waveform and is defined as:

$$V_{LS}(k) = [v(k) \ v(k-1) \ \dots \ v(k-L+1)]^T \quad (2.22)$$

$J_{LS}(k)$ is the Jacobian matrix which is the $L \times 2M$ matrix of first order partial derivatives of the residuals and is defined as:

$$J_{LS}(k) = [\nabla r_{LS}(k) \ \nabla r_{LS}(k-1) \ \dots \ \nabla r_{LS}(k-L+1)]^T \quad (2.23)$$

Therefore:

$$J_{LS}(k) = \begin{bmatrix} \sin(\Omega_k q_1) & \cos(\Omega_k q_1) & \dots & \sin((2M-1)\Omega_k q_1) & \cos((2M-1)\Omega_k q_1) \\ \sin(\Omega_k q_2) & \cos(\Omega_k q_2) & \dots & \sin((2M-1)\Omega_k q_2) & \cos((2M-1)\Omega_k q_2) \\ \vdots & \vdots & \vdots & \vdots & \vdots \\ \sin(\Omega_k q_L) & \cos(\Omega_k q_L) & \dots & \sin((2M-1)\Omega_k q_L) & \cos((2M-1)\Omega_k q_L) \end{bmatrix} \quad (2.24)$$

where

$$\Omega_k = \Omega_o + \Omega_d(k).$$

q_l at the k^{th} sample is defined as:

$$q_l = (k-l+1)T_s \quad (2.25)$$

In fact, the proposed goal function is the sum of residual squares for L consecutive

estimations. The solution for the estimation vector ($\hat{\Gamma}_{LS}(1:2M, k)$) minimizes the sum of residual squares for which the goal function gradient ($\nabla G_{LS}(k)$) becomes zero. The following vector equations are derived by substituting (2.21) into (2.19) and performing the gradient operation:

$$G_{LS}(k) = \frac{1}{2} \left\| J_{LS}(k) \hat{\Gamma}_{LS}(1:2M, k) - V_{LS}(k) \right\|^2 \quad (2.26)$$

$$\nabla G_{LS}(k) = J_{LS}^T(k) (J_{LS}(k) \hat{\Gamma}_{LS}(1:2M, k) - V_{LS}(k)) \quad (2.27)$$

Since $\nabla G_{LS}(k)$ is linear with respect to $\hat{\Gamma}_{LS}(1:2M, k)$, there exists a unique solution which is calculated by applying the minimization condition to (2.27) as follows:

$$\nabla G_{LS}(k) = J_{LS}^T(k) J_{LS}(k) \hat{\Gamma}_{LS}(1:2M, k) - J_{LS}^T(k) V_{LS}(k) = 0 \quad (2.28)$$

Therefore, $\hat{\Gamma}_{LS}(1:2M, k)$ is calculated as:

$$\hat{\Gamma}_{LS}(1:2M, k) = \left(J_{LS}^T(k) J_{LS}(k) \right)^{-1} J_{LS}^T(k) V_{LS}(k) \quad (2.29)$$

The fundamental frequency voltage amplitude estimate ($\hat{A}_1(k)$) is calculated as follows:

$$\hat{A}_1(k) = \sqrt{\hat{\Gamma}_{LS}^2(2, k) + \hat{\Gamma}_{LS}^2(1, k)} \quad (2.30)$$

$\hat{A}_1(k)$ is also called the voltage envelope which will be used by the Kalman filter to predict the instantaneous flicker level.

2.3. Instantaneous Flicker Level Prediction

Voltage flicker is described by amplitude modulation of the fundamental frequency component as [117]-[121], [133]-[135]:

$$v_{AM}(k) = (U_c(k) + v_F(k)) \sin(\Omega_o k T_s + \Theta) \quad (2.31)$$

where the low frequency fluctuation originating from a flicker source is represented by $v_F(k)$ and is called the IFL.

$(U_c(k) + v_F(k))$ is the voltage envelope. The fundamental frequency carrier waveform (i.e., 50 Hz or 60 Hz) is represented by $U_c(k) \sin(\Omega_o k T_s + \Theta)$. Basically, the flicker estimation includes a voltage envelope (VE) tracking step and an IFL estimation procedure. The fundamental frequency voltage amplitude ($\hat{A}_1(k)$) provides the voltage envelope estimate. As the flicker frequency range is approximately between 0.5 Hz and 30 Hz, the task of separating the IFL from an estimated VE is a challenging practice due to the low frequency nature of $v_F(k)$. The flicker estimation technique recommended by IEEE Standard 1453 is designed for analogue instrumentation [135]. However, the actual implementation considerations such as preventing filters from over-voltages or over-currents always need a more complicated design. Therefore, the implementation of a digital algorithm to reduce the cost of implementation has become an attractive alternative [121].

A digital implementation to estimate the IFL is presented based on the FFT and the amplitude modulation (AM) technique in [121]. Reference [133] presents an application of the pruned FFT algorithm for IFL measurement and a two-stage Kalman filter is proposed in [74]. However, none of them approaches the problem of frequency variation. The implementation of an FFT algorithm with a high frequency resolution imposes a big delay depending on the choice of base frequency. A high frequency

resolution also implies that a large window is used, which means that a significant number of samples load the DSP. For example, if the base frequency is considered to be 1 Hz, the estimation delay will be 1 s. On the other hand, arranging a full order Kalman filter needs counting for all harmonics which brings about the difficulty of dimensionality to the real-time estimation field and causes run-time jams in the digital signal processors (DSPs).

In the proposed technique, the VE is estimated by the proposed frequency adaptive LS algorithm which was presented in the previous section. Eqn. (2.30) provides an estimation of VE. This VE is fed to a Kalman filter to predict the IFL by developing the Kalman model state variables for the estimated VE. The Kalman model which is developed in this chapter is a modification of a two-stage model which has been used in [120], [74], whereas the first stage is replaced by the proposed LS algorithm and the Kalman filter performs the IFL estimation task. The stable response and lower computational burden of the proposed method make it feasible to apply the adaptive LSK method for IFL estimation in a real-time implementation. The estimated value of VE from (2.30) can be interpreted in the state space as:

$$\bar{A}_1(k+1) = \left. \left\{ x_{IFL4}(n) + x_{IFL1}(n) \cos(2 x_{IFL3}(n)T_s) - x_{IFL2}(n) \sin(2 x_{IFL3}(n)T_s) \right\} \right|_{n=k} \quad (2.32)$$

where

$\bar{A}_1(k+1)$ is the predicted value of $A_1(k+1)$ at the $(k+1)^{\text{th}}$ sample

At the n^{th} state:

$x_{IFL1}(n)$ is the IFL estimation

$x_{IFL2}(n)$ is the quadrature component of the IFL

$x_{IFL3}(n)$ is the total phase-angle of the IFL

$x_{IFL4}(n)|_{n=k}$ is the estimation of the fundamental carrier voltage level ($U_c(k)$).

It should be noted that the estimated voltage envelope by the LS technique at the k^{th} sample ($\hat{A}_1(k)$) is fed to the Kalman filter to predict its value at the $(k+1)^{\text{th}}$ sample ($\bar{A}_1(k+1)$). Although the k^{th} sample and the n^{th} state are conceptually different, the n^{th} state in the Kalman prediction model coincides with the k^{th} sample in the hybrid LSK model when $n=k$. In other words, n is the index number of the state at which the internal Kalman loop performs the prediction task and does not have any external equivalence, but it is synchronized to happen at the same time at which the LS algorithm estimates a value for the voltage envelope. The Kalman state vector is considered as:

$$x_{IFL}(n) = [x_{IFL1}(n) \quad x_{IFL2}(n) \quad x_{IFL3}(n) \quad x_{IFL4}(n)]^T \quad (2.33)$$

The extended Kalman model for the non-linear function which is presented in (2.32) is defined by the following equations:

$$x_{IFL}(n+1) = \Phi_{IFL}(x_{IFL}(n)) + \nu_n \quad (2.34)$$

$$b_{IFL}(n) = d_{IFL}(x_{IFL}(n)) + \Gamma_n \quad (2.35)$$

where

$x_{IFL}(n)$ is the state vector at the n^{th} state

Φ_{IFL} is the state transition function

d_{IFL} is the estimation function

$b_{IFL}(n)$ is the measurement of the desired signal

w_n is the process noise

v_n is the measurement noise.

The evolution of this model is based on the fact that at the $(n+1)^{\text{th}}$ state, the phasor of the IFL is rotated by the amount $(2 x_{IFL3}(n)T_s)$. Therefore, the state transition between the n^{th} and $(n+1)^{\text{th}}$ states for x_{IFL1} and x_{IFL2} is described as:

$$x_{IFL1}(n+1) + jx_{IFL2}(n+1) = (x_{IFL1}(n) + jx_{IFL2}(n))e^{j(2 x_{IFL3}(n)T_s)} \quad (2.36)$$

where $j = \sqrt{-1}$ the complex space operator. Eqns. (2.32) and (2.36) lead to a non-linear state transition equation which is expressed as:

$$x_{IFL}(n+1) = \begin{bmatrix} x_{IFL1}(n) \cos(2 x_{IFL3}(n)T_s) - x_{IFL2}(n) \sin(2 x_{IFL3}(n)T_s) \\ x_{IFL1}(n) \sin(2 x_{IFL3}(n)T_s) + x_{IFL2}(n) \cos(2 x_{IFL3}(n)T_s) \\ x_{IFL3}(n) \\ x_{IFL4}(n) \end{bmatrix} \quad (2.37)$$

The estimation function d_{IFL} is defined as:

$$d_{IFL}(x_{IFL}(n)) = x_{IFL4}(n) + x_{IFL1}(n) \cos(2 x_{IFL3}(n)T_s) - x_{IFL2}(n) \sin(2 x_{IFL3}(n)T_s) \quad (2.38)$$

Since the above equations are non-linear functions, the state transition and measurement equations are also non-linear. The extended Kalman filter incorporates the linearized state transition and measurement equations to perform the estimation process [13]. To obtain a linear system, it is assumed that there exists a (local/global) nominal estimation of the state trajectory $\hat{x}_{IFL}(n)$ and a (local/global) nominal output $\hat{b}_{IFL}(n)$

and let the state vector and measurement deviations be denoted as follows [64]:

$$\Delta x_{IFL}(n) = x_{IFL}(n) - \hat{x}_{IFL}(n) \quad (2.39)$$

$$\Delta b_{IFL}(n) = b_{IFL}(n) - \hat{b}_{IFL}(n) \quad (2.40)$$

Linear approximation can be obtained by using the first-order terms in the Taylor series expansions of Φ_{IFL} and d_{IFL} as follows:

$$\Delta x_{IFL}(n+1) = \Phi_{IFL}(n) \Delta x_{IFL}(n) + \Gamma_n \quad (2.41)$$

$$\Delta b_{IFL}(n) = D_{IFL}(n) \Delta x_{IFL}(n) + \Gamma_n \quad (2.42)$$

where

$\Phi_{IFL}(n)$ is the Jacobian matrices of Φ_{IFL} and

$D_{IFL}(n)$ is the Jacobian matrices of d_{IFL} .

$\Phi_{IFL}(n)$ and $D_{IFL}(n)$ are defined as:

$$\Phi_{IFL}(n) = \left. \frac{\partial \Phi_{IFL}(n)}{\partial x_{IFL}(n)} \right|_{x_{IFL}(n) = \hat{x}_{IFL}(n)} \quad (2.43)$$

$$D_{IFL}(n) = \left. \frac{\partial d_{IFL}(n)}{\partial x_{IFL}(n)} \right|_{x_{IFL}(n) = \hat{x}_{IFL}(n)} \quad (2.44)$$

Substituting Φ_{IFL} from (2.37) into (2.43) and d_{IFL} from (2.38) into (2.44), result in the

following equations for $\Phi_{IFL}(n)$ and $D_{IFL}(n)$:

$$\Phi_{IFL}(n) = \begin{bmatrix} \cos(2 \hat{x}_{IFL3}(n)T_s) & -\sin(2 \hat{x}_{IFL3}(n)T_s) & \Phi_{IFL1,3}(n) & 0 \\ \sin(2 \hat{x}_{IFL3}(n)T_s) & \cos(2 \hat{x}_{IFL3}(n)T_s) & \Phi_{IFL2,3}(n) & 0 \\ 0 & 0 & 1 & 0 \\ 0 & 0 & 0 & 1 \end{bmatrix} \quad (2.45)$$

$$D_{IFL}^T(n) = \begin{bmatrix} \cos(2 \hat{x}_{IFL3}(n)T_s) & & & & \\ -\sin(2 \hat{x}_{IFL3}(n)T_s) & & & & \\ 2 T_s (-\hat{x}_{IFL1}(n) \sin(2 \hat{x}_{IFL3}(n)T_s) - \hat{x}_{IFL2}(k) \cos(2 \hat{x}_{IFL3}(n)T_s)) & & & & \\ & & & & 1 \end{bmatrix} \quad (2.46)$$

where

$\hat{x}_{IFL1}(n)$ is the estimate of $x_{IFL1}(n)$

$\hat{x}_{IFL2}(n)$ is the estimate of $x_{IFL2}(n)$

$\hat{x}_{IFL3}(n)$ is the estimate of $x_{IFL3}(n)$

$\hat{x}_{IFL4}(n)$ is the estimate of $x_{IFL4}(n)$.

$\Phi_{IFL1,3}(n)$ and $\Phi_{IFL2,3}(n)$ are calculated as follows:

$$\Phi_{IFL1,3}(n) = 2 T_s (-\hat{x}_{IFL1}(n) \sin(2 \hat{x}_{IFL3}(n)T_s) - \hat{x}_{IFL2}(n) \cos(2 \hat{x}_{IFL3}(n)T_s)) \quad (2.47)$$

$$\Phi_{IFL2,3}(n) = 2 T_s (\hat{x}_{IFL1}(n) \cos(2 \hat{x}_{IFL3}(n)T_s) - \hat{x}_{IFL2}(n) \sin(2 \hat{x}_{IFL3}(n)T_s)) \quad (2.48)$$

The extended Kalman filter uses the previously estimated state $\hat{x}_{IFL}(n)$ to predict the state $\bar{x}_{IFL}(n+1)$ as follows:

$$\begin{cases} \bar{x}_{IFL}(n+1) = \Phi_{IFL}(n) \hat{x}_{IFL}(n) \\ \hat{x}_{IFL}(n) = [\hat{x}_{IFL1}(n) \quad \hat{x}_{IFL2}(n) \quad \hat{x}_{IFL3}(n) \quad \hat{x}_{IFL4}(n)]^T \end{cases} \quad (2.49)$$

The estimation vector $\hat{x}_{IFL}(n)$ is calculated as:

$$\hat{x}_{IFL}(n) = \bar{x}_{IFL}(n) + B_{IFL}(n)(b_{IFL}(n) - D_{IFL}(n)\bar{x}_{IFL}(n)) \quad (2.50)$$

where

$B_{IFL}(n)$ is the extended Kalman gain matrix, which is updated as:

$$B_{IFL}(n) = P_{IFL}^-(n) D_{IFL}^T(n) \left(D_{IFL}(n) P_{IFL}^-(n) D_{IFL}^T(n) + N_{CIFL} \right)^{-1} \quad (2.51)$$

where

N_{CIFL} is the measurement noise covariance and $P_{IFL}^-(n)$ is the predicted error covariance matrix which is calculated as:

$$P_{IFL}^-(n) = \Phi_{IFL}(n) \hat{P}_{IFL}(n-1) (\Phi_{IFL}(n))^T + Q_{IFL} \quad (2.52)$$

where

Q_{IFL} is the process noise covariance matrix and

$\hat{P}_{IFL}(n)$ is the estimated error covariance matrix which is calculated as:

$$\hat{P}_{IFL}(n) = (I_{4 \times 4} - B_{IFL}(n) D_{IFL}(n)) P_{IFL}^-(n) \quad (2.53)$$

where

$I_{4 \times 4}$ is the 4×4 identity matrix.

Figure 2.3 shows the proposed LSK algorithm to predict the IFL.

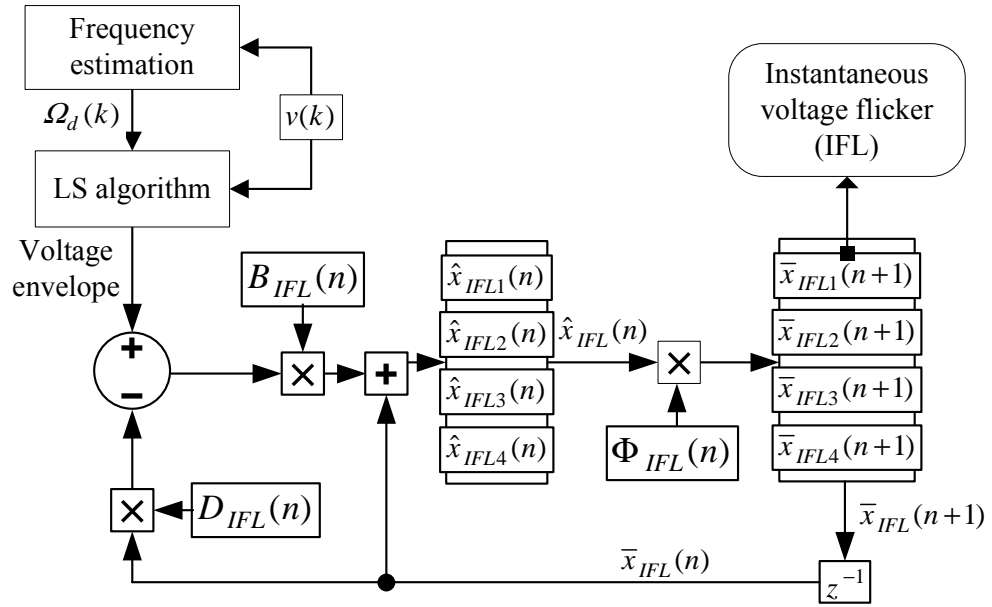


Figure 2.3. The proposed least-squares-Kalman (LSK) algorithm to predict the instantaneous flicker level (IFL).

2.4. Real-Time Implementation Experiments

The real-time implementation experiments have been carried out with two different DSP boards, namely the DS1104 and DS1103 [136]. The DS1104 has lower processing power than that of the DS1103. Implementing the proposed method on DS1104 can be done up to the sampling frequency of 1 kHz which is suitable for voltage envelope and flicker detection given that the harmonics higher than 500 Hz are of small amplitude or are filtered out by using an anti-aliasing filter. The sampling frequency on DS1103 can be much higher. The highest sampling frequency to implement the proposed LSK technique on DS1103 has been found to be 10 kHz based on experiments in the laboratory. Higher values of sampling frequency improve performance of the ANF and EPLL as presented in the following sections. However, the proposed LSK technique shows higher accuracy when implemented on a much lower sampling frequency and higher sampling frequency has a minimal effect to improve its accuracy.

The ANF and EPLL governing equations have been reviewed in Chapter 1. The EPLL and ANF have been digitized by using the trapezoidal form of the digital integrator in the MATLAB software as follows:

$$\frac{1}{s} \equiv T_s \frac{1+z^{-1}}{2(1-z^{-1})} \quad (2.54)$$

All algorithms are first built in the MATLAB/Simulink environment and, then, are compiled and uploaded to the DS1104 and DS1103 boards. The solver of the MATLAB software is set on the discrete mode to solve the differential equations in all case studies. The codes are compiled by the MATLAB software identically for both DS1104 and

DS1103 boards. The only difference is that the sampling frequency is set to 1 kHz for DS1104 but 10 kHz for DS1103.

2.4.1. Implementation 1: Sampling Frequency of 1 kHz

The proposed LSK technique is implemented in real-time by using a DS1104 R&D digital control board [136] and the results are presented in this section. The voltage waveforms are produced by using a programmable power supply [137]. The sampling frequency is 1 kHz, the nominal line-to-neutral rms voltage is 240 V, and the nominal fundamental frequency is 50 Hz. The voltages are sensed by voltage transducers [138] and fed into an analogue-to-digital (A/D) converter. The output of the A/D converter is connected to a computer on which the digital control board is mounted.

2.4.1.1. Case 1: Phasor Estimation in Presence of Frequency Drift

The power supply is programmed to produce frequency step changes of ± 0.1 Hz and 1.0 Hz in a sinusoidal voltage waveform while keeping the voltage amplitude at the value of $240\sqrt{2}$ V. Figure 2.4 (a) shows line-to-neutral voltage waveform. Figure 2.4 (b) shows the estimated fundamental frequency voltage amplitude. Figure 2.4 (c) shows the estimated frequency for ± 0.1 Hz frequency drifts.

Figure 2.5 (a) shows line-to-neutral voltage waveform. Figure 2.5 (b) shows the estimated fundamental frequency voltage amplitude. Figure 2.5 (c) presents the estimated frequency for 1.0 Hz frequency drift. The proposed LS technique shows a faster and more accurate estimation than ANF and EPLL techniques in detecting the

step frequency change and voltage amplitude. The LS technique shows faster and more accurate estimation than ANF and EPLL techniques.

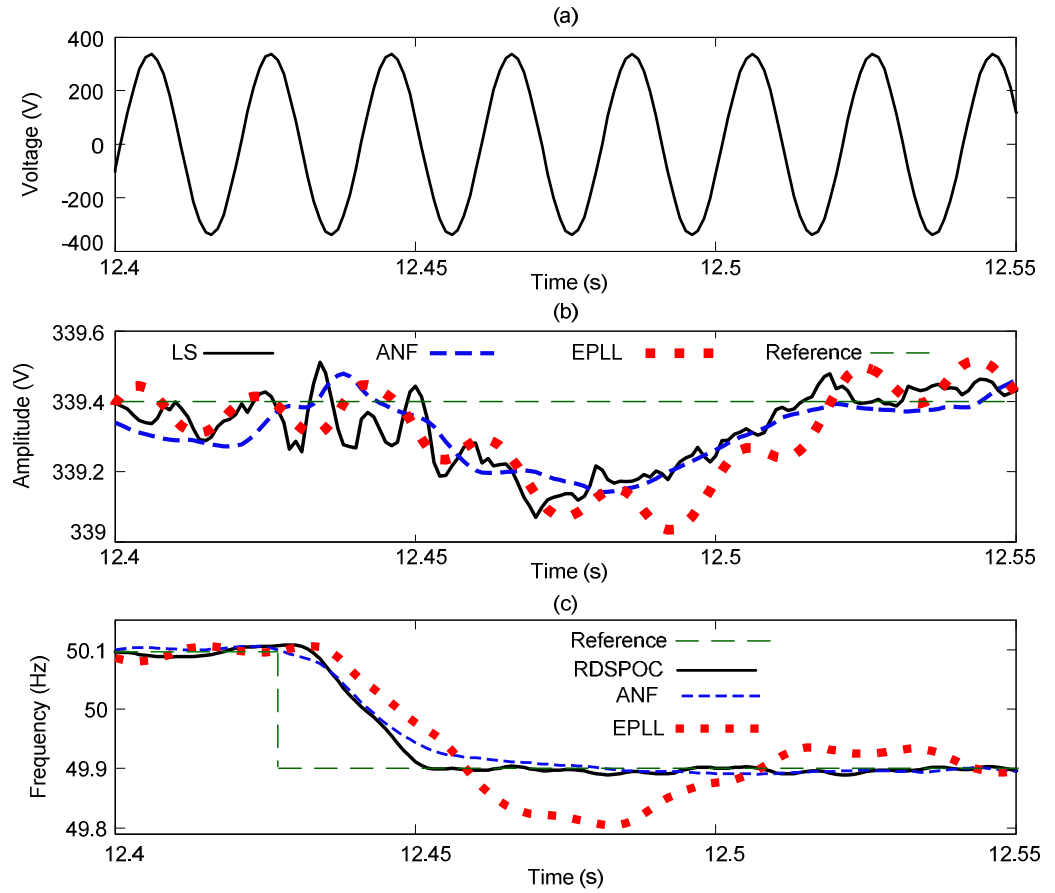


Figure 2.4. Case 1: ± 0.1 Hz frequency drift in a sinusoidal voltage

- (a) instantaneous line-to-neutral voltage waveform
- (b) estimated fundamental frequency voltage amplitude
- (c) estimated voltage frequency.

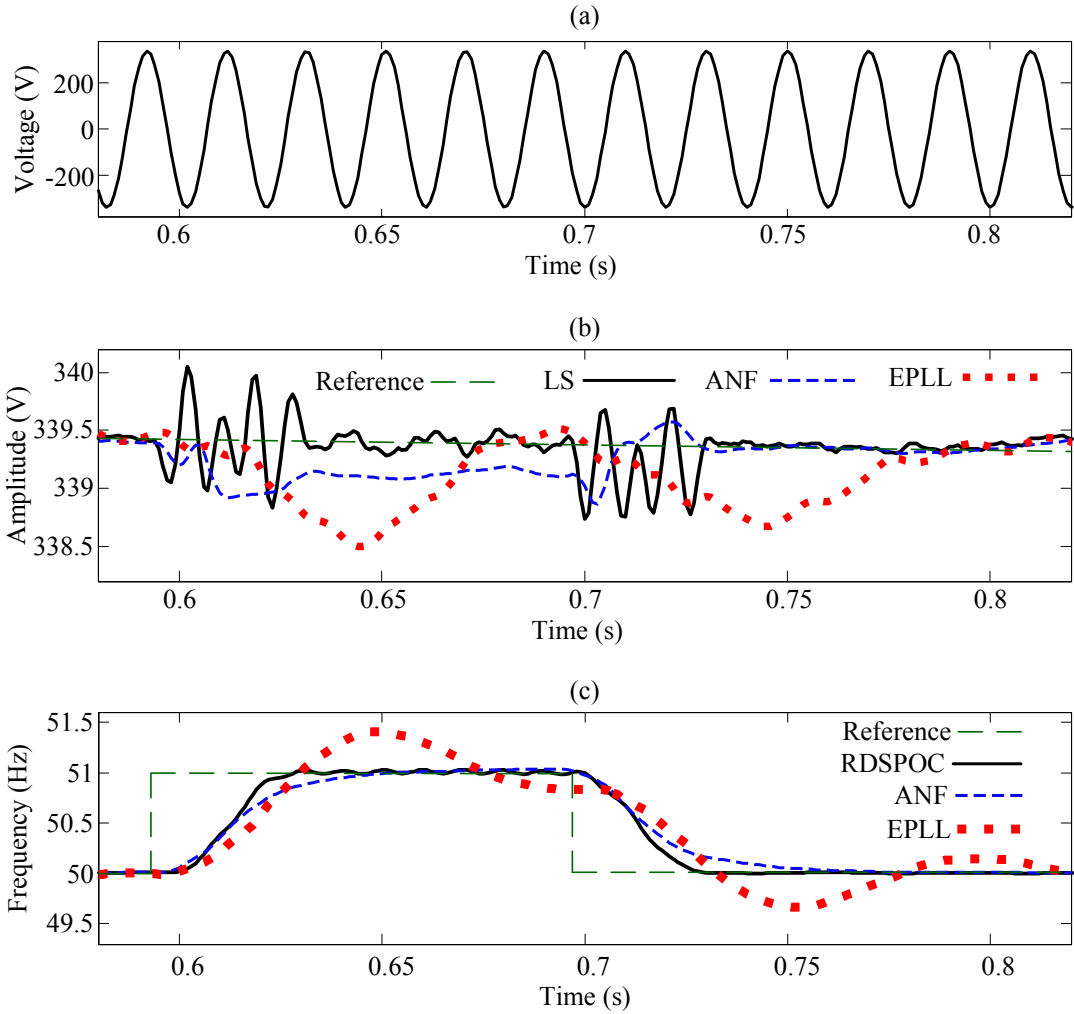


Figure 2.5. Case 1: 1 Hz frequency drift in a sinusoidal voltage

- (a) instantaneous line-to-neutral voltage waveform
- (b) estimated fundamental frequency voltage amplitude
- (c) estimated voltage frequency.

2.4.1.1. Case 2: Phasor Estimation in Presence of Frequency Drift and Harmonics

The power supply is programmed to produce a voltage waveform based on the IEC Standard 61000-4-13 definition for the third class test level to evaluate the performances of the LS, ANF, and EPLL techniques when the frequency changes in the presence of harmonic contamination. The fundamental frequency line-to-neutral voltage rms is 240 V. The harmonics content of the voltage waveform is presented in Table 2.1.

TABLE 2.1. CASE 2: PHASOR ESTIMATION IN PRESENCE OF FREQUENCY DRIFT AND HARMONICS, HARMONICS COMPONENT OF THE VOLTAGE WAVEFORM.

Harmonics order	Amplitude (V rms)	Phase-angle (radian)	Harmonics order	Amplitude (V rms)	Phase-angle (radian)
2	12	$\pi/6$	5	28.8	$\pi/3$
3	21.6	$\pi/4$	7	24.0	$\pi/2$
4	4.8	$\pi/3$	9	9.6	$2\pi/3$

Figure 2.6 (a) shows the line-to-neutral voltage waveform where a frequency step changes of 3.0 Hz is applied to the voltage, while the fundamental and harmonic components are kept constant at the aforementioned values. Figure 2.6 (b) shows the estimated fundamental frequency voltage amplitude and Figure 2.6 (c) shows the estimated frequency.

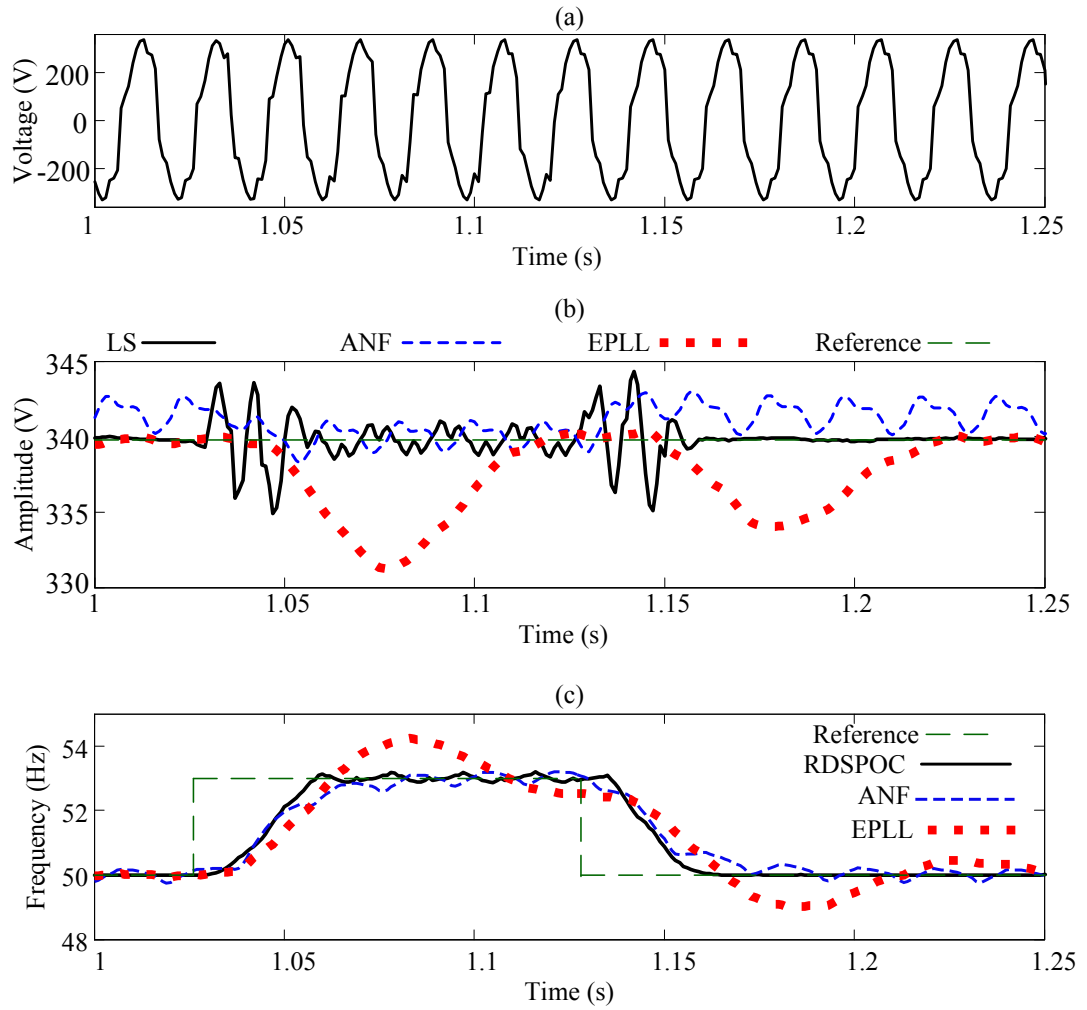


Figure 2.6. Case 2: 3 Hz frequency drift in presence of harmonic contamination

- (a) instantaneous line-to-neutral voltage waveform
- (b) estimated fundamental frequency voltage amplitude
- (c) estimated voltage frequency.

2.4.1.2. Case 3: Voltage Sag and Frequency Step Change

According to IEEE Standard 1159, a voltage sag is a decrease in rms voltage between 0.1 p.u. and 0.9 p.u. for durations from a half-cycle to 1 minute [139].

The algorithms in the technical literature to monitor and measure voltage variations are based on [140]:

- short-time Fourier transform
- analogue or digital filter banks
- wavelet transform using different wavelet kernels
- neural network classifiers
- fractal-base methods.

The proposed approach in this chapter belongs to the digital filter bank group which monitors and measures voltage variations based on the amplitude estimation through a digital frequency adaptive LS algorithm. Figure 2.7 (a) shows a voltage sag such that the line-to-neutral rms voltage drops from 240 V to 192 V and, at the same time, the voltage frequency increases to 52 Hz for 0.2 s. Figure 2.7 (b) shows the estimated voltage envelope and Figure 2.7 (c) shows the estimated frequency.

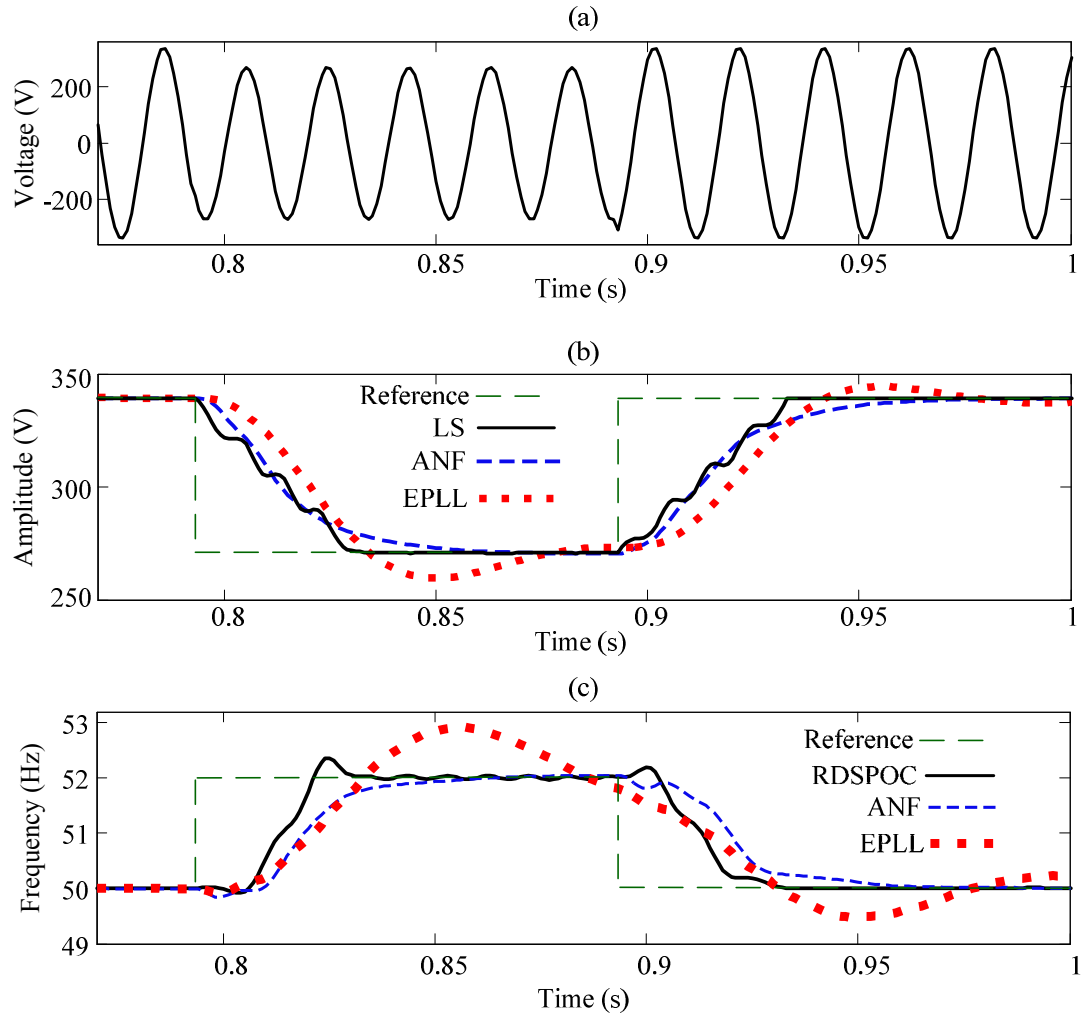


Figure 2.7. Case 3: voltage sag and 2 Hz frequency drift

- (a) instantaneous line-to-neutral voltage waveform
- (b) estimated fundamental frequency voltage amplitude
- (c) estimated voltage frequency.

2.4.2. Implementation 2: Sampling Frequency of 10 kHz

The proposed LSK technique is implemented in real-time by using a DS1103 R&D digital control board [136] and the results are presented in this section. The voltage waveforms are produced by using the same programmable power supply [137]. The sampling frequency can be increased to 10 kHz since DS1103 has a much more powerful processor. The nominal line-to-neutral rms voltage is 240 V, and the nominal fundamental frequency is 50 Hz. The voltages are sensed by voltage transducers [138] and fed into an analogue-to-digital (A/D) converter. The output of the A/D converter is connected to a computer on which the digital control board is mounted. All algorithms first are built in the MATLAB/Simulink environment; and, then, are compiled and uploaded to the DS1103 board. The solver of the MATLAB software is set on the discrete mode to solve the differential equations. The EPLL and ANF estimation accuracy can be improved by applying post-filtering stages. The LPFs with the cut-off frequency between 10 Hz and 30 Hz have been used for this purpose [8]-[10], [23], [48]-[52]. Applying smaller cut-off frequency for an LPF results in a more precise estimation although it creates a bigger estimation latency. Applying a second order LPF with the cut-off frequency of 10 Hz is in compliance with the requirements of IEC Standard 61000-4-30, as was explained in section 2.2.1. Since it is desired to have a minimum possible envelope estimation latency, applying an LPF with the cut-off frequency of 30 Hz seems to be the best option. However, applying the cut-off frequency of 20 Hz shows better disturbance rejection property for envelope estimation and flicker tracking. Therefore, a second order LPF with the cut-off frequency of 20 Hz

is applied to the amplitude estimation. It should be noted that applying any other LPF with the cut-off frequency of 10-30 Hz results in slightly different estimation accuracy and estimation latency.

2.4.2.1. Case 4: Frequency Drift and Harmonics

In this case, the performances of the proposed frequency adaptive LS, ANF, and EPLL techniques in the presence of frequency drift and harmonic contamination are evaluated. First, the power supply is programmed to produce frequency step changes of ± 0.1 Hz and 1.0 Hz in a sinusoidal voltage waveform while keeping the voltage amplitude constant at $240\sqrt{2}$ V.

Figure 2.8 (a) shows the line-to-neutral voltage waveform. Figure 2.8 (b) shows the estimated fundamental frequency voltage amplitude, and Figure 2.8 (c) shows the estimated frequency for ± 0.1 Hz frequency drifts. Figure 2.9 (a) shows the line-to-neutral voltage waveform. Figure 2.9 (b) shows the estimated fundamental frequency voltage amplitude, and Figure 2.9 (c) presents the estimated frequency for 1.0 Hz frequency drift.

The power supply is programmed to produce a voltage waveform which is contaminated with harmonics. Figure 2.10 shows the frequency spectrum of voltage waveform for 50 Hz fundamental frequency. Figure 2.11 (a) shows the line-to-neutral voltage waveform where a frequency step changes of 3.0 Hz is applied to the voltage. Figure 2.11 (b) shows the estimated fundamental frequency voltage amplitude and Figure 2.11 (c) shows the estimated frequency.

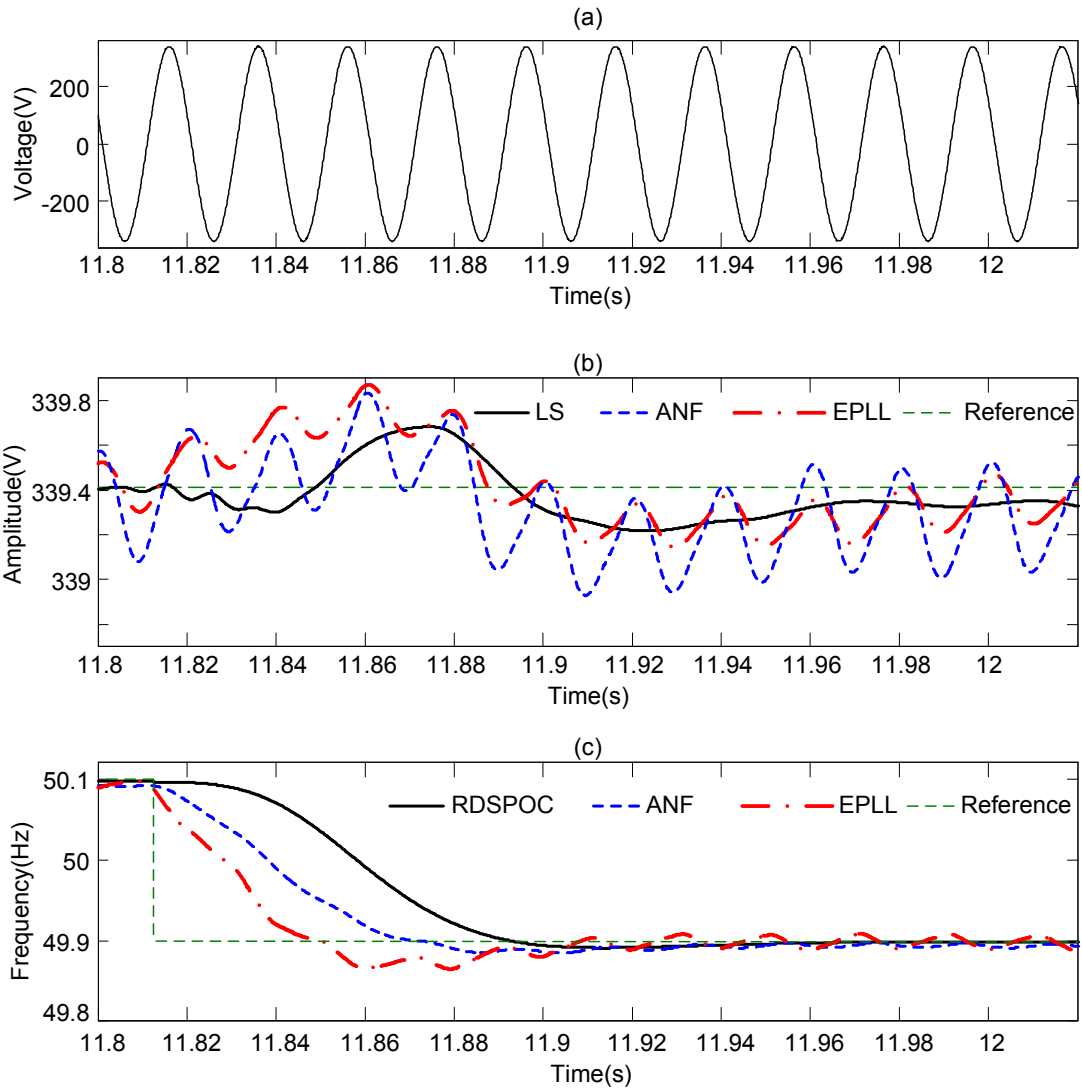


Figure 2.8. Case 4: ± 0.1 Hz frequency drift in a sinusoidal voltage

- (a) instantaneous line-to-neutral voltage waveform
- (b) estimated fundamental frequency voltage amplitude
- (c) estimated voltage frequency.

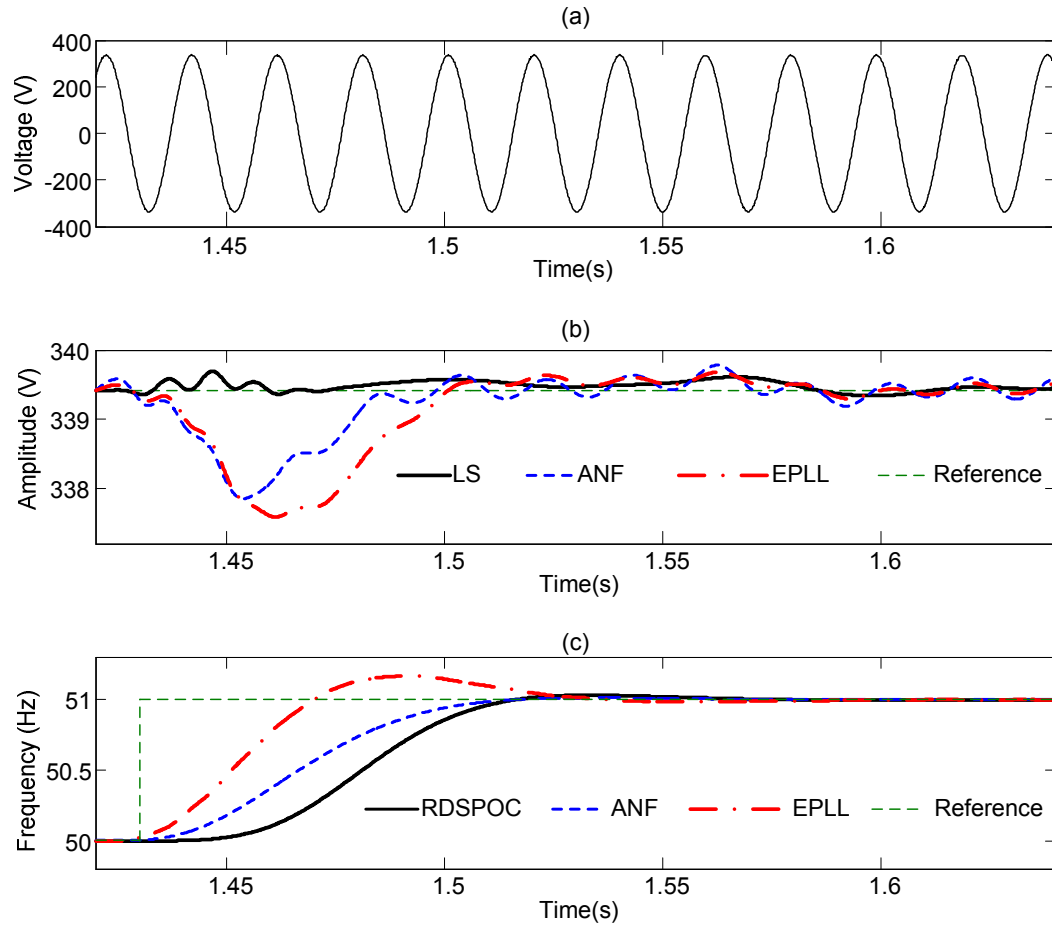


Figure 2.9. Case 4: 1 Hz frequency drift in a sinusoidal voltage

- (a) instantaneous line-to-neutral voltage waveform
- (b) estimated fundamental frequency voltage amplitude
- (c) estimated voltage frequency.

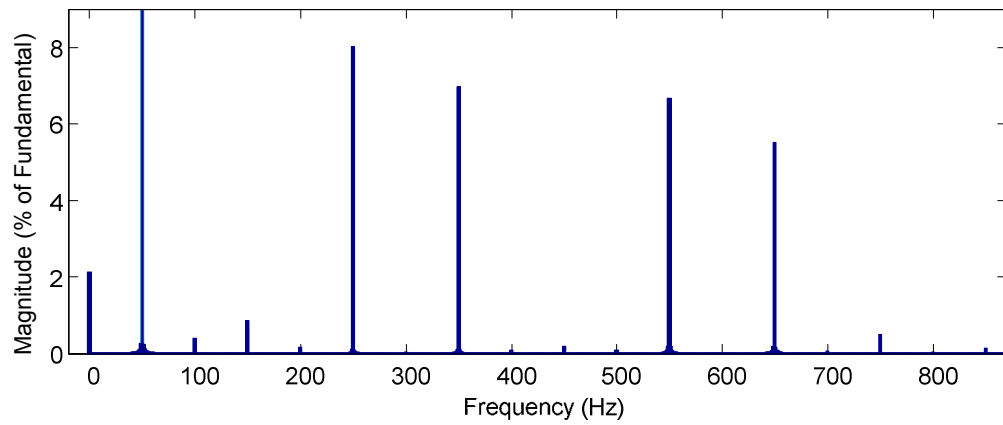


Figure 2.10. Case 4: 3 Hz frequency drift in presence of harmonic contamination

The harmonic spectrum of voltage waveform for 50 Hz fundamental frequency.

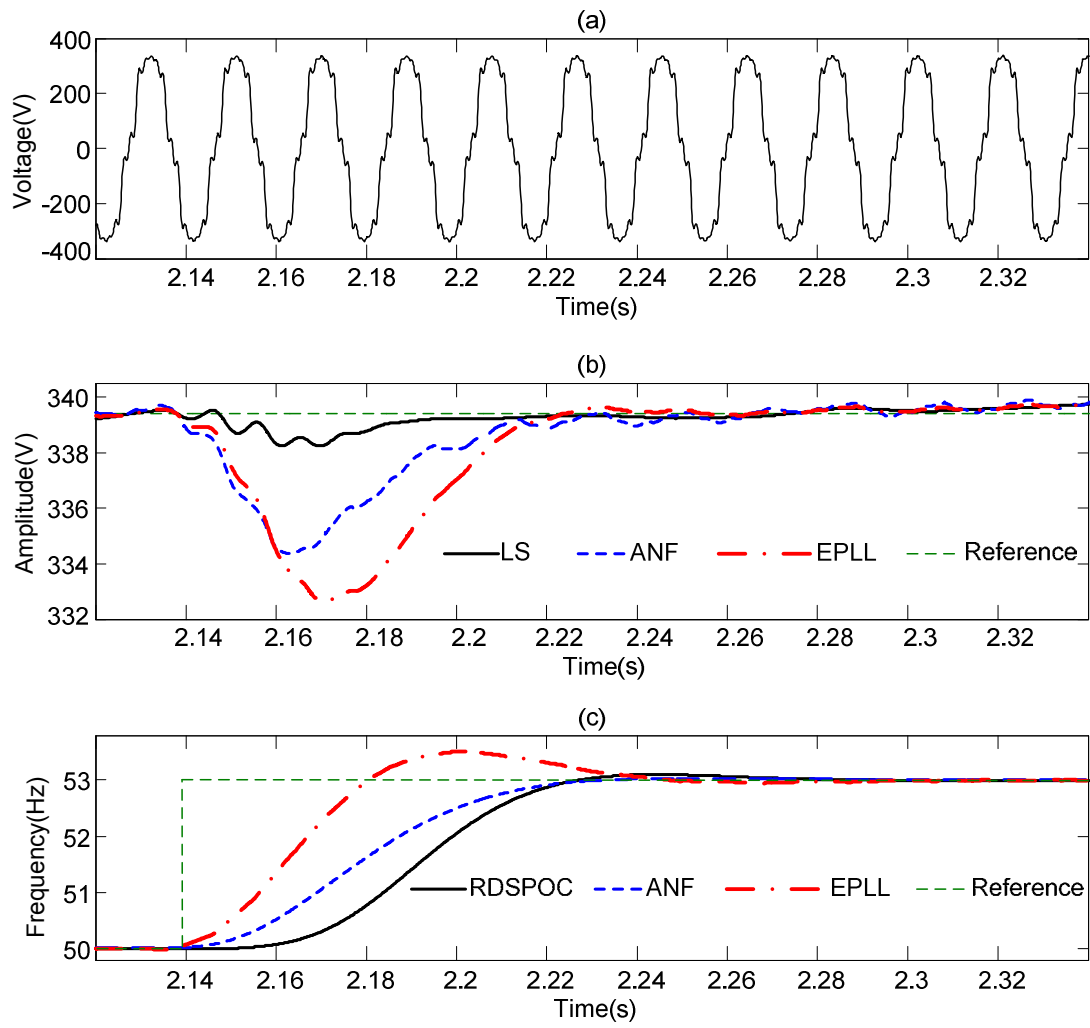


Figure 2.11. Case 4: 3 Hz frequency drift in presence of harmonic contamination

- (a) instantaneous line-to-neutral voltage waveform
- (b) estimated fundamental frequency voltage amplitude
- (c) estimated voltage frequency.

2.4.2.2. Case 5: Voltage Sag and Frequency Step Change

Figure 2.12 (a) shows a voltage sag such that the line-to-neutral rms voltage drops from 240 V to 214 V and, at the same time, the frequency decreases to 49 Hz. Figure 2.12 (b) shows the estimated voltage envelope and Figure 2.12 (c) shows the estimated frequency.

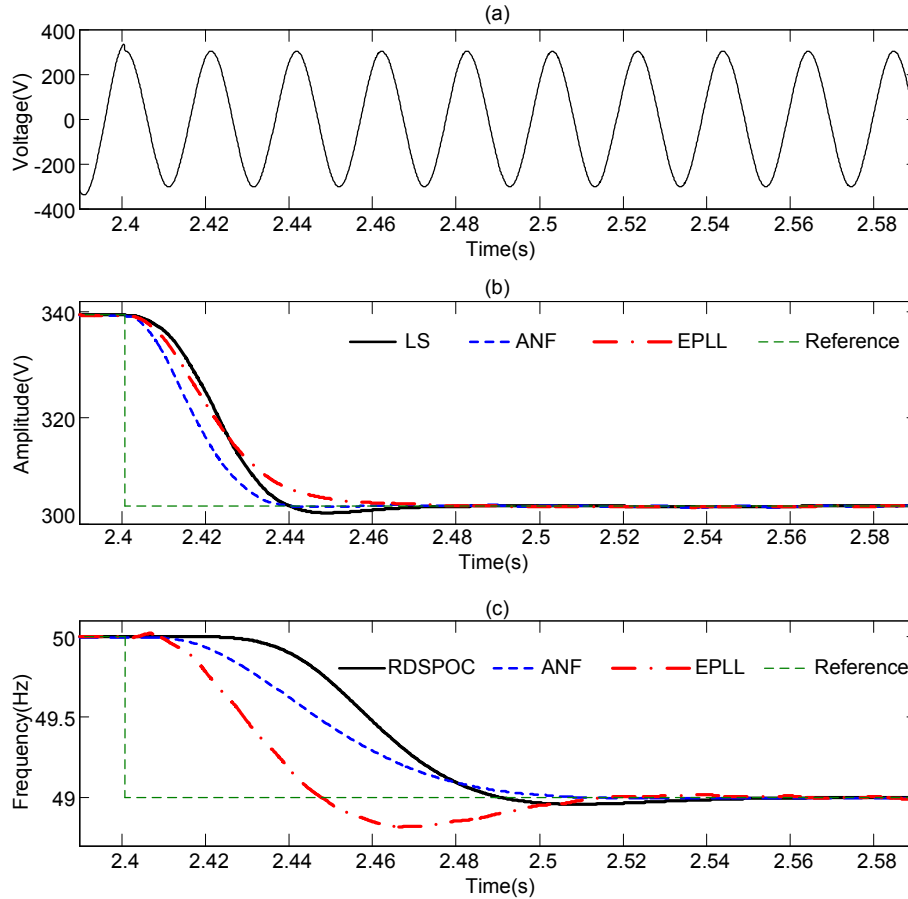


Figure 2.12. Case 5: voltage sag and -1 Hz frequency drift

- (a) instantaneous line-to-neutral voltage waveform
- (b) estimated voltage envelope
- (c) estimated voltage frequency.

2.4.2.3. Case 6: Triangle-Modulated Voltage Flicker

In this section, the results of IFL estimation for triangular-modulated voltage fluctuation by the DFT algorithm and the proposed LSK technique are presented and compared. The modulation frequencies are chosen to be 5 Hz and 4.167 Hz to evaluate the robustness of the proposed algorithm against unknown conditions and changes in the flicker frequency. The nominal line-to-neutral rms voltage is 240 V. The DFT filter base-frequency is set at 5 Hz [57] which uses seven terms to estimate the IFL [120] from the voltage waveform.

Figure 2.13 (a) shows a triangle-modulated voltage flicker with the modulation frequency of 5 Hz and modulation depth of 2% (4.8 V rms). Figure 2.13 (b) shows the IFL estimation by the DFT and LSK methods. Figure 2.14 (a) shows the estimated voltage envelope before post-filtering. Figure 2.14 (b) shows the estimated voltage envelope after post-filtering, and Figure 2.14 (c) shows the estimated voltage frequency.

Figure 2.15 (a) shows another triangle-modulated voltage flicker with the modulation frequency of 4.167 Hz (period of 240 ms) and modulation depth of 2% (4.8 V rms). As Figure 2.15 (b) shows, the DFT filter does not estimate the IFL correctly because its tuned base-frequency is not the same as the flicker frequency. The proposed LSK technique shows its superior performance due to its adaptive estimation approach, which accommodates the IFL frequency as a part of its internal prediction procedure. Figure 2.16 (a) shows the estimated voltage envelope before post-filtering. Figure 2.16 (b) shows the estimated voltage envelope after post-filtering and Figure 2.16 (c) shows the estimated voltage frequency.

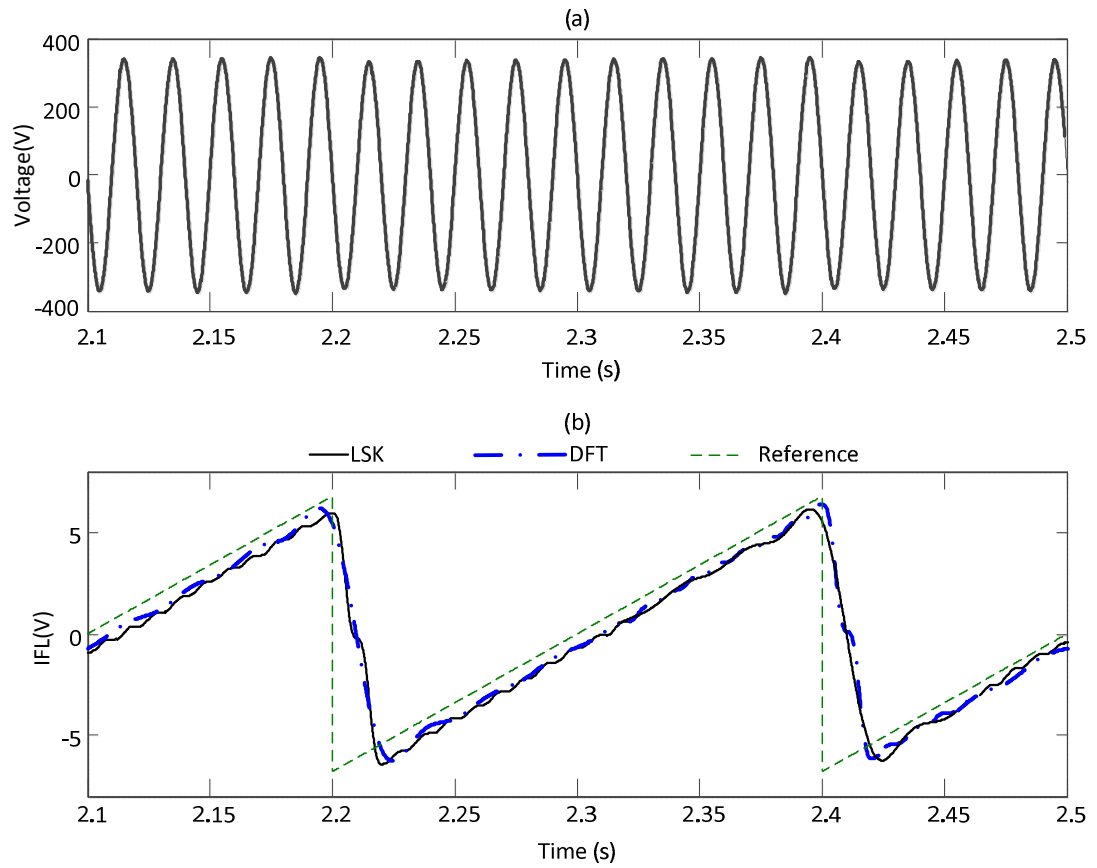


Figure 2.13. Case 6: 5 Hz triangular flicker with the modulation depth of 2%

(a) line-to-neutral instantaneous voltage waveform

(b) instantaneous flicker level (IFL) estimation.

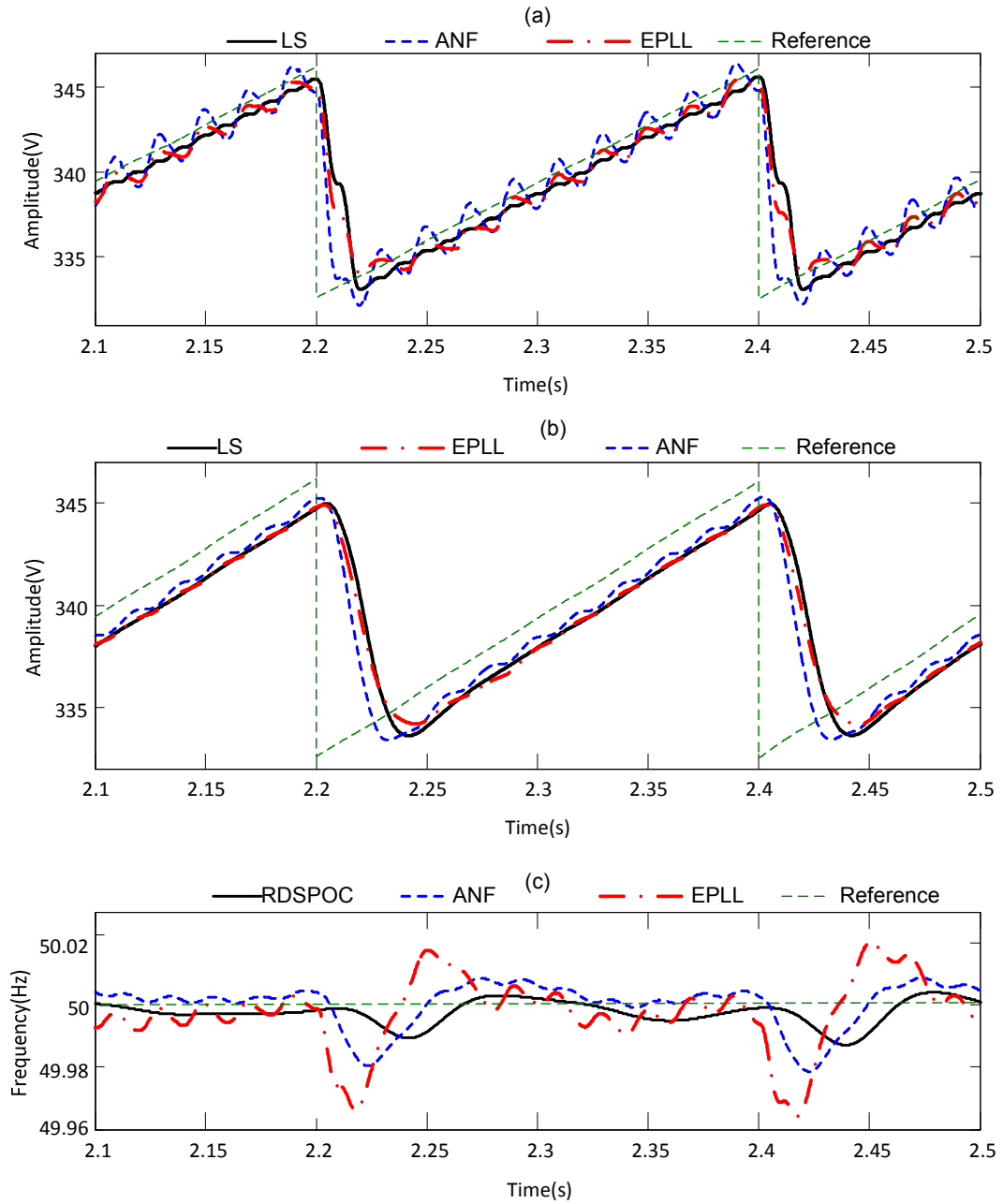


Figure 2.14. Case 6: 5 Hz triangular flicker with the modulation depth of 2%

(a) estimated voltage envelope before post-filtering

(b) estimated voltage envelope after post-filtering

(c) estimated voltage frequency.

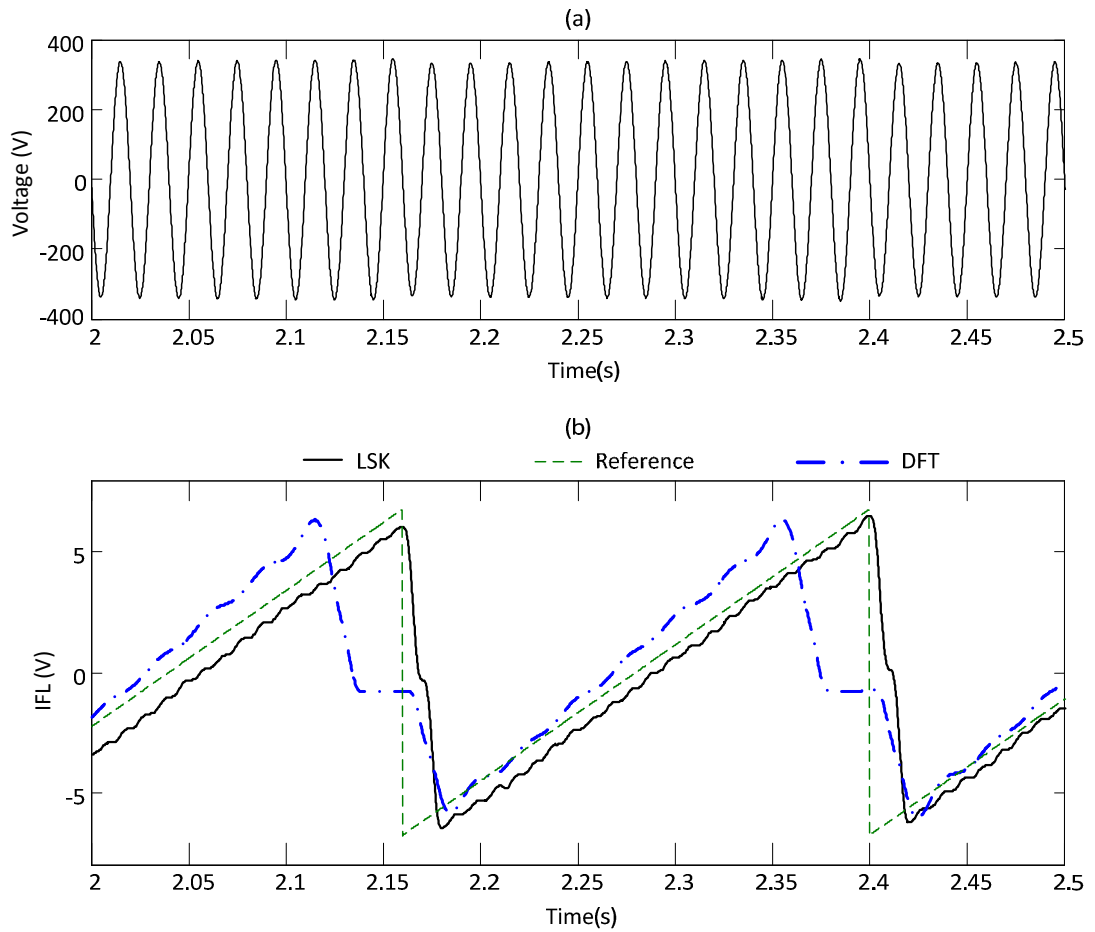


Figure 2.15. Case 6: 4.167 Hz triangular flicker with the modulation depth of 2%

(a) line-to-neutral instantaneous voltage waveform

(b) instantaneous flicker level (IFL) estimation.

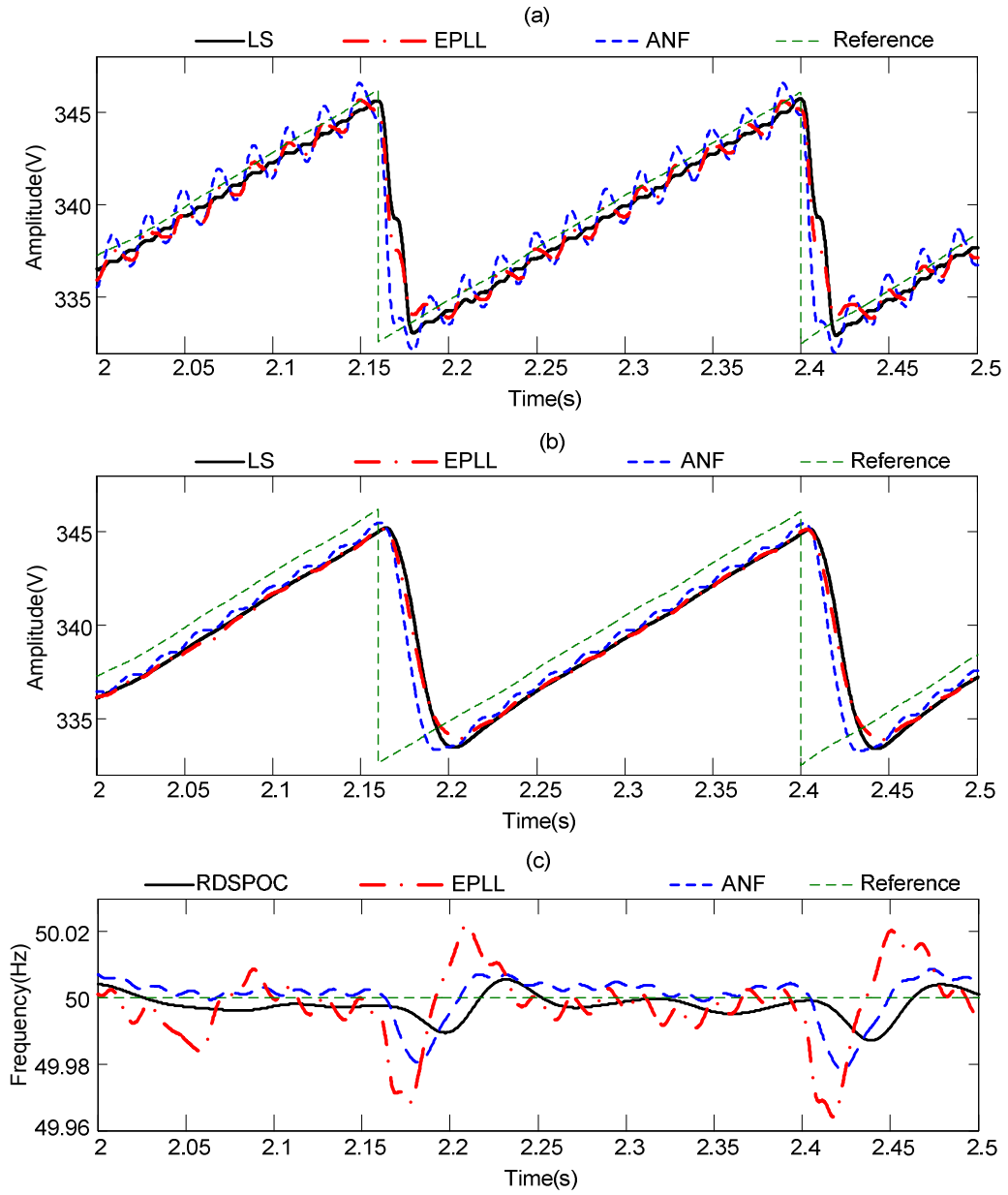


Figure 2.16. Case 6: 4.167 Hz triangular flicker with the modulation depth of 2%

(a) estimated voltage envelope before post-filtering

(b) estimated voltage envelope after post-filtering

(c) estimated voltage frequency.

2.4.2.4. Case 7: Square-Modulated Voltage Flicker

This section presents the IFL estimation results for square-modulated voltage flicker by the DFT and LSK techniques. The design of DFT filter is the same as the previous section. The flicker is produced with two modulation frequencies 5 Hz and 4.167 Hz to evaluate the performance of each approach for this type of variation in the voltage amplitude. The nominal line-to-neutral rms voltage is 240 V. Figure 2.17 shows a square-modulated voltage flicker and the IFL estimation for the modulation frequency of 5 Hz and modulation depth of 2%. Figure 2.18 (a) shows the estimated voltage envelope before post-filtering. Figure 2.18 (b) shows the estimated voltage envelope after post-filtering, and Figure 2.18 (c) shows the estimated voltage frequency.

Figure 2.19 (a) shows 2% square-wave modulated voltage flicker with the modulation frequency of 4.167 Hz (equivalent to the period of 240 ms). As Figure 2.19 (b) shows, the DFT filter fails to estimate the IFL close to the reference waveform because the frequency of the square-wave fluctuation is not an integer multiple of its base-frequency. The proposed LSK shows a better IFL estimation accuracy and follows the reference with better accuracy. Figure 2.20 (a) shows the estimated voltage envelope before post-filtering. Figure 2.20 (b) shows the estimated voltage envelope after post-filtering, and Figure 2.20 (c) shows the estimated voltage frequency.

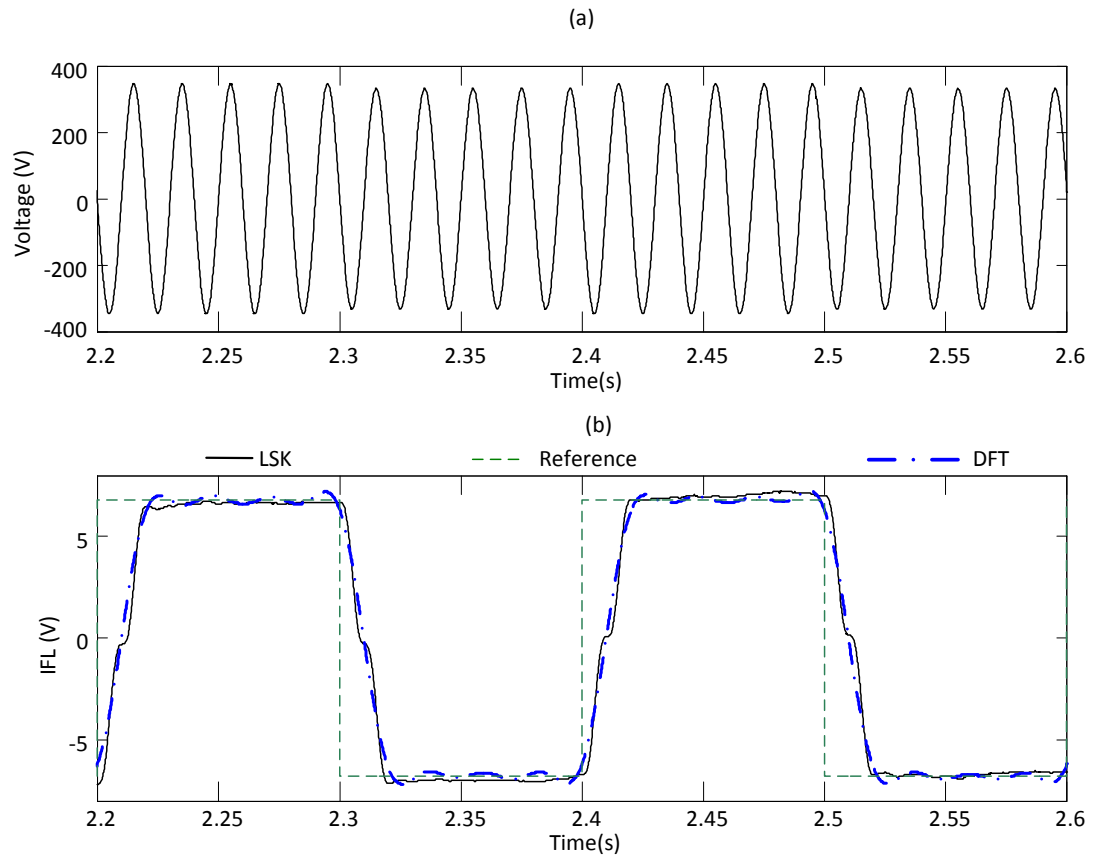


Figure 2.17. Case 7: 2% square-wave flicker at the modulation frequency of 5 Hz

(a) line-to-neutral instantaneous voltage waveform

(b) instantaneous flicker level (IFL) estimation.

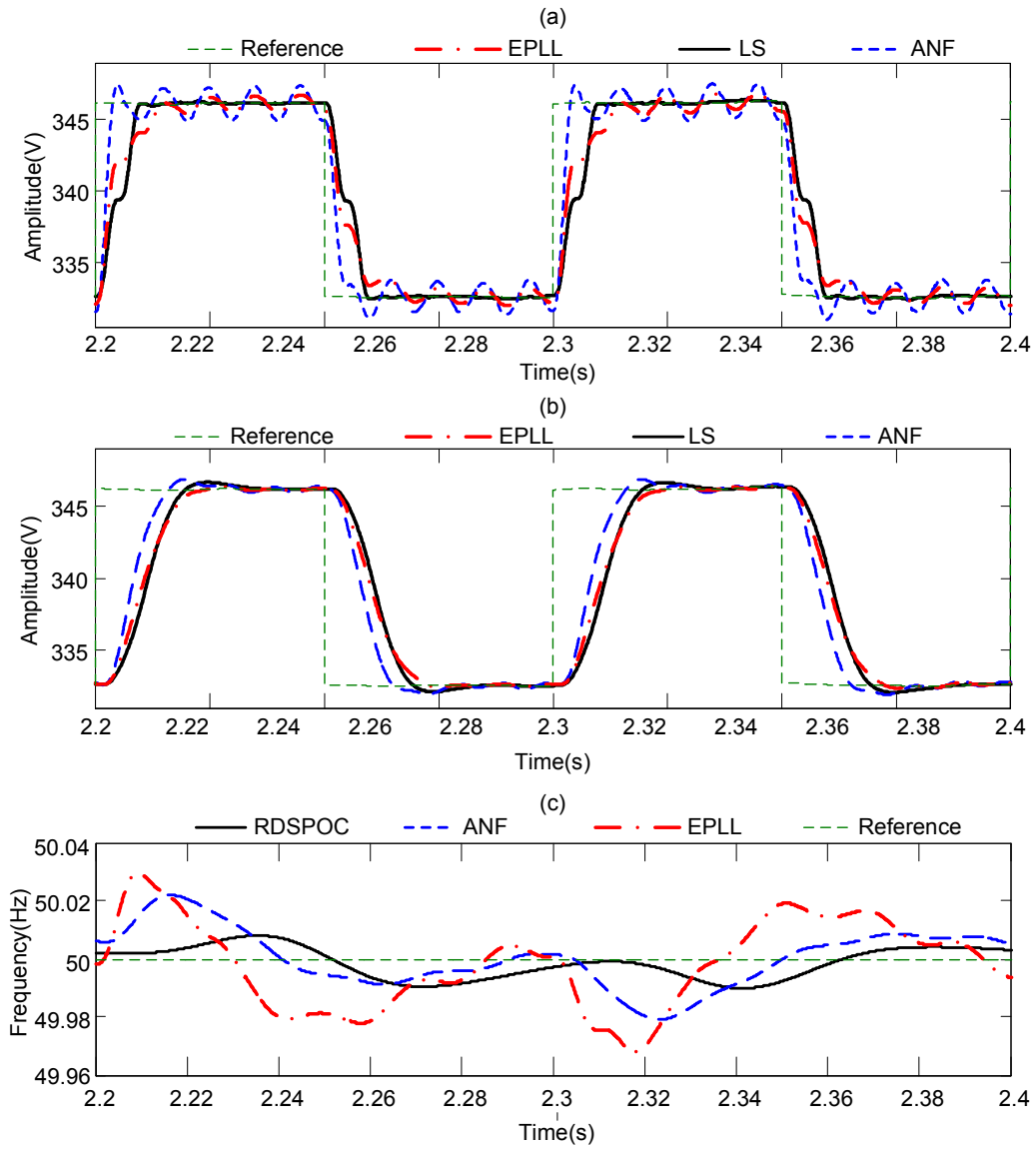


Figure 2.18. Case 7: 2% square-wave flicker at the modulation frequency of 5 Hz

(a) estimated voltage envelope before post-filtering

(b) estimated voltage envelope after post-filtering

(c) estimated voltage frequency.

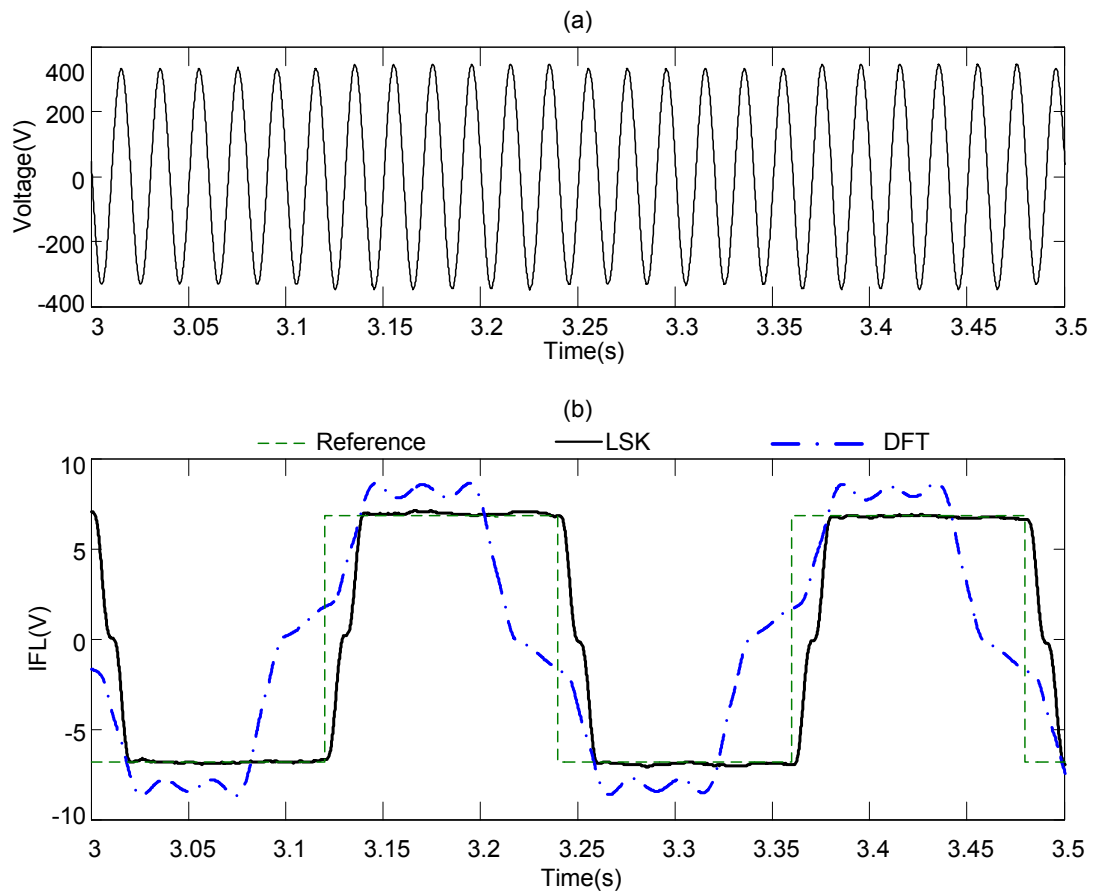


Figure 2.19. Case 7: 2% square-wave flicker at the modulation frequency of 4.167 Hz

(a) line-to-neutral instantaneous voltage waveform

(b) instantaneous flicker level (IFL) estimation.

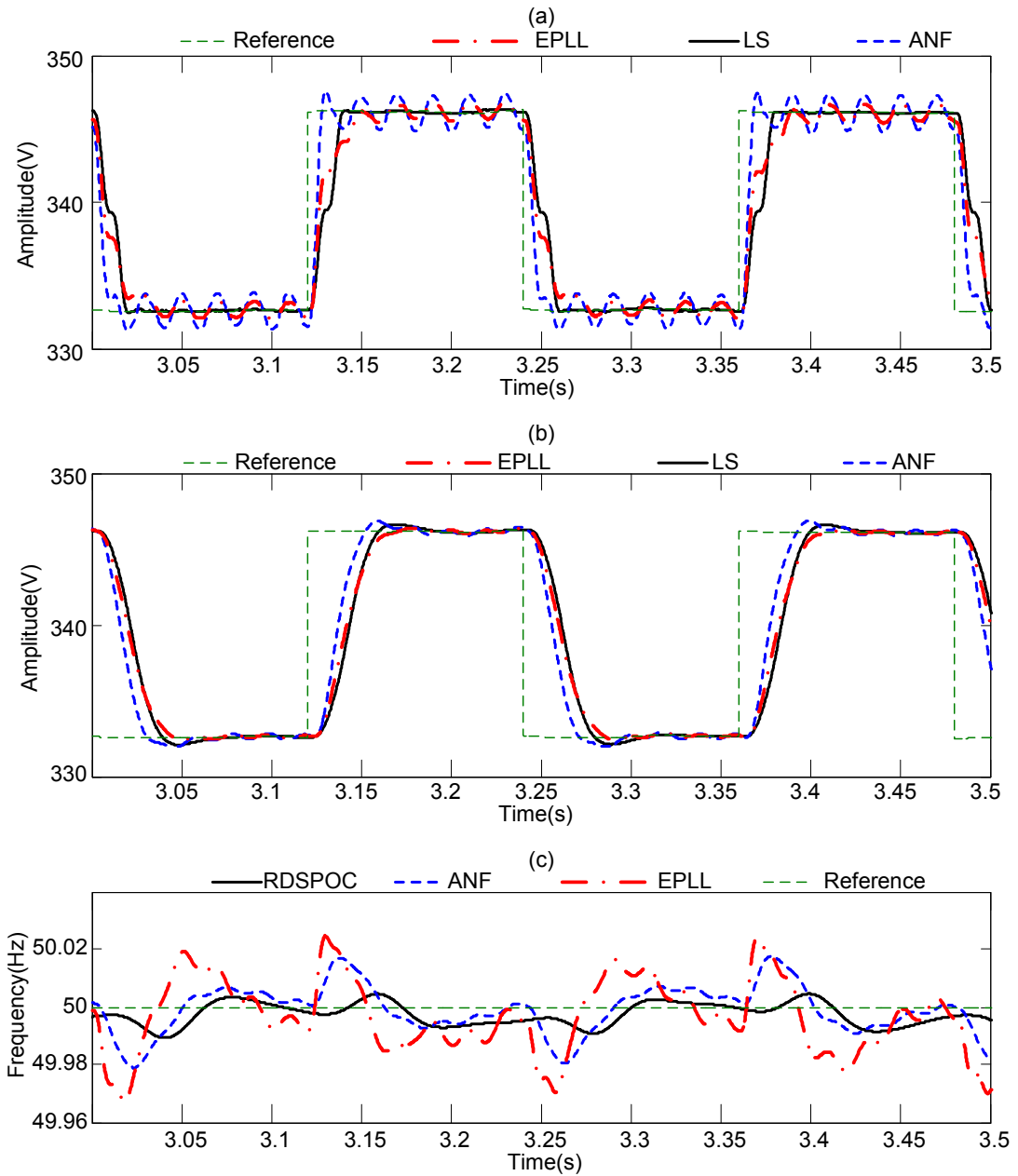


Figure 2.20. Case 7: 2% square-wave flicker at the modulation frequency of 4.167 Hz

(a) estimated voltage envelope before post-filtering

(b) estimated voltage envelope after post-filtering

(c) estimated voltage frequency.

2.4.2.5. Case 8: Flicker and Frequency Drift

In this case, a sinusoidal voltage waveform with the frequency of 49.0 Hz is produced and modulated by a square-wave voltage flicker. The voltage flicker frequency is 5 Hz with the modulation depth of 2%. Figure 2.21 (a) shows the line-to-neutral voltage waveform and Figure 2.21 (b) shows the estimated IFL by the LSK and DFT techniques. As seen in Figure 2.21 (b), the DFT estimation shows some oscillations around the reference value which are due to the Gibbs phenomenon [5] and frequency variation whereas the LSK estimation adapts itself with the frequency deviation. Figure 2.22 (a) shows the estimated voltage envelope before post-filtering. Figure 2.22 (b) shows the estimated voltage envelope after post-filtering and Figure 2.22 (c) shows the estimated voltage frequency.

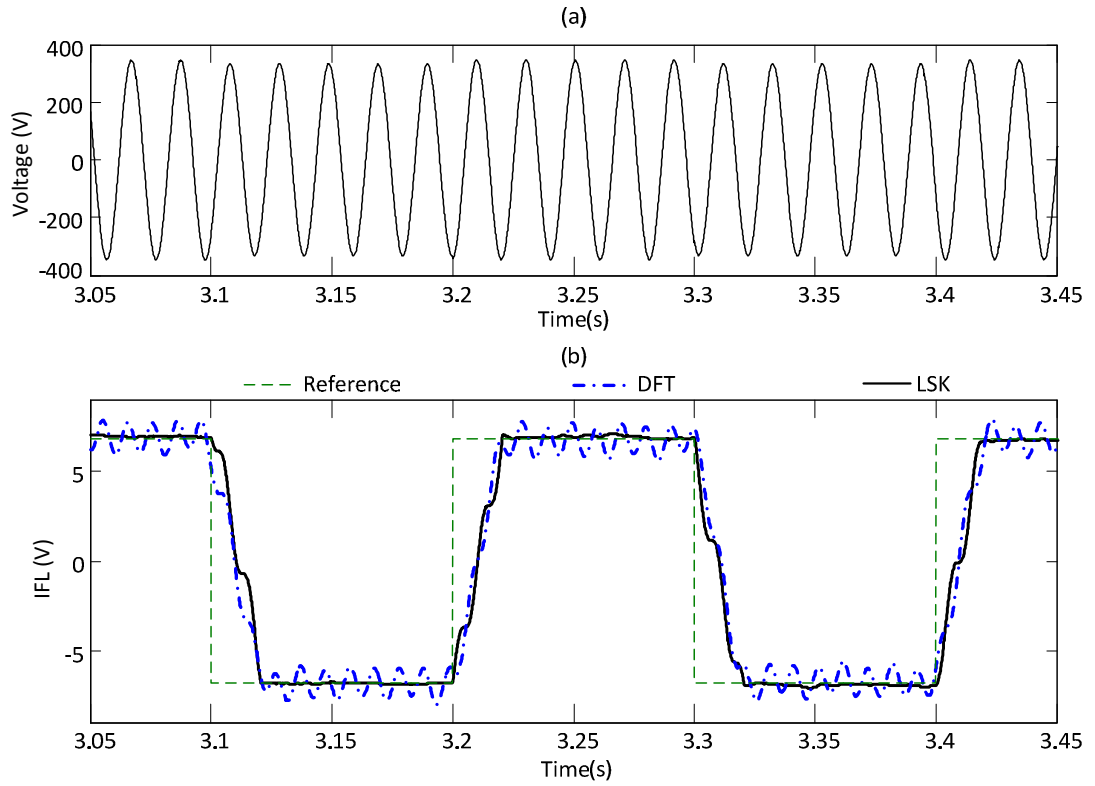


Figure 2.21. Case 8: flicker estimation in presence of frequency drift

(a) instantaneous line-to-neutral voltage waveform at 49 Hz

(b) instantaneous flicker level (IFL) estimation.

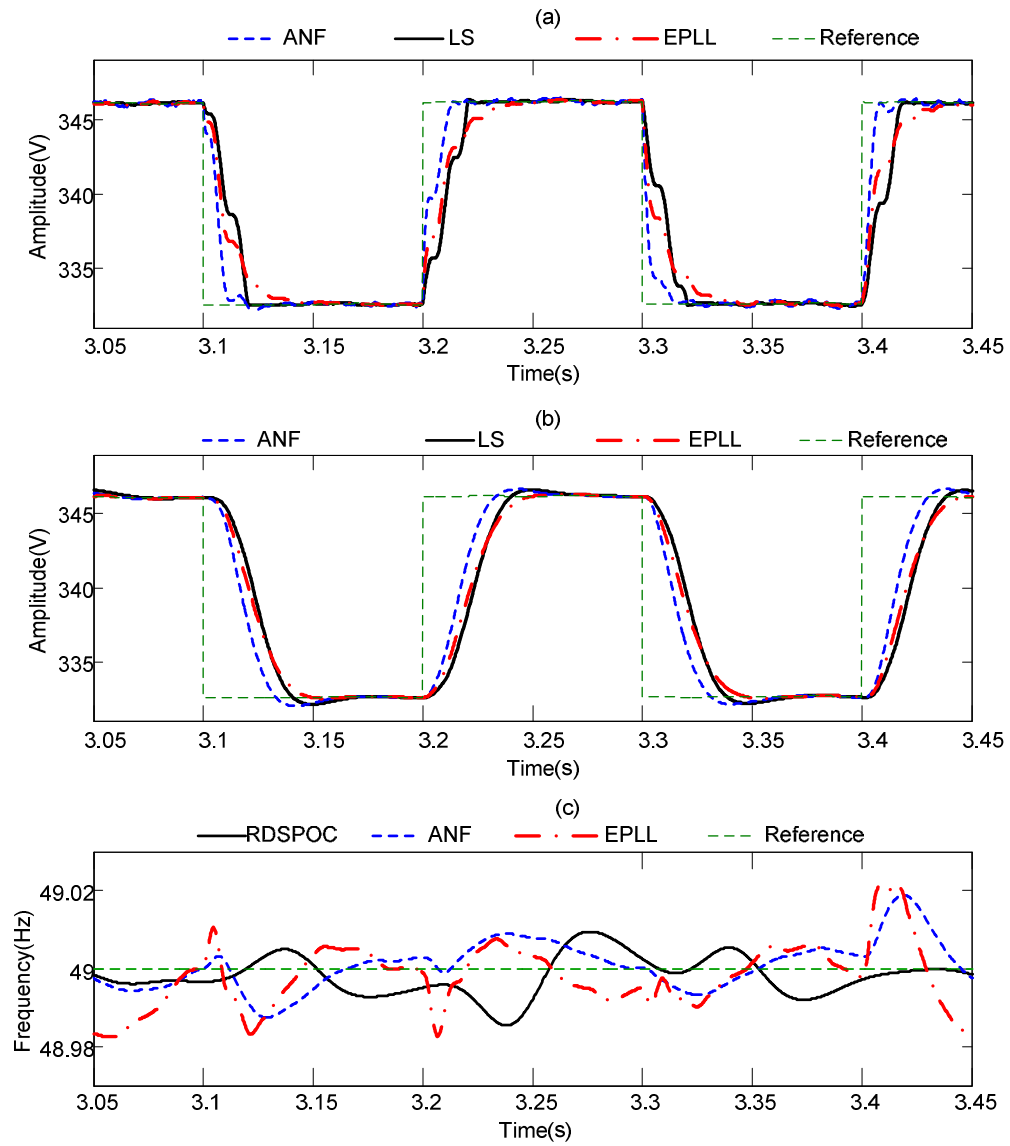


Figure 2.22. Case 8: flicker estimation in presence of frequency drift

(a) estimated voltage envelope before post-filtering

(b) estimated voltage envelope after post-filtering

(c) estimated voltage frequency.

2.4.2.6. Case 9: Noise Immunity

This section presents the results of frequency and amplitude estimation in the presence of noise contamination. Table 2.2 and Table 2.3 show the average absolute values of steady state frequency and amplitude estimation errors for frequency deviation of -1 Hz from 50 Hz respectively. The signal-to-noise-ratio (SNR) changes between 10 dB and 40 dB. The noise is a Gaussian zero-mean random signal. The reference value of frequency is 49.0 Hz in Table 2.2. The reference value of amplitude is $240\sqrt{2}$ V in Table 2.3.

TABLE 2.2. AVERAGE ABSOLUTE VALUE OF STEADY STATE FREQUENCY ESTIMATION ERROR FOR DIFFERENT LEVELS OF SNR AND FREQUENCY DRIFT OF -1 Hz, CASE 9.

SNR (dB)	RDSPOC	ANF	EPLL
10	0.0462	0.0635	0.0812
20	0.0146	0.0200	0.0257
30	0.0047	0.0070	0.0083
40	0.0016	0.0039	0.0029

TABLE 2.3. AVERAGE ABSOLUTE VALUE OF STEADY STATE AMPLITUDE ESTIMATION ERROR FOR DIFFERENT LEVELS OF SNR AND FREQUENCY DRIFT OF -1 Hz, CASE 9.

SNR (dB)	LS	ANF	EPLL
10	3.3879	3.7408	3.2174
20	1.0726	1.1844	1.0190
30	0.3420	0.3774	0.3256
40	0.1153	0.1273	0.1104

2.5. Conclusion

This chapter presented the real-time implementation of the frequency adaptive LS technique and Kalman filter to estimate the voltage envelope and predict the instantaneous voltage flicker in power systems. The frequency variation was tracked by using the recursive DSPOC (RDSPOC) technique. An LS technique was proposed to detect the fundamental frequency voltage envelope which updates its internal model according to the estimated frequency. Moreover, a hybrid least-squares-Kalman (LSK) technique was introduced to predict the instantaneous flicker level in real-time.

The modified structure of the proposed LSK method effectively decreases the DSP hardware demand such that on-line stable implementation of the Kalman filter becomes feasible. The presented results prove high accuracy and adaptive performance of the proposed LSK estimation technique in presence of harmonics, noise, frequency variations, and voltage fluctuations. The proposed LSK technique tracks the IFL more precisely than the DFT technique. The proposed adaptive LS technique shows better accuracy than that of the EPLL and ANF techniques for DSP implementation at a lower sampling frequency.

Chapter 3 : Real-Time Power System Phasors and Harmonics Estimation Using a New Decoupled Recursive-Least-Squares Technique

3.1. Introduction

The discrete Fourier transform (DFT) has been by far the most popular technique for real-time estimation of phasors and harmonics using digital signal processors (DSPs) in modern power systems [6], [7]. Nevertheless, the presence of decaying dc offsets [66] and frequency variations [141] are some of the remaining technical challenges for real-time implementation of DFT algorithms on DSPs.

On the other hand, the recursive-least-squares (RLS) technique is a well-established numerical method which can deal effectively with decaying dc offsets, power system frequency variations, and sub-synchronous oscillations [14], [79]-[98].

However, the mathematical complexity of the RLS technique hinders its practical application [85]. The existing technical literature on the RLS technique has not comprehensively addressed the issues of real-time implementation on typical DSPs for power system phasors and harmonics estimation. Although the computational complexity of the RLS technique has yet to be addressed itself, the RLS technique has

been proposed as a remedy to ease the heavy computational burden of Newton-type algorithms for power system phasors and harmonics estimation [79]-[82]. References [79]-[96] present simulation results and/or the results of off-line processing on the captured waveforms by using the RLS technique. References [14], [97], [98] report real-time implementation of the RLS technique for fundamental frequency phasor estimation on DSP platforms and do not discuss challenges of implementing higher orders of RLS technique for real-time harmonics estimation under the highly distorted power system environment.

The turnaround-time can be used as a metric to quantify the computational efficiency of real-time implementation on DSPs. The DSP turnaround-time is the total time taken between the submission of a program for execution and the return of the complete output which should be smaller than the sampling period (inverse of the sampling frequency) [14], [136]. The problem of reducing the DFT technique turnaround-time has been addressed by the recursive DFT (RDFT) technique [62], which however requires precautionary modifications to avoid instability when implemented on DSPs as discussed in [63]. The problem of real-time DFT implementation on DSPs becomes more challenging if the option of removing the anti-aliasing filter is considered, which would imply a higher sampling frequency according to the Nyquist-Shannon theorem [61].

The objective of this chapter is to fill the gap between off-line application of the RLS technique and its real-time implementation for power system phasors and harmonics estimation. This chapter establishes the mathematical basis to decouple and restructure the nonlinear form of RLS technique for real-time implementation on an off-the-shelf

DSP. The aim of introducing the new decoupled RLS (DRLS) technique is to reduce the turnaround-time on a DSP such that its real-time implementation becomes possible with a lower computational burden than that of the conventional RLS technique. Reduction of turnaround-time on a DSP allows application of higher sampling frequency and, therefore, increasing the bandwidth of harmonics estimation.

The proposed DRLS technique is also associated with a modified version of the RDSPOC frequency tracking technique of Chapter 2 to introduce a new robust frequency adaptive instantaneous symmetrical components estimation technique. The performance of the DRLS technique is compared with the adaptive linear combiner (ADALINE), RDFT, and EPLL techniques in the following sections. The presented simulation results prove the effectiveness, accuracy, and stability of the proposed DRLS technique for phasors and harmonics estimation. The presented real-time implementation experiments show considerable turnaround-time reduction of the DRLS technique in comparison with the conventional RLS technique according to the implementation on two different off-the-shelf research and development (R&D) DSPs.

The remaining of the chapter is organized as follows. Section 3.2 revisits the RLS technique nonlinear specific model for power system harmonics and phasors estimation in detail. Section 3.3 presents the proposed DRLS technique and the mathematical justifications for decoupling the RLS technique. Sections 3.3.3 and 3.3.4 respectively compare harmonics and phasor detection performance of the DRLS, ADALINE, and RDFT techniques through simulation studies and DSP real-time implementation experiments. Section 3.4 presents a new instantaneous symmetrical component extraction method based on the proposed DRLS technique. Section 3.4.1 compares the

performance of the DRLS and enhanced phase-locked loop (EPLL) techniques through simulation studies. Section 3.4.2 compares the DSP turnaround-time of DRLS and EPLL techniques. Section 3.5 concludes this chapter.

3.2. Recursive-Least-Squares Technique for Harmonics and Phasors Estimation

This section lays the basis of applying the RLS techniques in the nonlinear form for phasor estimation from a new perspective. The very detailed presented mathematical justification provides the main idea to introduce the new DRLS technique which will be introduced in Section 3.3.

A power system current or voltage waveform d which includes N harmonics can be numerically modelled in the discrete-time domain as:

$$d(k) = \sum_{i=1}^N A_i(k) \sin(2\pi f_o t_k + \Theta_i(k)) + A_{dc}(k) \quad (3.1)$$

where

$t_k = kT_s$ is the time of observation

T_s is the sampling period

f_o is the power system nominal fundamental frequency

$A_i(k)$ is the amplitude of the i^{th} harmonic

$\Theta_i(k)$ is the phase-angle of the i^{th} harmonic

$A_{dc}(k)$ is the dc component of the measured waveform at the k^{th} sample.

For the purpose of simplicity, (3.1) can be rewritten as follows:

$$d(k) = \sum_{i=1}^N A_i(k) \sin(\theta_i(k)) + A_{dc}(k) \quad (3.2)$$

where

$\theta_i(k) = 2\pi f_o k T_s + \Theta_i(k)$ is the total phase-angle of the i^{th} harmonic.

Eqn. (3.1) is a nonlinear equation with respect to the phase-angle $\Theta_i(k)$ and is approached in the nonlinear platform by using the RLS technique in this chapter. The

RLS technique fits the voltage or current waveform with the curve $\hat{d}_{RLS}(k)$ as:

$$\begin{cases} \hat{d}_{RLS}(k) = \sum_{i=1}^N \hat{A}_i(k) \sin(\hat{\theta}_i(k)) + \hat{A}_{dc}(k) \\ \hat{\theta}_i(k) = 2\pi f_o k T_s + \hat{\Theta}_i(k) \end{cases} \quad (3.3)$$

in which

$\hat{d}_{RLS}(k)$ is the estimate of $d(k)$

$\hat{A}_i(k)$ is the estimate of $A_i(k)$

$\hat{\theta}_i(k)$ is the estimate of $\theta_i(k)$

$\hat{\Theta}_i(k)$ is the estimate of $\Theta_i(k)$

$\hat{A}_{dc}(k)$ is the estimate of $A_{dc}(k)$.

The estimation error $e_{RLS}(k)$ is evaluated as:

$$e_{RLS}(k) = \hat{d}_{RLS}(k) - d(k) \quad (3.4)$$

The RLS technique is based on minimizing the sum of the weighted squares error (WSE) [142]. The WSE objective function $G_{WSE}(k)$ is defined as:

$$G_{WSE}(k) = \sum_{l=0}^{k-1} 0.5 \lambda^m e_{RLS}^2(k-l) \quad (3.5)$$

in which $0 \ll \lambda < 1$ is called the forgetting factor. The parameter λ gives the most recent error sample in the composition of the objective function more weight and significance. λ defines the memory time constant T_m which is calculated as [143]:

$$T_m = \frac{T_s}{1 - \lambda} \quad (3.6)$$

The error values older than T_m are weighted less than 36% of the sample at the k^{th} sample. This definition of the objective function gives the model the ability to track non-stationary processes.

Eqn. (3.5) can be transformed into the following vector format:

$$G_{RLS}(k) = 0.5 E_{RLS}^T(k) E_{RLS}(k) \quad (3.7)$$

where $E_{RLS}(k)$ is an $k \times 1$ vector which is defined as:

$$E_{RLS}(k) = \left[e_{RLS}(k), \lambda^{1/2} e_{RLS}(k-1), \dots, \lambda^{(k-1)/2} e_{RLS}(1) \right]^T \quad (3.8)$$

The estimation vector is defined as:

$$\hat{\Gamma}_{RLS}(k) = \left[\hat{A}_1(k), \hat{\Theta}_1(k), \dots, \hat{A}_N(k), \hat{\Theta}_N(k), \hat{A}_{dc}(k) \right]^T \quad (3.9)$$

The optimal (desired) vector is defined as:

$$\Gamma_{RLS}(k) = \left[A_1(k), \Theta_1(k), \dots, A_N(k), \Theta_N(k), A_{dc}(k) \right]^T \quad (3.10)$$

The estimation vector $\hat{\Gamma}_{RLS}(k)$ converges to the optimal vector $\Gamma_{RLS}(k)$ by minimizing the WSE goal function ($G_{WSE}(k)$). The estimation vector ($\hat{\Gamma}_{RLS}(k)$) minimizes $G_{WSE}(k)$ for which the gradient of the objective function ($\nabla G_{RLS}(k)$) becomes zero. $\nabla G_{RLS}(k)$ is calculated as follows:

$$\nabla G_{RLS}(k) = \frac{\partial G_{WSE}(k)}{\partial \hat{\Gamma}_{RLS}(k)} = E_{RLS}^T(k) \frac{\partial E_{RLS}(k)}{\partial \hat{\Gamma}_{RLS}(k)} \quad (3.11)$$

$$\frac{\partial E_{RLS}(k)}{\partial \hat{\Gamma}_{RLS}(k)} = \hat{X}_{RLS}(k) = \begin{bmatrix} \hat{x}^T(k) \\ \Lambda^{1/2} \hat{x}^T(k-1) \\ \vdots \\ \Lambda^{(k-1)/2} \hat{x}^T(1) \end{bmatrix} \quad (3.12)$$

$$\hat{x}(k) = \frac{\partial e_{RLS}(k)}{\partial \hat{\Gamma}_{RLS}(k)} \quad (3.13)$$

$\hat{x}(k)$ is an $(2N+1) \times 1$ vector for which the components are evaluated as follows:

$$\hat{x}(k) = [\hat{x}_1(k), \dots, \hat{x}_{2N+1}(k)]^T \quad (3.14)$$

$$\begin{cases} \hat{x}_{2i-1}(k) = \sin(\hat{\theta}_i(k)) & , 1 \leq i \leq N \\ \hat{x}_{2i}(k) = \hat{A}_i(k) \cos(\hat{\theta}_i(k)) & , 1 \leq i \leq N \\ \hat{x}_{2N+1}(k) = 1 \end{cases} \quad (3.15)$$

The estimation vector ($\hat{\Gamma}_{RLS}(k)$) is calculated by finding the root of WSE gradient ($\nabla G_{WSE}(k)$) through solving the following vector equation:

$$\nabla G_{WSE}(k) = E_{RLS}^T(k) \hat{X}_{RLS}(k) = 0 \quad (3.16)$$

This equation forms a nonlinear vector set with respect to $\hat{\Gamma}_{RLS}(k)$. Eqn. (3.16) can be expanded with respect to $\hat{\Gamma}_{RLS}(k)$ by using the first order Taylor series expansion of $E_{RLS}(k)$ as follows:

$$E_{RLS}(k) = E_{RLS}(k) \Big|_{\hat{\Gamma}_{RLS}(k)=0} + \frac{\partial E_{RLS}(k)}{\partial \hat{\Gamma}_{RLS}(k)} \hat{\Gamma}_{RLS}(k) \quad (3.17)$$

$\frac{\partial E_{RLS}(k)}{\partial \hat{\Gamma}_{RLS}(k)}$ is evaluated from (3.12), (3.14), and (3.15). $E_{RLS}(k)$ can also be rewritten

by using (3.4) and (3.8) as follows:

$$E_{RLS}(k) = \hat{D}_{RLS}(k) - D_{RLS}(k) \quad (3.18)$$

$$\hat{D}_{RLS}(k) = \left[\hat{d}_{RLS}(k), \Lambda^{1/2} \hat{d}_{RLS}(k-1), \dots, \Lambda^{(k-1)/2} \hat{d}_{RLS}(1) \right]^T \quad (3.19)$$

$$D_{RLS}(k) = \left[d(k), \Lambda^{1/2} d(k-1), \dots, \Lambda^{(k-1)/2} d(1) \right]^T \quad (3.20)$$

$E_{RLS}(k) \Big|_{\hat{\Gamma}_{RLS}(k)=0}$ is calculated as:

$$E_{RLS}(k) \Big|_{\hat{\Gamma}_{RLS}(k)=0} = \hat{D}_{RLS}(k) \Big|_{\hat{\Gamma}_{RLS}(k)=0} - D_{RLS}(k) \quad (3.21)$$

$\hat{D}_{RLS}(k) \Big|_{\hat{\Gamma}_{RLS}(k)=0} = 0$ according to (3.3). Therefore, $E_{RLS}(k) \Big|_{\hat{\Gamma}_{RLS}(k)=0}$ is evaluated as

follows:

$$E_{RLS}(k) \Big|_{\hat{\Gamma}_{RLS}(k)=0} = -D_{RLS}(k) \quad (3.22)$$

Applying (3.22) into (3.17), applying the equality $\left(\frac{\partial E_{RLS}(k)}{\partial \hat{\Gamma}_{RLS}(k)} = \hat{X}_{RLS}(k) \right)$ from (3.12)

into (3.17), and, then, substituting the resulting term for $E_{RLS}(k)$ from (3.17) into (3.16)

will produce the following equations:

$$\begin{aligned} \left(-D_{RLS}(k) + \hat{X}_{RLS}(k) \hat{\Gamma}_{RLS}(k) \right)^T \hat{X}_{RLS}(k) &= 0 \\ \hat{X}_{RLS}^T(k) \hat{X}_{RLS}(k) \hat{\Gamma}_{RLS}(k) &= \hat{X}_{RLS}^T(k) D_{RLS}(k) \\ \hat{\Gamma}_{RLS}(k) &= \left(\hat{X}_{RLS}^T(k) \hat{X}_{RLS}(k) \right)^{-1} \hat{X}_{RLS}^T(k) D_{RLS}(k) \end{aligned} \quad (3.23)$$

For convenience of notation, consider the following auxiliary matrices:

$$R(k) = \hat{X}_{RLS}^T(k) \hat{X}_{RLS}(k) \quad (3.24)$$

$$P_{RLS}(k) = \hat{X}_{RLS}^T(k) D_{RLS}(k) \quad (3.25)$$

where

$R(k)$ is called the input-waveform correlation matrix and

$P_{RLS}(k)$ is the cross-correlation matrix between the measurement and the input-waveform.

Therefore, $\hat{\Gamma}_{RLS}(k)$ can be rewritten in the following form according to (3.23):

$$\hat{\Gamma}_{RLS}(k) = R^{-1}(k)P_{RLS}(k) \quad (3.26)$$

The RLS technique uses recursive estimation of $R(k)$ and $P_{RLS}(k)$ to calculate $\hat{\Gamma}_{RLS}(k)$. Eqn. (3.24) can be rewritten in the following form according to (3.12):

$$R(k) = \sum_{l=1}^k A^{k-l} \hat{x}(l) \hat{x}^T(l) \quad (3.27)$$

and, therefore, $R(k-1)$ is calculated as:

$$R(k-1) = \sum_{l=1}^{k-1} A^{k-l-1} \hat{x}(l) \hat{x}^T(l) \quad (3.28)$$

Eqn. (3.27) can be rearranged in the following form:

$$R(k) = \hat{x}(k) \hat{x}^T(k) + A \sum_{l=1}^{k-1} A^{k-l-1} \hat{x}(l) \hat{x}^T(l) \quad (3.29)$$

The second term on the right-hand-side of (3.29) is equal to $AR(k-1)$ according to (3.28). Therefore, the following recursive equation holds true for $R(k)$:

$$R(k) = \hat{x}(k) \hat{x}^T(k) + AR(k-1) \quad (3.30)$$

Eqn. (3.25) can be rewritten in the following form according to (3.12) and (3.20):

$$P_{RLS}(k) = \sum_{l=1}^k A^{k-l} d(l) \hat{x}(l) \quad (3.31)$$

and, therefore, $P_{RLS}(k-1)$ is calculated as:

$$P_{RLS}(k-1) = \sum_{l=1}^{k-1} A^{k-l-1} d(l) \hat{x}(l) \quad (3.32)$$

Eqn. (3.31) can be rearranged in the following form:

$$P_{RLS}(k) = d(k) \hat{x}(k) + A \sum_{l=1}^{k-1} A^{k-l-1} d(l) \hat{x}(l) \quad (3.33)$$

The second term on the right-hand-side of (3.33) is equal to $\lambda P_{RLS}(k-1)$ according to (3.32). Therefore, the following recursive equation holds true for $P_{RLS}(k)$:

$$P_{RLS}(k) = d(k)\hat{x}(k) + \lambda P_{RLS}(k-1) \quad (3.34)$$

The following development can be made by substituting (3.30) and (3.34) into (3.26):

$$\begin{aligned} \hat{\Gamma}_{RLS}(k) &= R^{-1}(k) [d(k)\hat{x}(k) + \lambda P_{RLS}(k-1)] \\ &= R^{-1}(k) [d(k)\hat{x}(k) + \lambda R(k-1)\hat{\Gamma}_{RLS}(k-1)] \\ &= R^{-1}(k) \left[\begin{array}{l} d(k)\hat{x}(k) + \lambda R(k-1)\hat{\Gamma}_{RLS}(k-1) \\ + \hat{x}(k)\hat{x}^T(k)\hat{\Gamma}_{RLS}(k-1) - \hat{x}(k)\hat{x}^T(k)\hat{\Gamma}_{RLS}(k-1) \end{array} \right] \\ &= R^{-1}(k) \left[\hat{x}(k) [d(k) - \hat{x}^T(k)\hat{\Gamma}_{RLS}(k-1)] + R(k)\hat{\Gamma}_{RLS}(k-1) \right] \\ &= R^{-1}(k) [R(k)\hat{\Gamma}_{RLS}(k-1) - \hat{x}(k)e_{RLS}(k)] \\ &= R^{-1}(k)R(k)\hat{\Gamma}_{RLS}(k-1) - R^{-1}(k)\hat{x}(k)e_{RLS}(k) \end{aligned} \quad (3.35)$$

Therefore, $\hat{\Gamma}_{RLS}(k)$ is recursively calculated as follows:

$$\hat{\Gamma}_{RLS}(k) = \hat{\Gamma}_{RLS}(k-1) - e_{RLS}(k)R^{-1}(k)\hat{x}(k) \quad (3.36)$$

Calculating the inverse matrix $R^{-1}(k)$ poses a serious problem for real-time DSP implementation. Eqn. (3.30) can be rewritten by applying the matrix inversion lemma [142] as:

$$R^{-1}(k) = \frac{1}{\lambda} \left[R^{-1}(k-1) - \frac{R^{-1}(k-1)\hat{x}(k)\hat{x}^T(k)R^{-1}(k-1)}{\lambda + \hat{x}^T(k)R^{-1}(k-1)\hat{x}(k)} \right] \quad (3.37)$$

Therefore, $R^{-1}(k)$ is calculated recursively without using matrix inversion operation.

However, the RLS update process requires updating $R^{-1}(k)$ which is a $(2N+1)(2N+1)$ matrix. The calculation burden of RLS with respect to the model order (N) is of N^2 order.

3.3. Decoupled Recursive-Least-Squares Technique

This section presents the detailed mathematical justifications to develop the proposed DRLS technique for power system phasors and harmonics estimation. The DRLS technique is proposed based on decoupling the estimation process through restructuring it into $(N+1)$ units with smaller dimensions. According to (3.24), the genuine definition of input-waveform correlation matrix $R(k)$ can be considered as follows:

$$R(k) = \begin{bmatrix} [R_1(k)] & \cdots & \cdots & R_{1,2N+1}(k) \\ \vdots & \ddots & & \vdots \\ & & [R_{N-1}(k)] & \\ & & & [R_N(k)] \\ R_{2N+1,1}(k) & \cdots & \cdots & R_{dc}(k) \end{bmatrix} \quad (3.38)$$

Each $[R_i(k)]$ ($1 \leq i \leq N$) is a (2×2) matrix and $R_{dc}(k)$ is a scalar parameter. $[R_1(k)]$ -to- $[R_N(k)]$ matrices, and $R_{dc}(k)$ are placed on the main diagonal of $R(k)$. The other off-diagonal elements of $R(k)$ which are not included in the $[R_i(k)]$ matrices can be expanded as follows according to (3.12), (3.14), (3.15), and (3.24).

The following two equations are extracted for the last column of $R(k)$:

$$R_{2i-1,2N+1}(k) = \sum_{l=0}^{k-1} A^l \sin(\hat{\omega}_i(k-l)) \quad , 1 \leq i \leq N \quad (3.39)$$

$$R_{2i,2N+1}(k) = \sum_{l=0}^{k-1} A^l \hat{A}_i(k-l) \cos(\hat{\omega}_i(k-l)) \quad , 1 \leq i \leq N \quad (3.40)$$

For $(1 \leq i \leq N)$, $(1 \leq a \leq N)$, and $(i \neq a)$, the elements which are excluded from the

diagonal matrices $[R_i(k)]$ and are located in the upper triangle of $R(k)$ can be expanded as:

$$R_{2a-1,2i-1}(k) = \sum_{l=0}^{k-1} A^l \sin(\hat{\omega}_a(k-l)) \sin(\hat{\omega}_i(k-l)) \quad (3.41)$$

$$R_{2a-1,2i}(k) = \sum_{l=0}^{k-1} A^l \hat{A}_i(k-l) \sin(\hat{\omega}_a(k-l)) \cos(\hat{\omega}_i(k-l)) \quad (3.42)$$

$$R_{2a,2i-1}(k) = \sum_{l=0}^{k-1} A^l \hat{A}_a(k-l) \cos(\hat{\omega}_a(k-l)) \sin(\hat{\omega}_i(k-l)) \quad (3.43)$$

$$R_{2a,2i}(k) = \sum_{l=0}^{k-1} A^l \hat{A}_i(k-l) \hat{A}_a(k-l) \cos(\hat{\omega}_a(k-l)) \cos(\hat{\omega}_i(k-l)) \quad (3.44)$$

Owing to the fact that the value of A affects the time constant (T_m) and does not change the average model of RLS, A can be chosen to be in the very close neighbourhood of 1 ($A \rightarrow 1$) without loss of generality at this stage. Therefore, the average values of the summations on the right-hand-side of (3.39)-(3.44) become zeros according to the trigonometric functions properties. The average of (3.44), for example, is calculated as:

$$\begin{aligned} \bar{R}_{2a,2i} \Big|_{A \rightarrow 1} &= \frac{1}{T_o} \int_{t_k=0}^{t_k=T_o} R_{2a,2i}(k) dt_k = \\ &= \sum_{l=0}^{k-1} \left(\frac{A^l \Big|_{A \rightarrow 1}}{T_o} \int_{t_k=0}^{t_k=T_o} \hat{A}_i(k-l) \hat{A}_a(k-l) \cos(\hat{\omega}_a(k-l)) \cos(\hat{\omega}_i(k-l)) dt_k \right) = \\ &= \sum_{l=0}^{k-1} \frac{1}{T_o} \bar{\hat{A}}_i \bar{\hat{A}}_a \int_{t_k=0}^{t_k=T_o} \cos(\hat{\omega}_a(k-l)) \cos(\hat{\omega}_i(k-l)) dt_k \end{aligned} \quad (3.45)$$

where $T_o = 1/f_o$. In the average model, the amplitudes of the i^{th} and j^{th} harmonics can

be considered to have the local/global stationary average of $\bar{\hat{A}}_i$ and $\bar{\hat{A}}_a$ respectively.

Eqn. (3.45) can be expanded according to the trigonometric functions properties as follows.

$$\begin{aligned} \cos(\hat{a}(k-l))\cos(\hat{i}(k-l)) = \\ \frac{1}{2}\{\cos(\hat{a}(k-l) + \hat{i}(k-l)) + \cos(\hat{i}(k-l) - \hat{a}(k-l))\} \end{aligned} \quad (3.46)$$

$$\begin{cases} \hat{a}(k-l) + \hat{i}(k-l) = \hat{\Theta}_i(k-l) + \hat{\Theta}_a(k-l) + 2 f_o(i+a)(t_k - lT_s) \\ \hat{i}(k-l) - \hat{a}(k-l) = \hat{\Theta}_i(k-l) - \hat{\Theta}_a(k-l) + 2 f_o(i-a)(t_k - lT_s) \end{cases} \quad (3.47)$$

Therefore:

$$\begin{aligned} \int_{t_k=0}^{t_k=T_o} \cos(\hat{j}(k-l))\cos(\hat{i}(k-l)) dt_k = \\ \frac{1}{2} \int_{t_k=0}^{t_k=T_o} \cos(2 f_o(i+a)(t_k - lT_s) + \hat{\Theta}_i(k-l) + \hat{\Theta}_a(k-l)) dt_k + \\ \frac{1}{2} \int_{t_k=0}^{t_k=T_o} \cos(2 f_o(i-a)(t_k - lT_s) + \hat{\Theta}_i(k-l) - \hat{\Theta}_a(k-l)) dt_k \end{aligned} \quad (3.48)$$

The first term on the right-hand-side of (3.48) is calculated as:

$$\frac{1}{2} \int_{t_k=0}^{t_k=T_o} \cos(2 f_o(i+a)(t_k - lT_s) + \hat{\Theta}_i(k-l) + \hat{\Theta}_a(k-l)) dt_k = 0 \quad (3.49)$$

Owing to the fact that $i \neq a$, the second term on the right-hand-side of (3.48) will be calculated as:

$$\frac{1}{2} \int_{t_k=0}^{t_k=T_o} \cos(2 f_o(i-a)(t_k - lT_s) + \hat{\Theta}_i(k-l) - \hat{\Theta}_a(k-l)) dt_k = 0 \quad (3.50)$$

Therefore:

$$\bar{R}_{2a,2i} \Big|_{A \rightarrow 1} = 0 \quad (3.51)$$

The same analysis can be used for (3.39)-(3.43). This justification is also true for the

elements which are excluded from the diagonal matrices $[R_i(k)]$ in the lower triangle of $R(k)$ since it is a symmetrical matrix according to (3.24). Therefore, there is practically no need to update the elements of $R(k)$ with the average value of zero because they will have no effect on the average values of phasors and harmonics estimates.

The DRLS input-waveform correlation matrix ($R_o(k)$) is therefore defined as:

$$R_o(k) = \begin{bmatrix} [R_{o1}(k)] & 0 & \dots & \dots & 0 & 0 \\ 0 & \ddots & 0 & \dots & \vdots & 0 \\ \vdots & 0 & \ddots & & & \vdots \\ \vdots & \vdots & & [R_{oN-1}(k)] & 0 & \vdots \\ 0 & \dots & 0 & & [R_{oN}(k)] & 0 \\ 0 & 0 & \dots & \dots & 0 & R_{odc}(k) \end{bmatrix} \quad (3.52)$$

The proposed restructuring of the RLS model into the DRLS one is specifically possible for power system applications because the fundamental and harmonic waveforms are periodic. The integrity of the proposed model remains intact even in the case of dynamic changes and faults because the dynamic trend estimation has been accommodated in the DRLS governing equations in the parameter $R_{odc}(k)$. This arrangement of DRLS decouples the estimation process into $(N+1)$ units which work in parallel while use the accumulated estimation error to perform the estimation task individually.

In the proposed DRLS model, the error function $e_o(k)$ is evaluated as follows:

$$e_o(k) = -d(k) + \sum_{i=1}^N \hat{d}_i(k) + \hat{d}_{dc}(k) \quad (3.53)$$

$$\hat{d}_{dc}(k) = \hat{A}_{odc}(k) \quad (3.54)$$

$$\hat{d}_i(k) = \hat{A}_i(k) \sin(\hat{\omega}_i(k)) \quad , (1 \leq i \leq N) \quad (3.55)$$

The i^{th} unit of DRLS, ($1 \leq i \leq N$), estimates the i^{th} harmonic for which the inverse of $[R_{oi}(k)]$ is recursively updated as follows:

$$R_{oi}^{-1}(k) = \frac{1}{\Lambda} \left[R_{oi}^{-1}(k-1) - \frac{R_{oi}^{-1}(k-1) \hat{x}_{oi}(k) \hat{x}_{oi}^T(k) R_{oi}^{-1}(k-1)}{\Lambda + \hat{x}_{oi}^T(k) R_{oi}^{-1}(k-1) \hat{x}_{oi}(k)} \right] \quad (3.56)$$

$$\begin{cases} \hat{x}_{oi}(k) = \begin{bmatrix} \sin(\hat{\omega}_i(k)) & \hat{A}_i(k) \cos(\hat{\omega}_i(k)) \end{bmatrix}^T \\ \hat{\omega}_i(k) = 2 \text{ if}_o k T_s + \hat{\Theta}_i(k) \end{cases} \quad (3.57)$$

The estimation vector for the i^{th} unit $\hat{\Gamma}_{oi}(k)$ is updated as follows:

$$\begin{cases} \hat{\Gamma}_{oi}(k) = \hat{\Gamma}_{oi}(k-1) - e_o(k) R_{oi}^{-1}(k) \hat{x}_{oi}(k) \\ \hat{\Gamma}_{oi}(k) = \begin{bmatrix} \hat{A}_i(k) & \hat{\Theta}_i(k) \end{bmatrix}^T \end{cases} \quad (3.58)$$

The $(2N+1)^{\text{th}}$ unit of the DRLS estimates the decaying dc component. $R_{odc}^{-1}(k)$ is recursively updated as follows:

$$R_{odc}^{-1}(k) = \frac{1}{\Lambda} \left[R_{odc}^{-1}(k-1) - \frac{R_{odc}^{-1}(k-1) \hat{x}_{odc}(k) \hat{x}_{odc}^T(k) R_{odc}^{-1}(k-1)}{\Lambda + \hat{x}_{odc}^T(k) R_{odc}^{-1}(k-1) \hat{x}_{odc}(k)} \right] \quad (3.59)$$

$$\hat{x}_{odc}(k) = 1 \quad (3.60)$$

The dc component estimation is updated as follows:

$$\hat{A}_{odc}(k) = \hat{A}_{odc}(k-1) - e_o(k) R_{odc}^{-1}(k) \hat{x}_{odc}(k) \quad (3.61)$$

The DRLS technique is implemented by stacking $(N+1)$ individual unites. Figure 3.1 shows the proposed real-time DRLS technique modular implementation.

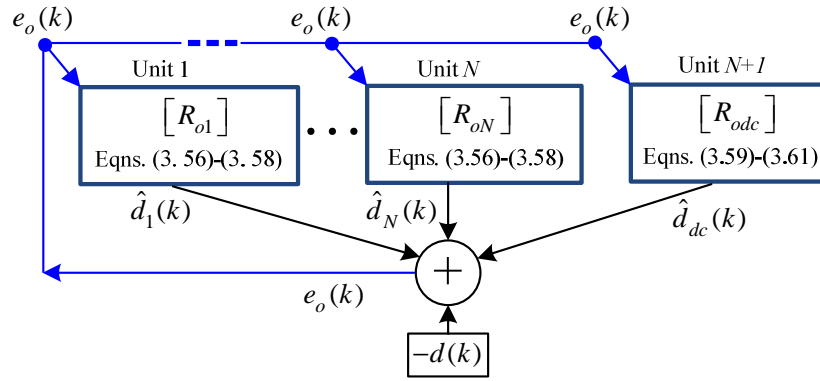


Figure 3.1. The proposed real-time DRLS technique modular implementation.

3.3.1. Initializing the DRLS Technique

The DRLS technique is a recursive technique which requires proper initialization. The key to the initialization of the DRLS is to analyse the input-waveform correlation matrices R_{oi} . Since the inverse of R_{oi} is used in (3.56), the determinant of R_{oi} should be a non-zero value to have a well-defined R_{oi}^{-1} which can be used for DRLS technique initialization.

R_{oi} of the i^{th} unit of DRLS is a 2×2 matrix which can be presented as:

$$R_{oi}(k) = \begin{bmatrix} R_{oi}^{1,1}(k) & R_{oi}^{1,2}(k) \\ R_{oi}^{2,1}(k) & R_{oi}^{2,2}(k) \end{bmatrix} \quad (3.62)$$

Elements of R_{oi} can be calculated as follows:

$$R_{oi}^{1,1}(k) = \sum_{l=0}^{k-1} A^l \sin^2(\hat{\theta}_i(k-l)) \quad (3.63)$$

$$R_{oi}^{1,2}(k) = R_{oi}^{2,1}(k) = \sum_{l=0}^{k-1} A^l \hat{A}_i(k) \cos(\hat{\theta}_i(k-l)) \sin(\hat{\theta}_i(k-l)) \quad (3.64)$$

$$R_{oi}^{2,2}(k) = \sum_{l=0}^{k-1} A^l \hat{A}_i^2(k) \cos^2(\hat{\gamma}_i(k-l)) \quad (3.65)$$

The average value of $R_{oi}^{1,1}(k)$, $R_{oi}^{1,2}(k)$, $R_{oi}^{2,1}(k)$, and $R_{oi}^{2,2}(k)$ can be calculated as follows:

$$\bar{R}_{oi}^{1,1} = \frac{1}{T_o} \int_{t_k=0}^{t_k=T_o} R_{oi}^{1,1}(k) dt_k = \quad (3.66)$$

$$\frac{1}{T_o} \sum_{l=0}^{k-1} \left(\int_{t_k=0}^{t_k=T_o} A^l \sin^2(\hat{\gamma}_i(k-l)) dt_k \right) =$$

$$\sum_{l=0}^{k-1} \frac{1}{T_o} \int_{t_k=0}^{t_k=T_o} A^l \sin^2(\hat{\gamma}_i(k-l)) dt_k$$

$$\bar{R}_{oi}^{1,2} = \bar{R}_{oi}^{2,1} = \frac{1}{T_o} \int_{t_k=0}^{t_k=T_o} R_{oi}^{1,2}(k) dt_k = \quad (3.67)$$

$$\frac{1}{T_o} \sum_{l=0}^{k-1} \left(\int_{t_k=0}^{t_k=T_o} A^l \hat{A}_i \sin(\hat{\gamma}_i(k-l)) \cos(\hat{\gamma}_i(k-l)) dt_k \right) =$$

$$\sum_{l=0}^{k-1} \frac{1}{T_o} \int_{t_k=0}^{t_k=T_o} A^l \hat{A}_i \sin(\hat{\gamma}_i(k-l)) \cos(\hat{\gamma}_i(k-l)) dt_k$$

$$\bar{R}_{oi}^{2,2} = \frac{1}{T_o} \int_{t_k=0}^{t_k=T_o} R_{oi}^{2,2}(k) dt_k = \quad (3.68)$$

$$\frac{1}{T_o} \sum_{l=0}^{k-1} \left(\int_{t_k=0}^{t_k=T_o} A^l \hat{A}_i^2 \cos^2(\hat{\gamma}_i(k-l)) dt_k \right) =$$

$$\sum_{l=0}^{k-1} \frac{1}{T_o} \int_{t_k=0}^{t_k=T_o} A^l \hat{A}_i^2 \cos^2(\hat{\gamma}_i(k-l)) dt_k$$

As seen from (3.66), $\bar{R}_{oi}^{1,1}$ is always a non-zero value. However, the values of $\bar{R}_{oi}^{1,2}$,

$\bar{R}_{oi}^{2,1}$, and $\bar{R}_{oi}^{2,2}$ depend on the values of $\hat{A}_i(k)$ and $\hat{\phi}_i(k)$.

The following results can be drawn from the above analysis:

- a. If $\hat{A}_i(k) = 0$, the values of $\bar{R}_{oi}^{1,2}$, $\bar{R}_{oi}^{2,1}$, and $\bar{R}_{oi}^{2,2}$ become zero, the determinant of R_{oi} becomes zero and the DRLS calculations cannot be initialized;
- b. If $\cos(\hat{\phi}_i) = 0$, the values of $\bar{R}_{oi}^{1,2}$, $\bar{R}_{oi}^{2,1}$, and $\bar{R}_{oi}^{2,2}$ become zero, the determinant of R_{oi} becomes zero and the DRLS calculations cannot be initialized.

Therefore, proper initialization of the DRLS technique depends on the values of the initial values for amplitude and phase-angle. The values of $\hat{A}_i(k)$ and $\cos(\hat{\phi}_i)$ should be non-zero at the initializing step as discussed above.

However, setting the non-zero initial values for $\hat{A}_i(k)$ and $\cos(\hat{\phi}_i)$ is a required condition to have a well-defined R_{oi}^{-1} and does not guarantee a stable and proper initialization since the conditions of the power system is unknown at the initial step.

Nevertheless, it is still possible to initialize the DRLS technique independent of the initial values of amplitude and phase-angle. To initialize the DRLS technique, the input-waveform correlation matrix resetting strategy [86] can be used. Setting the initial value of R_{oi} at any coefficient of the 2×2 identity matrix results in a well-defined R_{oi}^{-1} for the initial step. This approach has been used to initialize the DRLS calculations for MATLAB simulations and DSP real-time experiments in this chapter.

Figure 3.2 shows initialization of DRLS technique from zero for the sampling frequency of 10 kHz, $A = 0.97$. 1%, 20%, and 100% of the 2×2 identity matrix were

used as the initial values of for input-waveform correlation matrix to exemplify the initialization strategy. The reference value of the amplitude to be estimated is 1.0 p.u. As seen, the DRLS technique convergences to the reference value faster by setting bigger initial values for R_{oi} . However, the steady state estimate is the same for all initializations.

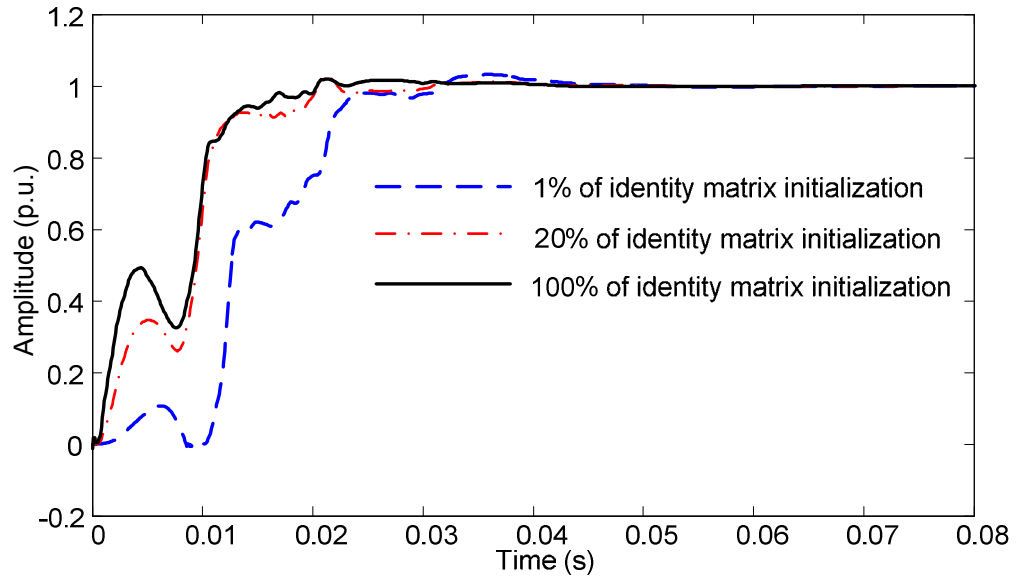


Figure 3.2. DRLS initialization from zeros by using 1%, 20%, and 100% of the 2×2 identity matrix for the initial value of input-waveform correlation matrix.

3.3.2. Comparison between RLS and DRLS Techniques

The advantages of the proposed DRLS technique are:

- i. The proposed DRLS technique directly estimates the amplitude and phase-angle of harmonics.

- ii. The input-waveform correlation matrix of the DRLS technique includes $N(2 \times 2)$ matrices and one scalar value while the conventional RLS technique requires a matrix of $(2N + 1)(2N + 1)$ dimension. Therefore, the computational complexity of the DRLS is of order N while that of the conventional RLS is of the order of N^2 .
- iii. The DRLS technique has the flexibility of using different forgetting factors for different units while the RLS technique does not provide this option as it will be presented in Section 3.3.4.
- iv. Eigen values calculation of the DRLS technique requires calculating the Eigen values of $N(2 \times 2)$ matrices and one scalar value which is straight forward and far less complicated than calculating the Eigen values of the $(2N + 1) \times (2N + 1)$ covariance matrix of the RLS technique.
- v. Therefore, covariance management techniques, such as the method presented in [86], become feasible to improve the estimation pace and dynamics of the DRLS technique for real-time DSP applications.

3.3.3. Simulation Studies

This section presents simulation studies in MATLAB-Simulink. The sampling frequency is 10 kHz. The practical range for the forgetting factor (λ) is 0.95-0.99 [98]. λ is 0.97 for DRLS and initial values of all R_{oi} matrices are set to the 2×2 identity matrix according to Section 3.3.1.

3.3.3.1. Case 1: Fault Simulation in MATLAB-Simulink

Figure 3.3 shows the power system which is simulated to study a voltage sag due to a

fault on a power distribution feeder.

In Figure 3.3:

the nominal power system frequency is 50 Hz,

the voltage source and Z_{eq} simulate a distribution equivalent network with the voltage level of 25 kV,

the equivalent impedance of the network (Z_{eq}) is $(0.625 + j5.208)\Omega$,

the 3 km feeder is the π model of all-aluminium-conductor (ACC) type cable for which:

positive sequence resistance and inductance are 0.2394 Ω/km and 1.1 mH/km respectively [144] and

the zero sequence resistance and inductance of the π model are 0.4599 Ω/km and 3.1 mH/km respectively [144].

A solid phase-to-phase-to-ground (A-B-G) fault is simulated on Bus 2 at 2.0 s. The governing equations of ADALINE2 and RDFT2 techniques have been reviewed in Chapter 1.

The voltage and current waveforms have been captured at Bus 1. The model order is 40 for DRLS, RDFT2, and ADALINE2. Figure 3.4 shows the three-phase voltage and current waveforms. Phase-A voltage is the reference for phase-angle estimation of phasors. As Figure 3.5-Figure 3.10 show, DRLS, ADALINE2 and RDFT2 converge to the same steady state values for amplitude and phase angle of voltage/current phasors which prove the equivalence of their average model in tracking phasors.

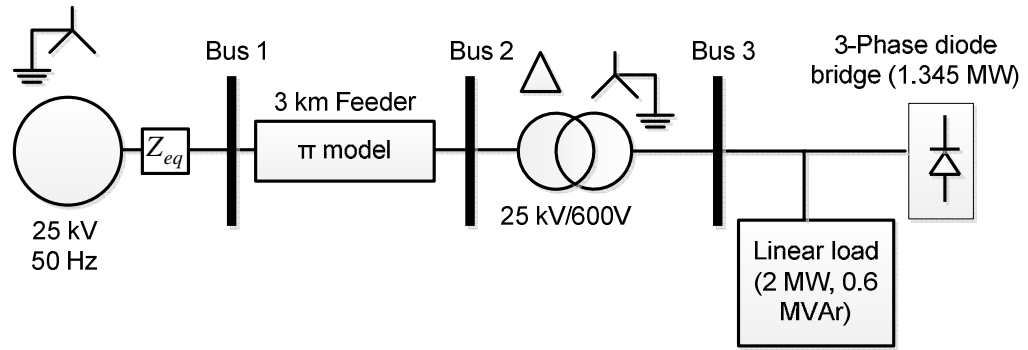


Figure 3.3. Case 1: Fault simulation

Simulated power system in the MATLAB-Simulink software.

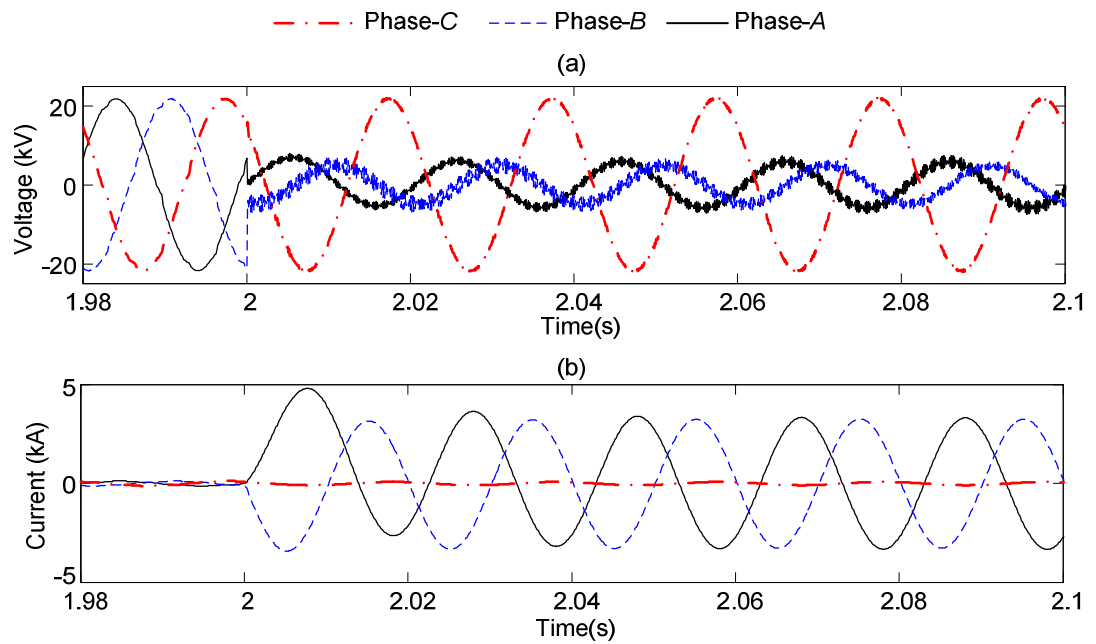


Figure 3.4. Case 1: Fault simulation

(a) three-phase line-to-neutral voltage waveforms

(b) three-phase line current waveforms.

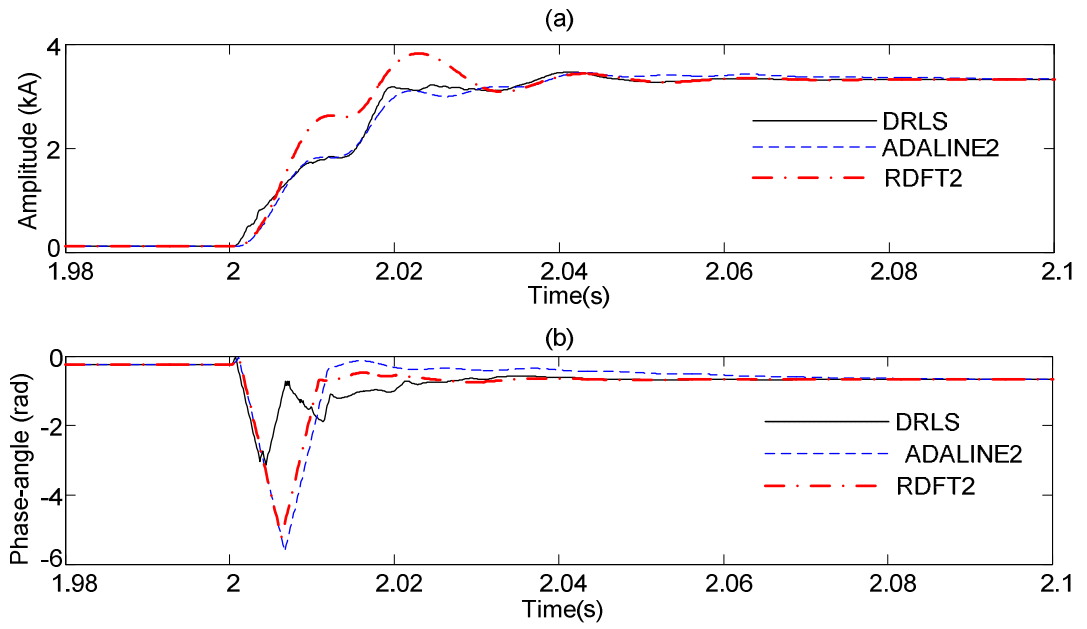


Figure 3.5. Case 1: Fault simulation

(a) phase-A fundamental frequency line current amplitude estimation

(b) phase-A fundamental frequency line current phase-angle estimation.

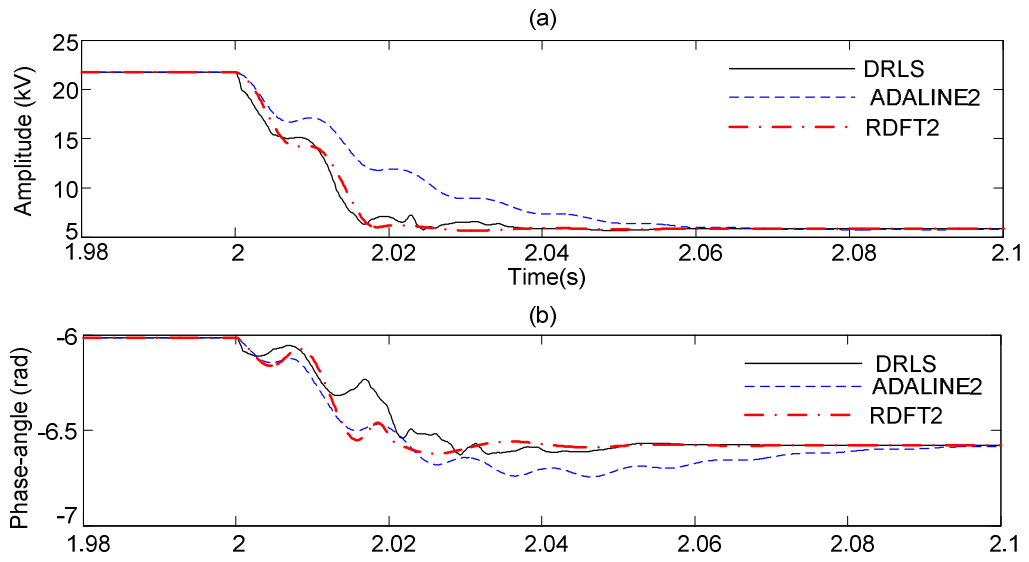


Figure 3.6 Case 1: Fault simulation

(a) phase-A-to-neutral fundamental frequency voltage amplitude estimation

(b) phase-A-to-neutral fundamental frequency voltage phase-angle estimation.

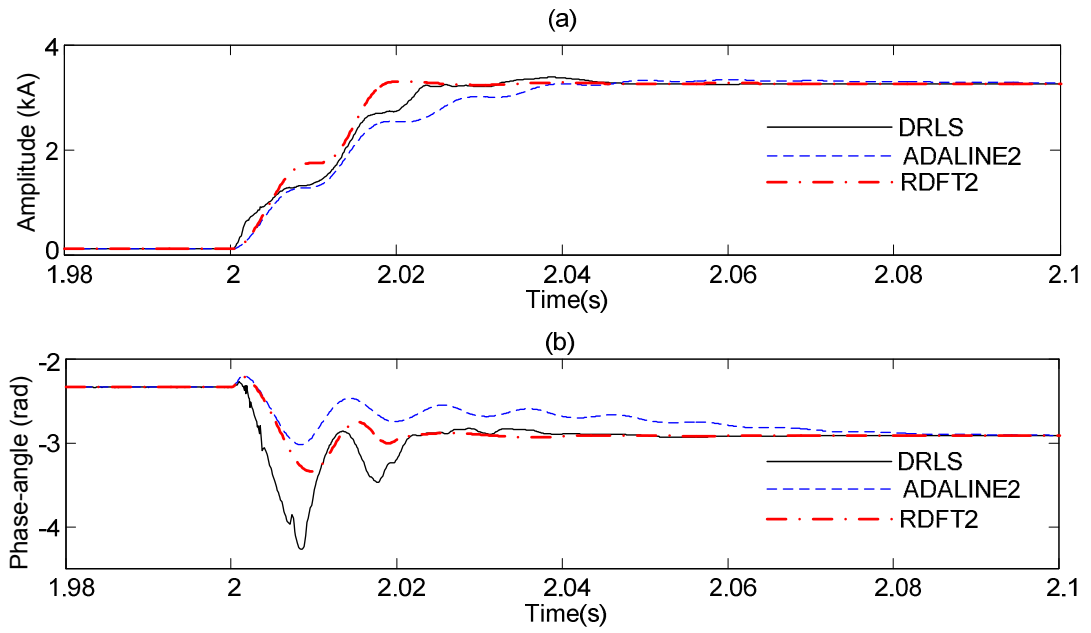


Figure 3.7. Case 1: Fault simulation

(a) phase-*B* fundamental frequency line current amplitude estimation

(b) phase-*B* fundamental frequency line current phase-angle estimation.

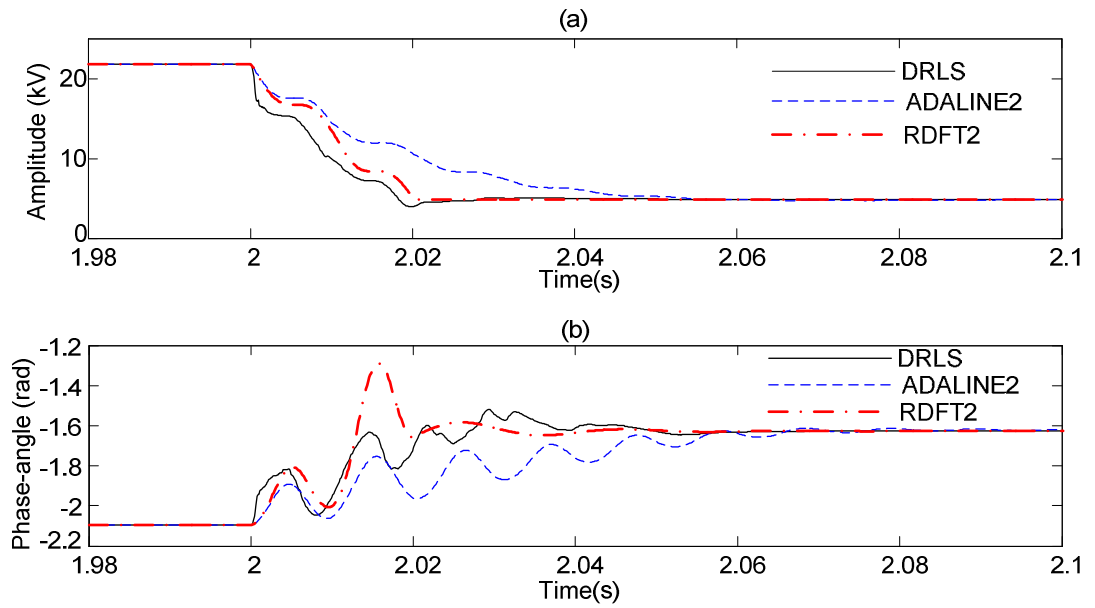


Figure 3.8. Case 1: Fault simulation

(a) phase-*B*-to-neutral fundamental frequency voltage amplitude estimation

(b) phase-*B*-to-neutral fundamental frequency voltage phase-angle estimation.

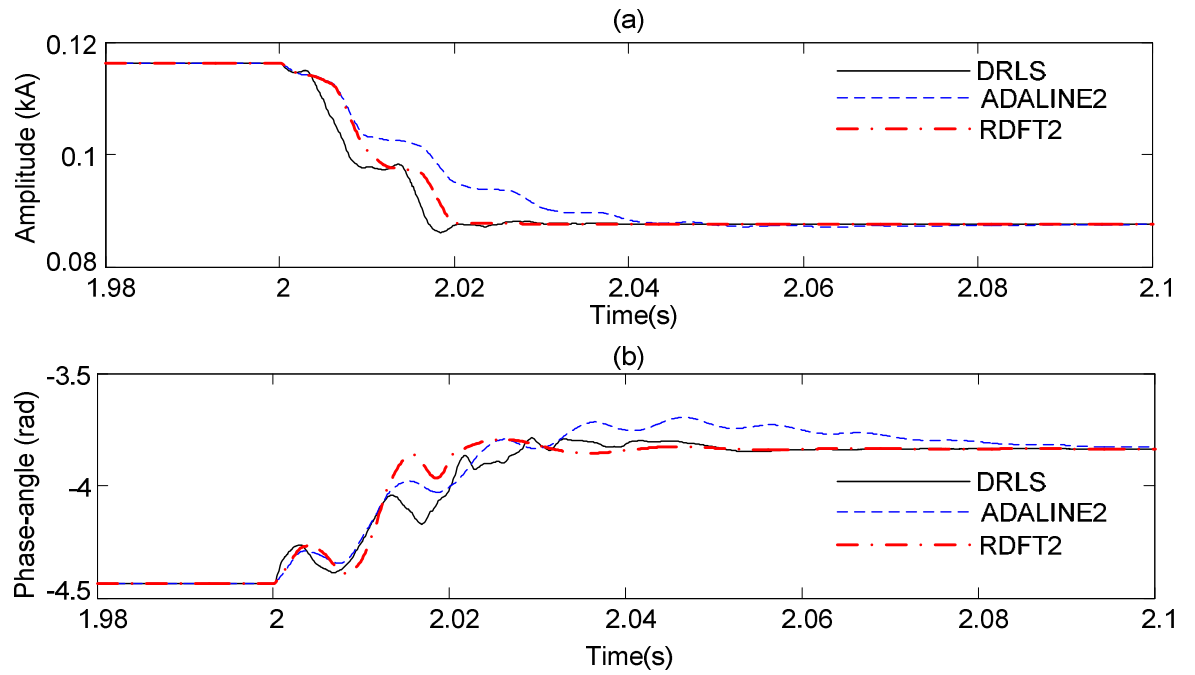


Figure 3.9. Case 1: Fault simulation

(a) phase-C fundamental frequency line current amplitude estimation

(b) phase-C fundamental frequency line current phase-angle estimation.

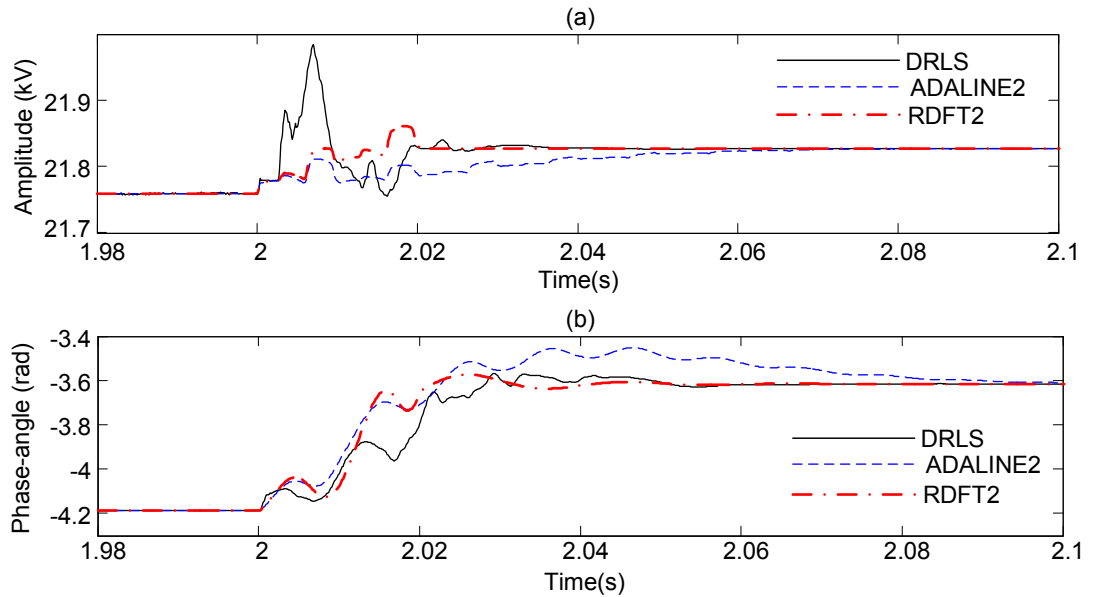


Figure 3.10. Case 1: Fault simulation

(a) phase-C-to-neutral fundamental frequency voltage amplitude estimation

(b) phase-C-to-neutral fundamental frequency voltage phase-angle estimation.

3.3.3.2. Case 2: Noise Immunity

This section presents estimation errors of DRLS, ADALINE and RDFT techniques for different signal-to-noise-ratios (SNR) levels. The noise is zero-mean Gaussian. The proposed DRLS technique shows better accuracy to cancel the higher levels of noise in comparison with the RDFT and ADALINE techniques according to Table 3.1

TABLE 3.1. CASE 2: AVERAGE VALUE OF ABSOLUTE ESTIMATION ERROR PERCENTAGE FOR DIFFERENT SNR LEVELS.

SNR (dB)	Technique		
	DRLS	ADALINE	RDFT
0	1.68	2.46	1.9
10	0.50	0.81	0.62
20	0.18	0.28	0.22
30	0.06	0.09	0.07
40	0.02	0.03	0.02

3.3.4. Real-Time DSP Implementation

3.3.4.1. Investigating Turnaround-Time on Different DSP Platforms

Table 3.2 and Table 3.3 present the turnaround-time of implementing DRLS, RLS, ADALINE, and RDFT techniques on the hardware platforms of DS1104 and DS1103 respectively for different model orders. The model order is the number of harmonics being estimated. The sampling frequency for DSP implementation should comply with the Nyquist-Shannon theorem such that the sampling frequency is at least twice the frequency of the highest order of harmonics in the voltage/current waveform [61]. If the highest order of harmonics (which is referred to as the model order in Table 3.2 and Table 3.3) is N , the sampling period equivalent to the Nyquist rate (T_{nqst}) is calculated as:

$$T_{nqst} = \frac{1}{2Nf_o} \quad (3.69)$$

The turnaround-time should be smaller than T_{nqst} for feasible real-time DSP

implementation of harmonics estimation. It should be noted that the Nyquist sampling rate ($2Nf_o$) is the minimum sampling frequency required to avoid the aliasing phenomenon and is not necessarily the DSP sampling frequency.

IEC Standard 61000-4-13 requires harmonics estimation up to the 40th order [146]. In this section, the harmonics estimation up to the 60th order is considered to investigate the required range by the IEC and beyond. ADALINE1, ADALINE2, RDFT1, and RDFT2 techniques have been reviewed in Chapter 1. As presented in Table 3.2, RLS, DRLS, RDFT1, RDFT2, ADALINE1, and ADALINE2 DSP implementation are feasible, according to the Nyquist-Shannon theorem, up to the order of 12, 40, 30, 28, 40, and 35 respectively on DS1104. Therefore, real-time implementation of DRLS and ADALINE1 techniques on the DS1104 can conduct harmonics estimation up the 40th order in compliance with the required harmonic bandwidth of IEC Standard 61000-4-13.

DS1103 has a much more powerful processor [136] which reduces the turnaround time for all techniques proportionally. As seen in Table 3.3, implementation of all techniques is feasible for the order of 60 except for the RLS technique which stops at the 20th order. Therefore, real-time implementation of DRLS, ADALINE1, ADALINE2, RDFT1, and RDFT2 on DS1103 meet the required harmonic bandwidth of IEC Standard 61000-4-13. Overall, the proposed DRLS shows better computational efficiency (smaller turnaround-time) in comparison with other techniques.

TABLE 3.2. TURNAROUND-TIME ON DS1104 R&D CONTROL BOARD (μ s).

Model Order	Technique						T_{ngst}
	DRLS	RLS	RDFT1	ADALINE1	RDFT2	ADALINE2	
1	10	14	9	12	10	15	1000
2	11	27	12	18	14	24	5000
3	17	42	14	24	20	32	3334
4	19	59	18	30	25	38	2500
5	23	91	22	36	27	44	2000
6	25	131	26	40	36	51	1667
7	28	186	36	43	46	55	1429
8	37	247	38	51	54	64	1250
9	40	347	48	56	65	72	1112
10	45	475	57	62	77	78	1000
11	48	612	70	66	95	83	910
12	56	737	84	71	103	87	834
13	59	946	95	78	115	98	770
14	64	1094	104	83	133	104	715
15	75	1327	116	86	137	107	667
16	84	1636	130	95	153	115	625
17	88	1855	136	102	167	127	589
18	97	2178	154	106	175	131	556
19	106	2545	164	110	202	138	527
20	112	3535	175	117	205	144	500
21	118	4478	191	121	225	150	477
22	127	5963	198	129	235	160	455
23	136	7187	215	134	250	164	435
24	140	8215	229	136	270	170	417
25	148	9484	243	141	290	176	400
26	153	10489	256	149	300	180	385
27	159	11650	268	153	320	186	371
28	165	15150	283	160	330	200	358
29	170	15283	298	164	350	204	345
30	173	15524	308	171	360	206	334
35	201	23749	370	192	430	236	286
40	231	34147	433	218	500	270	250
45	265	47839	504	245	580	300	223
50	298	64443	564	271	645	330	200
55	324	85571	630	297	720	370	182
60	348	108022	692	320	790	395	167

TABLE 3.3. TURNAROUND-TIME ON DS1103 R&D CONTROL BOARD (μ s).

Model Order	Technique						T_{ngst}
	DRLS	RLS	RDFT1	ADALINE1	RDFT2	ADALINE2	
1	3.4	4.4	3.4	4.0	3.6	4.4	10000
5	4.8	19.8	4.8	8.7	6.2	10	2000
10	6.4	78	6.8	14	9.6	16.5	1000
15	8.1	209	8.8	18.7	12.8	22.5	667
20	9.8	413.2	11.6	24.7	17.2	30	500
25	11.8	776.5	14.6	30.5	22.5	37	400
30	13.8	1315	18.4	36	27.1	44	334
35	16.2	2120	21.7	41	32.2	50	286
40	19.2	2990	25.2	46.5	38	57	250
45	21.4	4222	30.6	52	44	64	223
50	23.8	5693	35.4	57	51	71	200
55	25.8	7518	40.8	62.5	57	77	182
60	27.8	9477	45.6	68	63	84	167

3.3.4.2. Case 3: Real-Time Harmonics Estimation

A harmonics distorted voltage waveform is produced by using a programmable power supply [137]. The nominal fundamental frequency is 50 Hz. The voltage waveform is sensed by a voltage transducer [147] and fed into an analogue-to-digital converter (ADC) which digitizes the waveforms for the DSP input. The model order is 40 for the DRLS technique, RDFT1 arrangement, and ADALINE1 arrangement. The implementation has been carried out on the DS1103 board and the sampling frequency is 4 kHz.

One of the benefits of the decoupled model of DRLS is the possibility of assigning different forgetting factors for different units to control the required dynamics of each unit as discussed in Section 3.3. The forgetting factor for the first unit which estimates

the fundamental frequency component is 0.96 to track the changes faster. The forgetting factors for the other units which estimate harmonics are all 0.97 to provide a smoother response.

Figure 3.11(a) shows the produced harmonics distorted voltage waveform by the power supply for which the voltage amplitude drops by 10%. Figure 3.11 (b) and (c) show the estimated fundamental and 5th harmonic amplitudes respectively. Figure 3.12 shows 7th, 11th, and 13th, harmonics amplitudes estimation.

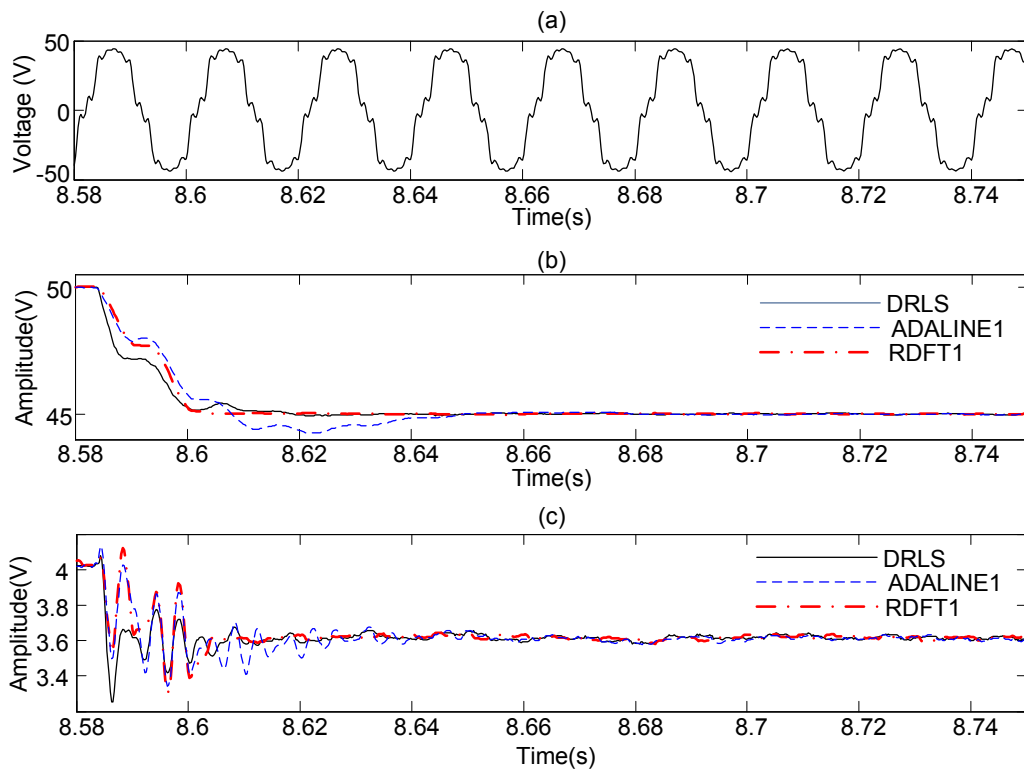


Figure 3.11. Case 3: Real-time harmonics estimation

- (a) line-to-neutral voltage waveform
- (b) fundamental component amplitude estimation
- (c) 5th harmonic amplitude estimation.

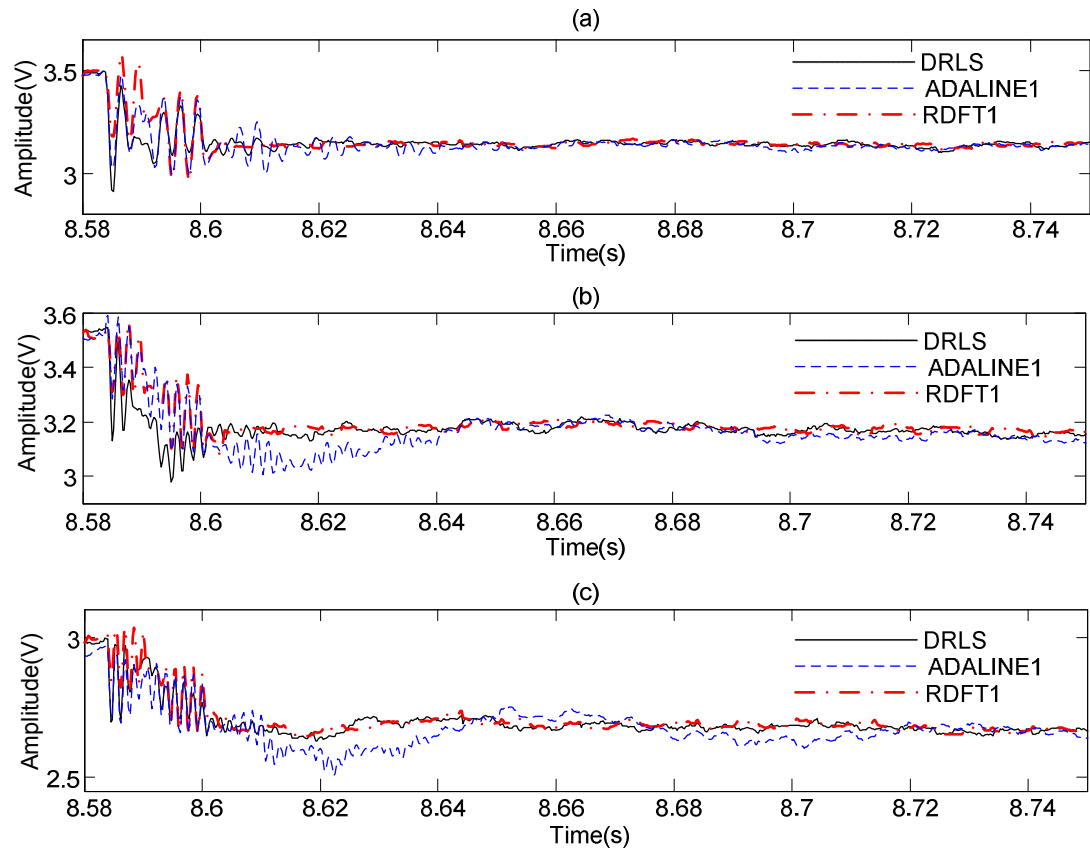


Figure 3.12. Case 3: Real-time harmonics estimation

- (a) 7th harmonic amplitude estimation
- (b) 11th harmonic amplitude estimation
- (c) 13th harmonic amplitude estimation.

3.4. Synchronized Phasors and Instantaneous Symmetrical Components Extraction by Using the DRLS Technique

Synchronized symmetrical components extraction is of paramount importance in power system application such as mode estimation [148], dynamic phasor estimation [149], stability margin assessment [150], state estimation [151], active distribution network monitoring [152], fault analysis [153], reactive power compensation [154], and grid fault-control schemes for distributed generation (DG) [155].

Several techniques have been used for symmetrical components extraction including DFT [68], KF [156], ADALINE [59], NTA [33], and PLLs [10], [53], [54], [58], [157], [158] for which their capability to produce synchronized estimates will be revisited in the following sections. All these techniques can effectively extract the amplitude of symmetrical components while each showing distinctive dynamics.

However, the DFT, KF, and ADALINE techniques do not produce synchronized estimates of phasors because they are frequency-domain techniques and they need to recover the concept of time for synchronization [10] such as application of a PLL to synchronize the ADALINE technique [59]. Moreover, they function based on linear decomposition of a waveform into its in-phase and quadrature-phase elements and using the inverse tangent of quadrature-to-in-phase ratio to extract the phase angle, while the sign of the in-phase element should be considered in a logic loop [57]. On the other hand, the NTA technique is capable of direct synchronized extraction of phase-angle which however requires incorporating recursive-least-squares (RLS) technique to reduce the heavy burden of computing the pseudo-inverse Jacobian matrix [79]-[82].

The PLLs are nonlinear techniques capable of direct synchronized phasor detection which are arguably the most widespread employed synchronization algorithms due to their structural simplicity and frequency adaptation feature [157]. However, PLLs are prone to errors where the signal amplitudes vary over a wide range [53], the three-phase power system is severely unbalanced or harmonics distorted [54], and dc components appear either caused by a fault or analogue-to-digital conversion stage [10].

The RLS technique has also been employed to estimate phasors in the nonlinear form [79]-[82], [85] and linear form [14], [83], [86], [92], [96]-[98] which both handle dc components, frequency variations, and fault conditions effectively. The linear form of RLS technique, presented in [14], [83], [86], [92], [96]-[98], shares the same shortcomings of DFT, KF, and ADALINE techniques as mentioned earlier. The nonlinear form of RLS technique, presented in [79]-[82], [85], produces synchronized estimates directly. However, the computational complexity of a high order RLS technique, which can accommodate harmonics, impedes its real-time application on digital signal processors (DSPs) [85].

The proposed DRLS technique reduces the computational complexity of the conventional RLS technique as presented in Section 3.3.4.1. This Section presents the application of the DRLS technique for synchronized phasors and instantaneous symmetrical components extraction. The presented RDSPOC frequency estimation technique of Chapter 2 is also modified for three-phase power systems. The DRLS technique is associated with the modified RDSPOC frequency tracking technique to deliver frequency adaptive estimates.

The DRLS technique directly extracts the synchronized voltage or current amplitudes

and phase-angles of three phases (A, B, and C) which are converted into the instantaneous zero ($d^0(k)$), positive ($d^+(k)$), and negative ($d^-(k)$) sequences based on the Fortescue theory as follows.

$$d^0(k) = \frac{1}{3} \left(\hat{A}_1^A(k) \sin(\hat{\theta}_1^A(k)) + \hat{A}_1^B(k) \sin(\hat{\theta}_1^B(k)) + \hat{A}_1^C(k) \sin(\hat{\theta}_1^C(k)) \right) \quad (3.70)$$

$$d^+(k) = \frac{1}{3} \left(\hat{A}_1^A(k) \sin(\hat{\theta}_1^A(k)) + \hat{A}_1^B(k) \sin(\hat{\theta}_1^B(k) + \frac{2}{3}) + \hat{A}_1^C(k) \sin(\hat{\theta}_1^C(k) - \frac{2}{3}) \right) \quad (3.71)$$

$$d^-(k) = \frac{1}{3} \left(\hat{A}_1^A(k) \sin(\hat{\theta}_1^A(k)) + \hat{A}_1^B(k) \sin(\hat{\theta}_1^B(k) - \frac{2}{3}) + \hat{A}_1^C(k) \sin(\hat{\theta}_1^C(k) + \frac{2}{3}) \right) \quad (3.72)$$

where

\hat{A}_1^A is the fundamental frequency voltage or current amplitude of phase-A,

\hat{A}_1^B is the fundamental frequency voltage or current amplitude of phase-B, and

\hat{A}_1^C is the fundamental frequency voltage or current amplitude of phase-C.

$\hat{\theta}_1^A$, $\hat{\theta}_1^B$, and, $\hat{\theta}_1^C$ are evaluated as follows:

$$\hat{\theta}_1^A(k) = \left(2 \ kT_s (f_o + \hat{f}_d) \right) + \hat{\mathcal{C}}_1^A(k) \quad (3.73)$$

$$\hat{\theta}_1^B(k) = \left(2 \ kT_s (f_o + \hat{f}_d) \right) + \hat{\mathcal{C}}_1^B(k) \quad (3.74)$$

$$\hat{\theta}_1^C(k) = \left(2 \ kT_s (f_o + \hat{f}_d) \right) + \hat{\mathcal{C}}_1^C(k) \quad (3.75)$$

in which

$\hat{\mathcal{C}}_1^A(k)$ is the estimate of the fundamental frequency voltage or current phase-angle by the DRLS technique for phase-A,

$\hat{\mathcal{C}}_1^B(k)$ is the estimate of the fundamental frequency voltage or current phase-angle by

the DRLS technique for phase-*B*, and

$\hat{\phi}_1^c(k)$ is the estimate of the fundamental frequency voltage or current phase-angle by the DRLS technique for phase-*C*.

The term $\left(2 kT_s \left(f_o + \hat{f}_d\right)\right)$ on the right-hand-side of (3.73)-(3.74) is generated by the modified three-phase RDSPOC frequency estimation technique. The RDSPOC technique was presented in Chapter 2. Figure 3.13 presents the modified three-phase RDSPOC frequency estimation technique.

In Figure 3.13:

v_A is the voltage waveform of phase-*A*

v_B is the voltage waveform of phase-*B*

v_C is the voltage waveform of phase-*C*

v_α is the α component of the three-phase-to- $\alpha\beta$ Clarke transformation from which the power system frequency is estimated

v_1 is the in-phase component of v_α , v_2 is the quadrature-phase component of v_α

f_o is the nominal power system frequency (which is 50 Hz or 60 Hz), $N_o = 1/(T_s f_o)$

\hat{f}_d is the estimated frequency drift for its nominal value (f_o).

According to the testing requirements in IEC Standard 61000-4-30 [176] (page 18), the power system frequency estimation bandwidth is 42.5-57.5 Hz for 50 Hz power systems and 51-69 Hz for 60 Hz power systems. Therefore, in Figure 3.13, the low-pass-filter (LPF) bandwidth is chosen to be 10 Hz which complies with the IEC Standard 61000-4-30 requirements for both 50 Hz and 60 Hz power systems. The LPF

of Figure 3.13 is a first order filter for which the cut-off frequency is 10 Hz. Figure 3.14 shows the proposed DRLS technique real-time implementation for instantaneous synchronized symmetrical components extraction where d_A , d_B , and d_C are three-phase instantaneous voltage or current waveforms.

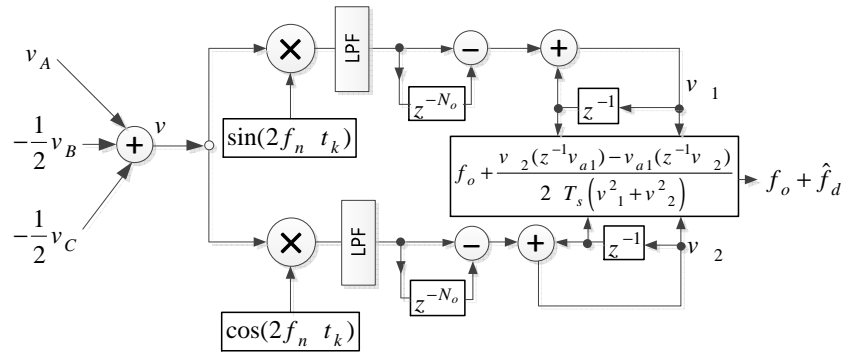


Figure 3.13. Implementation of the modified three-phase RDSPOC frequency estimation technique.

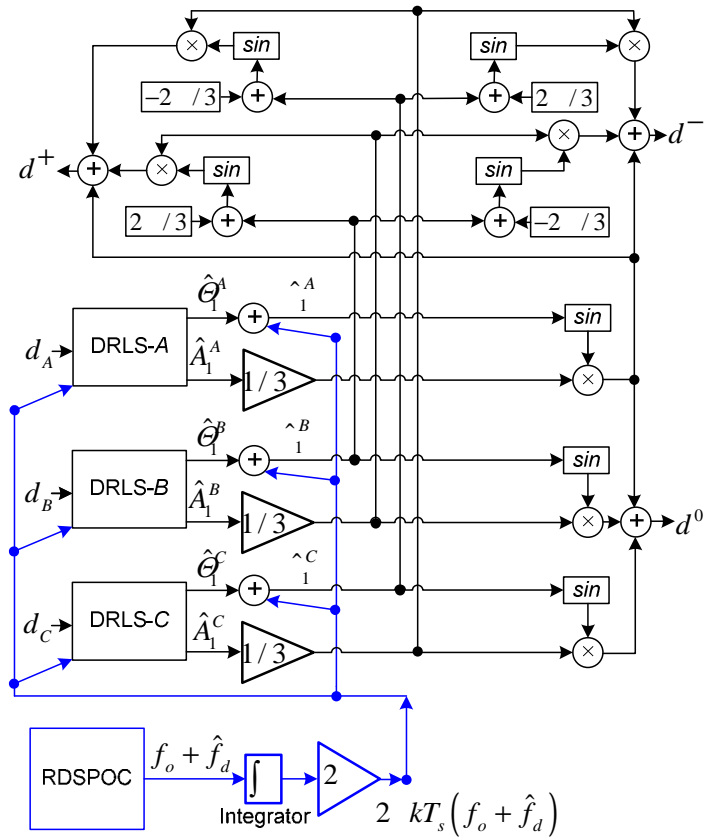


Figure 3.14. DRLS technique real-time implementation for instantaneous synchronized symmetrical components extraction.

3.4.1. Simulation Studies

This section presents the simulation studies results in MATLAB-Simulink. The sampling frequency is 4 kHz. A is 0.97 for DRLS and initial values of all R_{oi} matrices are set to the 2×2 identity matrix according to Section 3.3.1.

3.4.1.1. Case 4: Fault Condition

This section presents a fault simulation study in the MATLAB-Simulink. Figure 3.15 shows the radial distribution power system which is simulated to study a fault on the power distribution line.

In Figure 3.15:

the nominal power system frequency is 50 Hz,

the voltage source and Z_{eq} simulate a distribution equivalent network with the voltage level of 25 kV,

the equivalent impedance of the network (Z_{eq}) is $(0.625 + j5.208) \Omega$,

the distribution line cables (L1 and L2) are all-aluminium-conductor (ACC) type for which:

the π model positive sequence resistance and inductance are 0.3854 Ω/km and 1.8 mH/km respectively [144]

the zero sequence resistance and inductance of the π model are 0.7455 Ω/km and 5.1 mH/km respectively [144].

A solid single-phase-A-to-ground (A-G) fault is simulated on the Bus 3. The fault occurs at 2.01 s and is cleared at 2.11 s. For distribution applications, the arc

deionization and clearing is less than 11.5 cycles according to IEEE Standard C37.230 [159]. The first reclosing attempt is 0-5 s after the fault for distribution voltages less than 35 kV according to IEEE Standard C37.104 [160]. The reclosers reconnect the transmission line L1 0.2 s after fault at 2.21 s.

The voltage and current waveforms have been captured at Bus 1. The EPLL technique is an improved PLL-type technique which is proposed to handle harmonics and the dc components [10]. Both the DRLS and EPLL techniques accommodate odd harmonics up to the 17th in their governing equations in this case study. Figure 3.16 shows the three-phase voltage and current waveforms. Figure 3.17 and Figure 3.18 show extracted instantaneous zero, positive, and negative sequences for three-phase voltages and currents respectively. As seen in Figure 3.17, the DRLS technique shows a better track of current symmetrical sequences under fault condition and the subsequent reclosing operation.

Figure 3.19-Figure 3.21 show the amplitude and phase-angle estimates of three-phase currents. Figure 3.22-Figure 3.24 show the amplitude and phase-angle estimates of three-phase voltages. As seen in Figure 3.19, the DRLS delivers synchronous and stable estimation of the current amplitude and phase-angle of phase-A (which is involved in the fault) although EPLL temporarily loses its synchronism with the grid during the fault and reclosing operation and restores it only when the fault is cleared. Both DRLS and EPLL techniques show accurate and fast track of voltage amplitude and phase angle of phase-A as seen in Figure 3.22. The DRLS and EPLL techniques show synchronous and stable estimation of current amplitude and phase-angle in phase-B and -C which are not involved in the fault. Both DRLS and EPLL techniques show accurate and fast track

of voltage amplitude and phase-angle in three-phases.

This however does not mean undermining the overall stability of the EPLL technique for normal operation but highlights the difficulties to tune it for fault conditions which are arbitrary drastic changes. On the other hand, the proposed DRLS technique benefits from its inbuilt correlation procedure to cope with the drastic changes during fault conditions.

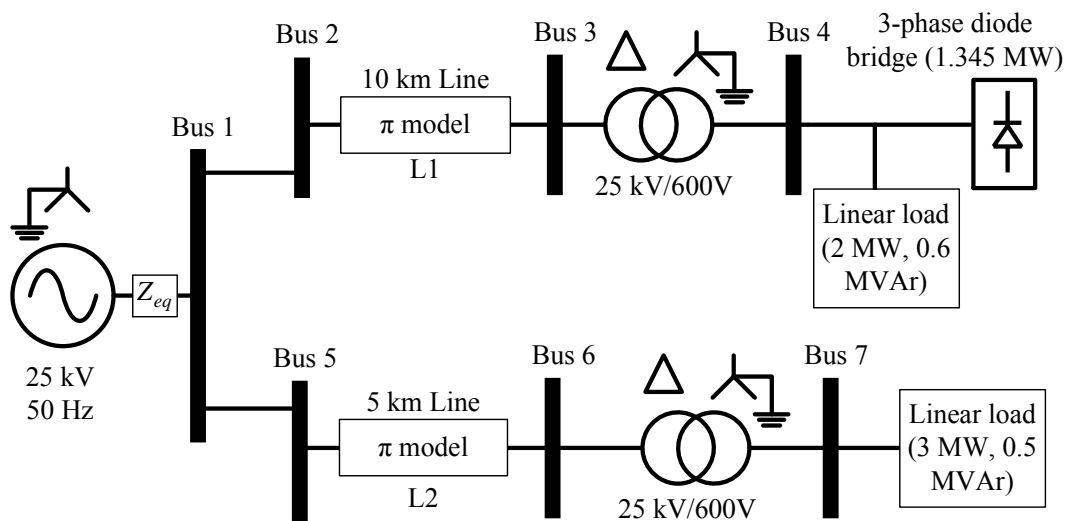


Figure 3.15. Case 4: Fault condition

Simulated radial power distribution system in MATLAB-Simulink.

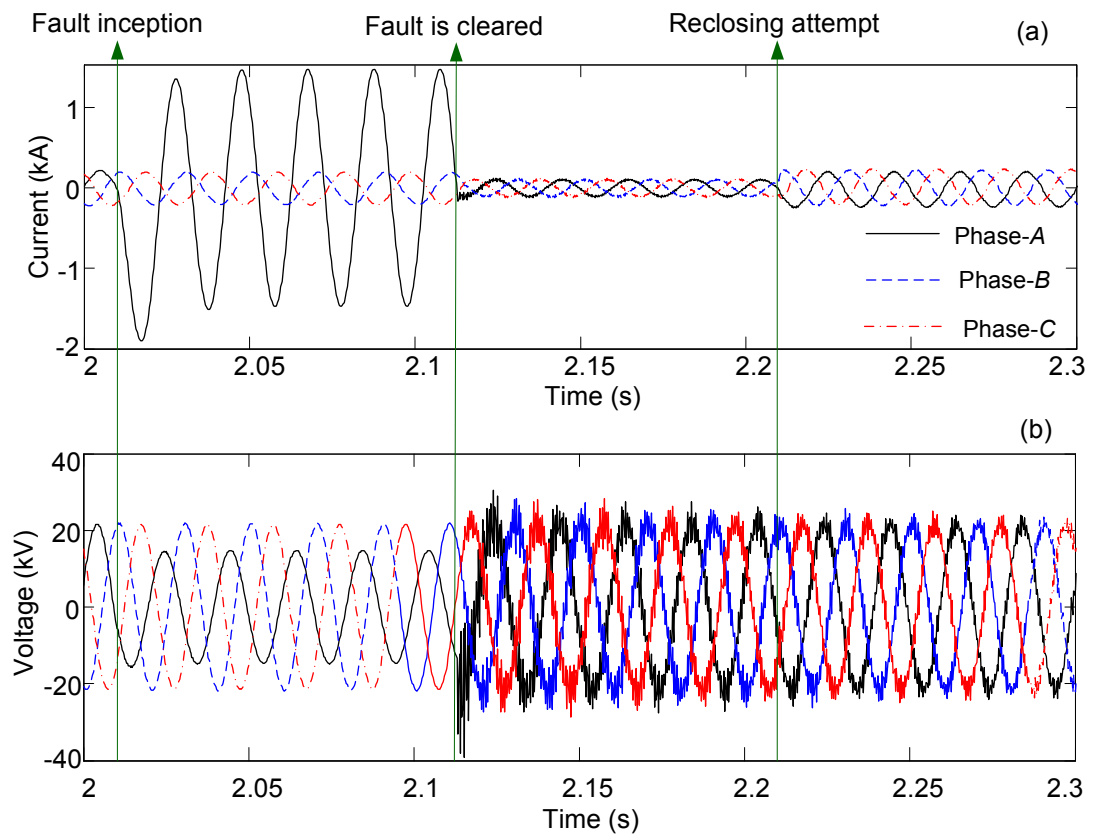


Figure 3.16. Case 4: phase-A-to-ground fault simulation

(a) three-phase current waveforms

(b) three-phase voltage waveforms.

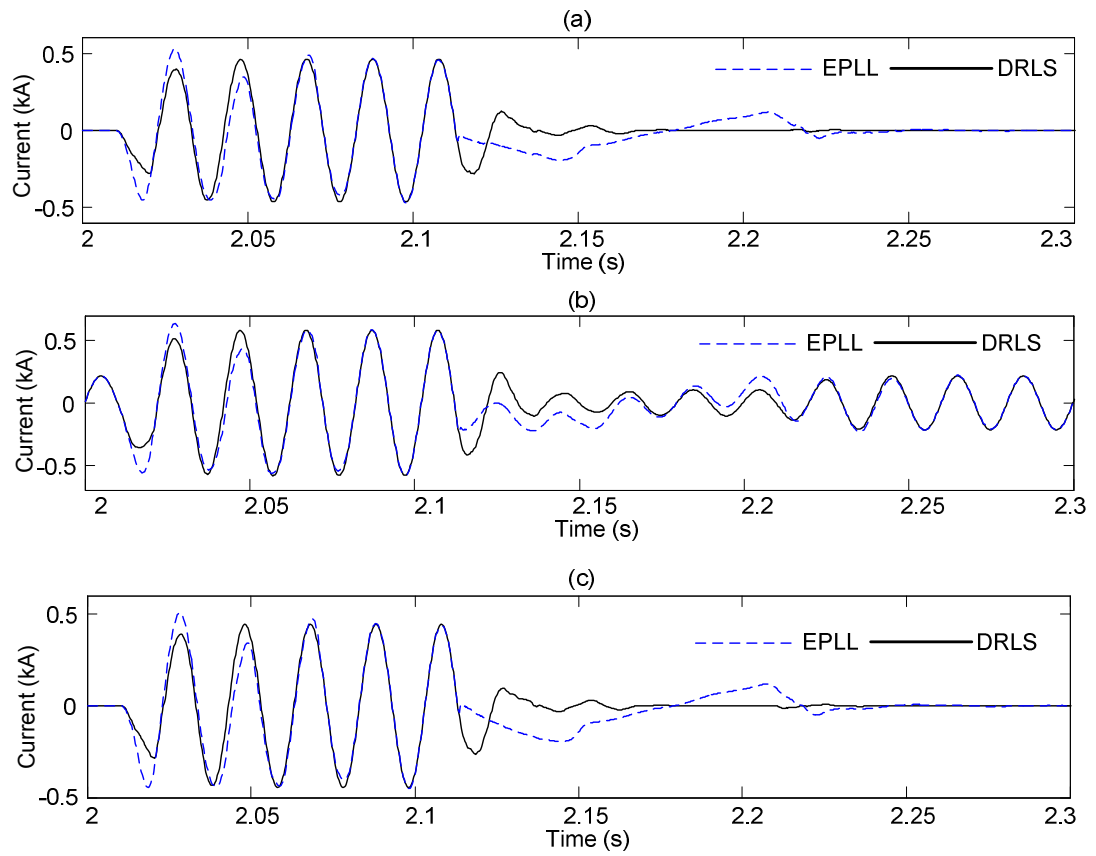


Figure 3.17. Case 4: phase-A-to-ground fault simulation

- (a) estimate of current instantaneous zero sequence
- (b) estimate of current instantaneous positive sequence
- (c) estimate of current instantaneous negative sequence.

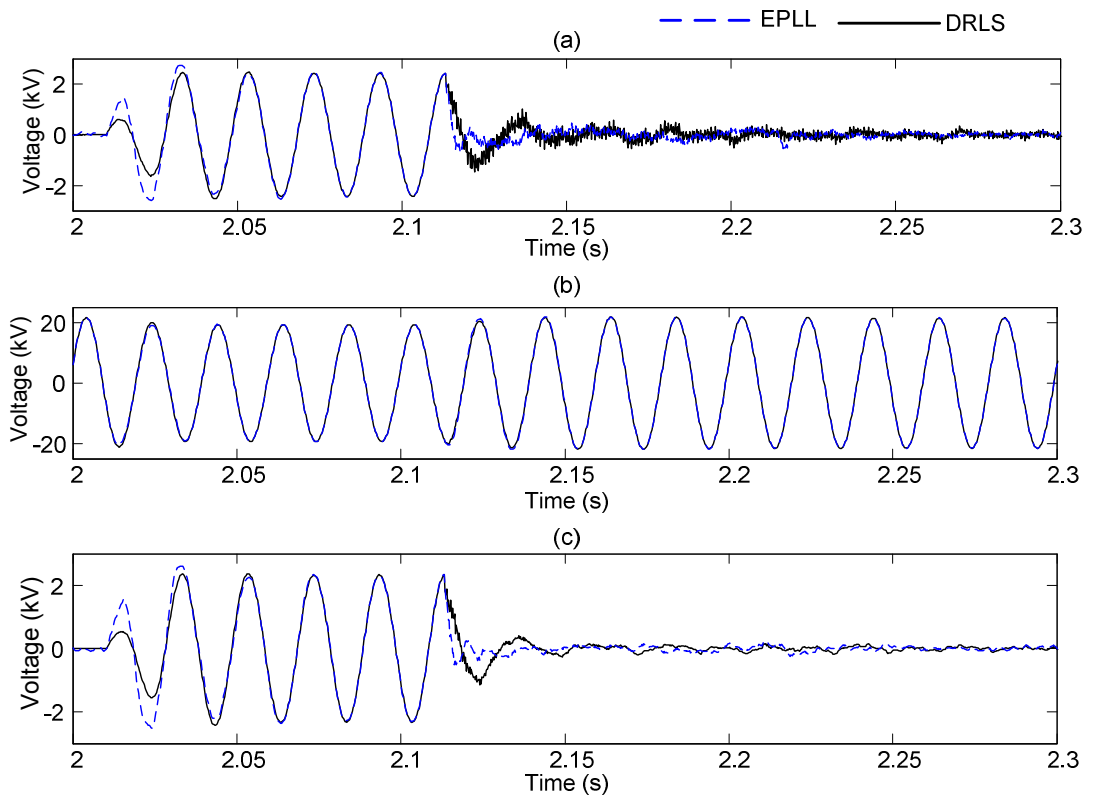


Figure 3.18. Case 4: phase-A-to-ground fault simulation

- (a) estimates of voltage instantaneous zero sequence
- (b) estimates of voltage instantaneous positive sequence
- (c) estimates of voltage instantaneous negative sequence.

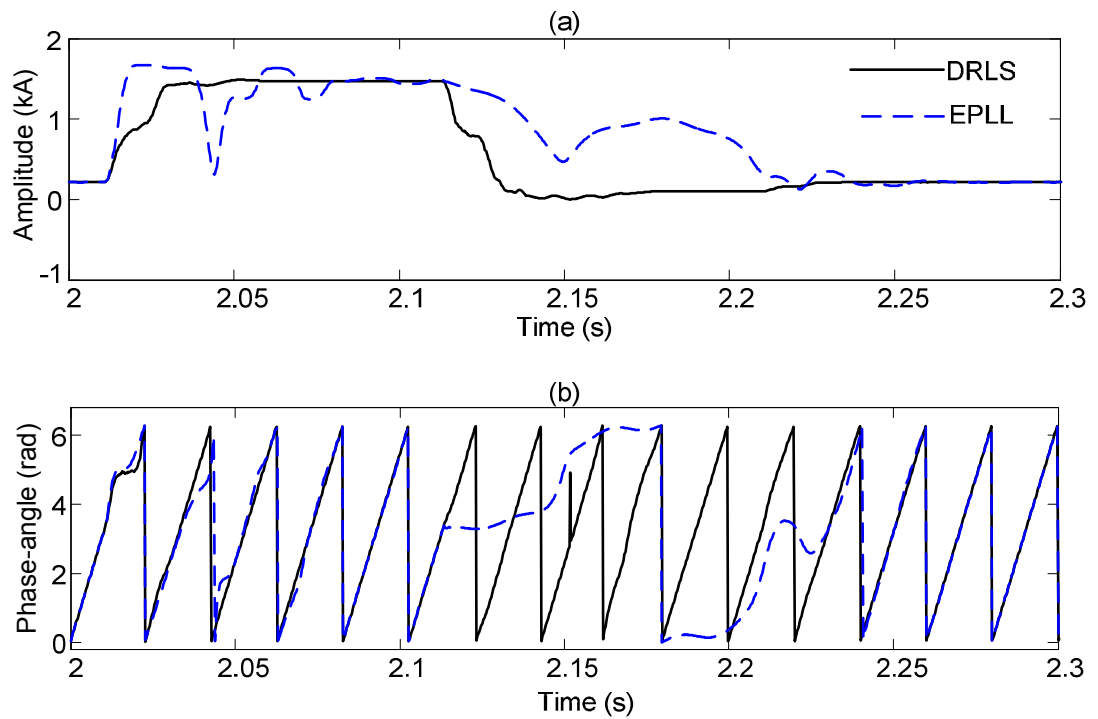


Figure 3.19. Case 4: phase-A-to-ground fault simulation

(a) phase-A current estimate of amplitude

(b) phase-A current estimate of phase-angle.

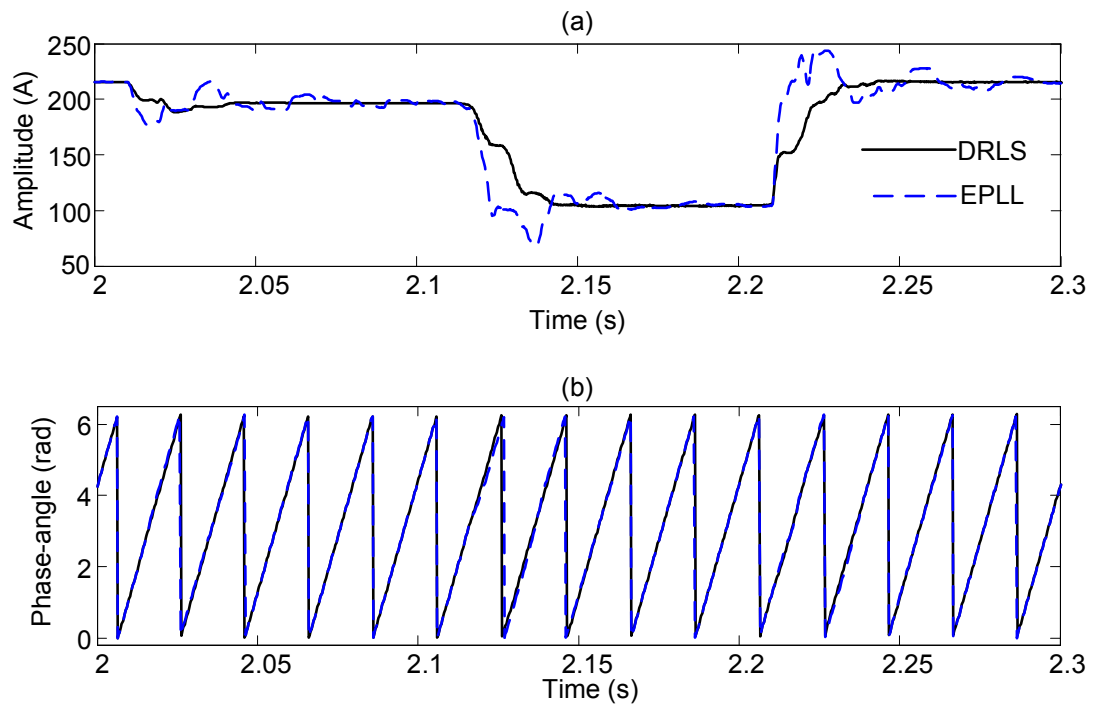


Figure 3.20. Case 4: phase-A-to-ground fault simulation

(a) phase-B current amplitude estimate

(b) phase-B current phase-angle estimate.

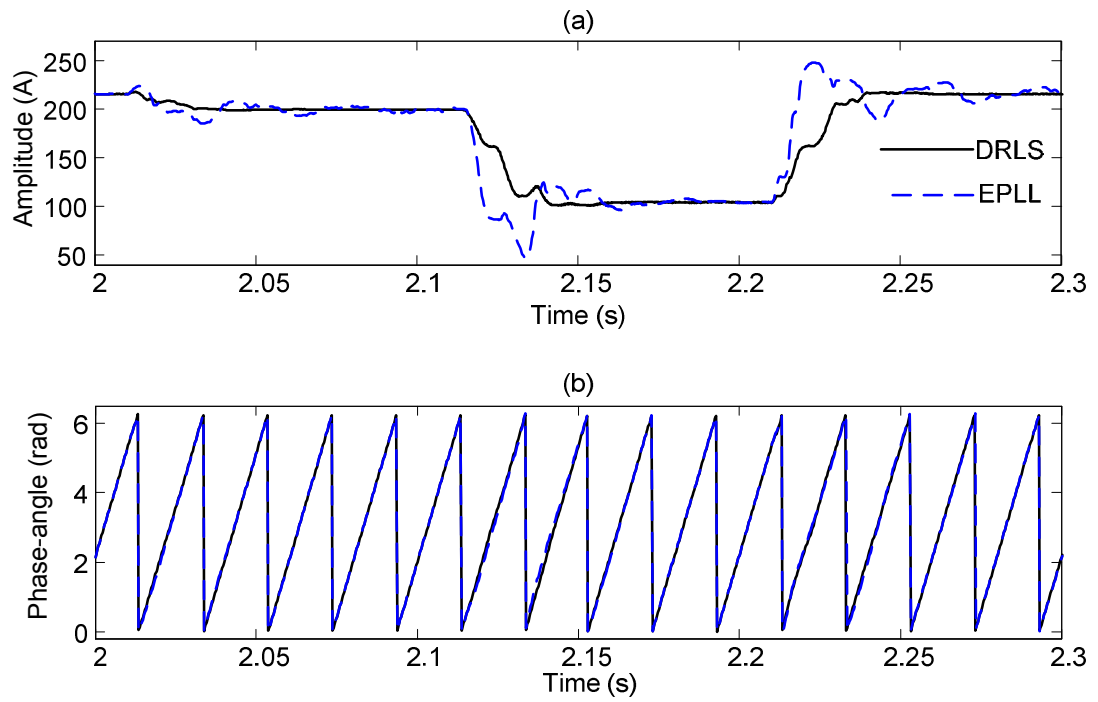


Figure 3.21. Case 4: phase-A-to-ground fault simulation

(a) phase-C current estimate of amplitude

(b) phase-C current estimate of phase-angle.

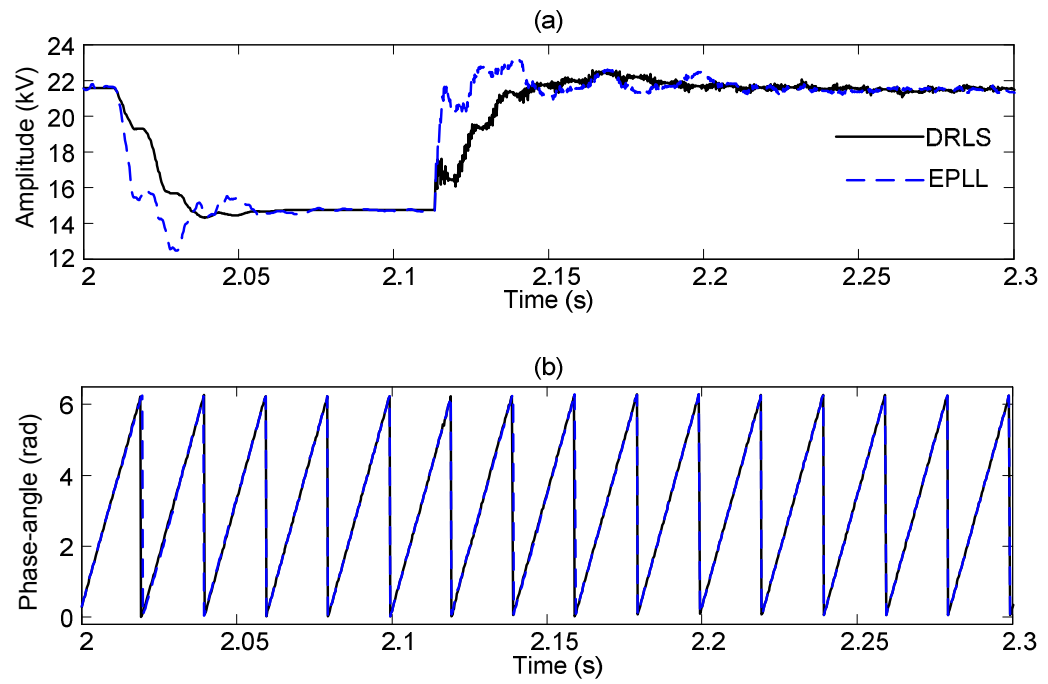


Figure 3.22. Case 4: phase-A-to-ground fault simulation

(a) phase-A-to-neutral voltage estimate of amplitude

(b) phase-A-to-neutral voltage estimate of phase-angle.

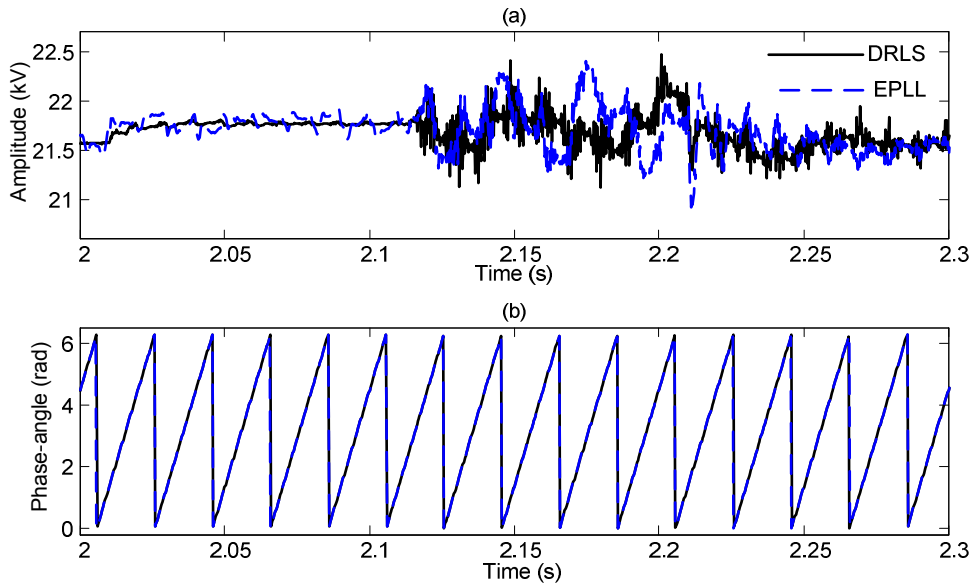


Figure 3.23. Case 4: phase-A-to-ground fault simulation

(a) phase-B-to-neutral voltage estimate of amplitude

(b) phase-B-to-neutral voltage estimate of phase-angle.

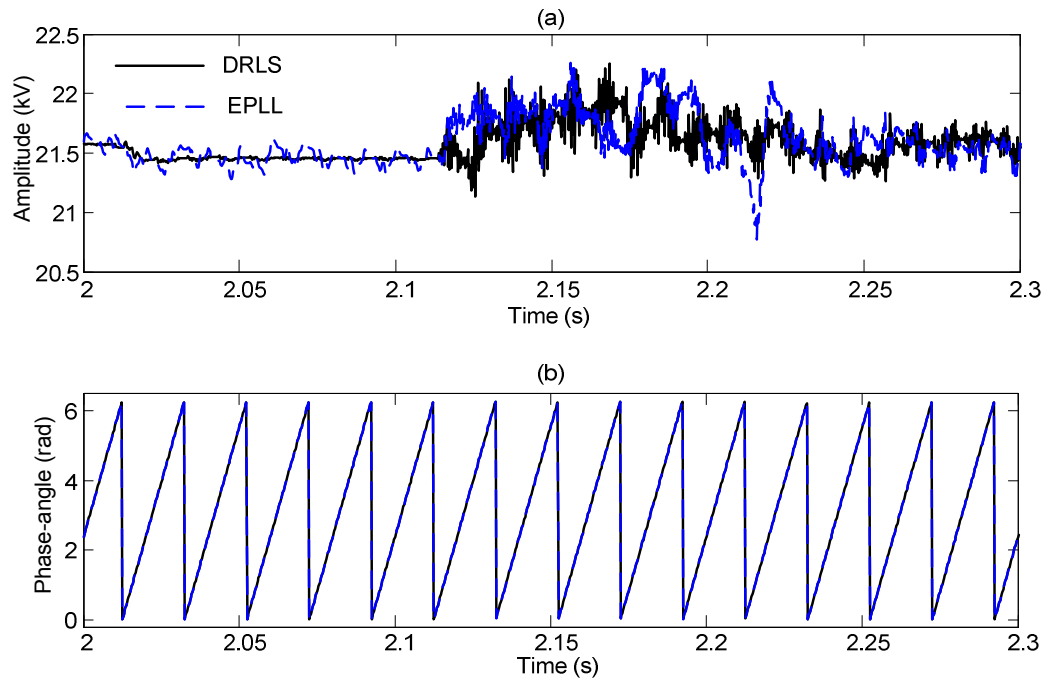


Figure 3.24. Case 4: phase-A-to-ground fault simulation

(a) phase-C-to-neutral voltage estimate of amplitude

(b) phase-C-to-neutral voltage estimate of phase-angle.

3.4.1.2. Case 5: Frequency Drift in a Balanced Three-Phase System

This section presents a case study to evaluate the performance of DRLS and EPLL techniques to track the phasors and instantaneous symmetrical components when the power system frequency drifts from 50.0 Hz to 49.0 Hz in a balanced three-phase system.

Figure 3.25 shows the three-phase voltage waveforms, Figure 3.26 shows the estimated instantaneous symmetrical components, Figure 3.27 shows estimates of line-to-neutral amplitude and phase-angle for phase-A, Figure 3.28 shows estimates of line-to-neutral amplitude and phase-angle for phase-B, and Figure 3.29 shows estimates of line-to-neutral amplitude and phase-angle for phase-C. Both DRLS and EPLL techniques show stable and accurate amplitude, phase-angle, and instantaneous symmetrical components estimation in a balanced three-phase system.

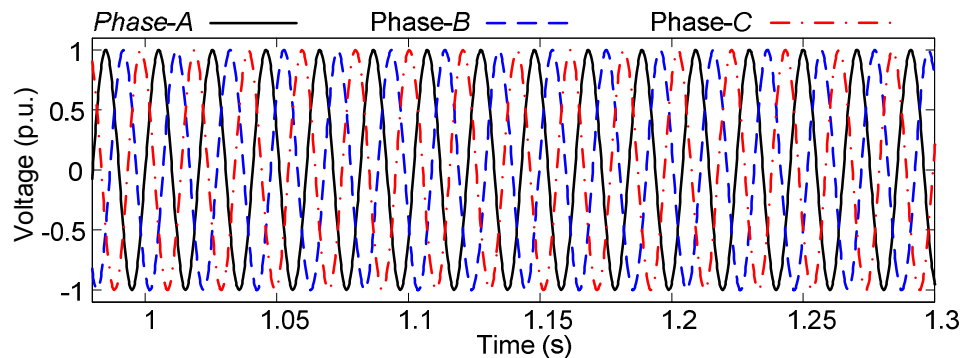


Figure 3.25. Case 5: Frequency drift in a balanced three-phase system

Three-phase voltage waveforms.

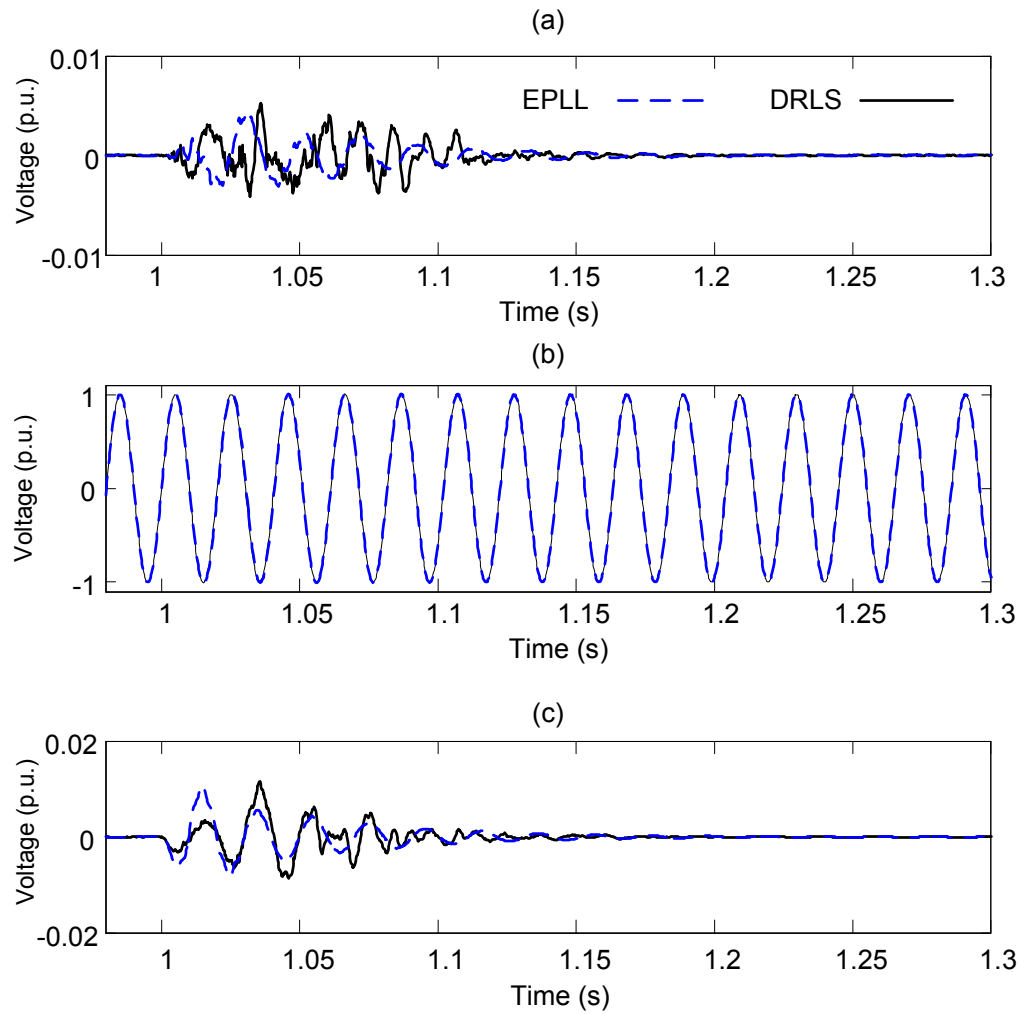


Figure 3.26. Case 5: Frequency drift in a balanced three-phase system

- (a) estimate of zero sequence
- (b) estimate of the positive sequence
- (c) estimate of the negative sequence.

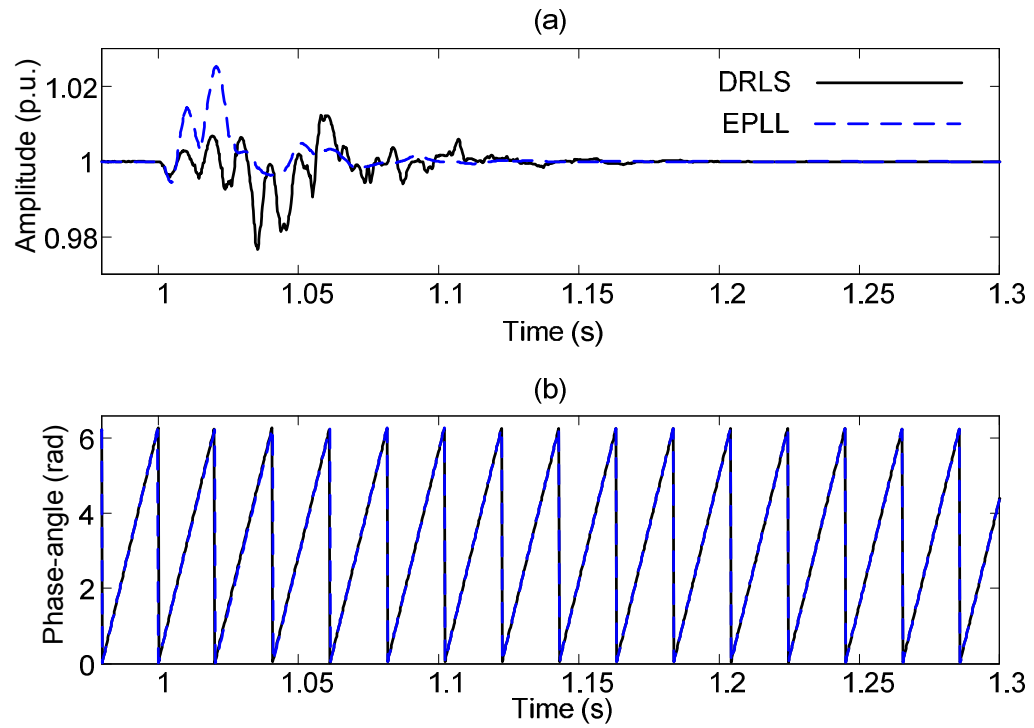


Figure 3.27. Case 5: Frequency drift in a balanced three-phase system

(a) phase-A-to-neutral amplitude estimate

(b) phase-A-to-neutral phase-angle estimate.

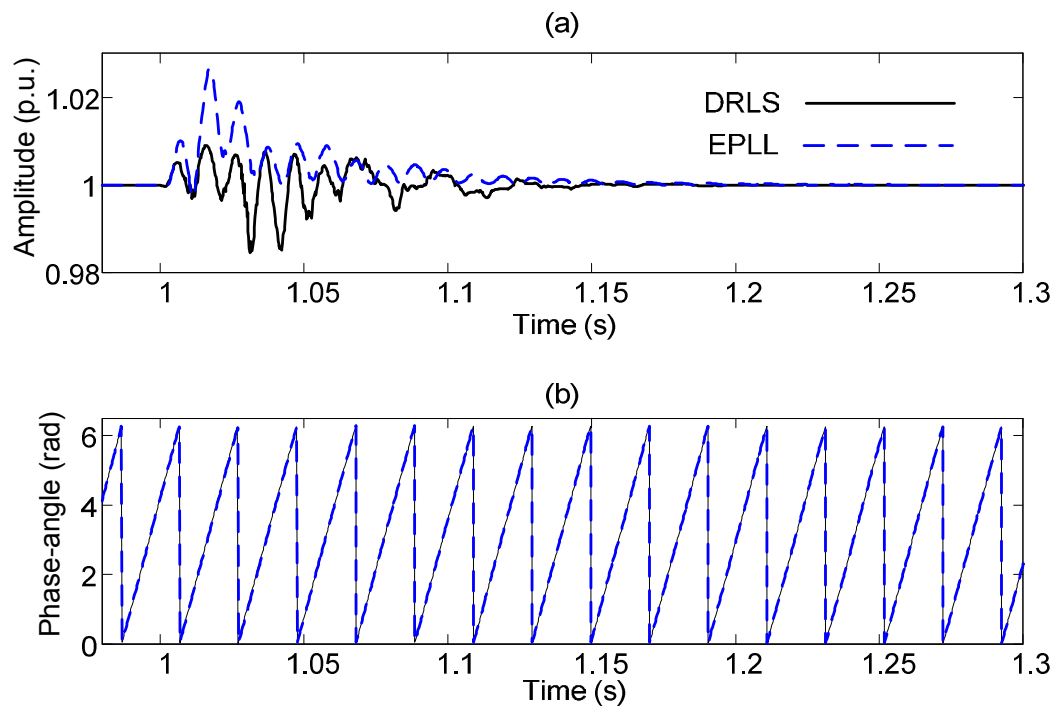


Figure 3.28. Case 5: Frequency drift in a balanced three-phase system

(a) phase-*B*-to-neutral amplitude estimate

(b) phase-*B*-to-neutral phase-angle estimate.

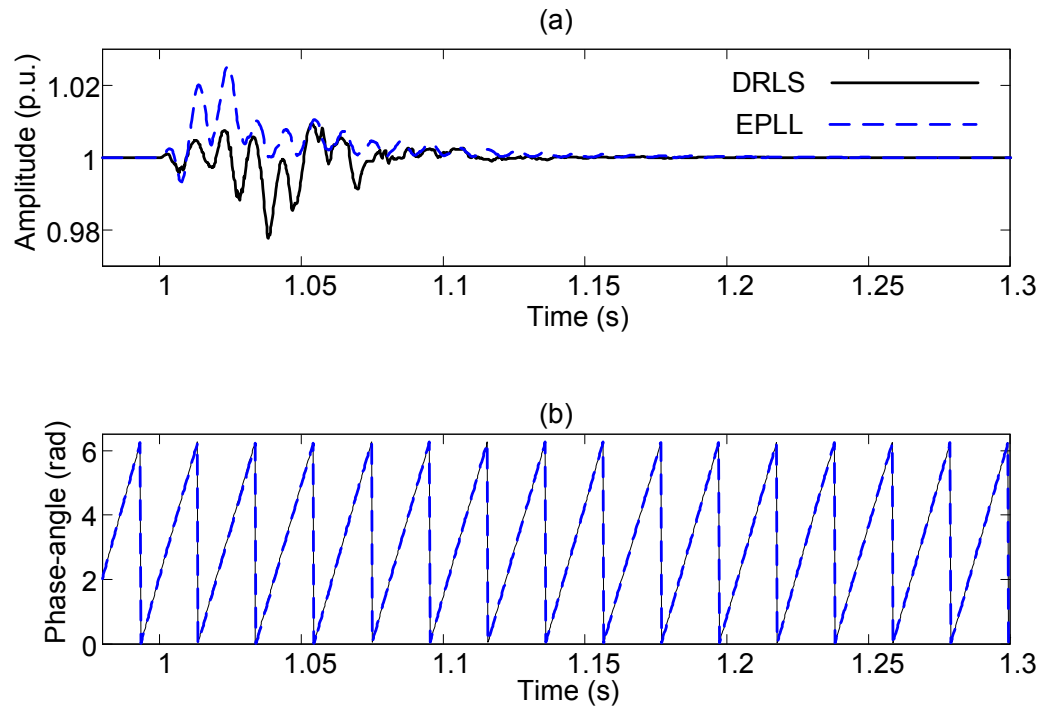


Figure 3.29. Case 5: Frequency drift in a balanced three-phase system

(a) phase-C-to-neutral amplitude estimate

(b) phase-C-to-neutral phase-angle estimate.

3.4.1.3. Case 6: Frequency Drift in an Unbalanced Three-Phase System

This section presents a case study to evaluate the performance of DRLS and EPLL techniques to track the phasors and instantaneous symmetrical components when the power system frequency drifts from 50.0 Hz to 49.0 Hz in an unbalanced three-phase system. The unbalanced three-phase system information is presented in Table 3.4.

Figure 3.30 shows the three-phase voltage waveforms, Figure 3.31 shows the estimated instantaneous symmetrical components, Figure 3.32 shows estimates of line-to-neutral amplitude and phase-angle for phase-A, Figure 3.33 shows estimates of line-to-neutral amplitude and phase-angle for phase-B, and Figure 3.34 shows estimates of line-to-neutral amplitude and phase-angle for phase-C. As seen in Figure 3.33, the DRLS technique shows faster and more stable estimation performance under the severe unbalance and drastic amplitude variation when compared with the EPLL technique.

TABLE 3.4. CASE 6: FREQUENCY DRIFT IN AN UNBALANCED THREE-PHASE SYSTEM, UNBALANCED SYSTEM INFORMATION.

	Amplitude (p.u.)	Phase-angle (rad)
Phase-A	1.0	0
Phase-B	0.1	$\frac{\pi}{3}$
Phase-C	0.7	$\frac{\pi}{2}$

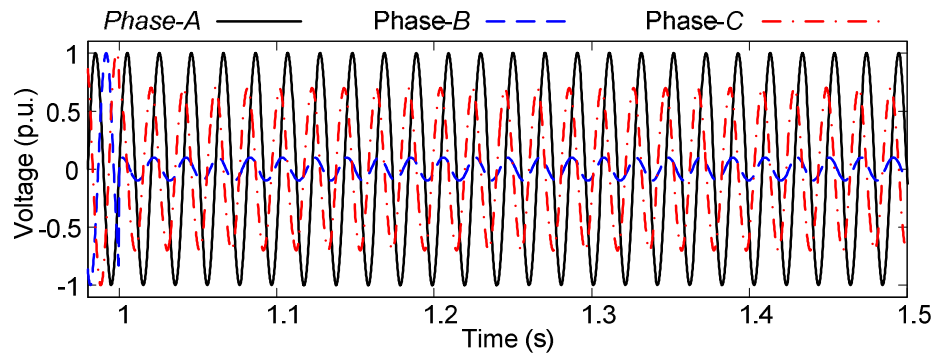


Figure 3.30. Case 6: Frequency drift in an unbalanced three-phase system

Three-phase voltage waveforms.

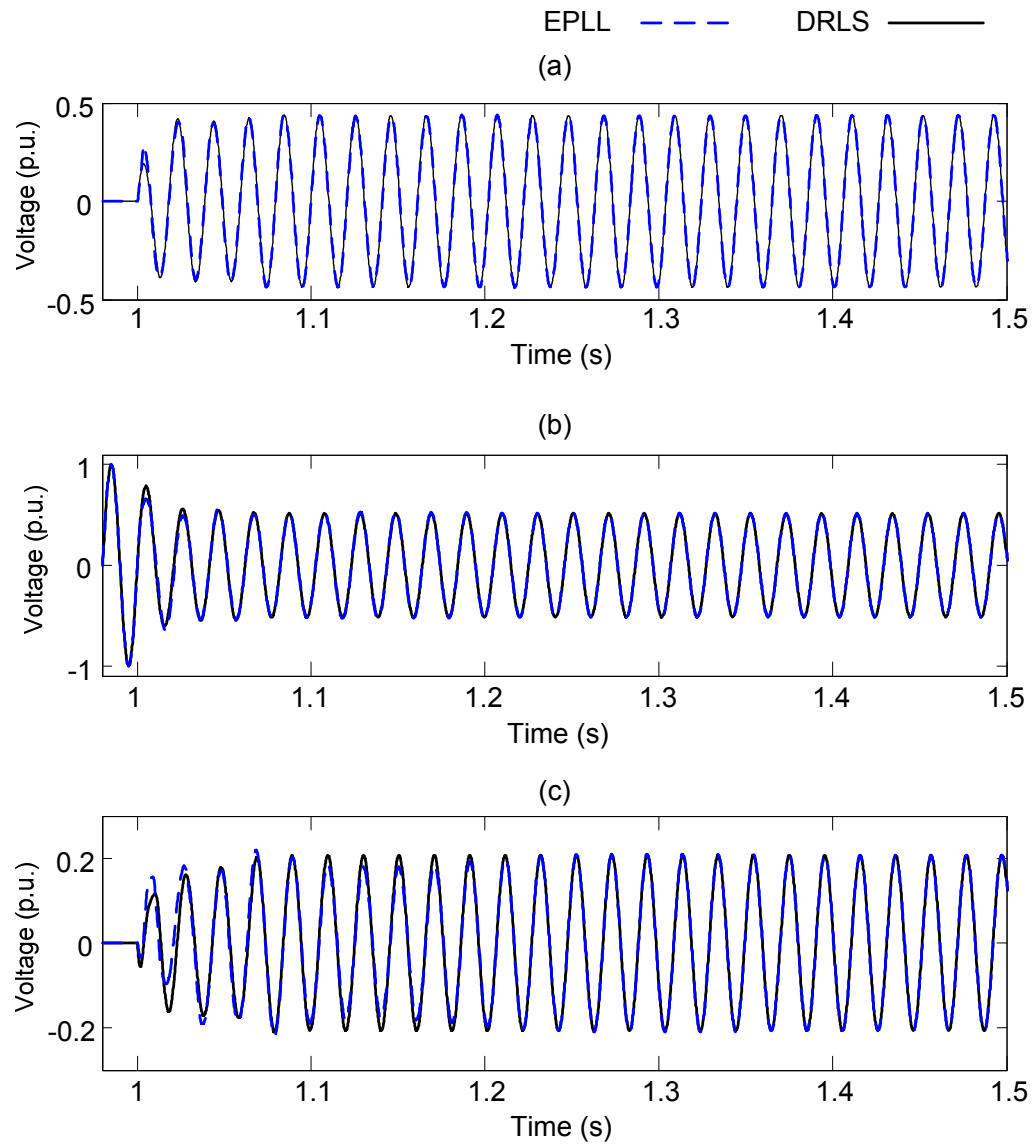


Figure 3.31. Case 6: Frequency drift in an unbalanced three-phase system

- (a) estimate of zero sequence
- (b) estimate of the positive sequence
- (c) estimate of the negative sequence.

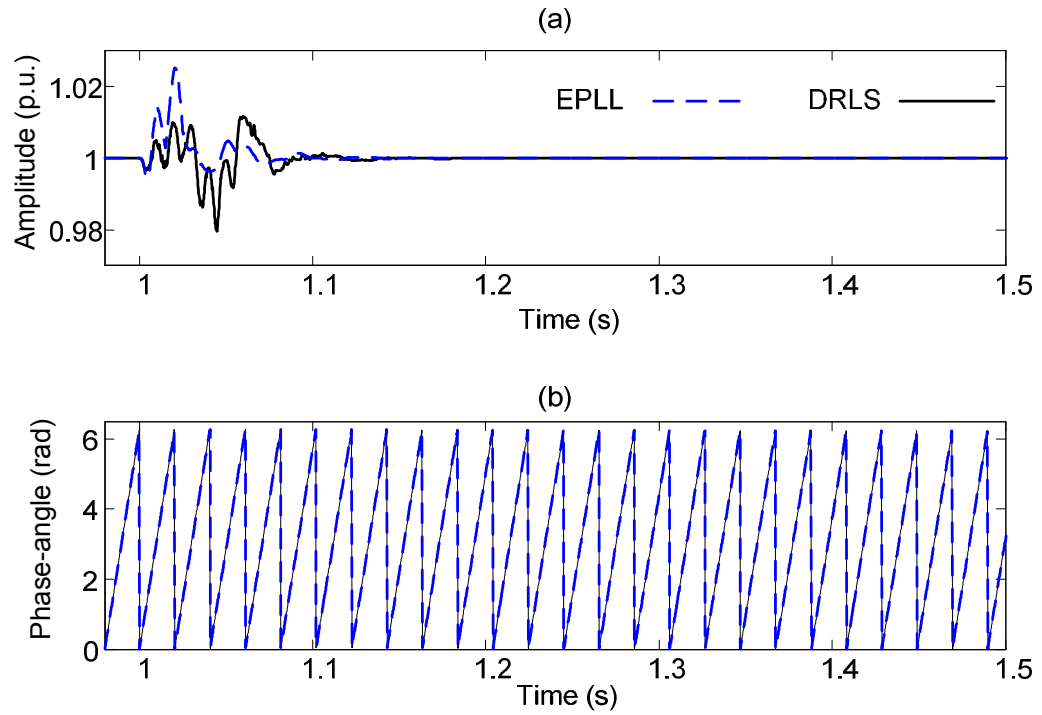


Figure 3.32. Case 6: Frequency drift in an unbalanced three-phase system

(a) phase-A-to-neutral amplitude estimate

(b) phase-A-to-neutral phase-angle estimate.

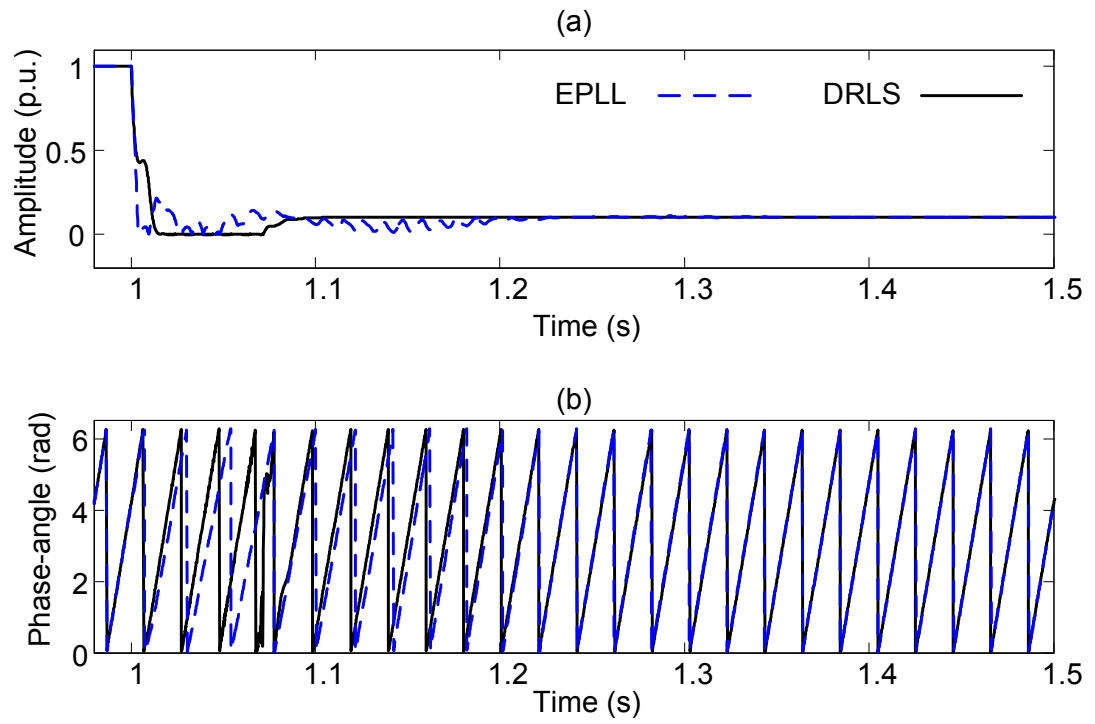


Figure 3.33. Case 6: Frequency drift in an unbalanced three-phase system

(a) phase-*B*-to-neutral amplitude estimate

(b) phase-*B*-to-neutral phase-angle estimate.

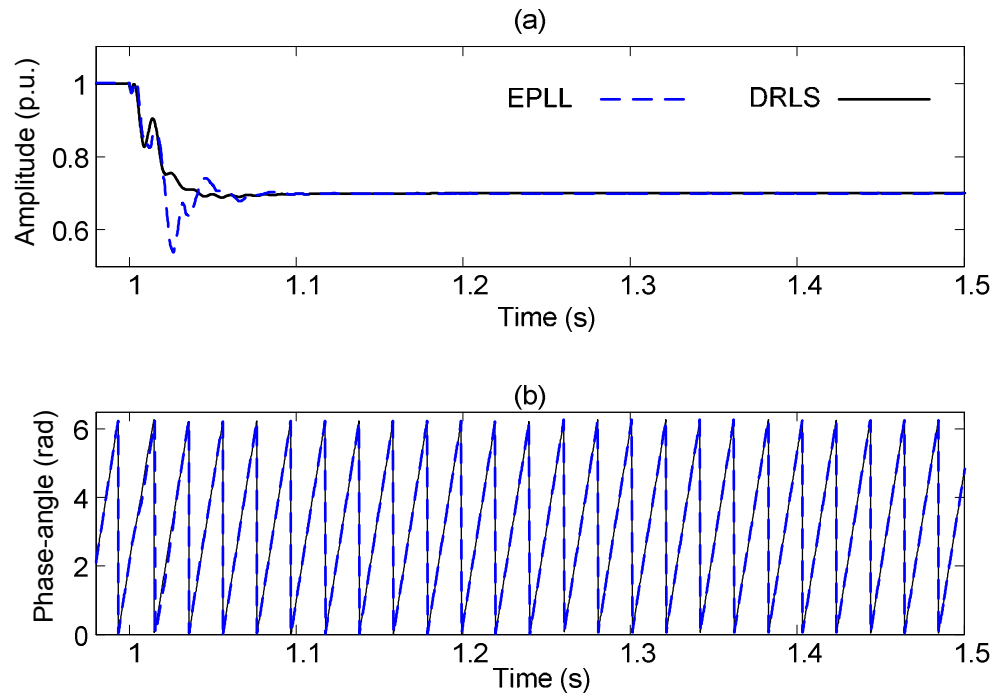


Figure 3.34. Case 6: Frequency drift in an unbalanced three-phase system

(a) phase-C-to-neutral amplitude estimate

(b) phase-C-to-neutral phase-angle estimate.

3.4.2. Investigating Turnaround-Time on Different DSP Platforms

Table 3.5 and Table 3.6 respectively present the turnaround-time of implementing DRLS, RLS, DRLS-RDSPOC, and EPLL techniques on the hardware platforms of DS1104 and DS1103 for different model orders. The model order is the number of harmonics being estimated.

IEC Standard 61000-4-13 requires harmonics estimation up to the 40th order [146] although IEEE Standard C37.118 considers harmonics up the 50th order [145]. In this section, the harmonics up to the 60th order are considered to cover the bandwidth of both standards, and beyond, for real-time implementation. The power system nominal frequency (f_o) is considered to be 50 Hz in this section. The discussion can be made for the 60 Hz power systems by simply multiplying the last column of each table by the factor of $(\frac{50}{60})$.

The real-time DSP implementation of DRLS, EPLL, and DRLS-RDSPOC techniques is feasible on the DS1104 board up to the order of 40 while the RLS technique stops at the 12th order according to Table 3.5. It should be noted the task of the RDSPOC is to track the changes in the frequency. The DRLS-RDSPOC turnaround-time becomes smaller than the EPLL one from the 45th order onward as marked in Table 3.5. This shows that the EPLL technique is a more computationally efficient technique where the waveforms are less distorted by harmonics.

The DS1103 board has a much more powerful processor which reduces the turnaround-time proportionally. The EPLL, DRLS, DRLS-RDSPOC techniques real-

time DSP implementation on DS1103 is feasible up to the 60th order while the RLS technique stops at the 20th order. The DRLS technique is more efficient than the EPLL after order 20 when implemented on DS1103 according to Table 3.6. The combined DRLS-RDSPOC technique is more computationally efficient than EPLL after order 25 when implemented on DS1103 according to Table 3.6. This proves that the DRLS and DRLS-RDSPOC are more efficient in the environments which are distorted by high orders of harmonics.

TABLE 3.5. TURNAROUND-TIME ON DS1104 R&D CONTROL BOARD (μ s).

Model Order	Technique				T_{nqst}
	DRLS	EPLL	DRLS- RDSPOC	RLS	
1	10	7.8	14	14	10000
5	23	17	30	91	2000
10	45	32	55	475	1000
<u>12</u>	56	36	68	<u>737</u>	<u>834</u>
15	75	49	96	1327	667
20	112	76	132	3535	500
25	148	106	164	9484	400
30	173	139	189	15524	334
35	201	187	217	23749	286
<u>40</u>	<u>231</u>	<u>239</u>	<u>250</u>	34147	<u>250</u>
45	265	305	288	47839	223
50	298	366	310	64443	200
55	324	437	335	85571	182
60	348	506	364	108022	167

TABLE 3.6. TURNAROUND-TIME ON DS1103 R&D CONTROL BOARD (μs).

Model Order	Technique				T_{ngst}
	DRLS	EPLL	DRLS- RDSPOC	RLS	
1	3.4	3.4	4	4.4	10000
5	4.8	4.4	5.4	19.8	2000
10	6.4	5.8	7.2	78	1000
15	8.1	7.2	8.8	209	667
20	9.8	11.4	10.8	413.2	500
25	11.8	13.6	12.8	776.5	400
30	13.8	15.8	14.8	1315	334
35	16.2	18	17.6	2120	286
40	19.2	20.6	20.2	2990	250
45	21.4	23.2	22.6	4222	223
50	23.8	25.8	24.4	5693	200
55	25.8	28.4	26.8	7518	182
60	27.8	32	28.8	9477	167

3.5. Conclusion

This chapter proposed the decoupled recursive-least-squares (DRLS) technique to bridge the gap between off-line applications of RLS technique and its implementation on DSPs for real-time power system phasors and harmonics estimation. Detailed mathematical justification of the new DRLS technique was presented in this chapter. The comparison between the proposed DRLS technique and the conventional RLS technique has shown considerable improvement in terms of reducing the turnaround-time on two different off-the-shelf R&D DSP platforms. The computational efficiency of the DRLS is also higher than the ADALINE and RDFT techniques. The DRLS technique also shows better noise immunity in comparison with that of the ADALINE and RDFT techniques.

The stability and accuracy of the DRLS technique are better than that of the EPLL technique under fault and unbalance conditions. The real-time DSP implementation efficiency of the DRLS technique is also comparable with that of the EPLL technique under low harmonics distortion but it is superior under higher harmonics distortion. The correct performance of the proposed DRLS technique has been evaluated by presenting MATLAB-Simulink simulation studies and real-time implementation experiments.

Chapter 4 : Real-Time Slow Sampling Estimation of Harmonics/Interharmonics and Phasors

4.1. Introduction

With the increased use of nonlinear loads, battery chargers, electronic ballasts, single-phase power supplies, motor drives, saturable devices, active power filters (APFs), harmonic distortions in voltage and current have become more serious than ever before [114], [115]. Harmonic pollution causes power quality (PQ) decline, extra losses in electric networks and cables, overheating of electrical machines, and malfunction of relays and breakers in power systems [161].

Harmonic estimation is an important part of monitoring, benchmarking and compensation practices in power systems. Phasor estimation is also a pivotal part in active/reactive power metering, WAMSs [162], protection devices [163], [164], power system reliability assessment [165], power system state estimation [166], and flicker mitigation [167].

The most widely utilized algorithms for harmonic analysis are the FFT and the DFT which, however, suffer from three major pitfalls namely aliasing, picket-fence effect, and leakage [5]. The aliasing problem can be fixed by using a low-pass filter. However, the picket-fence effect and leakage phenomenon need windowing and interpolation which demand extra computation [172].

Moreover, in the emerging smart grid paradigm, both power and information flows will be bidirectional [99]. Smart meters are the information gateways in the smart grid vision realization which will be placed across the grid in millions [100]. The IEC Smart Grid Standardization Roadmap defines power quality assessment as one of the features of smart meters [101]. Installing smart meters, which are a part of the advanced metering infrastructure (AMI), should be economically feasible to widen the cost-benefit margin [99], [107], [108]. On the other hand, over their lifespan, smart meters should be able to perform possible tasks which will be defined as the smart grid concepts continue to grow. This demands sparing some of the processing power and memory at the software implementation level since they will be installed once over their lifespan. One possible solution to reduce the hardware cost and spare microprocessors' memory is to use low band-width sensors and, consequently, adopting slow sampling phasor estimation techniques which need simple hardware templates. In addition, load signature and composite studies at the macro level with sampling rates as low as one sample per cycle can capture the electrical load characteristics [102]-[106]. In this regard, the multi-rate algorithms [110] and undersampling techniques [111]-[114] can be used to enhance the estimation efficiency and reduce the computational burden on DSPs.

However, estimation latency and non-stationary characteristics of electrical loads should be considered when applying slow sampling techniques. On the other hand, smart meters use network platforms such as ZigBee, a low-speed low-rate wireless personal area network (LR-WPAN) which complies with IEEE Standard 802.15.4, to report to the data centre every 15 minutes [100], [173]-[175]. In other words, there is a

question if the high sampling frequency measurement effort is actually discarded in digesting measurements and translating data into meaningful information while aggregation methods (such as the 3-second, 10-minute, and 2-hour aggregation methods of IEC Standard 61000-4-30 [176]) are practically used at the metering level. Moreover, diagnostics and protection tasks are usually assigned to the upstream protection relays and bay control units which are equipped with powerful processors and wide bandwidth sensors. Therefore, although applying a low sampling rate creates estimation delay, its application is possible as long as it can capture the characteristics of load variations and catch up with the smart meter reporting cycle.

The objective of this chapter is to propose a real-time undersampling technique for harmonics/interharmonics and phasors estimation. The well-known staggered undersampling technique is adopted to perform the spectral estimation at a lower sampling rate than that of the Nyquist theorem. A low computational modified gradient search (MGS) algorithm is proposed for real-time power system voltage/current spectral estimation. The estimation latency of the proposed method to perform time-frequency analysis and its computational complexity in comparison with the DFT and FFT algorithms are also discussed.

Moreover, the concept of staggered undersampling is extended for synchrophasor estimation in WMASs. The proposed extended staggered undersampling reduces the estimation delay in comparison with that of the conventional staggered undersampling. The proposed synchrophasor estimation technique is based on a direct transfer of waveform samples over the communication link. The synchrophasor detection task is performed in a control/data centre. The phase-angle information is preserved within the

transferred samples given that the communication network time reference is used to time-tag the samples. This technique could assist the adoption of communication technologies, such as broadband services, to monitor events across the power distribution network synchronously. The proposed method can bypass the errors of DSP time reference synchronization. The performance principle of this technique also makes it a reliable backup option for transmission level synchrophasor detection when a global positioning system (GPS) is not viable. The correct performance of the proposed method is demonstrated by simulation results obtained with MATLAB.

The chapter is organized as follows. Section 4.2 reviews the staggered undersampling concept. Section 4.3 presents the MGS algorithm for harmonics/interharmonics estimation, and Section 4.3.1 reviews the harmonic assessment via the grouping approach. Sections 4.3.2 and 4.3.3 include simulation studies and real-time implementation results respectively. Section 4.4 presents extended staggered undersampling for synchrophasor estimation in WAMSs and the simulation evaluations. Finally, Section 4.5 concludes the chapter.

4.2. Staggered Undersampling Concept

The main idea in staggered undersampling is to manipulate sparse samples of a signal to obtain a set equivalent to the one obtained by a substantially higher sampling frequency. This equivalence is possible for periodic signals [111]. The classic theory on sampling being the Nyquist theorem states that a band-limited signal can be exactly reconstructed from samples provided that the sampling rate is greater or equal to twice the bandwidth of the signal. Slower sampling would in principle introduce deviations in

the frequency content (aliasing). This can, however, be avoided if the signal belongs to a restricted class (e.g., periodic) and samples are:

- 1) taken at instants which are carefully chosen, and
- 2) precisely manipulated before performing spectral analysis [111].

Assume that a sampling frequency of $f_s = 2\text{kHz}$ is applied to a signal to map it to the discrete time domain which means a sampling period of 0.5 ms. If the power system fundamental frequency is considered to be $f_o = 50\text{ Hz}$, $N_o = f_s / f_o = 40$ samples represent a full cycle of the sinusoidal voltage/current waveform.

Although the Nyquist theorem requires the sampling frequency to be at least twice the highest frequency component existing in the waveform, the undersampling concept states that it is possible to reduce the sampling frequency to $(2000/\Delta)\text{ Hz}$ which can be considerably lower than the Nyquist frequency and, still, extract the same frequency components which could be extracted by following the Nyquist theorem. For example, if the downsampling factor (Δ) is 19, the sampling period will be $19 \times 0.5 = 9.5\text{ms}$ which means two samples per cycle for 50 Hz power systems. As the sampling frequency will be $2000/19 = 105.2632\text{ Hz}$, extracting frequency components up to $105.2632/2 = 52.6316\text{ Hz}$ is possible according to the Nyquist theorem. However, the undersampling concept proves that if Δ and the number of samples in one cycle of the fundamental frequency (N_o) are mutually coprime, the undersampling process provides a one-to-one relationship between the signal sampled based on the Nyquist theorem (d) and the undersampled signal (d_u) [111]. The relationship between d_u and d is:

$$d_u(k) = d(k\Delta) \quad (4.1)$$

As the relationship between d_u and d is one-to-one, every frequency component in d will be mapped into one and only one frequency component in d_u and vice versa. Consequently, a careful and proper spectral decomposition on the undersampled version of a signal (d_u) gives the same result that would be achieved by analysing d .

4.3. Modified Gradient Search Algorithm for Harmonics/Interharmonics Estimation

In this section, a simple MGS algorithm is introduced to estimate harmonics/interharmonics from an undersampled signal d_u . The proposed MGS algorithm shares the main features of the well-known linear vector fitting algorithms which use gradient search; but, it also uses the rate of change in the estimation error to adapt the vector weights. At the k^{th} sampling instance, for steady-state conditions, a non-sinusoidal periodic instantaneous voltage or current waveform is represented in the discrete-time based on the frequency components as:

$$d_u(k) = S_{dc} + \sum_{l=1}^{N_G} S_l \left(\cos(\phi_l^r) \sin(2klf_r T_s) + \sin(\phi_l^r) \cos(2klf_r T_s) \right) \quad (4.2)$$

where

N_G is the order of the estimation model which is determined according to the target application and DSP capability

f_r is the frequency resolution

T_s is the sampling period which is given by $T_s = 1 / f_s$

f_s is the sampling frequency

S_{dc} is the dc offset

S_l is the amplitude of the spectral component at lf_r Hz

θ_l^G is the phase-angle of the spectral component at lf_r Hz

and the power system fundamental frequency is equivalent to $l = f_o / f_r$.

IEC Standard 61000-4-7 recommends a frequency resolution of 5 Hz to estimate harmonics and interharmonics [57].

The following linear estimation model is considered for solving eqn. (4.2) and finding its $(2N_G + 1)$ unknowns as:

$$\hat{d}_u(k) = O(k, 1:2N_G + 1)\Lambda_k(1:2N_G + 1) \quad (4.3)$$

where $\hat{d}_u(k)$ is an estimation of $d_u(k)$ and $O(k, 1:2N_G + 1)$ is the observation vector at the k^{th} sample. $\Lambda_k(2N_G + 1)$ estimates S_{dc} , $\Lambda_k(1:2N_G)$ carries estimations of the $2N_G$ unknown in-phase and quadrature components such that $\Lambda_k(2l - 1)$ estimates $S_l \cos(\theta_l^G)$ and $\Lambda_k(2l)$ estimates $S_l \sin(\theta_l^G)$ at the k^{th} sample. Elements of $O(k, 1:2N_G + 1)$ are defined as:

$$\begin{cases} O(k, 2l - 1) = \sin(2klf_r T_s) \\ O(k, 2l) = \cos(2klf_r T_s) \\ O(k, 2N_G + 1) = 1 \end{cases} \quad 1 \leq l \leq N_G \quad (4.4)$$

To find a solution for $\Lambda_k(1:2N_G + 1)$, two error functions $e_{MGS}(k)$ and $e'_{MGS}(k)$ are considered which are evaluated as:

$$e_{MGS}(k) = d_u(k) - \hat{d}_u(k) \quad (4.5)$$

$$e'_{MGS}(k) = e_{MGS}(k) - e_{MGS}(k-1) \quad (4.6)$$

where

$e_{MGS}(k)$ is the estimation error at the k^{th} sample and

$e'_{MGS}(k)$ is the rate of change in the estimation error.

The goal is to minimize $G_1(k) = 0.5(e_{MGS}(k))^2$ and $G_2(k) = 0.5(e'_{MGS}(k))^2$ through an estimation process which uses updated information coming from new samples. The steepest descent direction for line search method is applied to minimize the weighted sum of G_1 and G_2 . The steepest descent direction is a search direction which creates the biggest decrease in an objective function [132]. The steepest descent directions for G_1 and G_2 are respectively calculated as:

$$p_1(k) = -\nabla G_1(k) = -e_{MGS}(k) \frac{\partial e_{MGS}(k)}{\partial \Lambda_k} \quad (4.7)$$

$$p_2(k) = -\nabla G_2(k) = -e'_{MGS}(k) \frac{\partial e'_{MGS}(k)}{\partial \Lambda_k} \quad (4.8)$$

According to eqns. (4.3) and (4.5), $\frac{\partial e(k)}{\partial \Lambda_k}$ is calculated as:

$$\frac{\partial e(k)}{\partial \Lambda_k} = \frac{\partial d_u(k)}{\partial \Lambda_k} - \frac{\partial \hat{d}_u(k)}{\partial \Lambda_k} = -O^T(k, 1:2N_G + 1) \quad (4.9)$$

where $O^T(k, 1:2N_G + 1)$ is the transpose of $O(k, 1:2N_G + 1) \cdot e'_{MGS}(k)$ and $\frac{\partial e'_{MGS}(k)}{\partial \Lambda_k}$

can be rewritten according to eqns. (4.5) and (4.6) as follows:

$$e'_{MGS}(k) = d_u(k) - d_u(k-1) - \hat{d}_u(k) + \hat{d}_u(k-1) \quad (4.10)$$

$$\frac{\partial e'_{MGS}(k)}{\partial \Lambda_k} = \frac{\partial}{\partial \Lambda_k} (d_u(k) - d_u(k-1)) - \frac{\partial \hat{d}_u(k)}{\partial \Lambda_k} + \frac{\partial \hat{d}_u(k-1)}{\partial \Lambda_k} \quad (4.11)$$

Owing to the fact that the previous iteration estimation $\hat{d}_u(k-1)$ and the measured values of $d_u(k)$ and $d_u(k-1)$ do not change with respect to the present estimation vector Λ_k , terms $\frac{\partial}{\partial \Lambda_k} (d_u(k) - d_u(k-1))$ and $\frac{\partial \hat{d}_u(k-1)}{\partial \Lambda_k}$ on the right hand side of eqn. (4.11) are equal to zero. Therefore, eqn. (4.11) is rewritten as:

$$\frac{\partial e'_{MGS}(k)}{\partial \Lambda_k} = -\frac{\partial d_u(k)}{\partial \Lambda_k} = -O^T(k, 1:2N_G+1) \quad (4.12)$$

Eqns. (4.7)-(4.12) result in the following expressions for the search direction vectors $p_1(k)$ and $p_2(k)$:

$$p_1(k) = e_{MGS}(k)O^T(k, 1:2N_G+1) \quad (4.13)$$

$$p_2(k) = e'_{MGS}(k)O^T(k, 1:2N_G+1) \quad (4.14)$$

where $e_{MGS}(k)$ and $e'_{MGS}(k)$ are evaluated from eqns. (4.5) and (4.6) respectively. The line search algorithm is adopted to update the estimation vector as follows:

$$\Lambda_{k+1}(1:2N_G+1) = \Lambda_k(1:2N_G+1) + \alpha_1 p_1(k) + \alpha_2 p_2(k) \quad (4.15)$$

where $\Lambda_{k+1}(1:2N+1)$ is the estimated vector for the next iteration ($k+1$). α_1 and α_2 are regulating factors which are respectively found to be 0.0035 and 0.0025 through testing different values to provide a stable and fast estimation. The estimation process which is described by eqns. (4.3)-(4.6) and (4.13)-(4.15) extracts the amplitude (S_l) and phase-angle (θ_l^G) of the l^{th} spectral component as follows:

$$S_l(k) = \sqrt{\Lambda_k(2l)^2 + \Lambda_k(2l-1)^2} \quad (4.16)$$

$$\theta_l^f(k) = \begin{cases} \text{Arc tan}(\Lambda_k(2l) / \Lambda_k(2l-1)) & , \Lambda_k(2l-1) \geq 0 \\ \text{Arc tan}(\Lambda_k(2l) / \Lambda_k(2l-1)) & , \Lambda_k(2l-1) < 0 \end{cases} \quad (4.17)$$

Figure 4.1 shows the real-time MGS harmonics/interharmonics estimation algorithm.

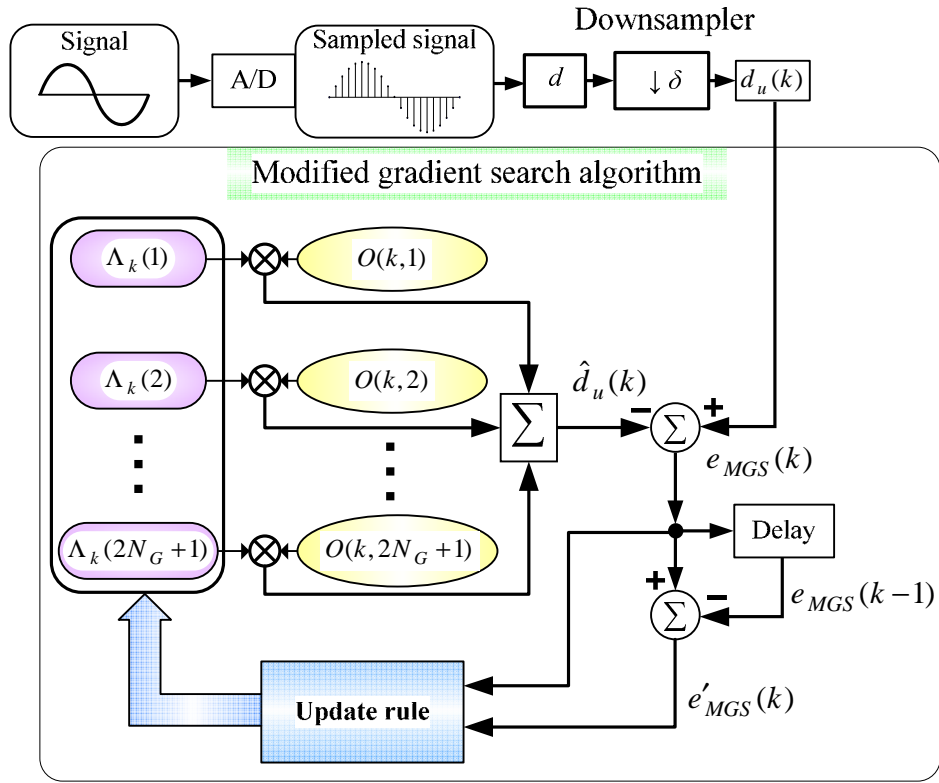


Figure 4.1. Real-time MGS harmonics/interharmonics estimation algorithm.

4.3.1. Harmonics Grouping and Smoothing

For the assessment of harmonics, the output of spectral analysis is first grouped to be the sum of squared intermediate frequencies' rms values between two adjacent harmonics according to the following formula for 50 Hz systems [57]:

$$C_g^2(k) = \left\{ \frac{S_{l-5}^2(k)}{4} + \sum_{i=-4}^{i=4} \left(\frac{S_{l+i}(k)}{\sqrt{2}} \right)^2 + \frac{S_{l+5}^2(k)}{4} \right\} \Bigg|_{l=10g} \quad (4.18)$$

where

S_l is the amplitude of a spectral component at $5l$ Hz

g is the considered harmonic group order which is corresponding to $l = 10g$ in the estimation model

C_g is the resulting rms value of the harmonic group g .

A smoothing of the signal shall be performed over the rms value C_g . The recommended smoothing filter by IEC Standard 61000-4-7 is a first-order low-pass filter with a time constant of 1.5 s as [57]:

$$\frac{1}{1.5s + 1} \quad (4.19)$$

where s is the Laplace complex variable.

Figure 4.2 shows a normalized digital realization of the above filter where $\alpha_1 = 0.0063$

and $\alpha_2 = 0.9937$.

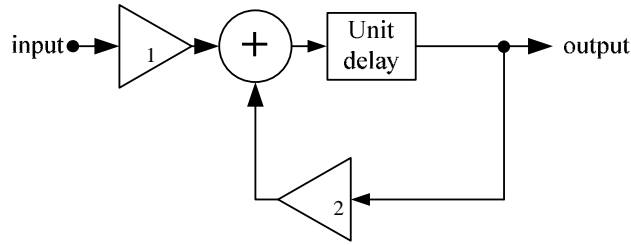


Figure 4.2. Realization of a digital smoothing low-pass filter.

4.3.2. Simulation Results

This section presents three simulation case studies in MATLAB-Simulink [177] to evaluate the performance of the proposed technique. The fundamental power system frequency is 50 Hz.

4.3.2.1. Case 1: Harmonics and Interharmonics

The signal, which is simulated in MATLAB-Simulink, is produced based on the IEC Standard 61000-4-13 definition for the second class test level [146]. The sampling frequency at which the estimation is carried out is 105.2632 Hz (the downsampling factor of 19). The simulated signal includes 1 p.u. fundamental frequency (50 Hz) with phase-angle of $\pi/3$ rad, 0.08 p.u. third harmonic with phase-angle of $2\pi/3$ rad, 0.09 p.u. fifth harmonic with phase-angle of $\pi/15$ rad, 0.03 p.u. second harmonic with phase-angle of 0.0 rad, and 0.05 p.u. of an interharmonic at 170 Hz with phase-angle of $\pi/4$ rad. The simulated signal is shown in Figure 4.3 which is captured at 200 kHz sampling frequency to mimic the analogue voltage waveform as much as possible. Figure 4.4 shows the undersampled waveform and the irregular sampling pattern which emerges because of the staggered undersampling. The estimated rms values for the fundamental frequency, harmonics and interharmonics are shown in Figure 4.5.

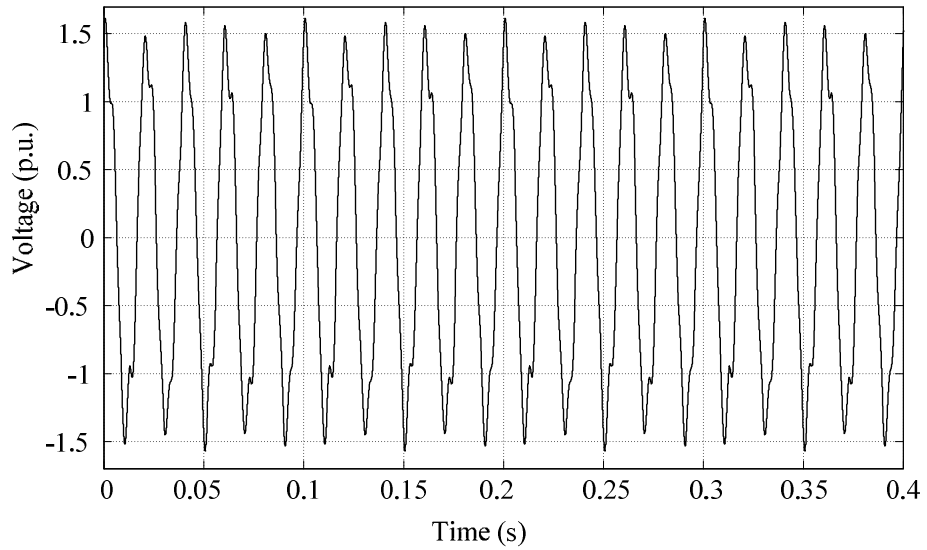


Figure 4.3. Case 1: Harmonics and interharmonics

Instantaneous voltage waveform contaminated by harmonics and interharmonics at the sampling frequency of 200 kHz.

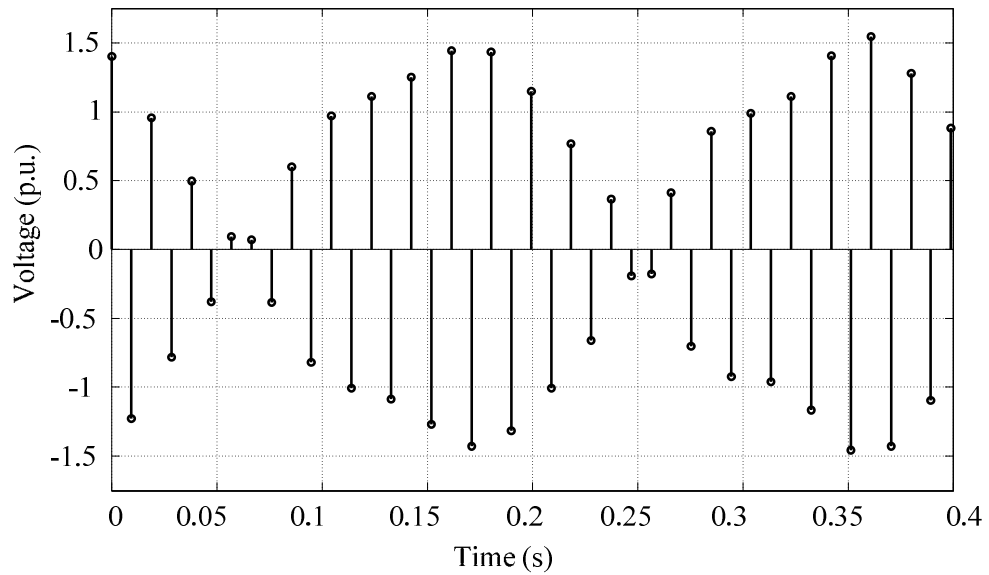


Figure 4.4. Case 1: Harmonics and interharmonics

Instantaneous voltage waveform contaminated by harmonics and interharmonics at the sampling frequency of 105.2632 Hz.

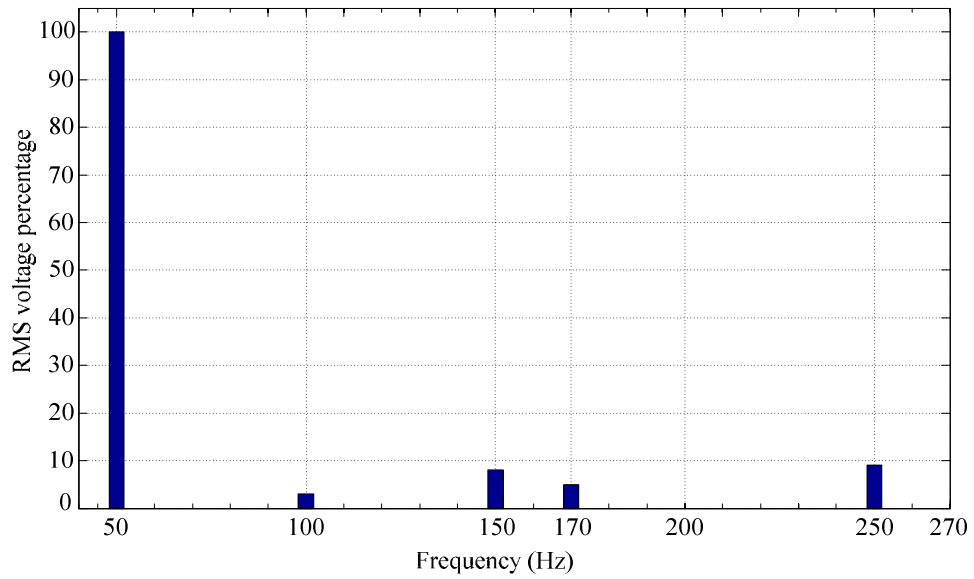


Figure 4.5. Case 1: Harmonics and interharmonics

Harmonics and interharmonics rms estimation (at 105.2632 Hz sampling frequency).

4.3.2.2. Case 2: Out-of-Resolution-Step Interharmonic Contamination

In this case, effects of a frequency component which is not an integer multiple of the frequency resolution on the fundamental frequency phasor estimation are presented. The sampling frequency at which the estimation is carried out is 105.2632 Hz (again the downsampling factor of 19). A voltage waveform is simulated which contains 1 p.u. fundamental frequency with angle of $\pi/15$ rad and 0.2 p.u. of an interharmonic at 177.5 Hz with phase-angle of $\pi/4$ rad. Figure 4.6 shows the simulated instantaneous voltage waveform and Figure 4.7 shows its undersampled version where the signal information is compressed into a few samples.

As Figure 4.8. and Figure 4.9 show, the 177.5 Hz interharmonic component, which fits in no integer multiple of 5 Hz, causes fluctuations in the estimated fundamental frequency rms voltage value and phase-angle. The fundamental frequency rms voltage estimation shows fluctuations in the range of $\pm 0.22\%$ around the actual value and the estimation of the fundamental frequency phase-angle shows fluctuations in the range of ± 0.11 degrees around the actual value.

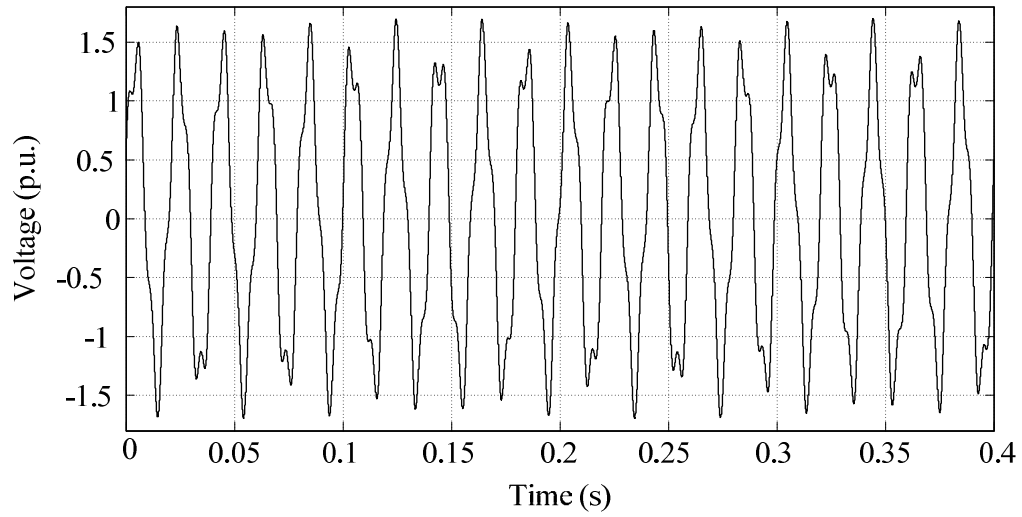


Figure 4.6. Case 2: Out-of-resolution-step interharmonic contamination

Voltage waveform contaminated by the 177.5 Hz interharmonic component at the sampling frequency of 200 kHz.

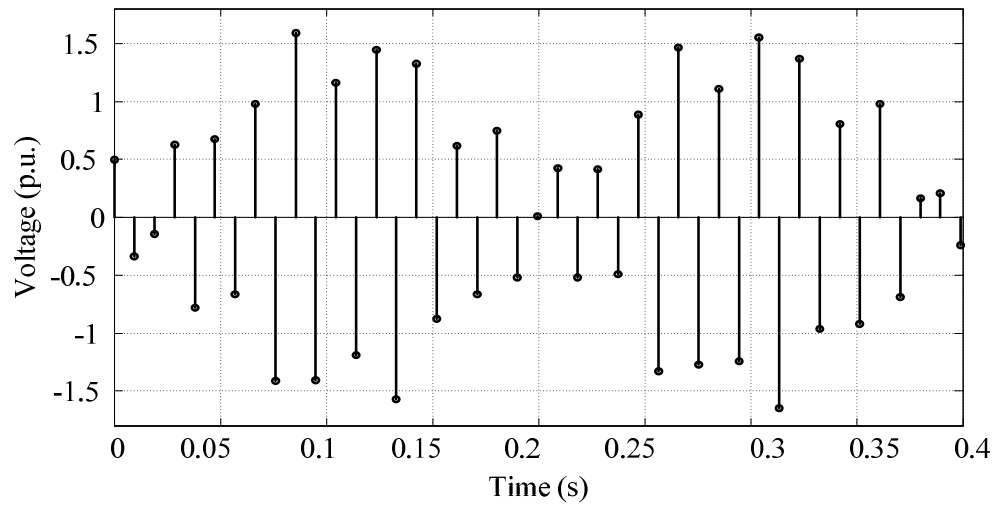


Figure 4.7. Case 2: Out-of-resolution-step interharmonic contamination

Voltage waveform contaminated by the 177.5 Hz interharmonic component at the sampling frequency of 105.2632 Hz.

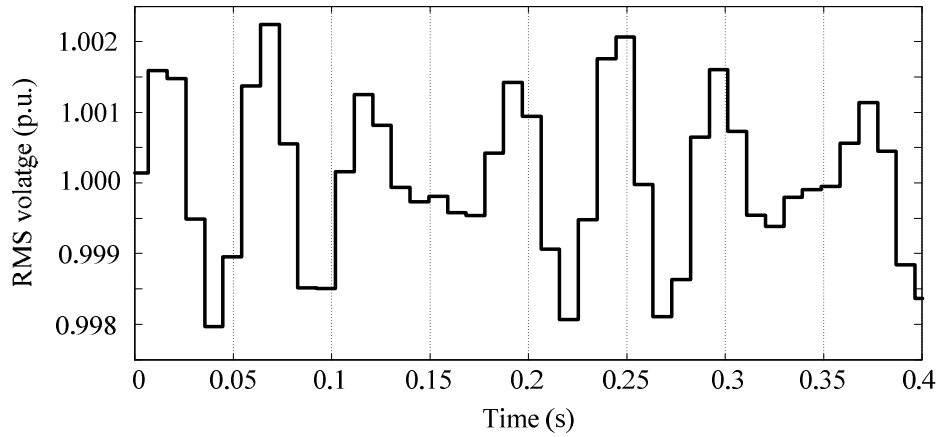


Figure 4.8. Case 2: Out-of-resolution-step interharmonic contamination

The fundamental frequency rms voltage estimation in presence of the 177.5 Hz interharmonic (at 105.2632 Hz sampling frequency).

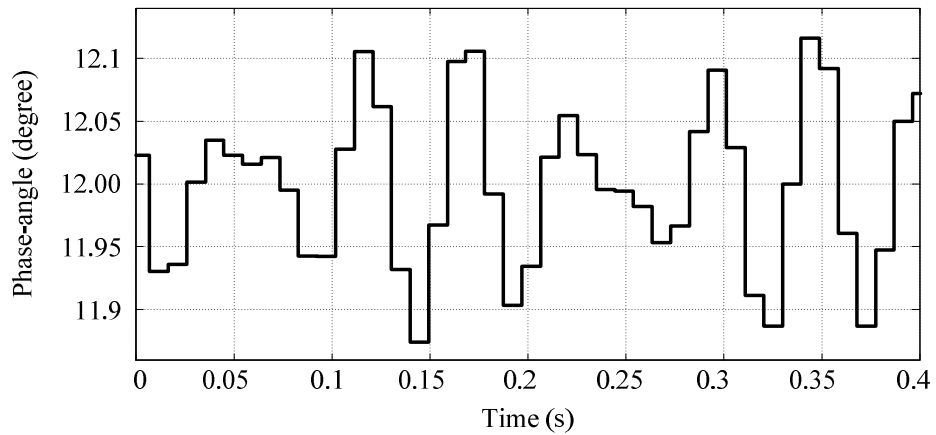


Figure 4.9. Case 2: Out-of-resolution-step interharmonic contamination

The fundamental frequency phase-angle estimation in presence of the 177.5 Hz interharmonic (at 105.2632 Hz sampling frequency).

4.3.2.3. Case 3: Non-Stationary Load and Estimation Latency

This case presents performance of the MGS algorithm to track non-stationary changes in the load current and voltage. The estimation latency of the MGS algorithm at different downsampling factors and with different frequency resolutions are also presented. The simulated non-stationary voltage and current waveforms are shown in Figure 4.10 and Figure 4.11 respectively. The estimation performance and latency are evaluated at the down sampling factors of 3 (the sampling frequency of $2000/3=666.6667$ Hz) and 19 (the sampling frequency of $2000/19=105.2632$ Hz) for the frequency resolution of 5 Hz in Figure 4.12-Figure 4.16. The estimated fundamental and harmonic voltage amplitudes are shown in Figure 4.12 and Figure 4.13. The estimated fundamental and harmonic current amplitudes are shown in Figure 4.14 and Figure 4.15. The reference active power and the estimated active power are shown in Figure 4.16. The maximum demand should be measured with less than 1% error according to IEC Standard 62052-21 [178]. The peak demand in Figure 4.16 is 0.3725 p.u. The estimated peak demand value with the downsampling factors of 19 and 3 are respectively 0.3762 p.u. (-0.98% error) and 0.3721 (0.12% error). The area under the active power curve (Figure 4.16) is the consumed energy which is billed according to the kWh price. The kWh price is cleared every 5 minutes in the Australian electricity market as an example [179]. For end-users, the electricity price remains fixed even for a much longer period depending on the regulations and the distribution retailer/operator contract with the customers. The area under the reference active power curve (which is equivalent to the energy consumption) is 18.6823 [p.u.×second], the estimated area with

the downsampling factor of 19 is 18.7230 [p.u.×second] (-0.22% error), and the estimated area with the downsampling factor of 3 is 18.7109 [p.u.×second] (-0.15% error) for the 60 s period in Figure 4.16.

As seen in Figure 4.12-Figure 4.15, the MGS algorithm tracks the changes in the current and voltage waveforms with some delays. Two defining factors for estimation latency and estimation sharpness (to track fast changes) are the downsampling factor (see Section 4.2 for definition) and the frequency resolution (Eqn. (4.2)). The estimation latency with respect to the downsampling factor (δ) and the frequency spectrum resolution (f_r) is summarised in Table 4.1. The equivalent sampling frequency for the downsampling factor of δ is $(2000/\delta)$ Hz in Table 4.1. It should be noted that the downsampling factor of 1 is equivalent to the dense sampling. As Table 4.1 shows, the estimation latency increases as the downsampling factor increases and the value of frequency spectrum resolution decreases. Therefore, the frequency spectrum resolution can be selected according to the required functions of the meter, e.g. if the aim of the measurement is to estimate harmonics (multiples of 50 Hz) the bottom row of the Table 4.1 can be referred to. If the aim of estimation is to produce high resolution frequency-domain analysis, a high frequency resolution will be assigned in the MGS model. For example, from a statistical frequency-domain point of view based on high resolution spectral estimation, the voltage flicker can be measured by extracting interharmonics [180]. Therefore, the frequency resolution of 5 Hz will be assigned in the MGS model.

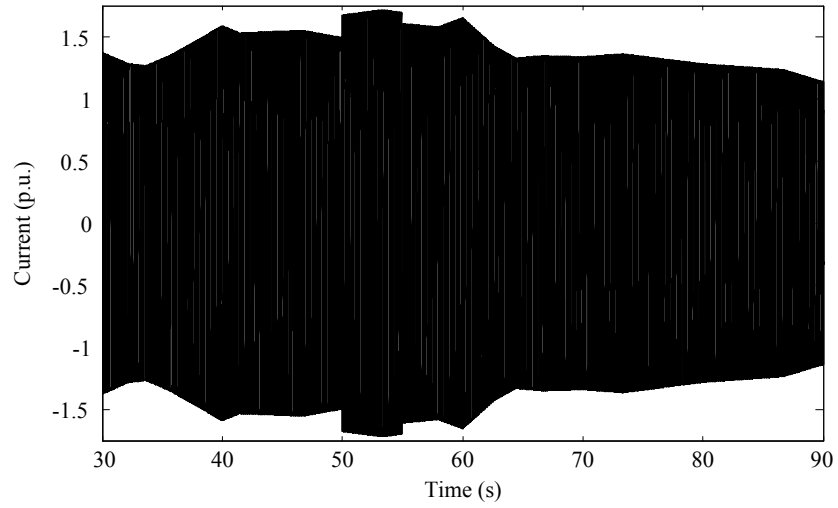


Figure 4.10. Case 3: Non-stationary load and estimation latency
Non-stationary current waveform.

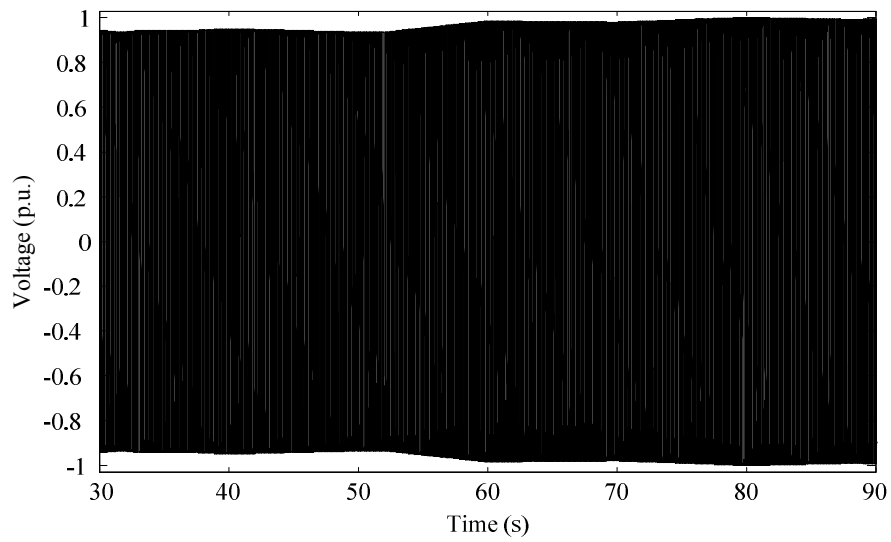


Figure 4.11. Case 3: Non-stationary load and estimation latency
Non-stationary voltage waveform.

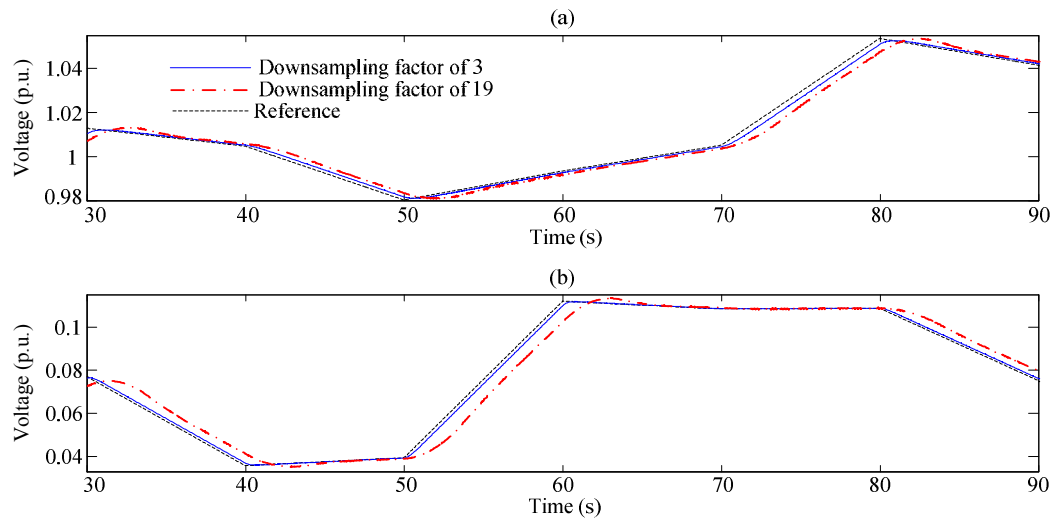


Figure 4.12. Case 3: Non-stationary load and estimation latency

(a) fundamental frequency voltage amplitude estimations at the downsampling factors of 19 and 3

(b) third harmonic voltage amplitude estimations at the downsampling factors of 19 and 3.

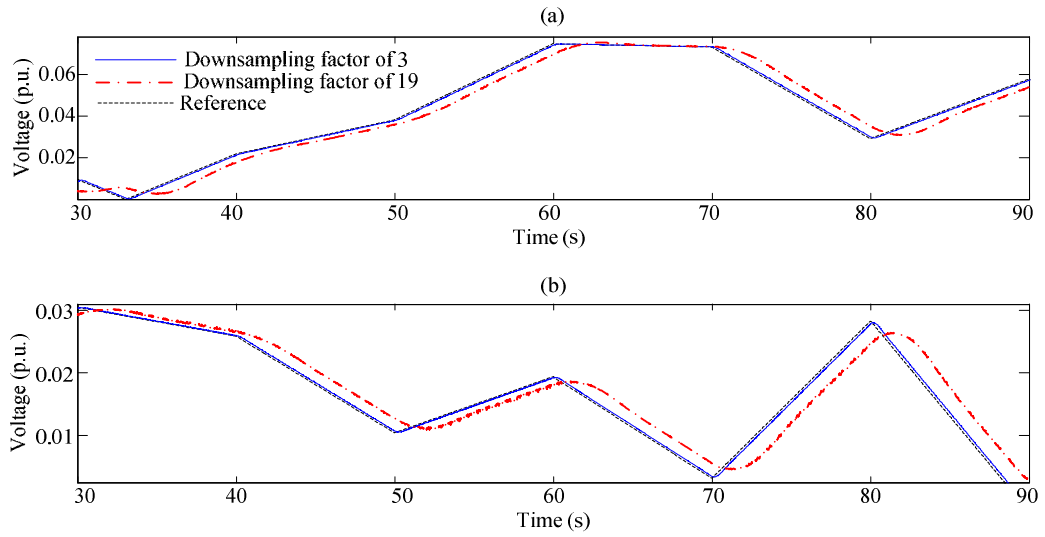


Figure 4.13. Case 3: Non-stationary load and estimation latency

(a) fifth harmonic voltage amplitude estimations at the downsampling factors of 19 and

3

(b) seventh harmonic voltage amplitude estimations at the downsampling factors of 19

and 3.

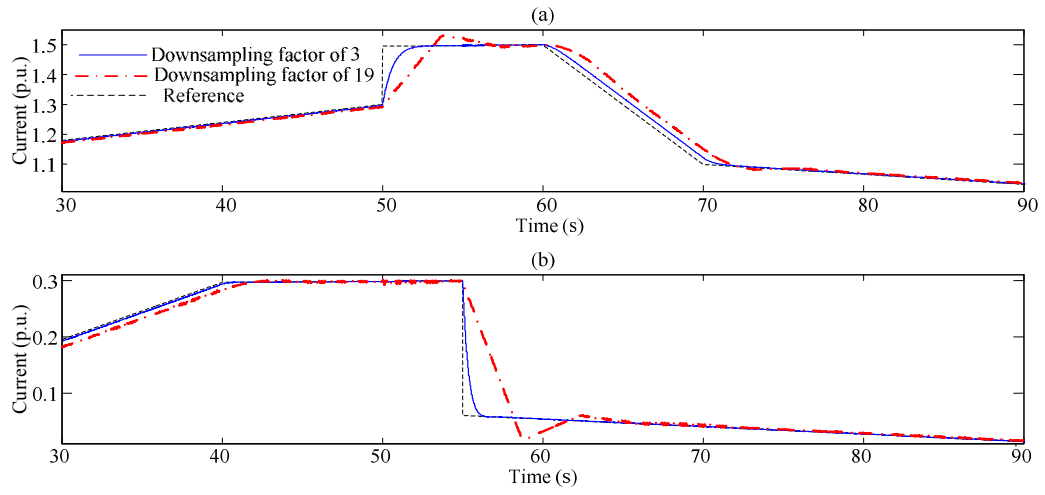


Figure 4.14. Case 3: Non-stationary load and estimation latency

(a) fundamental frequency current amplitude estimations at the downsampling factors of 19 and 3

(b) third harmonic current amplitude estimations at the downsampling factors of 19 and

3.

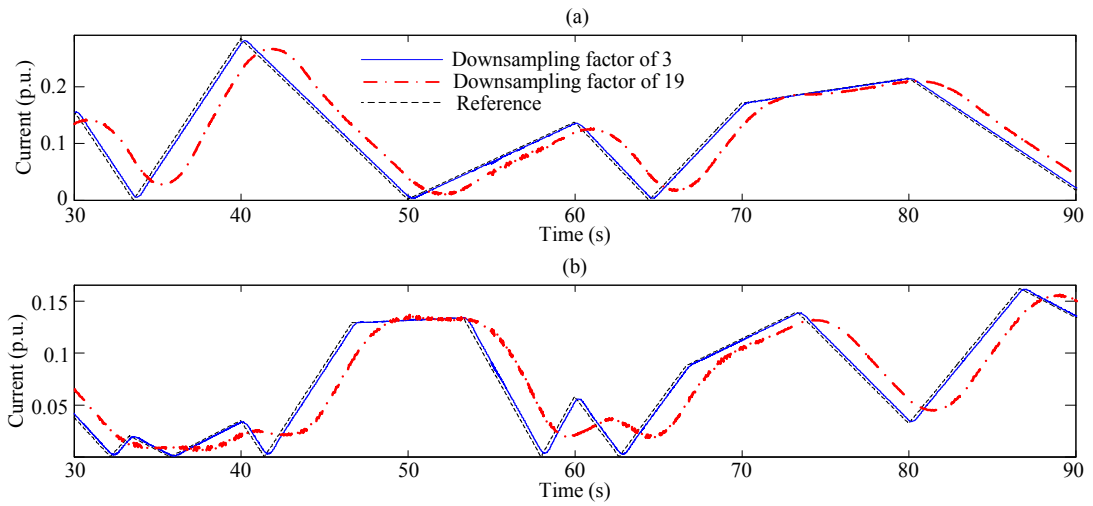


Figure 4.15. Case 3: Non-stationary load and estimation latency

(a) fifth harmonic current amplitude estimations at the downsampling factors of 19 and

3

(b) seventh harmonic current amplitude estimations at the downsampling factors of 19

and 3.

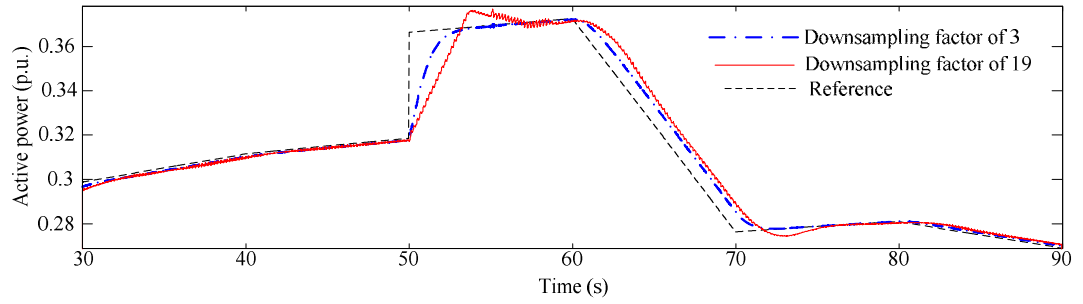


Figure 4.16. Case 3: Non-stationary load and estimation latency

Active power estimation at the downsampling factors of 19 and 3.

TABLE 4.1. ESTIMATION LATENCY FOR DIFFERENT DOWNSAMPLING FACTORS (δ) AND SPECTRAL ESTIMATION FREQUENCY RESOLUTIONS (f_r).

		Down sampling factor (Δ)							
		1	3	7	9	11	13	17	19
Frequency resolution (f_r , Hz)	5	0.20 s	0.60 s	1.40 s	1.80 s	2.2 s	2.6 s	3.40 s	3.80 s
	10	0.10 s	0.30 s	0.70 s	0.90 s	1.1 s	1.3 s	1.7 s	1.90 s
	25	0.04 s	0.12 s	0.28 s	0.36 s	0.44 s	0.52 s	0.68 s	0.76 s
	50	0.02 s	0.06 s	0.14 s	0.18 s	0.22 s	0.26 s	0.34 s	0.38 s

4.3.3. Real-Time Implementation

The real-time implementation results for the proposed MGS estimation algorithm are presented in this section. The proposed MGS estimation algorithm has been implemented on a DS1104 R&D digital control board [136]. The voltage waveforms are produced by a programmable power supply [181]. The current is sensed by a current transducer [182], and the voltage is sensed by a voltage transducer [138]. Figure 4.17 shows the schematic of the experimental setup. Some of existing metering equipment, such as ADE5166/ADE5169/ADE5566/ADE5569 energy measurement ICs, digitizes the voltage and current waveforms via a high resolution sigma-delta analogue to digital converter (ADC). This ADC outputs a signed, two's complement, 24-bit data-word [183]. The ADC, which is provided for DS1104, outputs a 12-bit signed word in the parallel mode and a 16-bit signed word in the multiplex mode [136]. Since instantaneous current and voltage waveforms should be captured simultaneously, the parallel mode with the ADC resolution of 12-bit has been used. The genuine accuracy of the proposed estimation method without the contribution of ADCs' resolution is presented in the previous section where the simulation results are presented.

The fundamental frequency is 50 Hz, the fundamental frequency rms voltage is 240 V. The sampling frequency is $2000/19=105.2632$ Hz. It may be confusing that producing this sampling frequency needs a DSP with high resolution on the sampling frequency. However, practically, the resolution on the sampling time steps is the main factor. 105.2632 Hz sampling frequency is simply the equivalence of capturing one sample out of every 19 samples from a signal which have been sampled at 2 kHz. In other words, by setting the sampling interval at $19/2000=9.5$ ms, the estimation will be

carried out at 105.2632 Hz sampling frequency. Since the time step resolution of the DS1104 board is 0.05 ms, it can easily produce the 9.5 ms time step. The MGS model order is chosen to be $N = 128$ according to the hardware and DSP limitations. This choice of model order can estimate phasors up to 640 Hz with the frequency resolution of 5 Hz. The estimation vector includes $2 \times 128 + 1 = 257$ elements in which $2 \times 128 = 256$ elements are used to estimate the in-phase and quadrature components and one element is used for dc component removal. In addition to the estimation vector, two error functions ($e_{MGS}(k)$ and $e'_{MGS}(k)$) are also used in the MGS algorithm. At the DSP implementation level, the proposed MGS algorithm requires $2 \times 128 + 1 + 2 = 259$ real multiplications and 259 real additions. The same estimation will be achieved by using either an FFT or a DFT algorithm for which the computational effort will be discussed next. The sampling frequency in the following discussion is the minimum required sampling frequency to have the bandwidth of 640 Hz (according to the Nyquist theorem) which is solely used to discuss the arithmetic operations of the FFT and the DFT algorithms. To have the same bandwidth ($128 \times 5 = 640$ Hz) and frequency resolution (5 Hz) by using the FFT algorithm, a $2 \times 128 = 256$ -point FFT algorithm is required. The aforementioned number of points ($256 = 2^8$) and frequency resolution (5 Hz) dictate the sampling frequency of $256 \times 5 = 1280$ Hz. This is also the minimum sampling frequency to have the bandwidth of 640 Hz according to the Nyquist theorem. A 256-point FFT algorithm requires $(256/2) \log_2 256 = 1024$ complex multiplications and $256 \log_2 256 = 2048$ complex additions according to the well-known radix-2 Cooley-Tukey FFT algorithm [5]. It should be noted that the number of points for the

radix-2 Cooley–Tukey FFT algorithm should be a power of 2. However, at the DSP implementation level, a complex number should be decomposed into its real and imaginary parts. Therefore, in fact, the FFT algorithm requires $2 \times 1024 = 2048$ real multiplications and $2048 \times 2 = 4096$ real additions. The DFT algorithm, at the sampling frequency of 1280 Hz, requires $1280 / 5 \times 2 = 512$ real multiplications and $2 \times (256 - 1) = 510$ real additions to extract every single frequency component at 5 Hz frequency resolution (which means a window of samples over a 200 ms time-slot according to IEC Standard 61000-4-7). Therefore, the DFT algorithm requires $128 \times 512 = 65536$ real multiplications and $128 \times 510 = 65280$ real additions to cover the 640 Hz bandwidth with the frequency resolution of 5 Hz. The recursive implementation of the DFT algorithm requires $2 \times 128 = 256$ real multiplications and 512 real additions to produce the same results. However, the recursive DFT algorithm is sensitive to the frequency variations and requires windowing and interpolation if the power system frequency changes [172], [184], [63]. On the other hand, the frequency is considered as a parameter which can be fed into the proposed MGS algorithm since it is a curve-fitting algorithm.

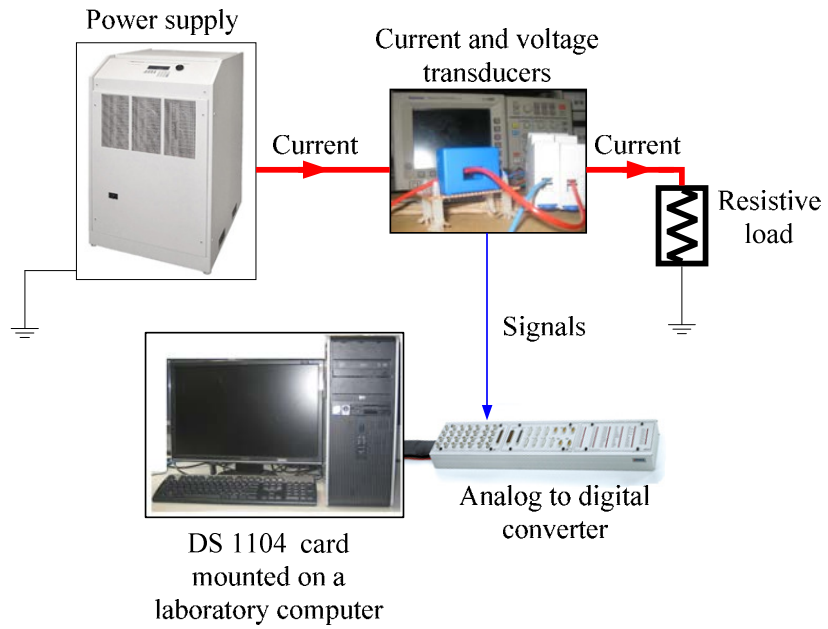


Figure 4.17. Schematic of the laboratory setup for real-time implementation.

4.3.3.1. Case 4: Quasi-Stationary Third Harmonic Variation

A 3rd harmonic fluctuating current waveform has been emulated according to one of the IEC Standard 61000-4-7 examples [57]. The 3rd harmonic voltage is produced by the programmable power supply. The produced voltage is connected to a 265 Ω resistor. The current is sensed by a current transducer to provide a signal for the digital control board input. Figure 4.18 presents the current waveform captured at the current transducer output terminal which shows a dc offset in the sensor output. Figure 4.19 shows an undersampled version of the current sensor output. Since the proposed model allocates one of the estimation vector elements for dc component estimation, it tracks the dc offset which has been added by the transducer internal operation as can be seen in Figure 4.20. The total expected rms value I_{rms} is defined as [57]:

$$I_{rms} = \sqrt{\frac{1}{N_{rms}} \sum_{l=1}^{N_{rms}} (d(l))^2} \quad (4.20)$$

where N_{rms} is the number of samples in one period of the event which are used for the calculation of rms value. Figure 4.21 shows the third harmonic group rms (C_3) estimation. The expected rms current value which is obtained by using eqn. (4.20) at 20 kHz sampling frequency is 0.6322 A and the smooth rms value calculated at 105.2632 Hz sampling frequency is 0.644 A which shows a -1.83 % error. The reason to use the 20 kHz sampling frequency to produce the expected rms value is that the DS1104 limit for the sampling frequency is 20 kHz based on our experiment in the laboratory. Since the sampled current waveform at 20 kHz is closer to the actual analogue current waveform, the rms calculation at this sampling rate has been used as

the best existing reference to compare it with the estimated value. Figure 4.22 shows the spectral estimation and the third harmonic group which is used to estimate the rms current value.

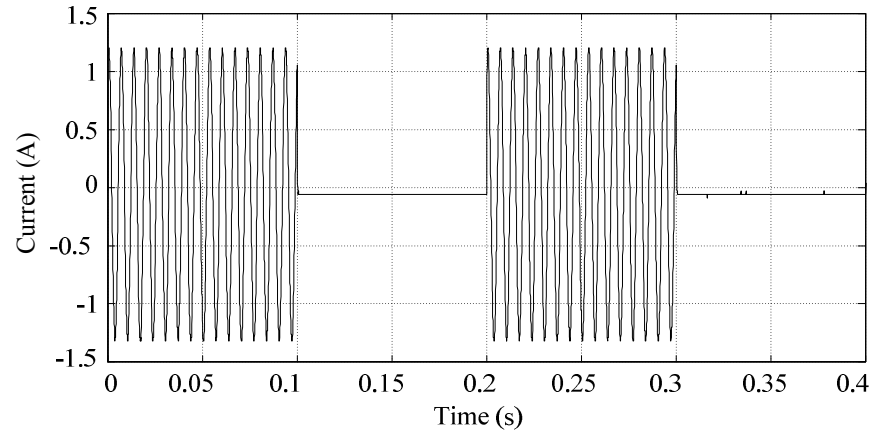


Figure 4.18. Case 4: Quasi-stationary third harmonic variation

Instantaneous current waveform sensed by a current transducer and captured by DS1104 at the sampling frequency of 20 kHz.

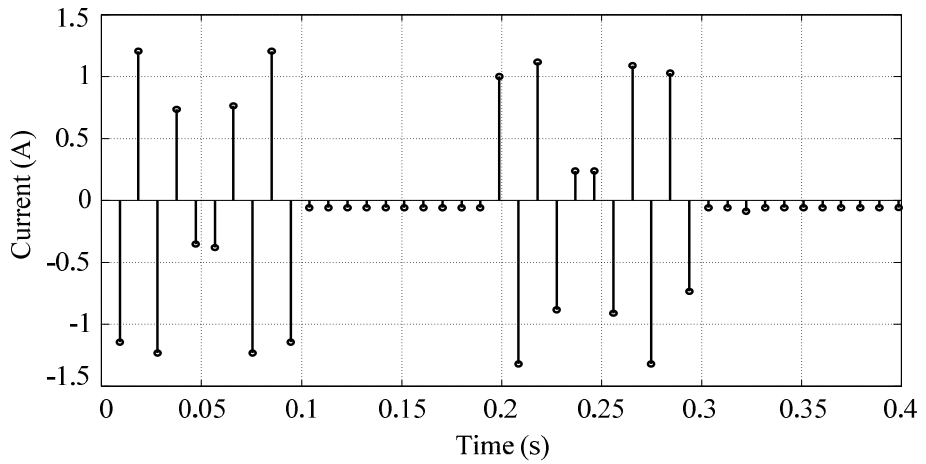


Figure 4.19. Case 4: Quasi-stationary third harmonic variation

Instantaneous current waveform sensed by a current transducer and captured by DS1104 at the sampling frequency of 105.2632 Hz.

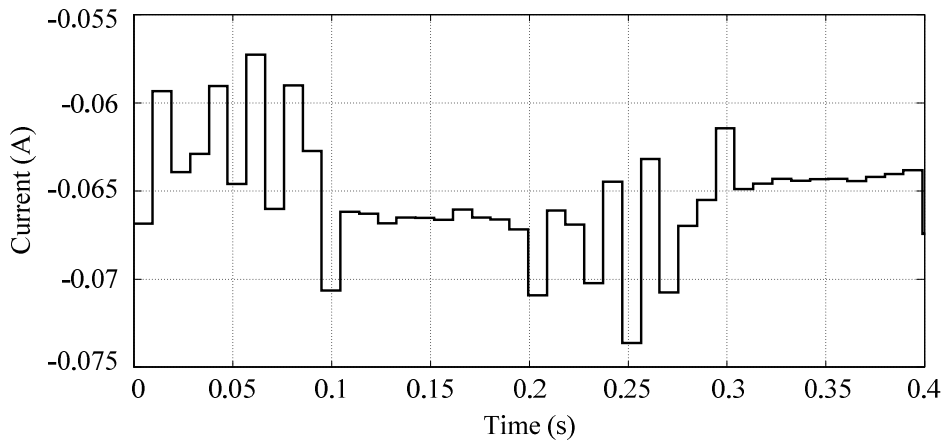


Figure 4.20. Case 4: Quasi-stationary third harmonic variation

The dc offset estimation from the current transducer output signal (at 105.2632 Hz sampling frequency).

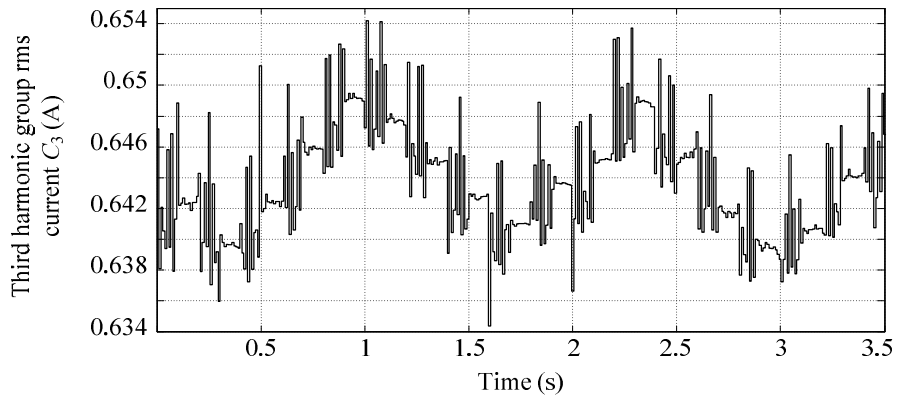


Figure 4.21. Case 4: Quasi-stationary third harmonic variation

Third harmonic group rms voltage C_3 estimation (at 105.2632 Hz sampling frequency).

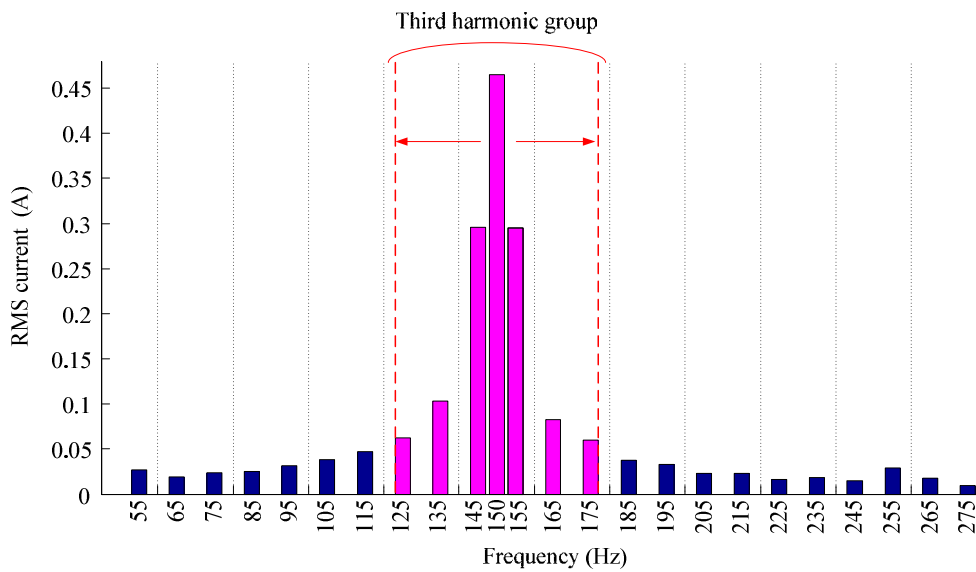


Figure 4.22. Case 4: Quasi-stationary third harmonic variation

Spectral estimation (at 105.2632 Hz sampling frequency).

4.3.3.2. Case 5: Harmonics Estimation

The programmable power supply used for real-time implementation is able to produce harmonics but cannot produce any interharmonic and this is a hardware limitation in this research. The power supply is programmed to produce a voltage waveform based on the IEC Standard 61000-4-13 definition for the third class test level as presented in Table 4.2 [146]. The produced voltage waveform which is captured by a digital oscilloscope at 250 kHz sampling frequency is shown in Figure 4.23 and its undersampled version which is captured at 105.2632 Hz sampling frequency by DS1104 is shown Figure 4.24. Table 4.2 presents the harmonics estimation results. It should be considered that the reference values in this table are the values which have been used to program the power supply. However, the power supply control system may show some errors to follow these reference values. This is a part of uncertainty in conducting the experiment. In addition, the noise created by the sensors and the power electronics switches may contaminate the samples as can be seen in Figure 4.23 .

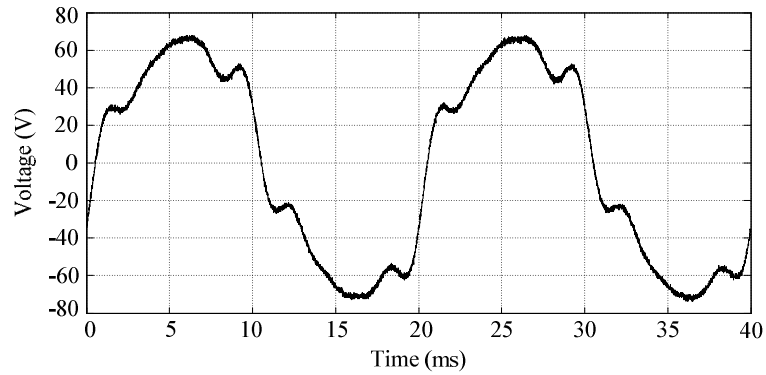


Figure 4.23. Case 5: Harmonics estimation

Line-to-neutral instantaneous voltage waveform which is captured by a digital oscilloscope at the sampling frequency of 250 kHz.

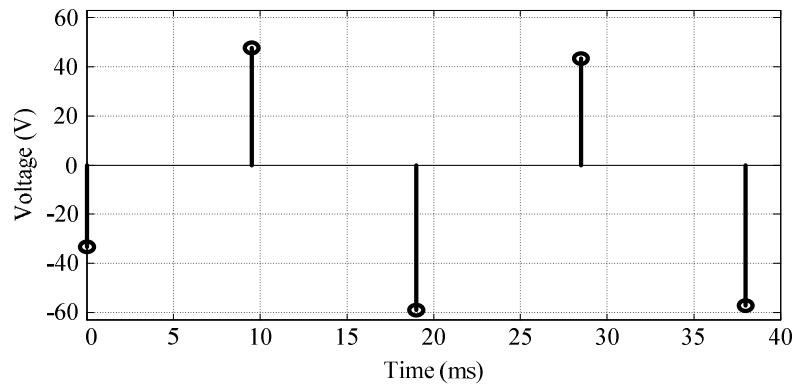


Figure 4.24. Case 5: Harmonics estimation

Undersampled line-to-neutral instantaneous voltage waveform which is captured by DS1104 at 105.2632 Hz sampling frequency.

TABLE 4.2. CASE 5: HARMONICS ESTIMATION.

Harmonic order	Reference rms value (V)	Estimated rms value(V)	Reference phase-angle (degrees)	Estimated phase-angle (degrees)
1	50.0	49.9217	0.0	0.0
2	2.5	2.4819	30.0	30.1
3	4.5	4.4618	45.0	45.3
4	1.0	0.9758	60	60.5
5	6.0	5.7771	60	60.5
7	5.0	4.6598	90.0	91.1
9	2.0	1.7961	120.0	122.0

4.3.3.3. Case 6: Desktop Personal Computer Load

The total current of a desktop personal computer (PC) and a liquid crystal display (LCD) monitor is captured to estimate the fundamental frequency current amplitude, active power and reactive power. The voltage waveform of the outlet to which the PC and LCD are connected has also been captured. The estimation has been done by using two MGS algorithm implementation options from Table 4.1. The MGS algorithm has been implemented for the downsampling factor of 19 (the sampling frequency of 2000/19 Hz) with the frequency resolution of 50 Hz (multiples of 50 Hz) and the dense sampling (the sampling frequency of 2 kHz) with the frequency resolution of 5 Hz (multiples of 5 Hz). IEC Standard 61000-4-7 recommends the sliding window DFT method, which uses a sliding window with the fixed length of 200 ms for 50 Hz power systems, for harmonics/interharmonics estimation. The 200 ms sliding window DFT algorithm has been implemented in this case for comparison. The dense sampling at 2 kHz is used for the sliding window DFT algorithm to avoid delays due to downsampling. Figure 4.25 and Figure 4.26 show the captured current and voltage waveforms. Figure 4.27, Figure 4.28, Figure 4.29, and Figure 4.30 show the estimated fundamental frequency current amplitude, voltage amplitude, active power, and reactive power respectively. The total active energy estimations, for the snapshot of Figure 4.29, by the DFT algorithm, the MGS algorithm at the downsampling factor of 19 with 50 Hz frequency resolution, and the dense sampling MGS algorithm with 5 Hz frequency resolution are respectively 2184.6 [W×second], 2185.9 [W×second], and 2171 [W×second]. The total reactive energy estimation, for the snapshot of Figure 4.30, by the DFT algorithm, the MGS algorithm at the downsampling factor of 19 with 50 Hz

frequency resolution, and the dense sampling MGS algorithm with 5 Hz frequency resolution are respectively -775.3 [VAr×second], -786.4 [VAr×second], and -772.2 [VAr×second].

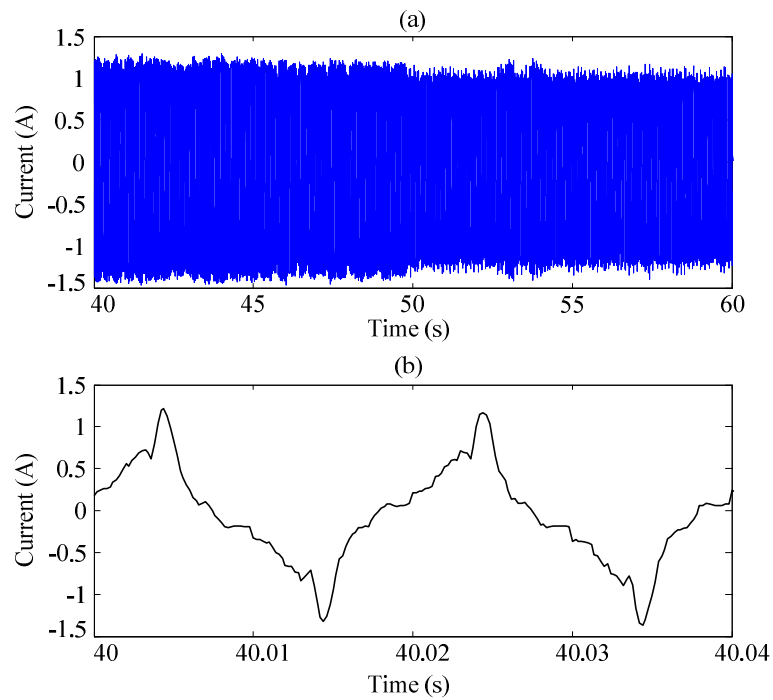


Figure 4.25. Case 6: Desktop personal computer load

(a) current waveform

(b) a magnified section of the current waveform.

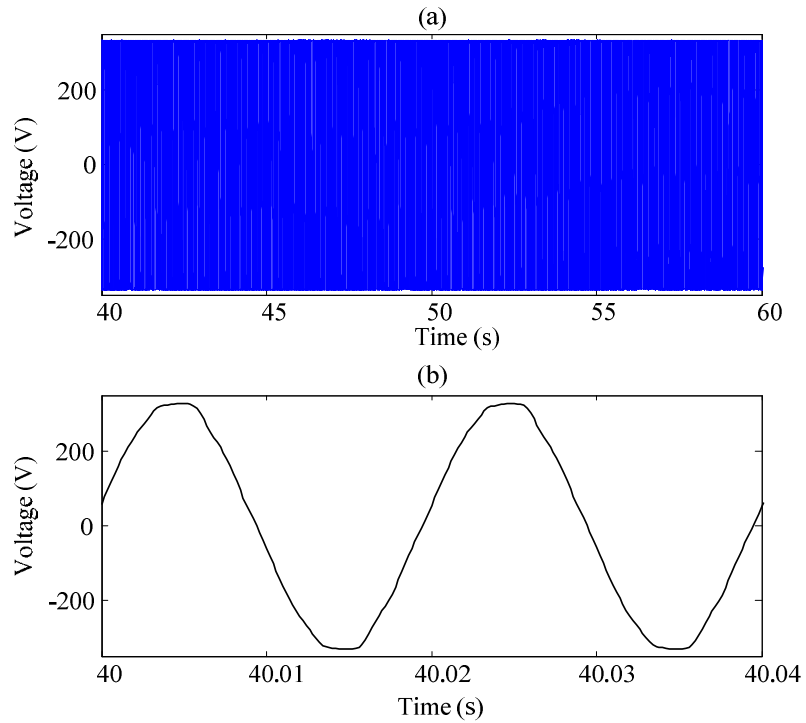


Figure 4.26. Case 6: Desktop personal computer load

(a) phase-to-neutral voltage waveform

(b) a magnified section of the phase-to-neutral voltage waveform.

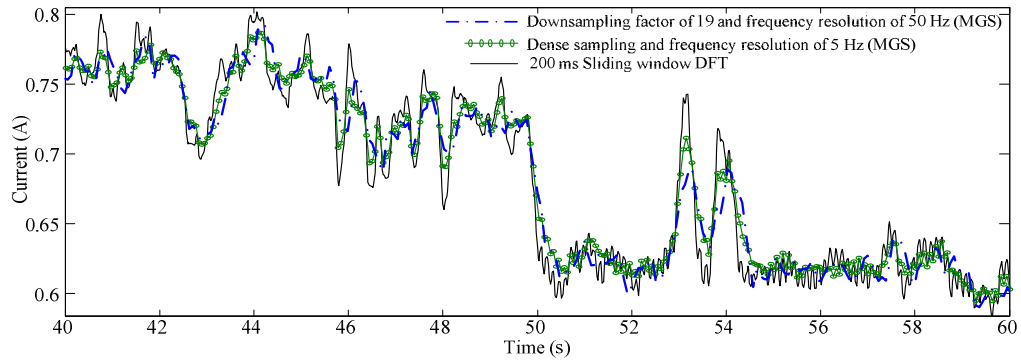


Figure 4.27. Case 6: Desktop personal computer load

The fundamental frequency current amplitude estimation.

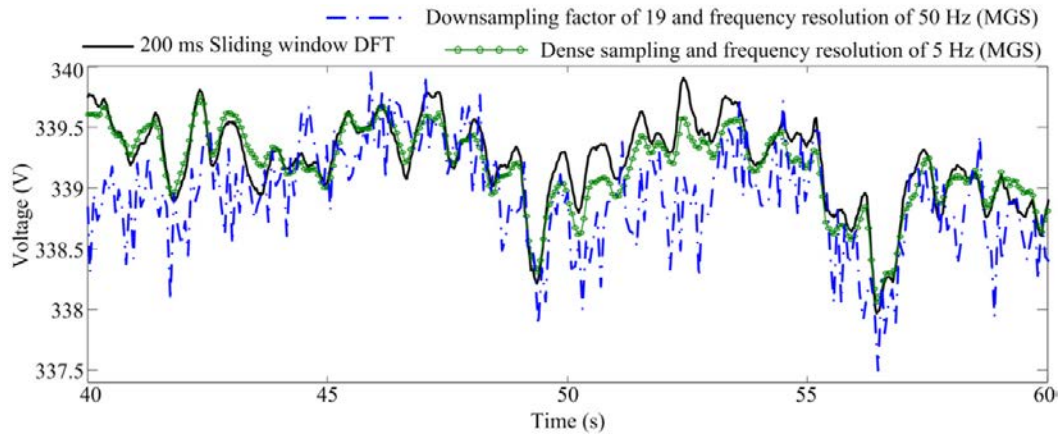


Figure 4.28. Case 6: Desktop personal computer load

The fundamental frequency voltage amplitude estimation.

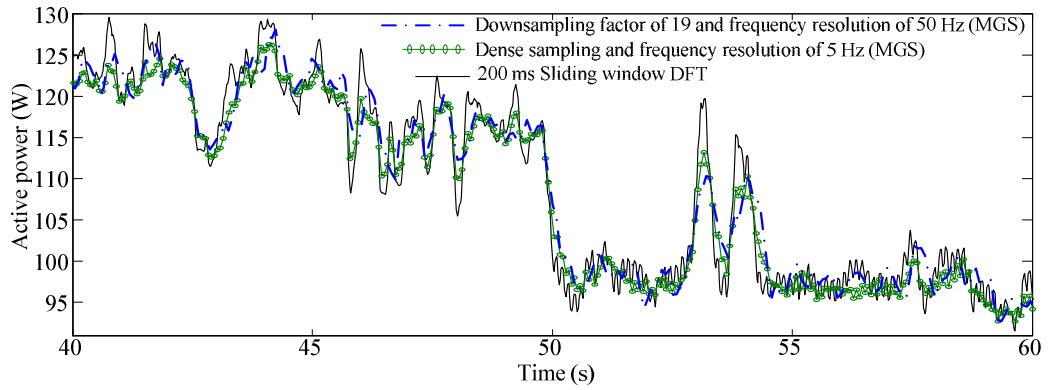


Figure 4.29. Case 6: Desktop personal computer load

Active power estimation.

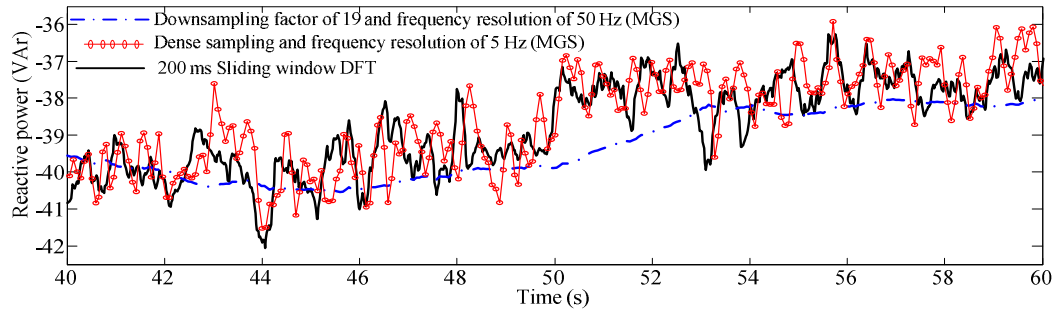


Figure 4.30. Case 6: Desktop personal computer load

Reactive power estimation.

4.4. Extending the Undersampling Concept for Synchrophasor Estimation in Wide-Area Measurement Systems

Recent developments in wide-area measurements systems (WAMSs) present opportunities for more applications to utilize them to improve flexible AC transmission system (FACTS) controllers performance [37], voltage security [38], state estimation [39], wind generation integration to power transmission systems [40], power system model validation [41], and protection schemes [42]. In principle, WAMSs rely on phasor measurement units (PMUs) to collect synchrophasor data across the transmission network.

Moreover, power flow may become bidirectional within distribution networks and

upstream transmission systems under the smart grid paradigm due to high penetration of distributed generation [185], [99]. PMU applications at distribution level offer a higher visibility to manage power flows through fault event monitoring [186], synchronous harmonics detection [187], state estimation [188], and islanding detection [152].

However, communication delays [189], [190], inter-operation of a multi-supplier PMU system [191], PMU installation cost [162], and system reliability [192] are some of the technical challenges in realizing real-time WAMSs applications in power systems.

The communication link delays, which range from 100 ms for fibre optics to 700 ms for satellite links, are generally attributed to the fixed delay, data rate, propagation delay, and random delay jitters [190]. The delays associated with data rate will be continually changing as utilities move towards using state-of-art technologies such as fibre optics and broadband services [193]-[195].

A number of techniques have also been proposed to compensate for the delays associated with the limitation on data rate including application of the predictor-corrector [37] and the power oscillation damping (POD) [196].

Phase-angle estimation accuracy [197], different methods used by individual vendors for data windowing, input filtering, phasor calculation, and anti-aliasing filter phase-shift compensation are challenges of interoperability even considering the most fundamental parts of WAMSs being the PMUs [191], [195], [198].

The PMU installation cost ranges between \$10k to \$70k depending upon the utility, location, and availability of communications [162]. Alternative sources of synchrophasor measurement can be digital distance relays since the additional cost

associated with equipping a distance relay with synchrophasor detection is negligible when compared with an ordinary digital relay [199]. However, since time synchronization is the secondary function of global positioning system (GPS), both PMUs and digital relays are at the mercy of service provided for the primary navigation functions of GPS to receive reliable synchronization on a wide bandwidth in the long-term [145].

The objective of this section is to propose a new synchrophasor estimation technique based on direct transfer of waveform samples over the communication link to the control/data centre, where the synchrophasor estimation task is performed. In the proposed technique, the transferred data are time-tagged with respect to the communication link time reference which can be finally synchronized to a common time reference e.g. universal time coordinate (UTC). The concept of staggered undersampling has also been extended to estimate the synchrophasors from the samples which have been collected at the communication link data rate. The extended staggered undersampling technique reduces the estimation latency of conventional staggered undersampling.

The advantages of this technique are bypassing the DSP clock synchronization errors and preserving time-domain characteristics (e.g. phase-angle and frequency). The presented technique, which relies on the communication link time-tagging, also lays the basis of a bottom-up approach to gain an insight into the transmission system events by observing the distribution network under the bidirectional power/data flow smart grid paradigm [101]. Its implementation requirements are what the residential area broadband internet services can already offer, e.g. event detection and frequency

estimation described in [186], [200]. As an example, the national broadband network (NBN) will be developed mainly on fibre optics communications across Australia [201]. Since the fibre optics can deliver reliable synchronism at the accuracy of $1\mu\text{s}$ or better, it meets the IEEE Standard C37.118 criterion as a source of time-tagging [145].

4.4.1. Synchrophasor Definition

The synchrophasor representation X_s of a the waveform $d(t_k)$ is the complex value in the following form [145]:

$$X_s = X_r + jX_i \quad (4.21)$$

$$X_r = \frac{X_m}{\sqrt{2}} \cos(\theta_s) \quad (4.22)$$

$$X_i = \frac{X_m}{\sqrt{2}} \sin(\theta_s) \quad (4.23)$$

The time-domain waveform $d(t_k)$ for which X_s is the phasor representation is defined as follows:

$$d(t_k) = X_m \cos(\Omega_o t_k + \theta_s) \quad (4.24)$$

where

$t_k = kT_s$ is the discrete time instance of observation

k is the sampling index

T_s is the sampling period

Ω_o is the power system angular frequency, and

$X_m / \sqrt{2}$ is the rms value of waveform $d(t_k)$

θ_s is the instantaneous phase-angle relative to a cosine function at nominal system frequency synchronized to UTC.

This angle is defined to be 0° when the maximum of x occurs at the UTC second rollover (1 pulse per second (PPS) time signal), and -90° when the positive zero crossing occurs at the UTC second rollover.

Synchrophasor measurements shall be synchronized to UTC with accuracy sufficient to meet the accuracy requirements of IEEE Standard C37.118 [145]. The system must be capable of receiving time from a highly reliable source which can provide sufficient time accuracy to keep the total vector error (TVE) within the $\pm 1\%$ limits [145]. Therefore, the time reference of the PMU should be synchronized with UTC to extract the correct phase-angle θ_s from x .

The most common technique for determining the phasor representation of an input signal is to use data samples taken from the waveform and apply the DFT to compute the phasor [162]. The DFT can be used to estimate the values of X_r and X_i for which their relationship with θ_s and X_m is defined by (4.22) and (4.23).

If the difference between the DSP internal clock and UTC is T_d , \hat{X}_r and \hat{X}_i will be calculated by using DFT as follows:

$$\hat{X}_r = \frac{\Omega_o}{2\sqrt{2} T_s} \sum_k^{k-N_o+1} d(t_k) \cos(\Omega_o(t_k - T_d)) \quad (4.25)$$

$$\hat{X}_i = -\frac{\Omega_o}{2\sqrt{2} T_s} \sum_k^{k-N_o+1} d(t_k) \sin(\Omega_o(t_k - T_d)) \quad (4.26)$$

where \hat{X}_r and \hat{X}_i are estimates of X_r and X_i respectively. $N_o = 2 / (\Omega_o T_s)$.

Equations (4.25) and (4.26) are simplified according to the trigonometric identities as follows:

$$\hat{X}_r = \frac{X_m}{\sqrt{2}} \cos(\theta_s + \Omega_o T_d) \quad (4.27)$$

$$\hat{X}_i = \frac{X_m}{\sqrt{2}} \sin(\theta_s + \Omega_o T_d) \quad (4.28)$$

As seen from (4.27) and (4.28), the estimated phase-angle is offset by $(\Omega_o T_d)$. The values of \hat{X}_r and \hat{X}_i only estimate the correct corresponding values for X_r and X_i if T_d becomes zero. When the PMU clock is synchronized to UTC, T_d becomes zero and phase-angle estimation is correct. The synchronization is achieved by using a sampling clock which is phase-locked to the one-pulse-per-second signal provided by a GPS receiver. The receiver may be built in the PMU, or may be installed in the substation and the synchronizing pulse distributed to the PMU and to any other device which requires it [162]. Therefore, onsite synchrophasor estimation accuracy depends on how precise the time synchronism is performed at the PMU or substation location. This poses a real challenge for interoperability in multi-supplier PMU systems [191].

4.4.2. Extended Staggered Undersampling for Synchrophasor Detection

The proposed synchrophasor detection technique is based on direct transfer of instantaneous waveform samples through the communication link. The synchrophasor detection is carried in the control/data centre.

Although the limitation on the data rate portrays a delay in the time-domain [190], it

is seen as slow sampling observation of an event from the frequency-domain perspective in the proposed technique. The main idea is to collect the samples of voltage/current waveforms at the communication link data rate and time-tag them according to the communication system time reference to perform the synchrophasor estimation at the control/data centre. The advantage of this approach is that the time synchronization is not required at the point of measurement but the synchronization happens once at the control/data centre.

Although the dedicated WAMS infrastructure typically uses a data rate of 25 to 60 samples per second (25-60 Hz) [37], [145], the sampling frequency to extract a phasor from a 50 Hz waveform should be higher than 100 Hz (100 samples per second) according to the Nyquist-Shannon theory. Therefore, using the communication link data rate requires considering an undersampling technique to avoid the aliasing phenomenon. The delays associated with phasor and frequency estimation from an undersampled waveform have been characterised in Section 4.3.2.3 of this chapter.

The challenges to extract synchrophasors from waveform samples captured at the rate of communication link are considering the effect of time reference and reducing the delay of undersampled phasor detection as the following subsections will discuss.

4.4.2.1. Effect of Time Reference

As mentioned in Section 4.4.1, synchrophasors detection depends on the correct time reference. This subsection presents the mathematical justification to show that the instantaneous waveform of fundamental frequency component reconstructed by the DFT technique carries the correct phase-angle independently of the time reference of

the DSP. The same concept but a different technique has recently been proposed for distribution level synchrophasor monitoring in [152].

The instantaneous waveform of fundamental frequency component can be reproduced by using values of \hat{X}_r and \hat{X}_i at the point of measurement where there is a time difference of T_d between the DSP clock and UTC as follows:

$$\hat{d} = \sqrt{2} \left(\hat{X}_r \cos(\omega_o(t_k - T_d)) - \hat{X}_i \sin(\omega_o(t_k - T_d)) \right) \quad (4.29)$$

where \hat{d} is the estimate of $d(t_k)$. Substituting \hat{X}_r and \hat{X}_i from (4.27) and (4.28) results in the following equation:

$$\hat{d} = X_m \cos(\omega_s + \omega_o T_d) \cos(\omega_o(t_k - T_d)) - X_m \sin(\omega_s + \omega_o T_d) \sin(\omega_o(t_k - T_d)) \quad (4.30)$$

Simplifying the above equation by applying the angle sum identity results in :

$$\hat{d} = X_m \cos(\omega_o t_k - \omega_o T_d + \omega_s + \omega_o T_d) \quad (4.31)$$

and therefore:

$$\hat{d} = X_m \cos(\omega_o t_k + \omega_s) \quad (4.32)$$

Comparing (4.32) with (4.24) shows that they are identical. Therefore, the reproduced waveform \hat{d} has the same rms value and phase-angle as the original waveform $d(t_k)$ independent of the DSP time reference. This property allows direct estimation of phase-angle and rms values from the waveform samples collected from the point of measurement without onsite synchronization of the DSP clock to UTC. If samples are collected and time-tagged based on the communication system clock, the only place which requires synchronization to UTC is at the centre which performs the control and

monitoring procedures. This approach bypasses the errors associated with synchronizing the DSP clock to UTC. This is beneficial especially in the case of multi-device/multi-supplier systems since the samples of \hat{d} provided by PMUs, remote terminal units (RTUs), intelligent electronic devices (IEDs), and digital relays carry the correct phase-angle and rms values whether their time reference is synchronous to UTC or not.

4.4.2.2. Extended Staggered Undersampling

Since the rate at which the waveform samples can be transferred to the control/data centres is considerably below what Nyquist-Shannon theory requires, the extended staggered undersampling is proposed for synchrophasor estimation in this chapter.

Consider a periodic waveform at the power system fundamental frequency of f_o . It is assumed that harmonics higher than $(N_o/2-1)$ have been completely eliminated by a pre-filtering stage. Therefore, the sampling frequency of $f_{N_o} = N_o f_o$ can be used according to the Nyquist-Shannon theory to extract the waveform phasor. f_{N_o} is called the dense sampling frequency. Therefore, in the dense sampling, samples are taken every $1/f_{N_o}$ seconds. One period of the densely sampled waveform is represented by $N_o = f_{N_o} / f_o$ in the discrete-time domain to perform DFT.

The main idea in the staggered undersampling is to manipulate sparse samples of a waveform to obtain an equivalent set to the one obtained by dense sampling. The staggering undersampling is based on taking samples every Δ/f_{N_o} seconds such that Δ and N_o are mutually coprime integers. Δ is called the downsampling factor.

Applying the undersampling factor of Δ means that a lower sampling frequency is applied to estimate phasors. The undersampled values can be shuffled such that they can provide the image of one period of the signal [111]. The required shuffling maps the p^{th} sample of the undersampled waveform to the n^{th} position according to the following equation:

$$n' = (p'\Delta) \bmod(N_o) \quad (4.33)$$

where $(p'\Delta) \bmod(N_o)$ denotes the positive remainder of $(p'\Delta)$ divided by N_o . p' , n' , Δ , and N_o are integer numbers. A shuffling map for the case of $f_N = 2\text{kHz}$, $N_o = 40$, and $\Delta = 7$ for a waveform contaminated by the third harmonic is schematically exemplified in Figure 4.31.

The proposed extended staggered undersampling is based on considering the particular case of synchrophasor estimation from the reconstructed waveform of \hat{d} which is produced by using (4.25), (4.26), and (4.29). Since the waveform of \hat{d} only contains the fundamental frequency, choosing $N_o = 4$ is applicable to define the dense sampling frequency of $f_{N_o} = 4f_o$. The downsampling factor Δ can be any odd integer i.e. $\Delta \in \{3, 5, 7, \dots\}$. Using an undersampled waveform for real-time estimation will introduce an estimation delay proportional to the downsampling factor as discussed and characterized in Section 4.3.2.3. The delay associated with the downsampling factor of Δ is $\frac{\Delta}{f_o}$ seconds for phasor estimation according to Table 4.1.

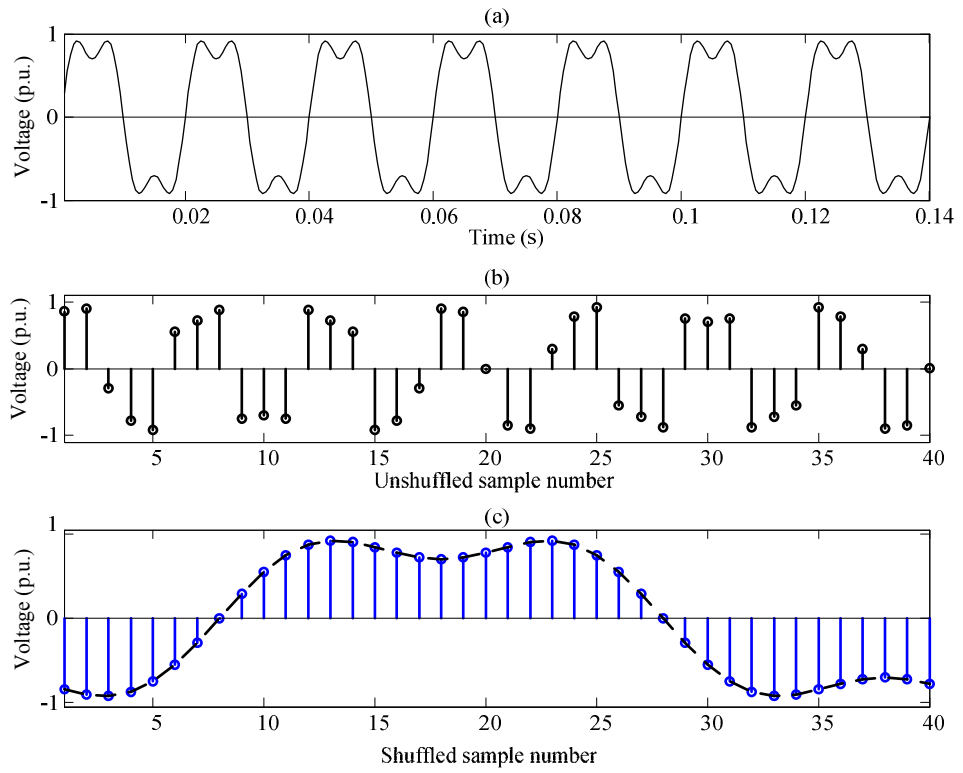


Figure 4.31. (a) Voltage waveform contaminated with the 3rd harmonic

(b) undersampled unshuffled waveform

(c) shuffled map of undersampled waveform.

Therefore, although using a bigger downsampling factor reduces the required data rate, it creates a bigger delay which degrades the time-resolution for event detection. The introduced extended staggering undersampling technique presents a solution to reduce the estimation delay.

The index map of (4.33) can be rewritten in the following form for the specific case of $N_o = 4$;

$$n' = (p'\Delta) \bmod(4) \quad (4.34)$$

This mapping presents a one-to-one relationship [111]. Proof of this one-to-one relationship will be revisited next by extending the concept of staggered undersampling.

Consider two values of p'_1 and p'_2 which are hypothetically mapped to the same position of n' as follows:

$$\begin{cases} n' = (p'_1\Delta) \bmod(4) \\ n' = (p'_2\Delta) \bmod(4) \end{cases} \quad (4.35)$$

Therefore:

$$(p'_1\Delta) \bmod(4) = (p'_2\Delta) \bmod(4) \quad (4.36)$$

$$(p'_1\Delta - p'_2\Delta) \bmod(4) = 0 \quad (4.37)$$

Since Δ is an odd integer and the solution space (SP) for both p'_1 and p'_2 is $SP = \{1, 2, 3, 4\}$, the only solution for (4.37) is that $p'_1 = p'_2$. This proves that the undersampling and the subsequent shuffling map are in a one-to-one relationship.

To extend the concept, (4.37) can be rewritten as:

$$(p'_1 - p'_2)\Delta = 4Q' \quad (4.38)$$

and reconfigured as:

$$(p'_1 - p'_2) \frac{\Delta}{2} = 2Q' \quad (4.39)$$

where Q' is an integer number which fits in the above equality. Eqn. (4.39) is indeed another presentation of (4.37) which has the same solution over SP . Since the solution $p'_1 = p'_2$ is the only solution for (4.37) over SP , this solution is valid over any subset of SP . $SP_1 = \{1, 2\}$ is a subset of SP on which the solution $p'_1 = p'_2$ is also valid. Therefore, solving (4.39) is equivalent to solving the following equation set over SP_1 :

$$\begin{cases} n' = (p'_1 \frac{\Delta}{2}) \bmod(2) \\ n' = (p'_2 \frac{\Delta}{2}) \bmod(2) \end{cases} \quad (4.40)$$

Interpretation of the above equation set is that the undersampling factor is $\frac{\Delta}{2}$ for the signal representation by $N_o = 2$ samples. In other words, the undersampling can be carried out for the dense sampling frequency of $f_{N_o} \Big|_{N_o=2} = N_o f_o = 2f_o$ and the undersampling factor of $\Delta' = \frac{\Delta}{2}$ if Δ is an odd integer. The only solution for (4.40) is the same solution for (4.37) which is $p'_1 = p'_2$. Therefore, the undersampling and shuffling map create a one-to-one relationship.

This justification means that the downsampling factor can be reduced to half of any odd integer number i.e. $\Delta' \in \left\{ \frac{3}{2}, \frac{5}{2}, \frac{7}{2}, \dots \right\}$ under the following conditions:

- (1) the waveform is band-limited to f_o ; and,

(2) the dense sampling frequency is $f_{N_o}' = 2f_o$.

Since waveform of \hat{d} has been pre-filtered and only contains the fundamental frequency component, it meets the former requirement. Therefore, sampling \hat{d} every $\frac{\Delta'}{2f_o}$ seconds meets the requirements to apply the proposed extended staggered undersampling. Application of the fractional undersampling factor Δ' reduces the phasor estimation delay to half of what would be imposed by the integer downsampling factor Δ .

4.4.2.3. Proposed Synchrophasor Detection Technique

The data message format for synchrophasor applications is defined by the IEEE Standard C37.118 which allocates 4 bytes to each synchrophasor in the rectangular format [145]. The first two bytes contain the real part of the phasor X_r and the second two bytes contain the imaginary part X_i . Figure 4.32 (a) shows the data frame when the synchrophasor is estimated onsite and transferred over the communication link.

Figure 4.32 (b) shows the proposed technique of transferring the waveform samples of \hat{d} through the communication link to the control/data centre where t_c is the communication network time reference which is used to time-tag the waveform samples. It should be noted that the proposed technique of Figure 4.32 (b) occupies the same space in the data frame as Figure 4.32 (a). Therefore, both techniques can be compared based on the same data rate of transfer over the communication link.

The proposed method accommodates two consecutive undersampled values of \hat{d} in

the data frame instead of X_r and X_i . If the communication link collects the samples of \hat{d} every $\frac{\Delta'}{f_o}$ seconds, the undersampling process can be carried out every $\frac{\Delta'}{2f_o}$ seconds because two samples of \hat{d} can be transferred per data frame according to Figure 4.32 (b).

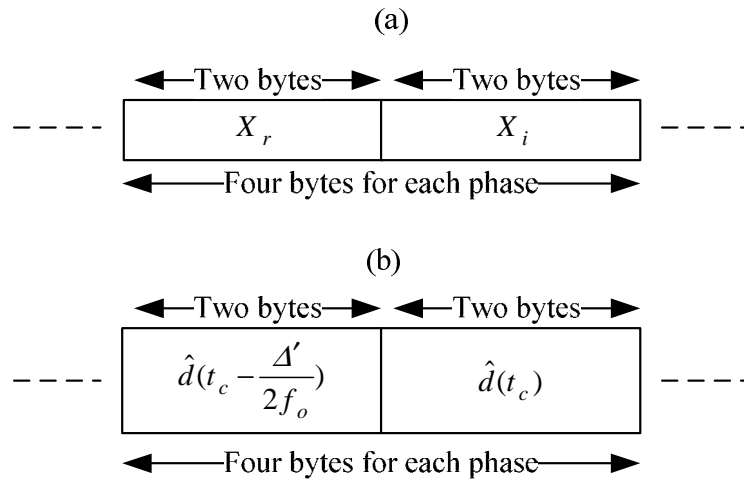


Figure 4.32. (a) Synchrophasor detection IEEE Standard C37.118

(b) Proposed technique to utilize the communication link to transfer samples of \hat{d} to the data centre.

4.4.3. Simulation Results

4.4.3.1. Case 7: Numerical Simulation

Figure 4.33 (a) shows a voltage waveform which includes 20% third and 10% fifth harmonics. The amplitude of the waveform changes from 1 p.u. to 1.1 p.u. and its phase-angle changes from 45 degrees to 60 degrees. The staggered undersampling factor of 3 and extended staggered undersampling factor of 1.5 have been used to estimate amplitude and phase-angle as presented in

Figure 4.33 (b) and (c). As seen, the proposed extended staggered undersampling techniques shows less estimation latency compared to the conventional staggered undersampling technique.

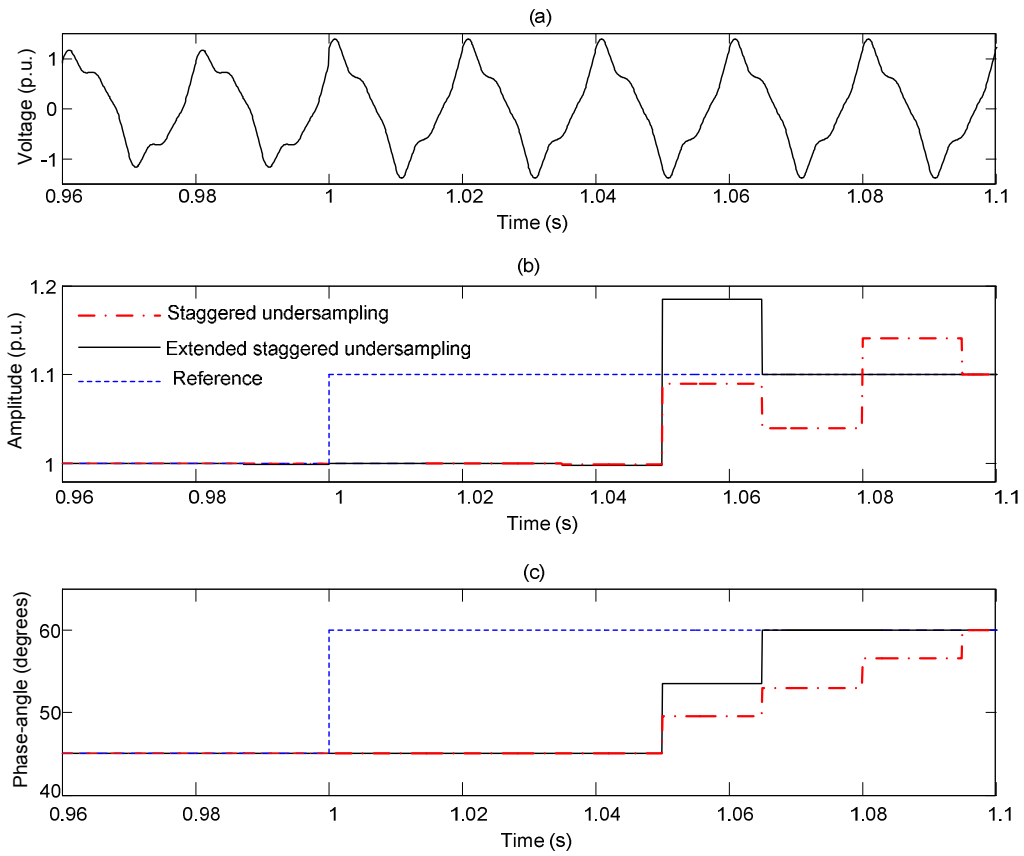


Figure 4.33. Case 7: Numerical simulation

- (a) voltage waveform
- (b) amplitude estimation
- (c) phase-angle estimation.

4.4.3.2. Case 8: MATLAB-Simulink Simulation

Figure 4.34 shows the IEEE 14-bus test system [202] which has been simulated in MATLAB-Simulink. The communication link reports the PMU estimates every 30 ms. Therefore, matching the proposed extended staggered undersampling technique requires considering $0.03 = \frac{\Delta'}{50}$ and $\Delta' = 1.5$ for the fundamental frequency of 50 Hz. A single-phase-A-to-ground fault is cleared on the line between buses 2 and 4 for which the current waveforms are shown in Figure 4.35. Figure 4.36 shows the rms values of voltage at buses 4 and 5. The voltage phase-angle of bus 5 with respect to bus 4 is also presented in Figure 4.36 (c). The current rms flowing from bus 3 to bus 4, current rms flowing from bus 4 to bus 5, phase-angle of current flowing from bus 3 to bus 4 with respect to bus 4, and phase-angle of current flowing from bus 4 to bus 5 with respect to bus 4 are presented in Figure 4.37. As seen, both PMU and extended staggered undersampling estimate the same steady-state values of rms and phase-angle although their estimation transition trajectories are different.

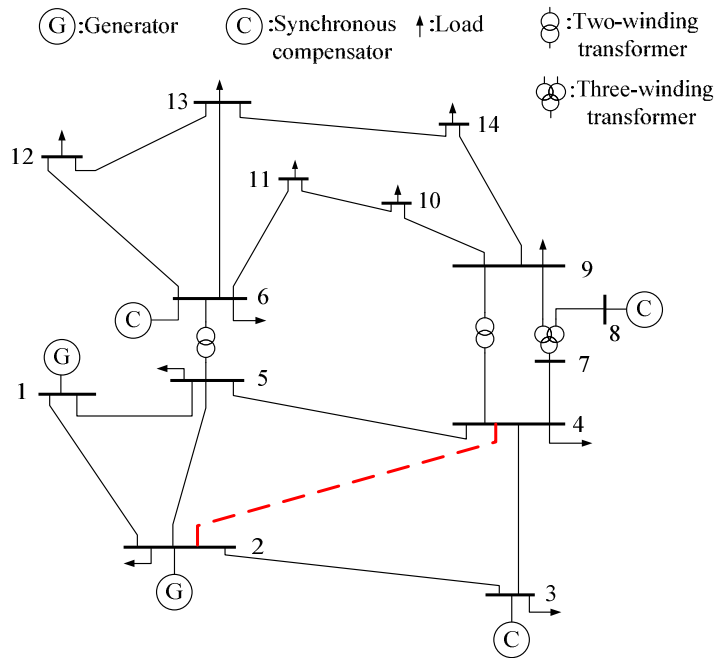


Figure 4.34. Case 8: MATLAB-Simulink simulation

IEEE 14-bus test system.

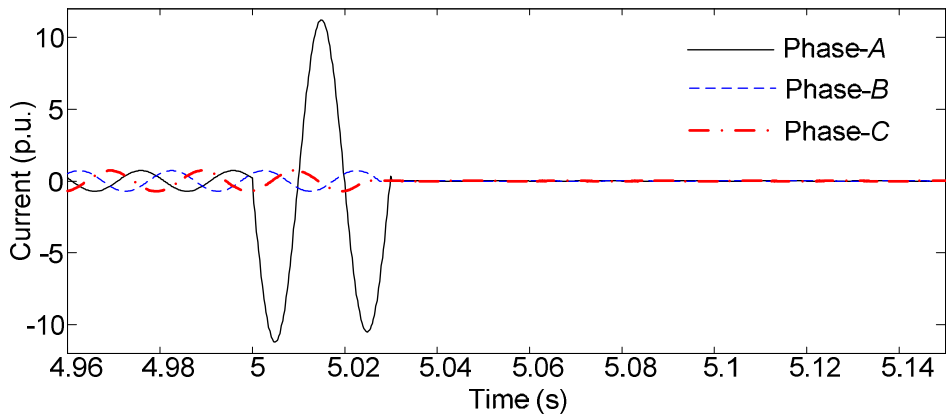


Figure 4.35. Case 8: MATLAB-Simulink simulation of phase-A-to-ground fault

Three-phase current waveforms flowing from bus 2 to bus 4.

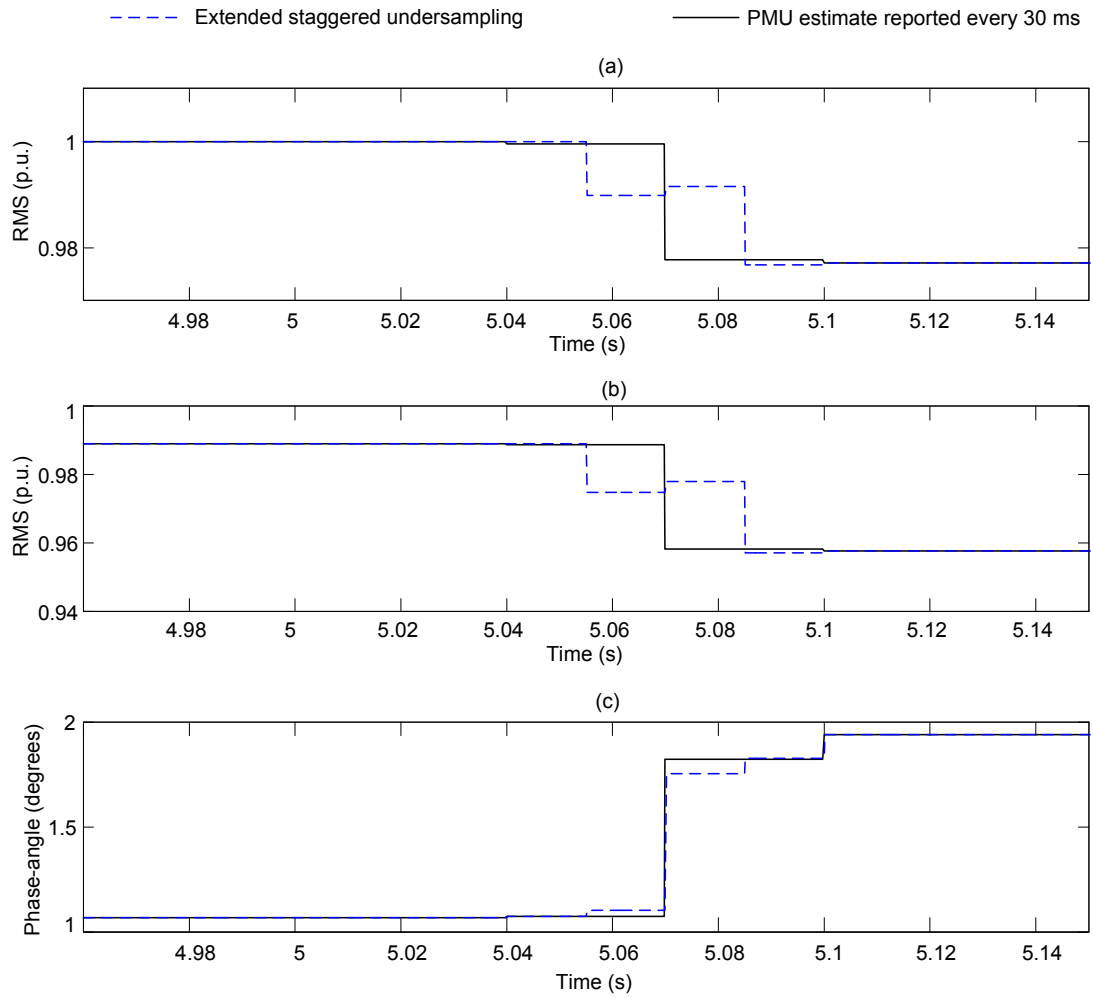


Figure 4.36. Case 8: MATLAB-Simulink simulation of phase-A-to-ground fault

(a) voltage rms at bus 5

(b) voltage rms at bus 4

(c) phase-angle of bus 5 voltage with respect to bus 4.

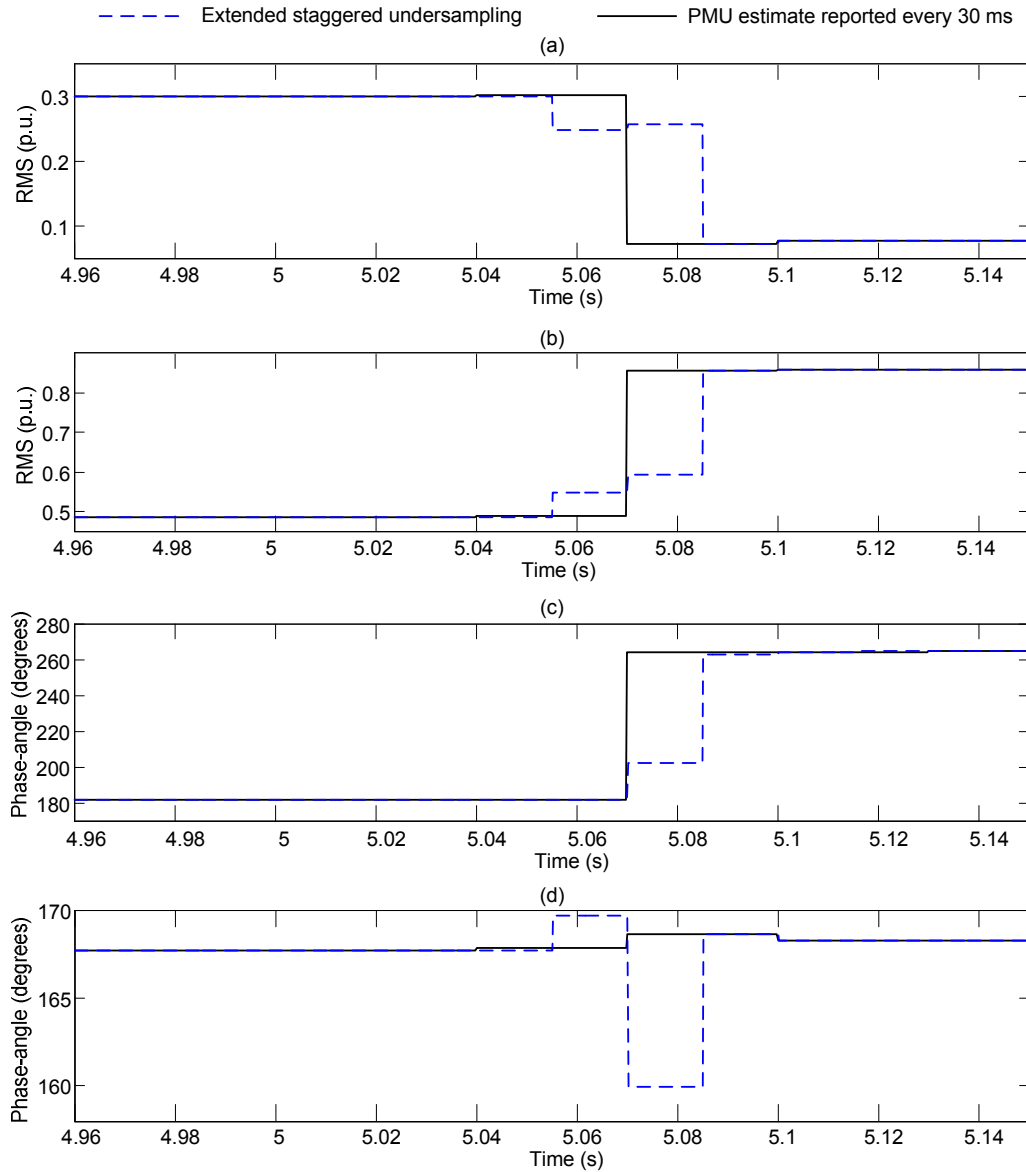


Figure 4.37. Case 8: MATLAB-Simulink simulation of phase-A-to-ground fault

(a) current rms flowing from bus 3 to bus 4

(b) current rms flowing from bus 4 to bus 5

(c) phase-angle of current flowing from bus 3 to bus 4 with respect to bus 4

(d) phase-angle of current flowing from bus 4 to bus 5 with respect to bus 4.

4.5. Conclusion

This chapter presented a real-time MGS technique to estimate harmonics and interharmonics. The proposed MGS technique has a lower computational burden on DSPs when compared with the DFT and the FFT algorithms. Application of the undersampling strategy to reduce the hardware requirement and processing power to a lower level has also been proposed. The proposed slow sampling MGS technique has been used to estimate harmonic/interharmonic components of voltage/current waveforms. The proposed technique has been evaluated through a selection of simulation studies and real-time implementation experiments. The estimation latency of the proposed technique in tracking non-stationary loads has been discussed and its computational effort is compared with that of the DFT and FFT algorithms. The proposed slow sampling MGS estimation technique shows comparable accuracy with the IEC Standard 61000-4-7 DFT method while having considerably lower computation burden on the DSP. The presented results prove accuracy, robustness and stable operation of the proposed technique in performing the assigned task of harmonics/interharmonics estimation.

This chapter also presented a new synchrophasor detection technique based on extended staggered undersampling for WAMSs applications. Application of extended staggered undersampling reduces the estimation latency to half of what is associated with the conventional staggered undersampling. The proposed synchrophasor detection technique utilizes the communication link to transfer the samples of the waveform directly to a control/data centre in which the synchrophasor detection will be carried out. The proposed technique promises the benefit of using a limited bandwidth from an

existing communication link to monitor the events synchronously. This technique can be implemented by using communication networks such as broadband internet connections which are or will be widely available at the distribution level. The proposed method also bypasses the errors associated with synchronising the DSP floating clock with UTC since phase-angle information is preserved within the transferred samples. This technique can improve WAMS reliability if used as a secondary procedure for transmission level synchrophasor detection in case of GPS unavailability. The correct performance of the proposed method has been demonstrated by simulations in MATLAB software.

Chapter 5 : Slow Sampling Real-time Optimization Approach to Estimate Power System Frequency

5.1. Introduction

The task of accurate power system frequency measurement has become more important to control the dynamic load-generation balance due to electricity industry deregulation [20] and ever-increasing distributed generation (DG) penetration into the power grid [203], [204]. Efficient low bandwidth sensing techniques for frequency and phasor estimation contribute to the economical realization of the smart grid vision for phasor measurement units (PMUs) [17], [162], frequency disturbance recorders (FDRs) [18], wide-area control (WAC) and special protection scheme (SPS) [205], failure diagnosis [206], load-shedding and load-restoration functions [207], power quality [27], and accommodating renewable energy resources [208].

The power system frequency encompasses information about the system operation and dynamics [17], [18]. It is a universal parameter across the entire interconnected power system [19]. This characteristic gives the frequency estimation the same value at the distribution level as it has at the transmission level to control and monitor the power flow [18]. Moreover, the increasing penetration of DG and plug-in electric vehicles (PEVs) [203] at the distribution level will transform the power flow from being almost unidirectional in the traditional utility environment to being bidirectional under the smart grid paradigm [99]. Although PMUs and FDRs have been installed in a limited

number [17], smart sensors and smart meters will be placed across the distribution grids in millions [107]. Therefore, the advent of smart sensors and meters provides an unprecedented access to the power grid information to control the bidirectional power flow and monitor the frequency at the distribution level with low-cost smart sensors. These metering gateways enable smart grid to perform control, diagnostics, and monitoring tasks through a two-way communication system in a feasible cost-benefit margin [99], [209]. One solution to extract power system information from a few observations, decrease the smart sensors' data acquisition requirements and hardware cost is to reduce the rate of sampling by adopting undersampling strategies [111], [210]-[212].

However, slow sampling techniques compromise the frequency estimation speed. The effects of delays associated with the undersampling on estimating the frequency of the power system have not been addressed in the technical literature comprehensively. One way of considering this problem is to look upon some recent dense sampling techniques as benchmarks in our effort to adopt a slow sampling technique. This will give us a sense of how fast the existing frequency estimation techniques perform. For instance, the well-established PLL type techniques show an average settling time of 0.2 s to track step frequency changes in a harmonic distorted environment [114], [49]. Reference [184], as another example, presents a DFT demodulation frequency estimation method which has been designed to comply with the endorsed requirements by the North American Synchrophasor Initiative (NASPI). The presented method of [184] shows a settling time of 0.27 s to track step frequency changes. This delay is, of course, the result of compromising the estimation pace to have a distortion free and stable response

in presence of harmonics, interharmonics, and noise contamination.

The objective of this chapter is to introduce a slow sampling real-time power system frequency estimation algorithm, which can show comparable estimation speed with those of the aforementioned dense sampling methods. The advantage of adopting a slow sampling strategy is to reduce digital signal processor (DSP) requirements. Another important motivation behind developing this technique is to embed the FDR estimation task with no extra installation at the distribution level based on collecting a few observations of waveform samples. The introduced frequency estimation method is based on the Newton-type algorithm and the least squares (NTA-LS) approach which is applied to a window of voltage waveform samples with a specific length. The performance of the proposed method has been evaluated through MATLAB-Simulink simulation studies and real-time DSP implementation experiments.

The rest of this chapter is organized as follows. Sections 5.2 and 5.3 describe a new hybrid Newton-type algorithm and least squares (NTA-LS) frequency estimation method and mathematical development respectively. Section 5.4 reviews the decomposition of single-phase to orthogonal components (DSPOC) and PLL frequency estimation techniques. Section 5.5 includes the simulation study results. Section 5.6 presents the real-time implementation results and evaluates field performance of the NTA-LS method through mimicking power system operation by using a hardware power system simulator and a programmable power supply. Section 5.7 concludes the chapter.

5.2. Newton-Type Algorithm and Least Squares Method for Power System Frequency Estimation

The main idea of the proposed method is formed around the fact that the phase-angle of the voltage waveform changes proportionally with time during frequency drifts [145]. This phenomenon happens if the phasor measurement is set on the nominal power system frequency (50 Hz or 60 Hz). Figure 5.1 shows the fundamental frequency voltage phase-angle ($\theta(t_k)$) with respect to time where f_d is the frequency drift from the nominal power system frequency.

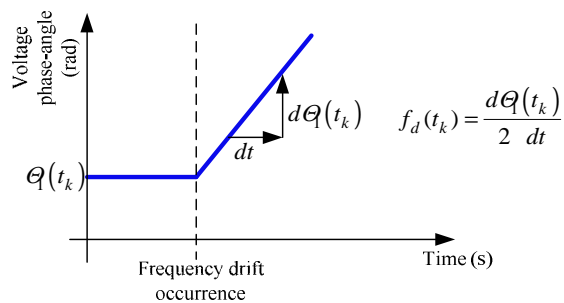


Figure 5.1. Principle of frequency estimation from the phase-angle.

As it is shown in Figure 5.1, the simplest way to extract the frequency drift is to differentiate the phase-angle $\theta(t_k)$ with respect to time. The DFT-based demodulation techniques adopt this path [25]. Another option is to use the PLL technique which applies a loop filter and the gradient search method to estimate the slope of the phase-angle [19], [114], [49]. However, the PLL shows some delays because of the loop low-pass filter (LPF) time constant [49].

The method proposed in this chapter is based on estimating the phase-angle $\theta_1(t_k)$ by using the Newton-type algorithm (NTA) and, then, extracting the frequency drift based on the least squares (LS) minimization technique [132]. The LS algorithm estimates the $\theta_1(t_k)$ slope which is 2 times the frequency drift. A peak notch filter is used as a pre-filtering stage to separate the fundamental frequency component which is of interest to estimate the power system frequency. This pre-filtering stage also helps to reduce the digital signal processor (DSP) arithmetic operation by rejecting harmonics. Figure 5.2 shows the magnitude and phase response of the peak notch filter with the centre frequency of 50.0 Hz respectively. The peak notch filter is a cascade six-order Butterworth filter with bandwidth of 10 Hz. This bandwidth allows estimation of frequency according to the requirements of IEC Standard 61000-4-30 [176].

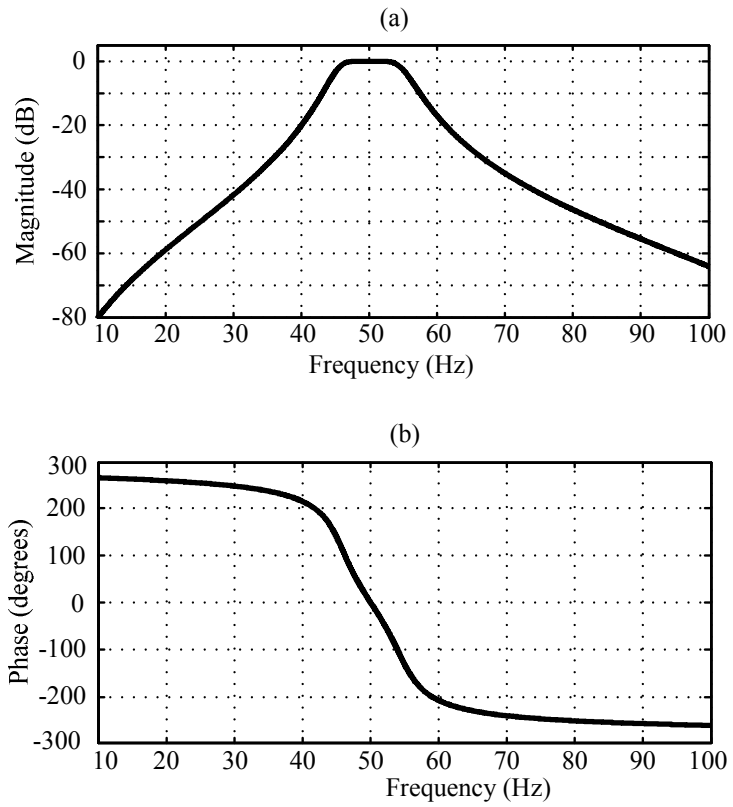


Figure 5.2. (a) Magnitude response of the peak notch filter

(b) Phase response of the peak notch filter.

The fundamental frequency line-to-neutral voltage at a given power system node which is sampled at the k^{th} instance is defined as [32]-[34]:

$$v(k) = h_{NTA}(X_{NTA}(k)) + \epsilon_k \quad (5.1)$$

where

h_{NTA} is the estimation function

$X_{NTA}(k)$ is a time-varying estimation vector

ϵ_k is a random noise vector.

It should be noted that the frequency is a universal component across the power system so the voltage waveform $v(k)$ is the phase-to-neutral waveform in the case of a single-phase power system or any of the phase-to-neutral voltage waveforms (phase-A, -B, or -C) in the case of a three-phase power system.

For the purpose of frequency estimation, the following time-varying vector is defined:

$$X_{NTA}(k) = [V_{NTA}(k) \quad \Theta_{NTA}(k) \quad V_{NTAdc}(k)]^T \quad (5.2)$$

where

$V_{NTA}(k)$ is the fundamental frequency line-to-neutral voltage amplitude

$\Theta_{NTA}(k)$ is the fundamental frequency line-to-neutral voltage phase-angle

$V_{NTAdc}(k)$ is the dc offset component of the captured instantaneous voltage waveform.

The estimation function is defined as:

$$h_{NTA}(X_{NTA}(k)) = V_{NTAdc}(k) + V_{NTA}(k) \sin(2\pi f_o k / f_s + \Theta_{NTA}(k)) \quad (5.3)$$

where

f_o is the power system nominal fundamental frequency and

f_s is the sampling frequency.

The sampling frequency is chosen to be $2000/7=285.71$ Hz and is equivalent to the downsampling factor of 7 with respect to 2 kHz based on the staggered undersampling concept [111]. The selection of the undersampling factor is based on the estimation latency analysis, which was presented in Chapter 4. This selection is a trade-off between the estimation latency and the goal of keeping the sampling frequency at a low value. Choosing a smaller undersampling factor will increase the sampling frequency while choosing a bigger undersampling value will increase the estimation latency.

The estimation error at the k^{th} sample according to the generic model of (5.1) and the estimation function of (5.3) is calculated as:

$$e_{NTA}(k) = h_{NTA}(X_{NTA}(k)) - v(k) \quad (5.4)$$

Owing to the fact that the number of unknowns in (5.2) and (5.3) is three, the error vector is of dimension three which is desired to converge to zero as the following equation states:

$$E_{NTA}(X_{NTA}(k)) = [e_{NTA}(k) \quad e_{NTA}(k-1) \quad e_{NTA}(k-2)]^T = 0_{3 \times 1} \quad (5.5)$$

where

$0_{3 \times 1}$ is a 3×1 zeros vector.

The estimation vector at the $(k+1)^{\text{th}}$ sample ($X_{NTA}(k+1)$) can be calculated by solving the vector equation in (5.5). Having the k^{th} estimation vector ($X_{NTA}(k)$), there exists an unknown correction vector ($\Delta X_{NTA}(k)$) which has to be determined so that the following holds true:

$$E_{NTA}(X_{NTA}(k) + \Delta X_{NTA}(k)) = 0_{3 \times 1} \quad (5.6)$$

The following linear expansion is obtained by using the Taylor series expansion of the

$E_{NTA}(X_{NTA}(k) + \Delta X_{NTA}(k))$ in the close neighbourhood of $X_{NTA}(k)$:

$$E_{NTA}(X_{NTA}(k) + \Delta X_{NTA}(k)) = E_{NTA}(X_{NTA}(k)) + J_{NTA}(k)\Delta X_{NTA}(k) \quad (5.7)$$

where

$J_{NTA}(k)$ is the Jacobian matrix which is the 3×3 matrix of first partial derivatives of

the errors and is calculated as:

$$J_{NTA}(k) = \begin{bmatrix} \frac{\partial e_{NTA}(k)}{\partial V_{NTA}(k)} & \frac{\partial e_{NTA}(k)}{\partial \Theta_{NTA}(k)} & \frac{\partial e_{NTA}(k)}{\partial V_{NTAdc}(k)} \\ \frac{\partial e_{NTA}(k-1)}{\partial V_{NTA}(k-1)} & \frac{\partial e_{NTA}(k-1)}{\partial \Theta_{NTA}(k-1)} & \frac{\partial e_{NTA}(k-1)}{\partial V_{NTAdc}(k-1)} \\ \frac{\partial e_{NTA}(k-2)}{\partial V_{NTA}(k-2)} & \frac{\partial e_{NTA}(k-2)}{\partial \Theta_{NTA}(k-2)} & \frac{\partial e_{NTA}(k-2)}{\partial V_{NTAdc}(k-2)} \end{bmatrix} \quad (5.8)$$

where:

$$\frac{\partial e_{NTA}(k)}{\partial V_{NTA}(k)} = \sin(2 f_o k / f_s + \Theta_{NTA}(k)) \quad (5.9)$$

$$\frac{\partial e_{NTA}(k)}{\partial \Theta_{NTA}(k)} = V_{NTA}(k) \cos(2 f_o k / f_s + \Theta_{NTA}(k)) \quad (5.10)$$

$$\frac{\partial e_{NTA}(k)}{\partial V_{NTAdc}(k)} = 1 \quad (5.11)$$

Eqns. (5.6) and (5.7) result in the following equation to calculate $\Delta X_{NTA}(k)$:

$$J_{NTA}(k)\Delta X_{NTA}(k) = -E_{NTA}(X_{NTA}(k)) \quad (5.12)$$

The above equation can be solved by defining the objective function to be the sum of error squares as:

$$G_{NTA}(k) = \frac{1}{2} \sum_{l=k-2}^k e_{NTA}^2(l) \quad (5.13)$$

The correction vector to satisfy (5.6) and minimize (5.13) is obtained according to the Newton method [132] and the linear Taylor expansion model of (5.7) as:

$$\Delta X_{NTA}(k) = -\left(\nabla^2 G_{NTA}(k)\right)^{-1} \nabla G_{NTA}(k) \quad (5.14)$$

where

$\nabla G_{NTA}(k)$ is the gradient of the objective function.

$\nabla^2 G_{NTA}(k)$ is the Hessian matrix of the objective function which are calculated according to the error function of (5.4) and the objective function of (5.13) as follows:

$$\nabla G_{NTA}(k) = \frac{\partial G_{NTA}(k)}{\partial X_{NTA}(k)} = \sum_{l=k-2}^k e_{NTA}(l) \nabla e_{NTA}(l) = J_{NTA}^T(k) E_{NTA}(X_{NTA}(k)) \quad (5.15)$$

$$\begin{aligned} \nabla^2 G_{NTA}(k) &= \frac{\partial^2 G_{NTA}(k)}{\partial X_{NTA}^2(k)} \\ &= \sum_{l=k-2}^k \nabla e_{NTA}(l) \nabla e_{NTA}^T(l) + \sum_{l=k-2}^k e_{NTA}(l) \nabla^2 e_{NTA}(l) \\ &= J_{NTA}^T(k) J_{NTA}(k) + \sum_{l=k-2}^k e_{NTA}(l) \nabla^2 e_{NTA}(l) \end{aligned} \quad (5.16)$$

Since the considered Taylor model of (5.7) is linear, the terms $\left(\sum_{l=k-2}^k e_{NTA}(l) \nabla^2 e_{NTA}(l)\right)$

on the right hand side of (5.16) become zero and the Hessian matrix $\nabla^2 G_{NTA}(k)$ is obtained as:

$$\nabla^2 G_{NTA}(k) = J_{NTA}^T(k) J_{NTA}(k) \quad (5.17)$$

By substituting (5.15) and (5.17) into (5.14), the following formula for the correction vector is obtained:

$$\Delta X_{NTA}(k) = -\left(J_{NTA}^T(k)J_{NTA}(k)\right)^{-1} J_{NTA}^T(k)E_{NTA}(k) \quad (5.18)$$

The next iteration estimation vector is updated as:

$$X_{NTA}(k+1) = X_{NTA}(k) + \Delta X_{NTA}(k) \quad (5.19)$$

When the power system frequency is 50.0 Hz, the estimated voltage phase-angle by (5.4)-(5.19) is a constant value. However, if the power system frequency changes, the voltage phase-angle becomes a time-varying function of the frequency drift value. Since the NTA fundamental frequency is set to 50 Hz, the frequency drift from 50 Hz will appear in $\Theta_{NTA}(k)$ as a result of the modulation effect on the phase-angle. The NTA estimated values for the line-to-neutral fundamental frequency voltage phase-angle ($\Theta_{NTA}(k)$) are fed to an LS optimiser to track the instantaneous frequency drift.

Another Taylor series estimation platform is developed to process the data in $\Theta_{NTA}(k)$ which is based on the LS estimation model. The LS model for the time-varying phase-angle is expressed as:

$$\Theta_{NTA}(k) = \Theta_c(k) + (k)t_k \quad (5.20)$$

where

$t_k = kT_s$ is the discrete time of observation,

T_s is the sampling period,

(k) estimates the frequency drift from 50.0 Hz in the power system, and

$\Theta_c(k)$ is the constant part of the phase-angle estimation.

In the assembled LS problem to solve (5.20), the objective function ($F_{LS}(k)$) has the following form:

$$F_{LS}(k) = \frac{1}{2} \|R_{LS}(k)\|^2 \quad (5.21)$$

$$R_{LS}(k) = H_{LS}(k)\hat{\Gamma}_{LS}(k) - \Theta(k) \quad (5.22)$$

where

$\| \cdot \|$ is the Euclidean norm function [132]

Θ_k is a vector which contains m consecutive estimations of the voltage phase-angle by the Newton method which is defined as:

$$\Theta_k^T = [\Theta_{NTA}(k), \dots, \Theta_{NTA}(k-m+1)] \quad (5.23)$$

where

m is chosen to be 10 after testing different values of m to have a stable response.

$R_{LS}(k)$ is the vector of residual values ($r_{LS}(l)$) at the k^{th} sample for a window of m data points which is defined as:

$$R_{LS}^T(k) = [r_{LS}(k) \quad \dots \quad r_{LS}(k-m+1)] \quad (5.24)$$

$$r_{LS}(l) = \Theta_c(l) + (l)t_l - \Theta_{NTA}(l), \quad k-m+1 \leq l \leq k \quad (5.25)$$

where

$\hat{\Gamma}_{LS}(k)$ is the estimation matrix which is defined as:

$$\hat{\Gamma}_{LS}^T(k) = [\Theta_c(k) \quad (k)] \quad (5.26)$$

$H_{LS}(k)$ is the $m \times 2$ partial derivatives of the residual values ($r_{LS}(l)$) at the k^{th} sample which is calculated as:

$$H_{LS}^T(k) = [\nabla r_{LS}(k), \dots, \nabla r_{LS}(k-m+1)] \quad (5.27)$$

where

$\nabla r_{LS}(l)$ is calculated as:

$$\nabla r_{LS}^T(l) = [1 \quad t_l], \quad k-m+1 \leq l \leq k \quad (5.28)$$

Therefore, $H_{LS}(k)$ is obtained as:

$$H_{LS}^T(k) = \begin{bmatrix} 1 & \cdots & 1 \\ t_k & \cdots & t_{k-m+1} \end{bmatrix} \quad (5.29)$$

$\hat{\Gamma}_{LS}(k)$ is estimated by minimizing the norm of the residual vector based on the LS algorithm as [132]:

$$\hat{\Gamma}_{LS}(k) = [\Theta_c(k) \quad (k)]^T = (H_{LS}^T(k)H_{LS}(k))^{-1} H_{LS}^T(k)\Theta_k \quad (5.30)$$

As it is shown in Figure 5.1, the derivative of the phase-angle ($\Theta_{NTA}(k)$) with respect to time is the frequency drift from its nominal value (f_o). Differentiating the Taylor series of (5.20) with respect to time results in:

$$f_d(k) = \frac{\partial \Theta_{NTA}(t_k)}{2 \partial t} = \frac{\partial}{2 \partial t} (\Theta_c(k) + (k)t_k) = \frac{(k)}{2}$$

Therefore, the frequency drift ($f_d(k)$) is calculated as:

$$f_d(k) = \frac{(k)}{2} \quad (5.31)$$

The power system frequency is estimated by adding the frequency drift to the nominal power system frequency as follows:

$$f_k = f_o + f_d(k) \quad (5.32)$$

Figure 5.3 shows the proposed NTA-LS frequency estimation algorithm where z^{-1} is the unit delay.

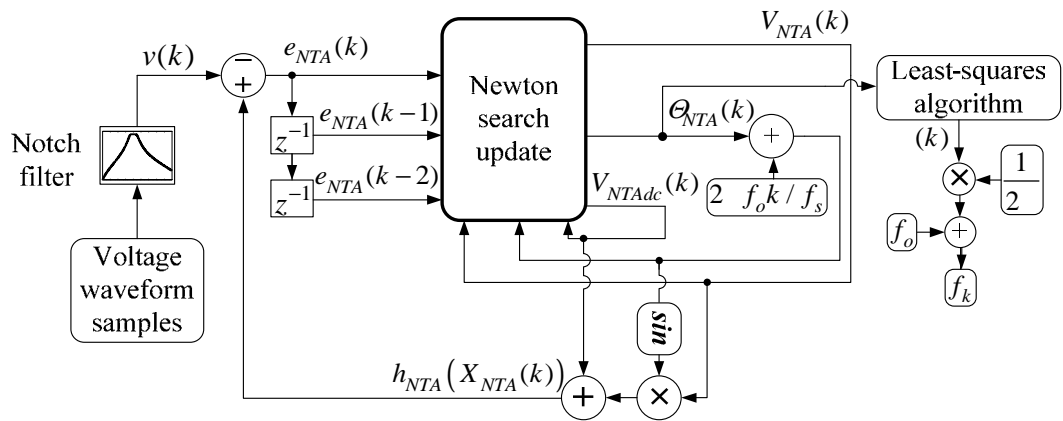


Figure 5.3. NTA-LS algorithm to estimate power system frequency.

5.3. Mathematical Development

This section presents the mathematical analysis and applied simplifications to implement the proposed NTA-LS method.

5.3.1. Newton Technique Algorithm Development

The equation presented in (5.18) uses inversion of the Hessian matrix $(J_{NTA}^T(k)J_{NTA}(k))^{-1}$. Based on the fact that $\det(J_{NTA}^T(k)) = \det(J_{NTA}(k))$, the determinant of $(J_{NTA}^T(k)J_{NTA}(k))$ is calculated as:

$$\det(J_{NTA}^T(k)J_{NTA}(k)) = \det(J_{NTA}^T(k))\det(J_{NTA}(k)) = \det(J_{NTA}(k))^2 \quad (5.33)$$

where

$\det(\)$ calculates determinant of a matrix.

Therefore, analysing determinant of $J_{NTA}(k)$ indicates if the inversion can be done properly. $\det(J_{NTA}(k))$ is calculated as:

$$\begin{aligned} \det(J_{NTA}(k)) &= \det \left(\begin{bmatrix} \sin(\theta'_{k-1}) & V_{NTA}(k)\cos(\theta'_{k-1}) \\ \sin(\theta'_{k-2}) & V_{NTA}(k-2)\cos(\theta'_{k-2}) \end{bmatrix} \right) \\ &- \det \left(\begin{bmatrix} \sin(\theta'_k) & V_{NTA}(k)\cos(\theta'_k) \\ \sin(\theta'_{k-2}) & V_{NTA}(k-2)\cos(\theta'_{k-2}) \end{bmatrix} \right) \\ &+ \det \left(\begin{bmatrix} \sin(\theta'_k) & V_{NTA}(k)\cos(\theta'_k) \\ \sin(\theta'_{k-1}) & V_{NTA}(k-1)\cos(\theta'_{k-1}) \end{bmatrix} \right) \end{aligned} \quad (5.34)$$

where

$$\theta'_k = \frac{2}{f_s} \frac{f_o k}{f_s} + \Theta_{NTA}(k).$$

At each iteration, the voltage amplitude and phase-angle are assigned to the values

which have been updated through the previous estimation by (5.18) and (5.19) for three consecutive voltage samples to maintain the algorithm stability. Therefore, the following equalities hold true for the three consecutive samples which are involved in the estimation:

$$\begin{aligned} V_{NTA}(k) &= V_{NTA}(k-1) = V_{NTA}(k-2) \\ \Theta_{NTA}(k) &= \Theta_{NTA}(k-1) = \Theta_{NTA}(k-2) \end{aligned} \quad (5.35)$$

Eqn. (5.34) is rewritten as follows:

$$\begin{aligned} \det(J_{NTA}(k)) &= V_{NTA}(t_k) (\sin(\theta'_{k-1}) \cos(\theta'_{k-2}) - \cos(\theta'_{k-1}) \sin(\theta'_{k-2})) \\ &- V_{NTA}(k) (\sin(\theta'_k) \cos(\theta'_{k-2}) - \cos(\theta'_k) \sin(\theta'_{k-2})) \\ &+ V_{NTA}(k) (\sin(\theta'_k) \cos(\theta'_{k-1}) - \cos(\theta'_k) \sin(\theta'_{k-1})) \\ &= V_{NTA}(k) (\sin(\theta'_{k-1} - \theta'_{k-2}) - \sin(\theta'_k - \theta'_{k-2}) + \sin(\theta'_k - \theta'_{k-1})) \end{aligned} \quad (5.36)$$

and:

$$\begin{aligned} \theta'_{k-1} - \theta'_{k-2} &= 2 \pi f_o / f_s \\ \theta'_k - \theta'_{k-2} &= 4 \pi f_o / f_s \\ \theta'_k - \theta'_{k-1} &= 2 \pi f_o / f_s \end{aligned} \quad (5.37)$$

Eqn. (5.36) is simplified into the following form by using trigonometric functions properties and substituting $f_o = 50$ Hz and $f_s = \frac{2000}{7}$ Hz:

$$\begin{aligned} \det(J_{NTA}(k)) &= V_{NTA}(t_k) (2 \sin(2 \pi f_o / f_s) - \sin(4 \pi f_o / f_s)) \\ &= V_{NTA}(k) (2 \sin(2 \pi f_o / f_s) - 2 \sin(2 \pi f_o / f_s) \cos(2 \pi f_o / f_s)) \\ &= 2 V_{NTA}(k) \sin(2 \pi f_o / f_s) (1 - \cos(2 \pi f_o / f_s)) \\ &= 4 V_{NTA}(k) \sin(2 \pi f_o / f_s) (\sin(\pi f_o / f_s))^2 \\ &= 4 \sin(0.35 \pi) \sin(0.175 \pi)^2 V_{NTA}(k) = 0.973 V_{NTA}(k) \end{aligned} \quad (5.38)$$

Therefore, determinant of the Hessian matrix will not become zero if $V_{NTA}(k) \neq 0$ during the estimation process. To avoid possible singularity in cases of abrupt changes,

term $(J_{NTA}^T(k)J_{NTA}(k))^{-1}$ will be replaced by a scalar value of 0.2 if $V_{NTA}(k)=0$. This conditional alteration produces enough momentum to revive the solution from singularity.

5.3.2. Least-Squares Technique Development

The second stage of the estimation technique works based on the LS estimation equation which uses matrix operations as presented in (5.30). This section presents a closed form formula for (5.30) which has been used to avoid heavy matrix operation in real-time. Recalling (5.30), the LS estimation vector is calculated as:

$$\hat{\Gamma}_{LS} = (H_{LS}^T(k)H_{LS}(k))^{-1} H_{LS}^T(k)\Theta_k$$

The first term on the right hand side is expanded according to (5.29) as:

$$H_{LS}^T(k)H_{LS}(k) = \begin{bmatrix} 1 & \cdots & 1 \\ t_k & \cdots & t_{k-m+1} \end{bmatrix} \begin{bmatrix} 1 & t_k \\ \vdots & \vdots \\ 1 & t_{k-m+1} \end{bmatrix} = \begin{bmatrix} \sum_{l=k-m+1}^k 1 & \sum_{i=k-m+1}^k t_l \\ \sum_{l=k-m+1}^k t_l & \sum_{l=k-m+1}^k t_l^2 \end{bmatrix} \quad (5.39)$$

where

$$t_k = kT_s$$

$$T_s = 1/f_s.$$

The terms on the right hand side can be reduced to the following equations:

$$a' = \sum_{l=k-m+1}^k 1 = m \quad (5.40)$$

$$\begin{aligned}
b' &= \sum_{l=k-m+1}^k t_l = T_s \sum_{l=1}^m (k-m+l) = T_s \left(\sum_{l=1}^m (k-m) + \sum_{l=1}^m l \right) = \\
&T_s (m(k-m) + m(m+1)/2) = mT_s (k + 0.5(1-m))
\end{aligned} \tag{5.41}$$

in which:

$$\sum_{l=1}^m l = \frac{m(m+1)}{2}.$$

$$\begin{aligned}
c' &= \sum_{l=k-m+1}^k t_l^2 = T_s^2 \sum_{l=1}^m (k-m+l)^2 \\
&= T_s^2 \left((k-m) \sum_{l=1}^m ((k-m) + 2i) + \sum_{l=1}^m l^2 \right) \\
&= (k-m)T_s^2 (m(k-m) + m(m+1)) + \frac{T_s^2 m(2m+1)(m+1)}{6} \\
&= mT_s^2 \left((k+1)(k-m) + \frac{(2m+1)(m+1)}{6} \right)
\end{aligned} \tag{5.42}$$

where the sum of integers squared which is also called square pyramid numbers is calculated as:

$$\sum_{l=1}^m l^2 = \frac{m(2m+1)(m+1)}{6}.$$

Therefore, by using (5.40)-(5.42), $(H_k^T H_k)^{-1}$ is calculated as:

$$\left(H_{LS}^T(k) H_{LS}(k) \right)^{-1} = \frac{1}{a'c' - b'^2} \begin{bmatrix} c' & -b' \\ -b' & a' \end{bmatrix} \tag{5.43}$$

The same approach can be used to find a closed form for term $(H_{LS}^T(k) H_{LS}(k))^{-1} H_{LS}^T(k)$ which results in the following alternative equations for (5.30), (5.32) respectively:

$$\hat{\Gamma}_{LS}(k) = \frac{1}{a'c' - b'^2} \begin{bmatrix} \sum_{l=k-m+1}^k c' \Theta_{NTA}(l) - b' t_l \Theta_{NTA}(l) & \sum_{l=k-m+1}^k -b' \Theta_{NTA}(l) + a' t_l \Theta_{NTA}(l) \end{bmatrix}^T \quad (5.44)$$

$$f_k = f_o + \frac{\sum_{l=k-m+1}^k -b' \Theta_{NTA}(l) + a' t_l \Theta_{NTA}(l)}{(1/2)(a'c' - b'^2)} \quad (5.45)$$

This equation reduces the computational burden by replacing matrix inversion with basic math operations for real-time implementation.

5.4. Methods for Comparison

This section reviews the DSPOC and PLL techniques which will be implemented to conduct the comparative studies.

5.4.1. DSPOC Algorithm to Estimate Power System Frequency

The DSPOC technique has been used for power system frequency estimation in PMUs [184], [213]. The recursive implementation of DSPOC is used in the comparative studies. The recursive implementation of DSPOC, as presented in Chapter 2, is shown in Figure 5.4.

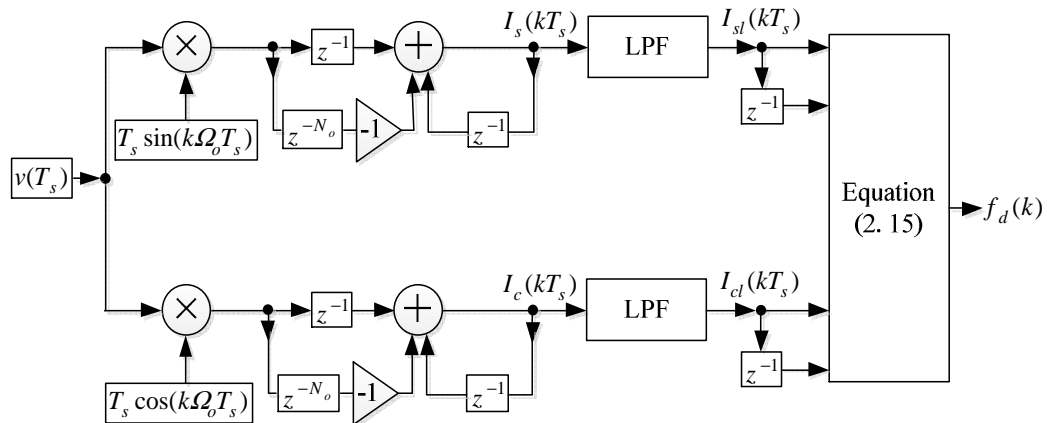


Figure 5.4. Recursive implementation of the DSPOC frequency estimation.

5.4.2. Phase-Locked-Loop Technique

PLL has been widely applied to estimate frequency and synchronize power electronics devices with grid [208], [214], [215]. The structure of a single-phase PLL which exists in the MATLAB-Simulink library is shown in Figure 5.5. The details of each component and the settings of parameters can be found in [216]. The “mod” function calculates the positive remainder of the integrator output with respect to 2 in Figure 5.5.

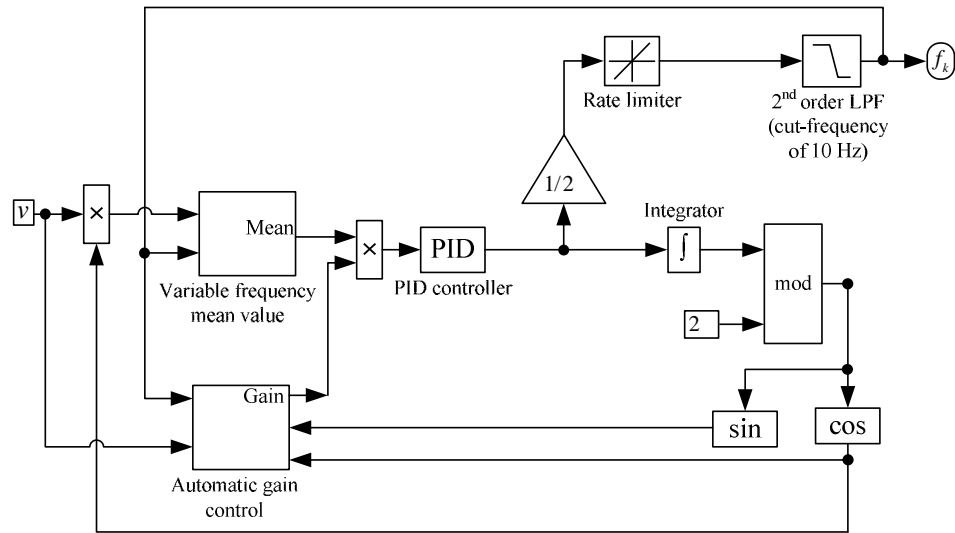


Figure 5.5. MATLAB-Simulink single-phase PLL [216].

5.5. Simulation Studies

This section presents the simulation results to evaluate the frequency estimation performance of the proposed NTA-LS method and compares it with the NTA, DSPOC, and PLL techniques. The power system nominal frequency is 50.0 Hz and the sampling frequency is $2000/7 = 285.71$ Hz. The voltage waveform has been used to estimate frequency. The implemented NTA is based on the NTA frequency estimation in [32], which was reviewed in Chapter 1. The simulations are conducted in the MATLAB-Simulink software.

5.5.1. Case 1: Frequency Step Change

In this case, a step frequency change is simulated in which the voltage frequency changes from 50.0 Hz to 59.0 Hz at 3.0 s. As Figure 5.6 shows, maximum steady state error for NTA-LS, NTA, DSPOC, and PLL are 0.002 Hz, 0.004 Hz, 0.009 Hz, and 0.002 Hz respectively. The settling time is the time taken by the response to converge in to the $\pm 5\%$ error range in estimating the final value [184]. It should be noted that the final value is the value of the frequency drift from the nominal value (50 Hz or 60 Hz). The settling times for NTA-LS, NTA, DSPOC, and PLL are 0.248 s, 0.507 s, 0.507 s, and 0.528 s respectively.

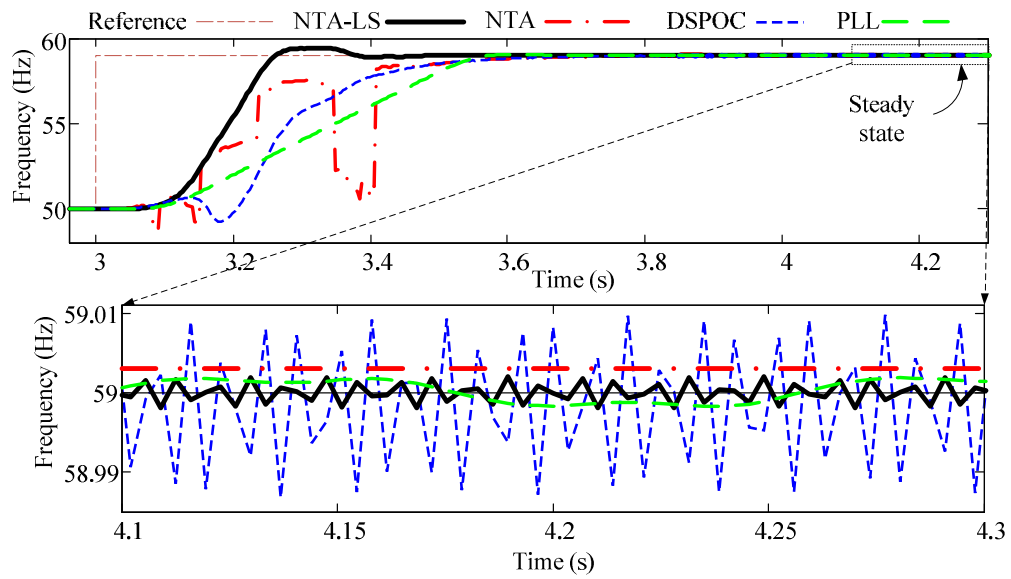


Figure 5.6. Case 1: frequency step change

Frequency estimation at 285.71 Hz sampling frequency by the NTA-LS, NTA, DSPOC, and PLL techniques.

5.5.2. Case 2: Voltage Step

This case presents the effect of voltage step on the frequency estimation. The voltage amplitude drops from 1.0 p.u. to 0.8 p.u., as Figure 5.7 (a) shows, while the frequency remains unchanged at 50 Hz. The estimated frequency is shown in Figure 5.7 (b). The DSPOC and NTA-LS show smaller over/undershoot than that of NTA and PLL before restoring to the correct value.

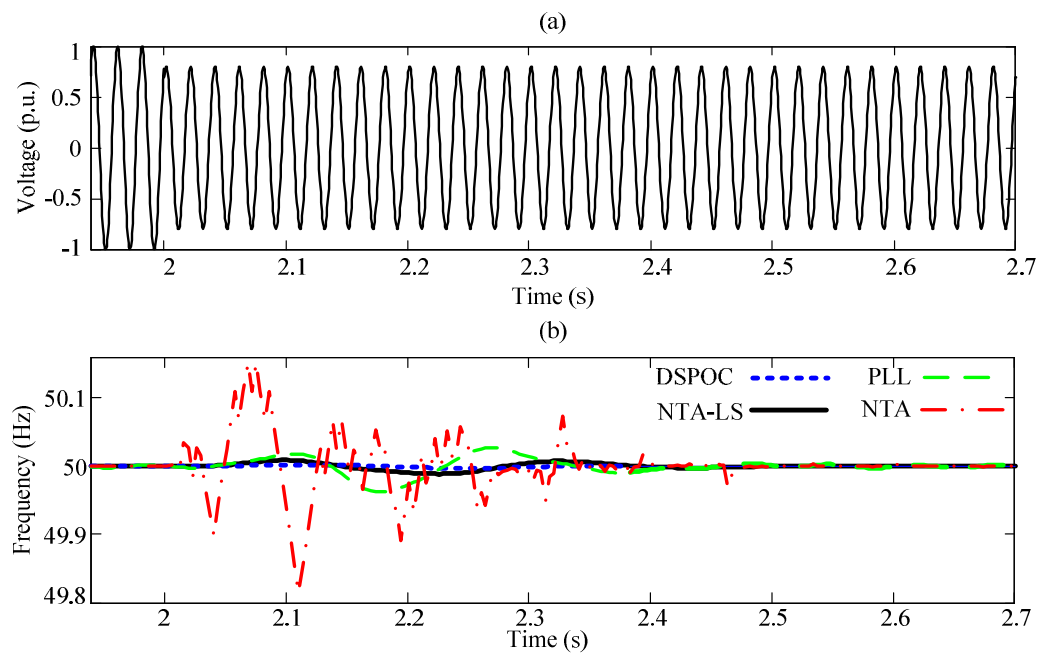


Figure 5.7. Case 2: voltage step

(a) frequency estimation at 285.71 Hz sampling frequency by the NTA-LS, NTA,

DSPOC, and PLL techniques

(b) voltage waveform.

5.5.3. Case 3: Harmonic/Interharmonic Contamination

In this section, the performance of NTA-LS, NTA, PLL, and DSPOC algorithms is examined in the presence of harmonic/interharmonic contamination. The phase-A line-to-neutral voltage waveform comprises of 1.0 p.u. fundamental frequency, 0.03 p.u. second harmonic, 0.08 p.u. third harmonic, 0.015 p.u. fourth harmonic, 0.09 p.u. fifth harmonic, and 0.075 p.u. seventh harmonic based on the definition for the second level test class in IEC Standard 61000-4-13 [146]. All harmonic components are $\pi/4$ rad apart from the fundamental component. The frequency is programmed to change from 50.0 Hz to 49.0 Hz at 3.0 s to observe the frequency estimation performance under the simulated condition.

Figure 5.8 shows the simulated voltage waveform and a magnified snapshot of the voltage waveform. Figure 5.9 shows the estimated voltage frequency by the NTA-LS, NTA, DSPOC, and PLL methods. *TVE* calculation is described in the Appendix. The NTA settling time is 0.4760 s and its maximum steady state error is 0.0148 Hz (maximum *TVE* of 0.0949 %). The DSPOC settling time is 0.43 s and its maximum steady state error is 0.001 Hz (maximum *TVE* of 0.0064 %). The NTA-LS settling time is 0.262 s and its maximum steady state error is 0.0002 Hz (maximum *TVE* of 0.0013%). The PLL settling time is 0.297 s and its maximum steady state error is 0.006 Hz (maximum *TVE* of 0.0385%). Figure 5.10 shows the estimated frequency for a voltage waveform with 1.0 p.u. fundamental and 0.2 p.u. of an 110 Hz interharmonic. The frequency changes from 50.0 to 56.0 Hz at 1.0 s.

The NTA-LS, NTA, DSPOC, and PLL maximum steady state errors are 0.001 Hz,

0.05 Hz, 0.006 Hz, and 0.002 Hz respectively. The NTA-LS, NTA, DSPOC, and PLL maximum steady state *TVEs* are 0.006%, 0.28%, 0.03%, and 0.01% respectively. The settling times for NTA-LS, NTA, DSPOC, and PLL are 0.18 s, 0.218 s, 0.40 s, and 0.39 s respectively.

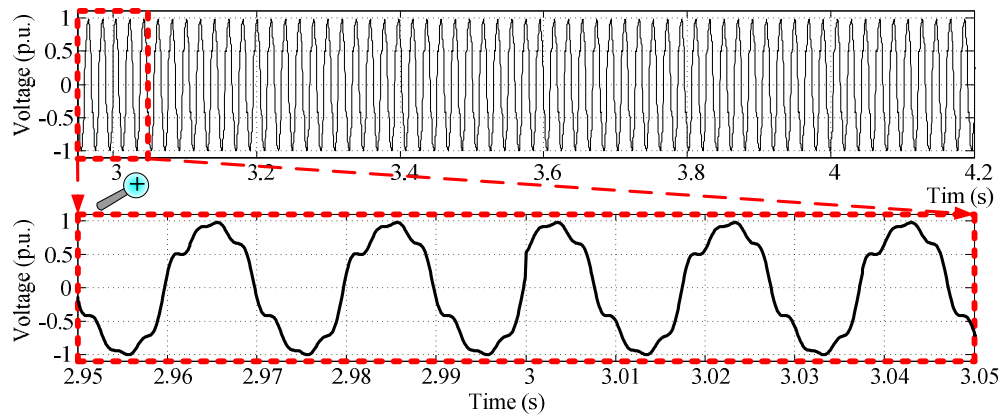


Figure 5.8. Case 3: Harmonic contamination

Instantaneous voltage waveform captured at 10 kHz sampling frequency.

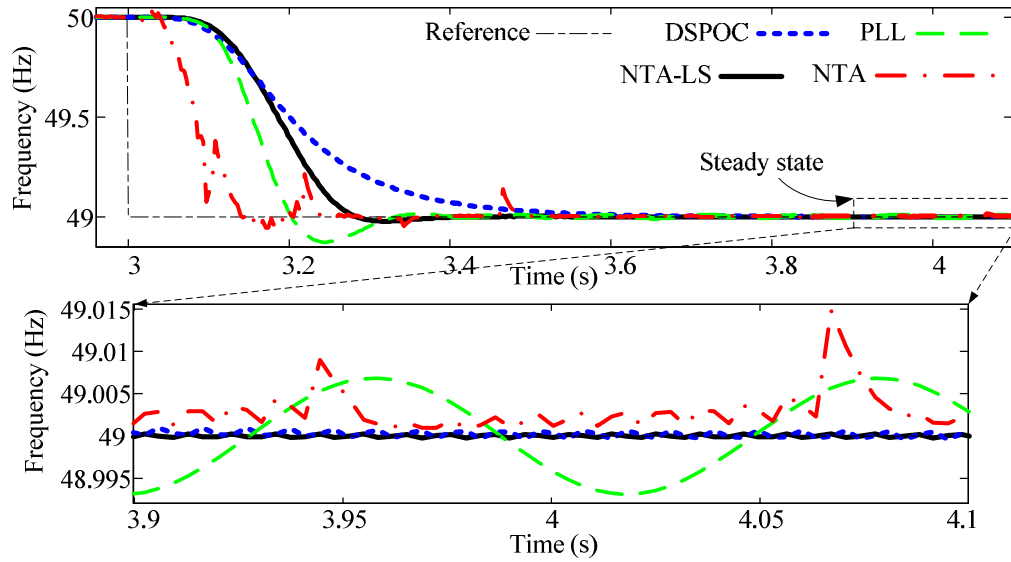


Figure 5.9. Case 3: Harmonic contamination

Frequency estimation at 285.71 Hz sampling frequency by the NTA-LS, NTA, DSPOC, and PLL techniques.

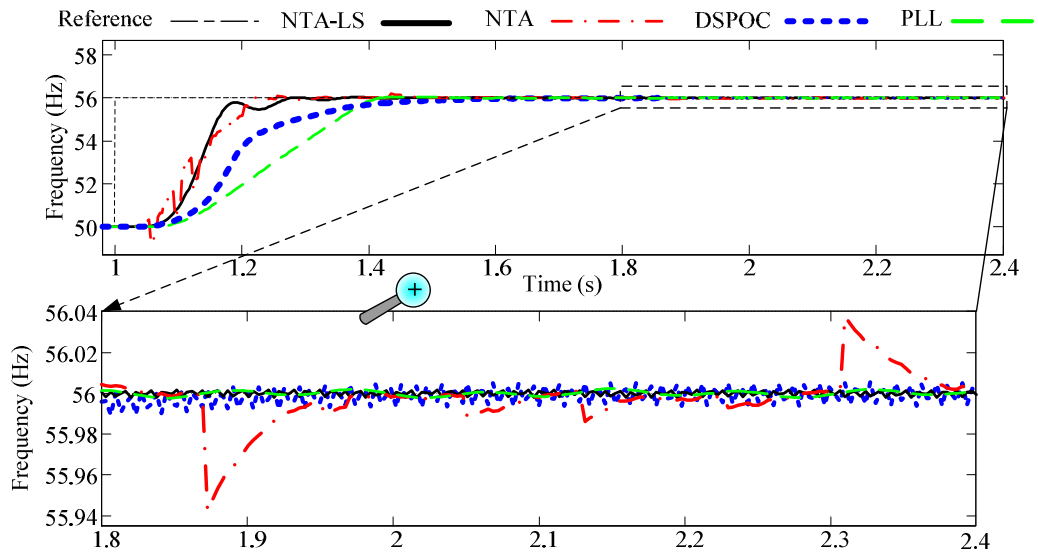


Figure 5.10. Case 3: Interharmonic contamination

Frequency estimation at 285.71 Hz sampling frequency by the NTA-LS, NTA, DSPOC, and PLL techniques.

5.5.4. Case 4: Noise Immunity

This section evaluates the robustness of the proposed method against noise contamination. A zero mean Gaussian noise is added to the 1.0 p.u. fundamental component voltage waveform. The signal-to-noise-ratio (*SNR*) is 10 dB. The voltage frequency changes from 50.0 Hz to 54.0 Hz at 1.0 s. Figure 5.11 shows the simulated voltage waveform and Figure 5.12 shows the frequency estimation. The maximum steady state errors for NTA-LS, NTA, PLL, and DSPOC are 0.009 Hz, 0.071 Hz, 0.032 Hz, and 0.0103 Hz respectively. The maximum steady state *TVEs* for NTA-LS, NTA, PLL, and DSPOC are 0.0524%, 0.4131%, 0.1862%, and 0.06%.

Coloured noise is conveniently generated by passing white noise through an LPF [217], [218]. When the dense sampling frequency is considered to be 2 kHz, the cut-off frequency should be smaller than the half of the dense sampling frequency (1000 Hz) according to the discussions of Chapter 4. Accordingly, the LPF is chosen to be a first order filter with the cut-off frequency of 950 Hz. Table 5.1 and Table 5.2 respectively show the average *TVEs* for compliance levels 0 and 1 according to IEEE Standard C37.118-2005 at different coloured noise levels. $|\Omega_e|$ is the angular frequency estimation error absolute value.

Another type of noise in the electrical systems is cyclostationary noise which shows periodically time-varying properties [219], [220]. The noise is produced based on the cyclostationary noise model of [220]. The noise is modulated at the frequency of 500 Hz. Table 5.3 and Table 5.4 respectively show the average *TVEs* for compliance levels 0 and 1 according to IEEE Standard C37.118-2005 at different cyclostationary

noise levels.

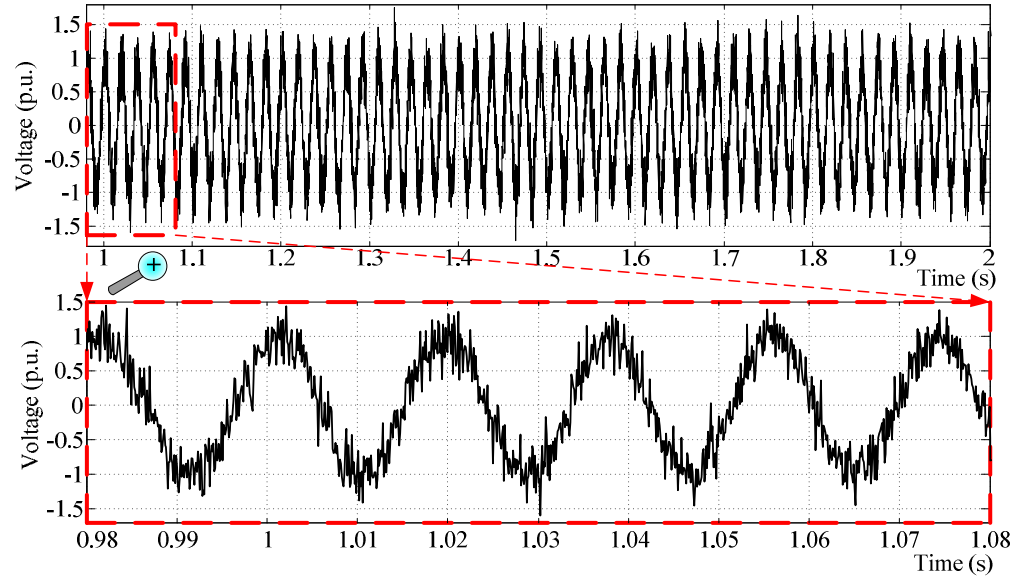


Figure 5.11. Case 4: Noise immunity

Voltage waveform contaminated with a zeros mean Gaussian noise, $SNR=10$ dB,
captured at 10 kHz.

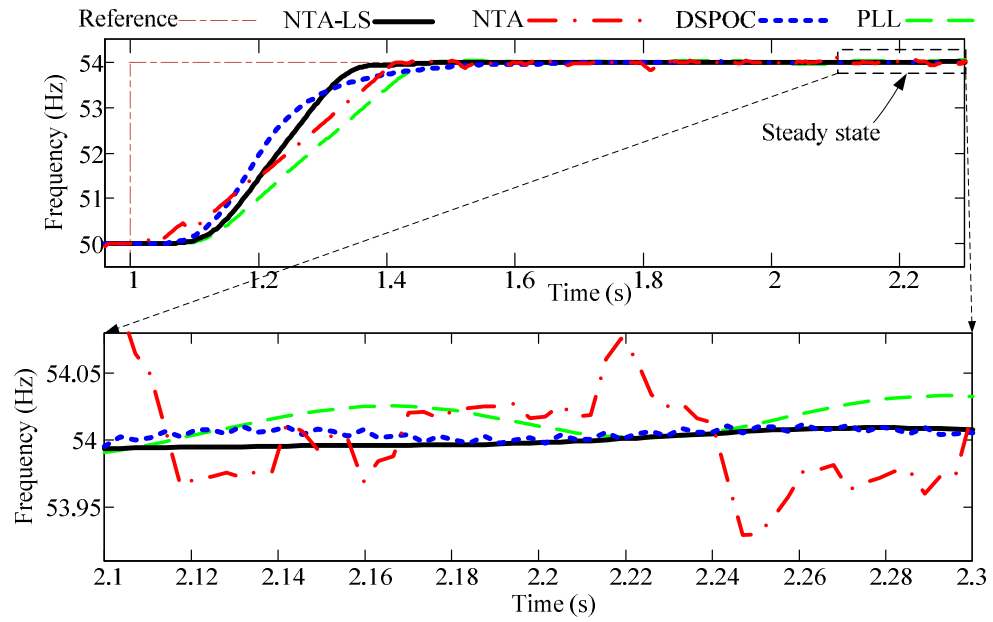


Figure 5.12. Case 4: Noise immunity

The estimated frequency in presence of a Gaussian noise, $SNR=10$ dB, estimation at 285.71 Hz sampling frequency.

TABLE 5.1. CASE 4: NOISE IMMUNITY FOR COLOURED NOISE AND COMPLIANCE LEVEL 0, *TVE* FOR DIFFERENT LEVELS OF COLOURED NOISE FOR 0.5 HZ FREQUENCY DRIFT.

<i>SNR</i> (dB)	Average <i>TVE</i> (%)				Average $ \Omega_e $ (radian/s)			
	NTA-LS	NTA	DSPOC	PLL	NTA-LS	NTA	DSPOC	PLL
0	0.19	1.62	0.17	0.40	0.19	1.61	0.17	0.40
5	0.10	0.16	0.09	0.20	0.11	0.20	0.09	0.20
10	0.06	0.12	0.05	0.12	0.06	0.15	0.05	0.12
15	0.03	0.10	0.03	0.07	0.03	0.11	0.03	0.07
20	0.02	0.05	0.016	0.04	0.02	0.06	0.016	0.04
25	0.01	0.04	0.01	0.02	0.01	0.05	0.01	0.02
30	0.006	0.02	0.005	0.01	0.006	0.02	0.005	0.01

TABLE 5.2. CASE 4: NOISE IMMUNITY FOR COLOURED NOISE AND COMPLIANCE LEVEL 1, *TVE* FOR DIFFERENT LEVELS OF COLOURED NOISE FOR -5.0 HZ FREQUENCY DRIFT.

<i>SNR</i> (dB)	Average <i>TVE</i> (%)				Average $ \Omega_e $ (radian/s)			
	NTA-LS	NTA	DSPOC	PLL	NTA-LS	NTA	DSPOC	PLL
0	0.21	2.75	0.70	0.80	0.20	2.83	0.65	0.70
5	0.12	0.87	0.37	0.57	0.11	0.90	0.35	0.55
10	0.07	0.80	0.21	0.40	0.06	0.86	0.19	0.32
15	0.04	0.71	0.12	0.25	0.03	0.61	0.11	0.23
20	0.02	0.32	0.07	0.15	0.02	0.31	0.06	0.13
25	0.01	0.30	0.04	0.09	0.01	0.30	0.04	0.08
30	0.008	0.10	0.03	0.05	0.007	0.11	0.03	0.05

TABLE 5.3. CASE 4: NOISE IMMUNITY FOR CYCLOSTATIONARY NOISE AND COMPLIANCE LEVEL 0, *TVE* FOR DIFFERENT LEVELS OF CYCLOSTATIONARY NOISE FOR -0.5 HZ FREQUENCY DRIFT.

SNR (dB)	Average <i>TVE</i> (%)				Average $ \dot{\Omega}_e $ (radian/s)			
	NTA-LS	NTA	DSPOC	PLL	NTA-LS	NTA	DSPOC	PLL
0	0.26	1.14	0.22	0.56	0.26	1.15	0.20	0.54
5	0.15	0.40	0.135	0.36	0.15	0.35	0.13	0.36
10	0.09	0.25	0.08	0.2	0.09	0.25	0.074	0.2
15	0.05	0.22	0.042	0.11	0.04	0.24	0.4	0.11
20	0.03	0.10	0.023	0.07	0.03	0.12	0.025	0.07
25	0.01	0.08	0.013	0.04	0.01	0.08	0.013	0.04
30	0.008	0.06	0.007	0.03	0.008	0.06	0.007	0.03

TABLE 5.4. CASE 4: NOISE IMMUNITY FOR CYCLOSTATIONARY NOISE AND COMPLIANCE LEVEL 1, *TVE* FOR DIFFERENT LEVELS OF CYCLOSTATIONARY NOISE FOR 5.0 HZ FREQUENCY DRIFT.

SNR (dB)	Average <i>TVE</i> (%)				Average $ \dot{\Omega}_e $ (radian/s)			
	NTA-LS	NTA	DSPOC	PLL	NTA-LS	NTA	DSPOC	PLL
0	0.27	2.55	0.72	0.80	0.30	2.76	0.80	0.85
5	0.15	0.65	0.40	0.61	0.17	0.70	0.44	0.65
10	0.09	0.50	0.23	0.39	0.10	0.53	0.25	0.43
15	0.05	0.36	0.13	0.25	0.05	0.42	0.14	0.27
20	0.03	0.15	0.07	0.17	0.03	0.18	0.08	0.18
25	0.02	0.11	0.04	0.09	0.02	0.11	0.05	0.10
30	0.01	0.10	0.03	0.05	0.01	0.10	0.03	0.06

5.5.5. Case 5: Switching Notches and Harmonics

Figure 5.13 shows a dc motor which is fed from an inductive three-phase source (G_v and Z_G) through a six-pulse thyristor bridge. The dc motor is simulated by the equivalent circuit model of Figure 5.13. A pulse generator synchronized on the source voltages provides the trigger pulses for the six thyristors. The system has been simulated in the MATLAB-Simulink software. In Figure 5.13, G_v is an ideal three-phase voltage source with the voltage of 380 line-to-line rms. The source impedance (Z_G) is made of a 0.01Ω resistance and a 1 mH inductance. R' , L' and E' are respectively 1 Ω , 20 mH, and 120 V for the dc motor model. The voltage waveform is captured at B_1 . The fast Fourier transform (FFT) analysis on the voltage waveform has been done at 50 Hz and is shown in Table 5.5.

The voltage source is programmed to change the frequency from 50 Hz to 45 Hz at 2.0 s and the voltage waveform is shown in Figure 5.14. As seen in Figure 5.15, the maximum steady state errors for NTA-LS, NTA, DSPOC, and PLL are 0.016 Hz, 0.045 Hz, 0.012 Hz, and 0.03 Hz respectively.

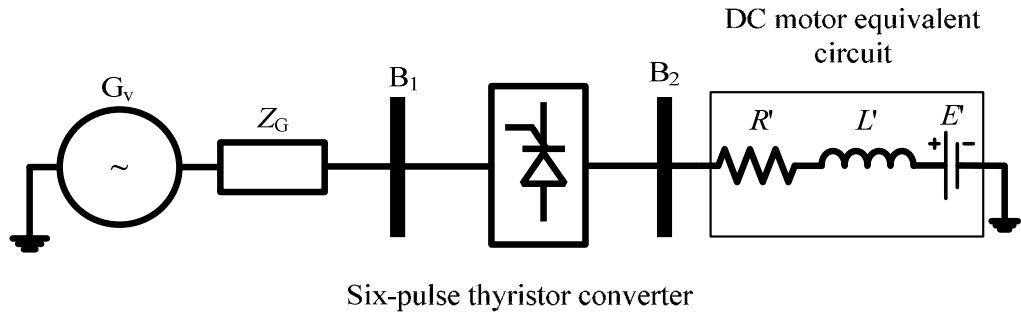


Figure 5.13. Case 5: Switching notches and harmonics

Simulated dc motor powered by a six-pulse thyristor converter.

TABLE 5.5. CASE 5: SWITCHING NOTCHES AND HARMONICS,
HARMONIC CONTENT OF THE VOLTAGE WAVEFORM AT B_1 .

Harmonic order	Percentage of the fundamental amplitude	Harmonic order	Percentage of the fundamental amplitude
5	4.90	23	3.19
7	2.08	25	2.75
11	3.69	29	3.08
13	2.52	31	2.87
17	3.40	35	3.06
19	2.67	37	2.82

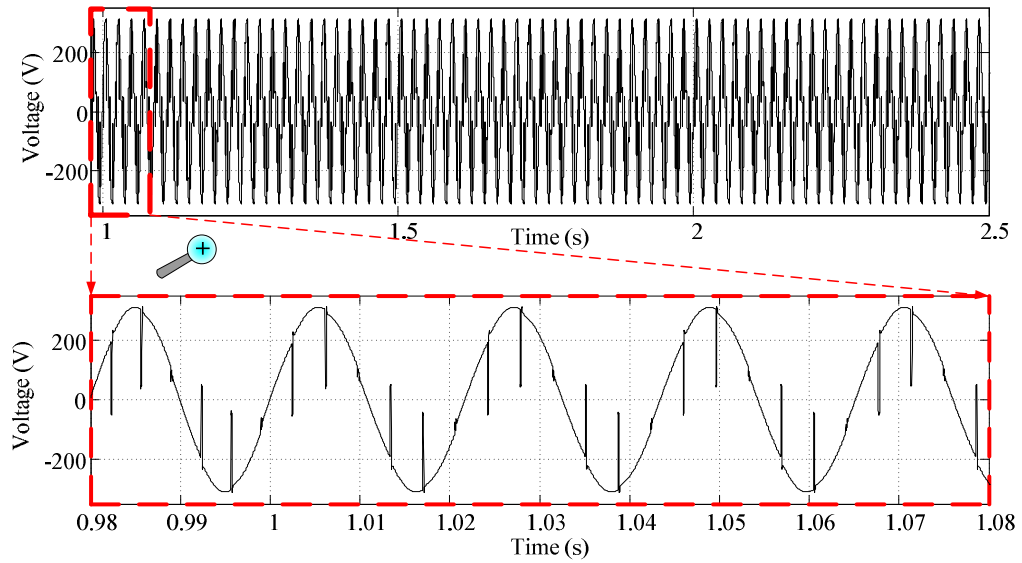


Figure 5.14. Case 5: Switching notches and harmonics

Phase-A line-to-neutral voltage waveform captured at 10 kHz.

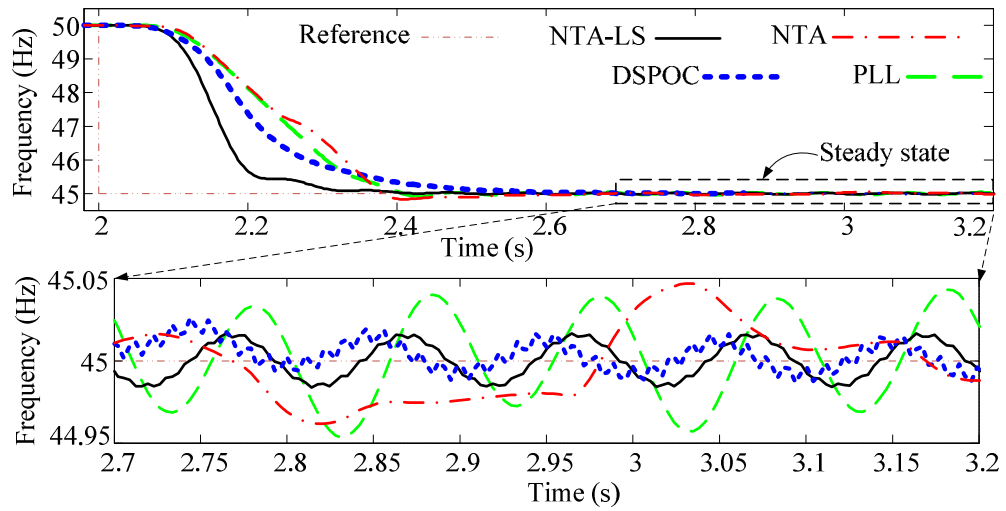


Figure 5.15. Case 5: Switching notches and harmonics

Frequency estimation at 285.71 Hz sampling frequency by the NTA-LS, NTA, DSPOC, and PLL techniques.

5.6. Real-Time Implementation

This section presents real-time implementation of the NTA-LS and DSPOC methods to track the power system fundamental frequency. The DS1104 R&D digital control board (dSPACE) is used for real-time implementation [136]. The voltage waveform is used to estimate the frequency. Three types of experiments have been conducted and the results are presented. The sampling frequency for the digital control board to implement all algorithms is 285.71 Hz and the nominal fundamental power system frequency is 50.0 Hz.

Three types of devices have been used to conduct the experiments as follows:

- Using a function generator to produce voltage waveforms;
- Using a power system simulator hardware; and
- Using a programmable power supply.

5.6.1. Case 6: Non-Sinusoidal Waveform Frequency Tracking

A triangle voltage waveform is produced by a function generator to produce a non-sinusoidal voltage waveform. The typical shape of the produced voltage at 50.0 Hz with 3.0 V amplitude is shown in Figure 5.16 (a) where the voltage waveform is captured by a digital oscilloscope at 100 kHz sampling frequency. The undersampled voltage waveform captured by the dSPACE at 285.71 Hz sampling frequency is shown in Figure 5.16 (b). The frequency of the produced voltage changes from 50.0 Hz to 49.0 Hz and the performance of the NTA-LS and DSPOC are presented in Figure 5.17. The NTA-LS algorithm estimates the correct frequency after 0.14 s and the DSPOC

completes its frequency estimation task after 0.30 s.

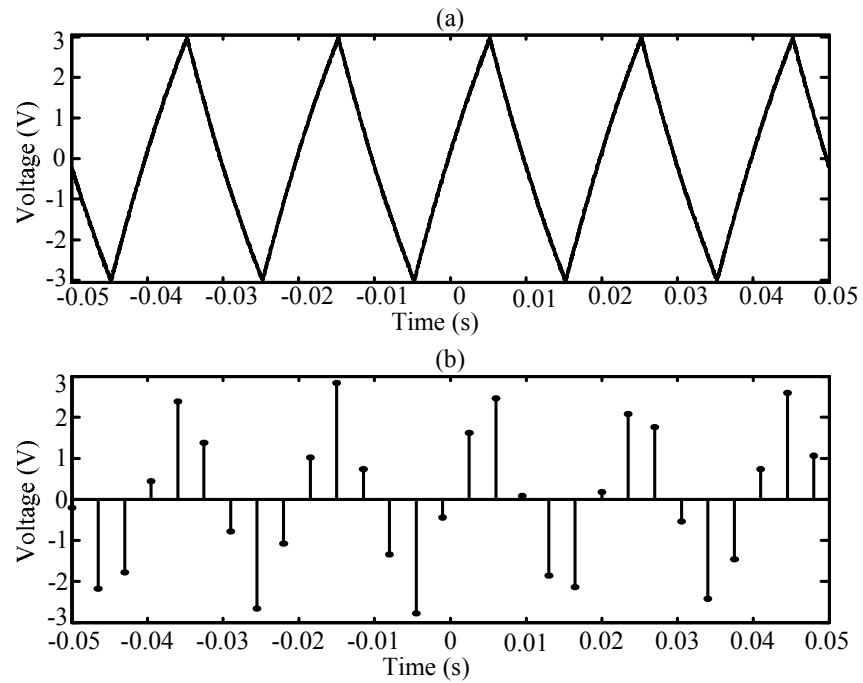


Figure 5.16. Case 6: Non-sinusoidal waveform frequency tracking

(a) the triangle voltage waveform produced by a function generator captured at 100 kHz by a digital oscilloscope

(b) the triangle voltage waveform produced by a function generator captured at 285.71 Hz by the dSPACE.

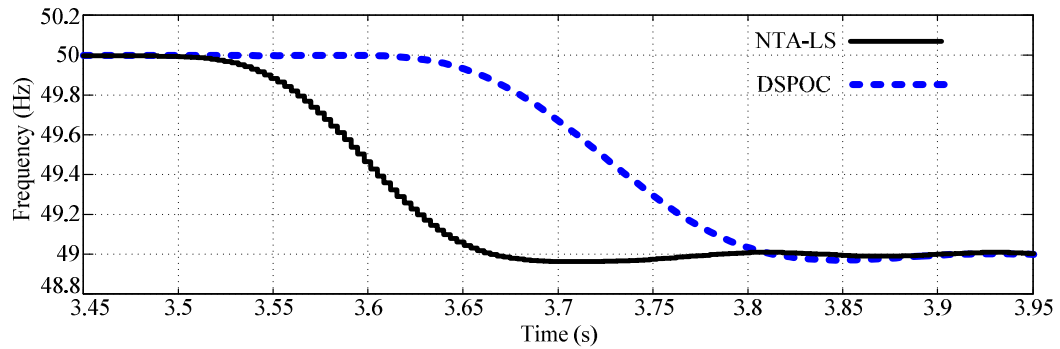


Figure 5.17. Case 6: Non-sinusoidal waveform frequency tracking

Frequency estimation at 285.71 Hz sampling frequency.

5.6.2. Case 7: Stepwise Dynamic Frequency Change

The function generator is used to produce a sinusoidal voltage waveform with constant amplitude of 3.0 V and variable frequency which changes from 46.0 Hz to 54.0 Hz in a stepwise manner to study the dynamic performance of the proposed method. The typical sinusoidal voltage waveform at the constant frequency of 50.0 Hz and its undersampled pattern are shown in Figure 5.18 (a) and Figure 5.18 (b) respectively. As Figure 5.19 shows, the NTA-LS estimation shows a faster dynamic than what the DSPOC method does in tracking the frequency variation.

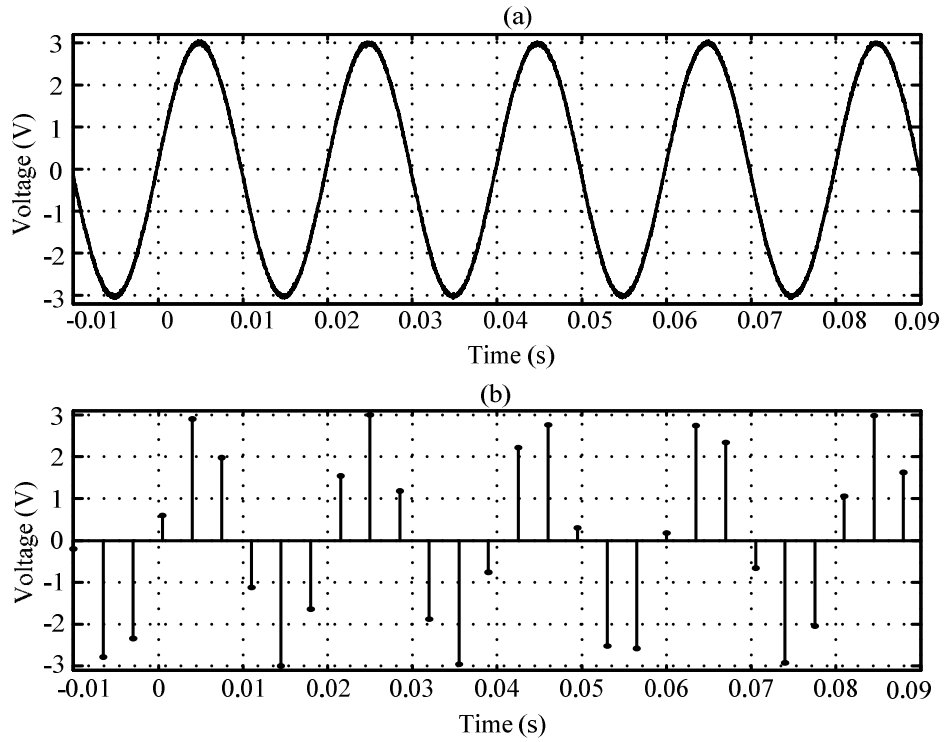


Figure 5.18. Case 7: Stepwise frequency change between 46.0 Hz and 54.0 Hz

(a) the typical sinusoidal voltage waveform produced by a function generator which is captured at 100 kHz sampling frequency by a digital oscilloscope

(b) the typical sinusoidal voltage waveform produced by a function generator which is captured at 285.71 Hz sampling frequency by the dSPACE.

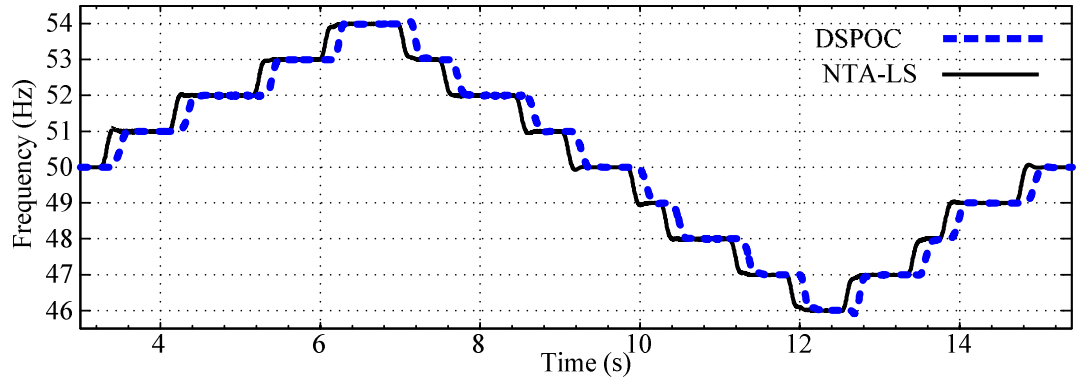


Figure 5.19. Case 7: Stepwise frequency change between 46.0 Hz and 54.0 Hz

Frequency estimation at 285.71 Hz sampling frequency.

5.6.3. Case 8: Power System Simulator Frequency Monitoring

In this case, two experiments have been conducted on the power system simulator (PSS1). The PSS1 is a hardware, scale model of a power system, designed to mimic real systems and modern practices [221]. The single-line diagram of the considered power system is shown in Figure 5.20 and Figure 5.21 shows the PSS1 laboratory setup. To describe the power system parameters in per unit, the base voltages are chosen to be 220 V/110 V (line-to-line) and the base currents are 5.25 A/10.5 A correspondingly. The base voltampere is 2 kVA for the whole system. The power system parameter values of Figure 5.20 for 50.0 Hz are presented in Table 5.6 [221]. In Table 5.6, X_d is the d -axis reactance, X'_d is the transient d -axis reactance, X''_d is the sub-transient d -axis reactance, X_q is the q -axis reactance, X'_q is the transient q -axis reactance, and X''_q is

the sub-transient q -axis reactance, X_2 is the negative sequence reactance, and X_0 is the zero sequence reactance of the generator.

Figure 5.22 (a) shows the typical phase-A line-to-neutral voltage waveform on B_1 at 50.0 Hz fundamental frequency which is captured by a digital oscilloscope at 100 kHz sampling frequency, when the resistive load and the capacitor bank are connected. The undersampled phase-A line-to-neutral voltage waveform for the aforementioned condition which is sampled at 285.71 Hz by the dSPACE is shown in Figure 5.22 (b).

The first experiment shows the effect of load switching on the power system frequency when the resistive load on B_4 is connected. The result is temporary drop in the generator frequency. The phase-A line-to-neutral voltage is captured at B_1 and is shown in Figure 5.23 (a). The reference generator frequency is measured by using the generator shaft speed which is provided as a voltage signal on the PSS1 front panel. The estimated frequency by the NTA-LS and DSPOC methods is presented in Figure 5.23 (b). The NTA-LS algorithm tracks the instantaneous changes faster than the DSPOC. The NTA-LS shows 0.10 s estimation delay and the DSPOC delay is around 0.24 s in this case. IEEE Standard C37.118-2005 defines the required PMU reporting rates of 10 and 25 times per second for 50 Hz power systems depending on the type of application. The NTA-LS frequency estimation matches the required PMU reporting rate of 10 times per second although its measurement will show 0.06 s delay for the reporting rate of 25 times per second.

The second experiment on the PSS1 is conducted by using the supervisory control and data acquisition (SCADA) system which controls and monitors the PSS1 operation. A frequency step change of -0.38 Hz is applied to the generator G by using the SCADA

frequency control system. The power system circuit is the same as shown in Figure 5.20 and the phase-A line-to-neutral voltage which is captured at B₁ is shown in Figure 5.24 (a). As seen in Figure 5.24 (b), the NTA-LS algorithm estimates the correct frequency after 0.10 s although the DSPOC estimation takes about 0.20 s in this case.

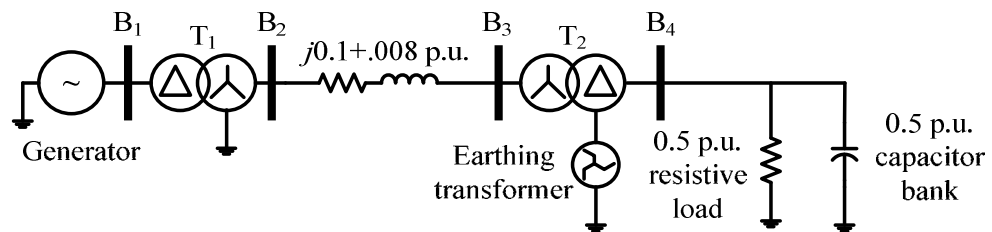


Figure 5.20. Case 8: Power system simulator frequency monitoring

Single-line diagram of the power system for the frequency estimation experiment on the PSS1.



Figure 5.21. Case 8: Power system simulator frequency monitoring

The power system simulator PSS1 in a laboratory setup for real-time power system frequency measurement experiment.

TABLE 5.6. CASE 8: POWER SYSTEM SIMULATOR FREQUENCY MONITORING
PARAMETER VALUES OF THE SIMULATED POWER SYSTEM COMPONENTS FOR FIGURE 5.20
AT 50.0 Hz.

System component	Line volts (V)	3-Phase (kVA)	Reactance (p.u.)	Resistance (p.u.)
Generator	220	6.5	-	-
X_d	-	-	0.478	-
X_q	-	-	0.167	-
X'_d	-	-	0.047	-
X'_q	-	-	0.167	-
X''_d	-	-	0.039	-
X''_q	-	-	0.191	-
X_2	-	-	0.044	-
X_0	-	-	0.017	-
Transformer T ₁	220/220	5.0	0.052	0.15
Transformer T ₂	220/110	2.0	0.13	0.054
Earthing transformer	220/110	2.0	0.018	0.074

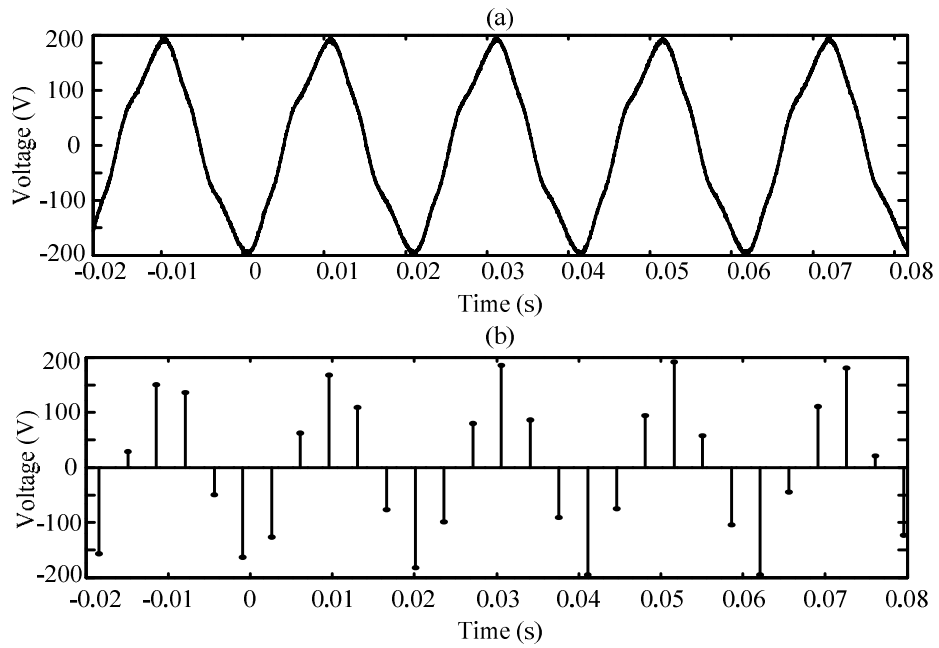


Figure 5.22. Case 8: Power system simulator frequency monitoring

(a) the typical phase-A line-to-neutral voltage captured at the sampling frequency of 100 kHz by a digital oscilloscope

(b) the typical phase-A line-to-neutral voltage captured at the sampling frequency of 285.71 Hz by the dSPACE.

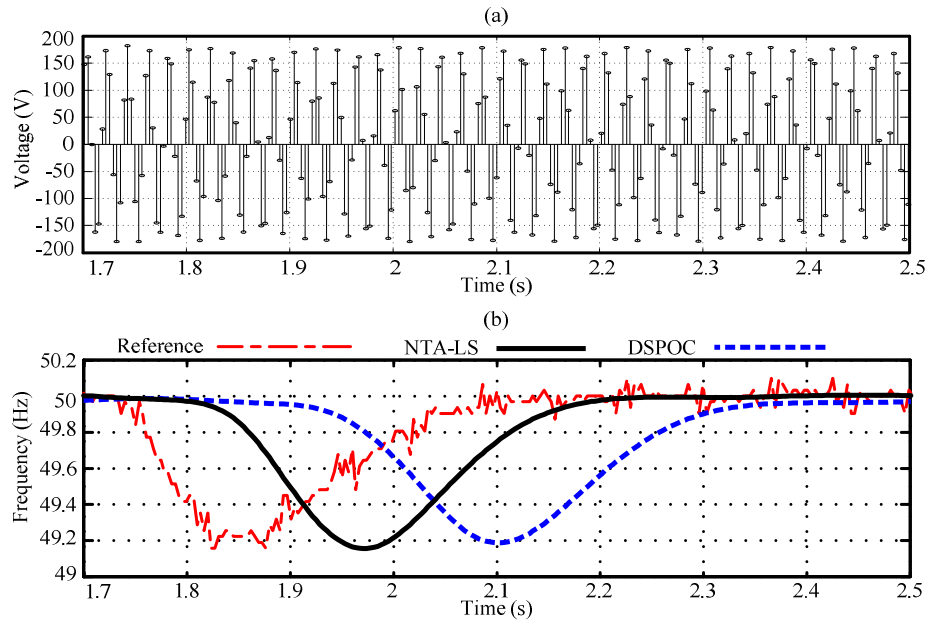


Figure 5.23. Case 8: resistive load switching

(a) phase-A line-to-neutral voltage waveform samples at 285.71 Hz sampling frequency

(b) frequency estimation at 285.71 Hz sampling frequency.

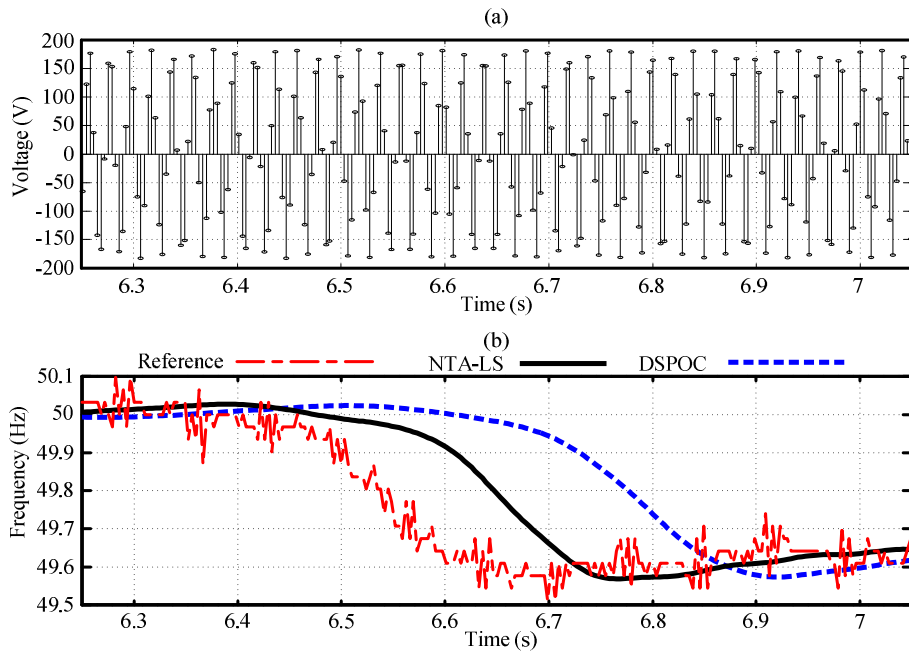


Figure 5.24. Case 8: step frequency change

(a) phase-A line-to-neutral voltage waveform samples at 285.71 Hz sampling frequency

(b) frequency estimation at 285.71 Hz sampling frequency.

5.6.4. Case 9: Harmonic Contamination and Ramp Frequency Variation

In this section, the single-phase voltage waveform is produced by a programmable power supply [222] and sensed by a voltage transducer which provides a signal for the dSPACE input. The fundamental frequency of the produced voltage is 50.0 Hz and its fundamental rms value is 240 V, which are chosen according to the distribution frequency and voltage level of the Australian electricity network. The voltage harmonic contamination level is the same as Case 3, but all harmonic components are in phase with the fundamental component. This voltage waveform with a fixed fundamental frequency of 50.0 Hz which is captured by a digital oscilloscope at 100 kHz and its undersampled version are shown in Figure 5.25 (a) and (b) respectively.

The voltage fundamental frequency is programmed to change monotonously from 50.0 Hz to 50.5 Hz during 0.5 s in presence of the aforementioned harmonic contamination level. The undersampled voltage waveform of the line-to-neutral is shown in Figure 5.26 (a). Figure 5.26 (b) shows the estimated frequency by the NTA-LS and DSPOC methods. The NTA-LS method shows faster estimation performance than the DSPOC one, but both approaches complete the frequency estimation task with the same accuracy.

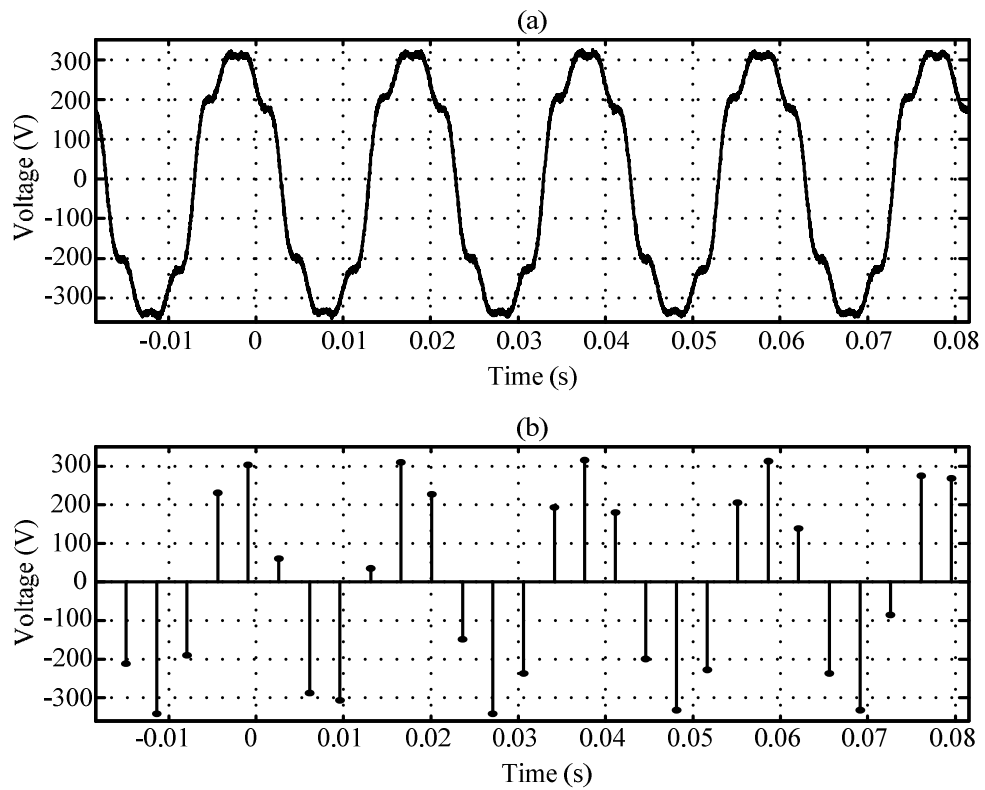


Figure 5.25. Case 9: Harmonic contamination and ramp frequency variation

(a) line-to-neutral voltage waveform captured at 100 kHz sampling frequency by a digital oscilloscope

(b) line-to-neutral voltage waveform captured at 285.71 Hz sampling frequency by the dSPACE.

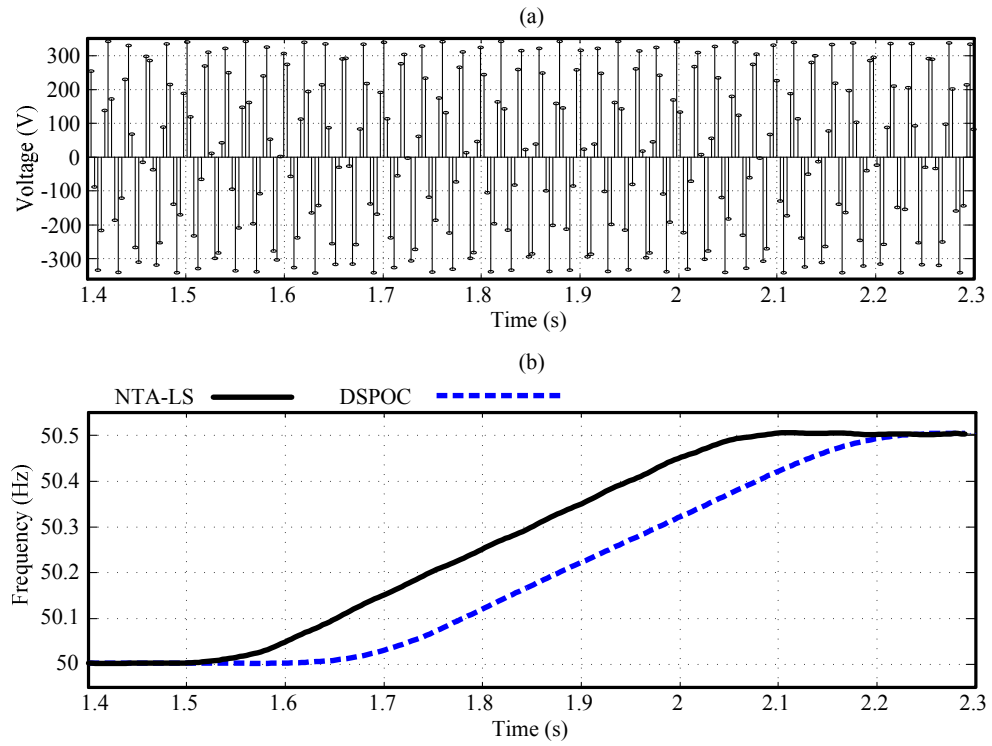


Figure 5.26. Case 9: Harmonic contamination and ramp frequency variation
 (a) undersampled line-to-neutral voltage waveform samples at 285.71 Hz sampling frequency
 (b) frequency estimation at 285.71 Hz sampling frequency.

5.7. Conclusion

This chapter presented a new real-time optimisation approach to estimate the instantaneous power system frequency based on slow sampling frequency implementation. The adopted optimisation approach is based on a two-stage mathematical model. The first stage is a Newton-type algorithm (NTA) which estimates the line-to-neutral voltage phase-angle and its variation. The second stage works based on the least-squares (LS) minimization technique which extracts the instantaneous power system frequency by processing the information in the NTA phase-angle estimation.

The correct performance of the proposed NTA-LS approach in presence of harmonics/interharmonics and noise is evaluated by presenting simulation results in MATLAB-Simulink environment. Moreover, the introduced method shows its precise and correct performance for real-time slow sampling implementation on a DSP platform through extensive real-time experiments. The proposed NTA-LS technique is more stable than the conventional NTA technique. The presented mathematical developments for NTA and LS techniques also improve their calculation efficiency for real-time DSP implementation. The proposed NTA-LS frequency estimation technique shows faster estimation speed and higher accuracy in comparison with the PLL, NTA, and DSPOC techniques for slow sampling frequency estimation according to the simulations results and experiments presented in this chapter.

Chapter 6 : Summary and Conclusion

In the previous chapters, the thesis documented the claims of originality summarised in Section 1.3 while providing technical literature overview to offer justification of the research motivation and base such claims. The simulation studies and real-time implementation results, which have been presented in Chapters 2-5, have proven the correct performance of the presented new estimation tools. The IEEE and IEC standards have been used to conduct the case studies and evaluate the performance of each method. Specifically, the thesis in each chapter offered the following.

Chapter 1 critically reviewed the ANF, EPLL, ADALINE, RDFT, LS, KF, NTA, and RLS techniques.

In **Chapter 2**, a new hybrid LSK technique was proposed for frequency adaptive voltage envelope and flicker estimation. The LS and Kalman techniques were critically revisited to modify them for stable DSP implementation. The DSPOC frequency estimation technique has also been modified for recursive implementation on DSPs. The correct and stable performance of the proposed LSK technique in presence of harmonics, frequency variation, voltage amplitude variations, and noise was evaluated by presenting extensive experimental results.

In **Chapter 3**, the RLS technique has been critically revisited. This very detailed analysis was used to introduce a new DRLS harmonics and phasors estimation technique for real-time DSP implementation. The concept of the DRLS technique is also extended for synchronized phasors and instantaneous symmetrical components

extraction. The proposed DRLS technique shows considerable improvement in terms of reducing the DSP turnaround-time when compared to the conventional RLS one. The presented simulation results prove its correct performance under drastic fault conditions and frequency variations. The DSP implementation experiments prove its correct, stable, and efficient performance for real-time phasors and harmonics estimation.

In **Chapter 4**, the estimation of harmonics and interharmonics based on the undersampling strategy was presented. The concept of staggered undersampling was used for harmonics/interharmonics estimation by using a very low sampling frequency. This chapter also presented an efficient MGS technique. The estimation accuracy and latency of the proposed MGS technique for different downsampling factors were also investigated. The staggered undersampling concept has been extended for synchrophasor detection in WAMSs. The presented simulation studies and real-time DSP experiments prove the correct performance of the proposed slow sampling technique for harmonics, interharmonics, and phasors estimation.

In **Chapter 5**, the problem of slow sampling real-time power system frequency estimation is addressed along with presenting a new NTA-LS technique. The effects of noise, harmonics, notches, voltage steps, and load switching on the proposed slow sampling frequency estimation technique were investigated by presenting extensive MATLAB simulations and real-time DSP experiments. The presented simulation case studies and experimental results prove correct, accurate, and robust performance of the proposed frequency estimation technique.

6.1. Conclusion

This thesis has focused on the application of new numerical optimisation techniques as tools for power system phasors, harmonics, and frequency estimation. The key objective was to introduce new numerical techniques as power system estimation tools for DSP implementation.

A critical analysis of the LS, KF, RLS, gradient search, and NTA techniques is provided. This very detailed analysis lays the basis to modify these techniques for accurate and stable power system parameters estimation.

The presented extensive simulation studies and real-time experiments resulted into the following findings and observations:

- ❖ A new least-squares-Kalman (LSK) technique was presented for frequency adaptive voltage envelope and flicker estimation in Chapter 2. The conventional LS technique relies on quantizing the power system frequency and repeating the calculations to find the optimum answer. The proposed frequency adaptive LS technique eliminates the inherent calculation redundancy of the conventional LS technique and significantly improves the LS technique estimation efficiency. The two-layer form of KF for flicker estimation requires prior knowledge of the number of harmonics which distort the voltage waveform. Accommodating a large number of harmonics in the KF equations brings a huge computational burden and impedes its practical application. Besides, there is always the possibility that some harmonic components appear in the power system which have not been assigned in the KF equations. Chapter 2 presents a solution to modify the KF technique by

replacing the envelope tracking layer of KF with the presented frequency adaptive LS technique. The proposed LSK method effectively improves the efficiency and stability of the KF for DSP implementation by accommodating the dc component and high order harmonics in the residual term of LS technique. The correct performance of the proposed LSK method in presence of harmonics, noise, frequency variations, and voltage fluctuations has been evaluated by conducting extensive real-time experiments on R&D DSPs. The accuracy of the LSK technique to track the IFL is superior to that of the DFT in presence of frequency drifts. The proposed adaptive LS technique has also shown higher accuracy than that of the EPLL and ANF techniques for DSP implementation when the sampling frequency becomes smaller due to hardware limitations.

- ❖ A new DRLS technique has been introduced in Chapter 3 to improve the computational efficiency and stability of the conventional RLS technique. The basis of developing the DRLS technique is presenting a new analysis on the average model of the nonlinear form of the RLS technique. The RLS technique is decoupled into parallel units for a modular implementation. Absence of presumed harmonic components will cause singularity in the conventional RLS technique, as it has been discussed in Chapter 1. The proposed new arrangement of DRLS technique rectifies the problem of singularity since each module is dedicated to track a single harmonic component. Real-time DSP implementation of the new DRLS technique has proven that it is considerably more computationally efficient when compared

with the conventional RLS technique according to the findings of Chapter 3. The fault simulation studies have also proven the DRLS technique superior performance in comparison to that of the EPLL technique. The DRLS technique is also more efficient than RDFT and ADALINE techniques to estimate harmonics and phasors in highly distorted power systems environments.

- ❖ The undersampling strategy has been investigated to estimate harmonics/interharmonics, and phasors of power systems in Chapter 4. The gradient search technique has also been revisited by proposing a new slow sampling modified gradient search (MGS) estimation technique. The aim of this chapter was to provide extensive simulation studies and real-time DSP experiments to verify the possibility of applying sampling frequencies lower than what the Nyquist-Shannon theorem defines. The application of undersampling has been presented in the technical literature based on the data windowing and FFT technique but iterative tracking of nonstationary loads has not been addressed comprehensively. The proposed slow sampling MGS technique successfully tracks the nonstationary load variations. The delays of applying the undersampling technique have been characterised and a guideline to choose the proper undersampling factor is presented in Chapter 4. The proposed slow sampling MGS harmonics/interharmonics estimation technique is also more efficient than the conventional undersampled DFT technique since it relays on iterative calculations and does not need data windowing. This chapter has also presented an extension of staggered

undersampling concept to reduce the estimations delays associated with undersampled estimates. This improvement in the estimation pace of undersampling technique and the fact that the communication delays can be seen as undersampling (as discussed in Chapter 4) form the basis to introduce a novel application of undersampling for WAMSs. The proposed extended staggered undersampling technique for synchrophasor estimation is a promising method to use the internet broadband services for distribution level WAMSs implementation and offers a reliable backup for transmission level synchrophasor detection in absence of GPS.

- ❖ This research work also reported a new real-time NTA-LS optimisation technique for slow sampling estimation of power system frequency in chapter 5. The new NTA-LS method significantly reduces the computational burden of conventional NTA. The proposed modification of NTA also improves its stability and presents a new solution to revive it from singularity during drastic changes in the voltage amplitude. The mathematical justifications of NTA and LS techniques also significantly reduce their matrix operations for more efficient DSP implementation. The NTA-LS technique shows better stability and estimation pace than the conventional NTA one. The estimation pace and accuracy of the NTA-LS technique is also superior to that of the DSPOC and PLL techniques for slow sampling frequency estimation. The NTA-LS reaches the required TVE level by the IEEE Standard C 37.118-2005 faster than the DSPOC and PLL techniques. The proposed NTA-LS technique frequency estimation accuracy is also superior to that of the NTA, PLL, and

DSPOC under the presence of noise, harmonics, interharmonics, frequency steps, voltage steps, and notches.

6.2. Future Research

The following future research is proposed in line with the application of numerical optimisation techniques for power system parameter estimation:

- Flicker estimation based on IFL detection by using KF and LS technique has been presented in this thesis. Voltage flicker is also considered in terms of interharmonic components in the power system technical literature. On the other hand, the RLS technique is capable of tracking state transitions and calculating autocorrelation matrixes recursively. Therefore, developing a platform to estimate the flicker based on interharmonic components extraction by using the proposed DRSL technique remains to be investigated.
- The EPLL technique is a simple and efficient technique which however requires further improvement under fault and severe unbalance conditions. The EPLL is controlled by its regulating parameters as discussed in Chapter 1. The EPLL regulating parameters are tuned based on nominal per-unit power system parameters and assuming a certain amount of unbalance in the power system. These settings do not remain optimum when there is a drastic change in the power system because of faults and severe unbalances. Tuning the EPLL under these conditions proves to be a very hard task which requires considering different scenarios and observing its performance under each one of them. Therefore, adding a supervisory mechanism to keep the EPLL

regulating parameters tuned, improve its accuracy, and enhance its estimation pace is yet another open field of research.

- The RLS technique has already been applied for a wide range of problems including power system parameter estimation and mode estimation. The RLS technique operation is greatly influenced by choosing its forgetting factor. The RLS dynamics is also controlled by its Eigenvalues. Therefore, developing supervisory strategies to regulate the forgetting factor and relocate the Eigenvalues to improve its tracking performance is a very interesting subject for future research.
- The presented linear form of MGS technique is capable of tracking harmonics and interharmonics. Expanding the MGS technique to a nonlinear form by using the Taylor series for direct symmetrical components extraction and improving its estimation pace is yet another subject for further investigation and evaluation.
- The concept of undersampling requires generalization for the specific case of real-time power system monitoring. Applying different downsampling factors from the conventional staggered undersampling requires further investigations to extract more diagnostics and improve the estimation delays. This is a potential research opportunity since it has not been addressed extensively in the context of power systems.
- The fact that the information is collected with some delays throughout the power systems has resulted in application of global positioning system (GPS) to synchronize the measurements in the time-domain as it has been discussed

thoroughly in the technical literature. In the frequency domain, these delays can be seen as sampling frequency modifications in terms of observing an undersampled event. The synchrophasor estimation based on extending the staggered undersampling concept has been presented in this thesis. Further investigation of the possibilities for real-time power network frequency-domain event-mapping, phase-angle bias cancelation, state estimation, and frequency tracking based on undersampling remains to be investigated for WAMSs applications.

Appendix: Total Vector Error

IEEE Std. C37.118-2005 defines the synchrophasor representation of a voltage signal with the amplitude of X'_m and phase-angle of ϱ as [145]:

$$A' = X'_r + jX'_i = (X'_m / \sqrt{2})(\cos(\varrho) + j \sin(\varrho)) \quad (\text{A. 1})$$

When there is an error in the frequency estimation, the phase-angle will change uniformly with respect to the time [145]. The measured synchrophasor is calculated as follows:

$$A'_m = (X'_m / \sqrt{2})(\cos(\varrho) + j \sin(\varrho)) \frac{1}{T} \int_0^T (\cos(\varrho_e t) - j \sin(\varrho_e t)) dt \quad (\text{A. 2})$$

$$A'_m = (X'_m / \sqrt{2})(\cos(\varrho) + j \sin(\varrho)) \frac{1}{-Tj\varrho_e} (\cos(\varrho_e T) - j \sin(\varrho_e T) - 1) \quad (\text{A. 3})$$

where ϱ_e is the angular frequency estimation error and T is the voltage waveform period. The total vector error (*TVE*) for steady state is calculated as [145]:

$$TVE(\varrho_e) = \sqrt{\frac{\|A' - A'_m\|^2}{\|A'\|^2}} = \left\| 1 - \frac{A'_m}{A'} \right\| \quad (\text{A. 4})$$

where A' is the theoretical vector. By substituting (A. 2) and (A. 3) into (A. 4), the *TVE* is calculated as:

$$TVE(\varrho_e) = \left\| 1 + \frac{1}{Tj\varrho_e} (\cos(\varrho_e T) - j \sin(\varrho_e T) - 1) \right\| \quad (\text{A. 5})$$

Since $TVE(\varrho_e) = TVE(-\varrho_e)$, *TVE* is an even function with respect to ϱ_e . Eqn. (A. 5) is therefore rewritten as:

$$TVE(\Omega_e) = \left\| 1 + \frac{1}{Tj|\Omega_e|} (\cos(|\Omega_e|T) - j \sin(|\Omega_e|T) - 1) \right\| \quad (\text{A. 6})$$

where $|\cdot|$ performs the absolute value function.

References

- [1] W. G. Morsi and M. E. El-Hawary, "A new perspective for the IEEE Standard 1459-2000 via stationary wavelet transform in the presence of nonstationary power quality disturbance," *IEEE Trans. Power Del.*, vol. 23, no. 4, pp. 2356-2365, 2008.
- [2] G. T. Heydt and Y. Liu, "Second harmonic components in power system voltages and currents," *IEEE Trans. Power Del.*, vol. 20, no. 1, pp. 521-523, 2005.
- [3] P. G. Kini, R. C. Bansal, and R. S. Aithal, "A novel approach toward interpretation and application of voltage unbalance factor," *IEEE Trans. Ind. Electron.*, vol. 54, no. 4, pp. 2315-2322, 2007.
- [4] B. Barahona, P. Sorensen, L. Christensen, T. Sorensen, H. K. Nielsen, and X.G. Larsen, "Validation of the standard method for assessing flicker from wind turbines," *IEEE Trans. Energy Convers.*, vol. 26, no. 1, pp. 373-378, 2011.
- [5] E. Chu, *Discrete and Continuous Fourier Transforms Analysis: Applications and Fast Algorithms*. Taylor and Francis Group, CRC Press, 2008.
- [6] H. C. Lin, "Power harmonics and interharmonics measurement using recursive group-harmonic power minimizing algorithm," *IEEE Trans. Ind. Electron.*, pp. 1-11, 2011.
- [7] F. Cupertino, E. Lavopa, P. Zanchetta, M. Sumner, and L. Salvatore, "Running DFT-based PLL algorithm for frequency, phase, and amplitude tracking in aircraft electrical systems," *IEEE Trans. Ind. Electron.*, vol. 58, no. 3, pp. 1027-103, 2011.
- [8] D. Yazdani, A. Bakhshai, G. Joos, and M. Mojiri, "A real-time three-phase selective-harmonic-extraction approach for grid-connected converters," *IEEE Trans. Ind. Electron.*, vol. 56, no. 10, pp. 4097-4105, 2009.
- [9] M. Karimi-Ghartemani, H. Karimi, and M.R. Iravani, "A magnitude/phase-locked loop system based on estimation of frequency and in-phase/quadrature-phase amplitudes," *IEEE Trans. Ind. Electron.*, vol. 51, no. 2, pp. 511-517, 2004.
- [10] M. Karimi-Ghartemani, B.-T. Ooi, and A. Bakhshai, "Application of enhanced phase-locked loop system to the computation of synchrophasors," *IEEE Trans. Power Del.*, vol. 26, no. 1, pp. 22-32, 2011.

- [11]A. Bhattacharya and C. Chakraborty, "A shunt active power filter with enhanced performance using ANN-based predictive and adaptive controllers," *IEEE Trans. Ind. Electron.*, vol. 58, no. 2, pp. 421-428, 2011.
- [12]R. Agha Zadeh, A. Ghosh, and G. Ledwich, "Combination of Kalman filter and least-error square techniques in power system," *IEEE Trans. Power Del.*, vol. 25, no. 4, pp. 2868-2880, 2010.
- [13]R. G. Brown and P. Y. C. Hwang, *Introduction to Random Signal Analysis and Kalman Filtering*. New York, John Wiley & Sons, 1983.
- [14]M.I. Marei, E.F. El-Saadany, M.M.A. Salama, "Experimental evaluation of envelope tracking techniques for voltage disturbances," *Elect. Power Syst. Res.*, vol. 80, no. 3, pp. 339-344, 2010.
- [15]T.T. Nguyen and X.J. Li, "Application of a z-transform signal model and median filtering for power system frequency and phasor measurements," *IET Gener. Transm. Distrib.*, vol. 1, no. 1, pp.72-79,2007.
- [16]V. Terzija and M. Djuric, "Direct estimation of voltage phasor, frequency and its rate of change using Newton's iterative method," *Int. J. Elec. Power & Energy Syst.*, vol. 16, no. 6, pp. 423-428,1994.
- [17]Z. Zhong, C. Xu, B. J. Billian, L. Zhang, S.-J. S. Tsai, R. W. Conners, V. A. Centeno, A. G. Phadke, and Y. Liu, "Power system frequency monitoring network (FNET) implementation," *IEEE Trans. Power Syst.*, vol. 20, no. 4, pp. 1914-1921, 2005.
- [18]Y. Zhang, P. Markham, T. Xia, L. Chen, Y. Ye, Z. Wu, Z. Yuan, L. Wang, J. Bank, J. Burgett, R. W. Conners, and Y. Liu, "Wide-area frequency monitoring network (FNET) architecture and applications," *IEEE Trans. Smart Grid*, vol. 1, no.2, pp. 159-168, 2010.
- [19]H. Karimi, M. Karimi-Ghartemani, and M. Iravani, "Estimation of frequency and its rate of change for applications in power systems," *IEEE Trans. Power Del.*, vol. 19, no. 2, pp. 472-480, 2004.

- [20]M. M. Begovic, P. M. Djuric, S. Dunlap, and A. G. Phadke, "Frequency tracking in power networks in the presence of harmonics," *IEEE Trans. Power Del.*, vol. 8, no. 2, pp. 480-486, 1993.
- [21]T. Radil, P. M. Ramos, and A. C. Serra, "New spectrum leakage correction algorithm for frequency estimation of power system signals," *IEEE Trans. Instrum. Meas.*, vol. 58, no. 5, pp. 1670-1679, 2009.
- [22]J.-Z. Yang and C.-W. Liu, "A precise calculation of power system frequency," *IEEE Trans. Power Del.*, vol. 16, no. 3, pp. 361-366, 2001.
- [23]M. Mojiri, M. Karimi-Ghartemani, and A. Bakhshai, "Estimation of power system frequency using an adaptive notch filter," *IEEE Trans. Instrum. Meas.*, vol. 56, no. 6, pp. 2470-2477, 2007.
- [24]M. Akke, "Frequency estimation method by demodulation of two complex signals," *IEEE Trans. Power Del.*, vol. 12, no. 1, pp. 157-163, 1997.
- [25]D. W. P. Thomas and M. S. Woolfson, "Evaluation of frequency tracking methods," *IEEE Trans. Power Del.*, vol. 16, no. 3, pp. 367-371, 2001.
- [26]C.-H. Huang, C.-H. Lee, K.-J. Shih, and Y.-J. Wang, "Frequency estimation of distorted power system signals using a robust algorithm," *IEEE Trans. Power Del.*, vol. 23, no. 1, pp. 41-51, 2008.
- [27]R. Chudamani, K. Vasudevan, and C. S. Ramalingam, "Real-time estimation of power system frequency using nonlinear least squares," *IEEE Trans. Power Del.*, vol. 24, no. 3, pp. 1021-1028, 2009.
- [28]A. Lopez, J.-C. Montao, M. Castilla, J. Gutierrez, M. D. Borrás, and J. C. Bravo, "Power system frequency measurement under nonstationary situations," *IEEE Trans. Power Del.*, vol. 23, no. 2, pp. 562-567, 2008.
- [29]M. S. Sachdev and M. M. Giray, "A least error squares technique for determining power system frequency," *IEEE Trans. Power App. Syst.*, vol. 104, no. 2, pp. 437-444, 1985.
- [30]Z. Salcic, S. K. Nguang, and Y. Wu, "An improved Taylor method for frequency measurement in power systems," *IEEE Trans. Instrum. Meas.*, vol. 58, no. 9, pp. 3288-3294, 2009.

- [31]L. L. Lai, W. L. Chan, C. T. Tse, and A. T. P. So, "Real-time frequency and harmonic evaluation using artificial neural networks," *IEEE Trans. Power Del.*, vol. 14, no. 1, pp. 52-59, 1999.
- [32]V. V. Terzija, M. B. Djuric, and B. D. Kovacevic, "Voltage phasor and local system frequency estimation using Newton type algorithm," *IEEE Trans. Power Del.*, vol. 9, no. 3, pp. 1368-1374, 1994.
- [33]V. V. Terzija and D. Markovic, "Symmetrical components estimation through nonrecursive Newton-type numerical algorithm," *IEEE Trans. Power Del.*, vol. 18, no. 2, pp. 359-363, 2003.
- [34]V. Terzija and V. Stanojevic, "Power quality indicators estimation using robust Newton-type algorithm," *IEE Proc.-Gener. Transm. Distrib.*, vol. 151, no. 4, pp. 477-485, 2004.
- [35]M. D. Kusljevic, "A simple recursive algorithm for frequency estimation," *IEEE Trans. Instrum. Meas.*, vol. 53, no. 2, pp. 335-340, 2004.
- [36]A. K. Pradhan, A. Routray, and A. Basak, "Power system frequency estimation using least mean square technique," *IEEE Trans. Power Del.*, vol. 20, no. 3, pp. 1812-1816, 2005.
- [37]N.R. Chaudhuri, D. Chakraborty, and B. Chaudhuri, "An architecture for FACTS controllers to deal with bandwidth-constrained communication," *IEEE Trans. Power Del.*, vol. 26, no. 1, pp. 188-196, 2011.
- [38]M. Glavic and T. Van Cutsem, "Wide-area detection of voltage instability from synchronized phasor measurements. Part I: Principle," *IEEE Trans. Power Syst.*, vol. 24, no. 3, pp. 1408-1416, 2009.
- [39]M. Zhou, V.A. Centeno, J.S. Thorp, and A.G. Phadke, "An alternative for including phasor measurements in state estimators," *IEEE Trans. Power Syst.*, vol. 21, no. 4, pp. 1930-1937, 2006.
- [40]M. El Moursi, G. Joos, and C. Abbey, "A secondary voltage control strategy for transmission level interconnection of wind generation," *IEEE Trans. Power Electron.*, vol. 23, no. 3, pp. 1178-1190, 2008.

- [41]J. Dagle, "North American SynchroPhasor Initiative - An update of progress," *44th Hawaii International Conference on System Sciences*, 2011, pp. 1-4.
- [42]M.M. Eissa, M.E. Masoud, and M.M.M. Elanwar, "A novel back up wide area protection technique for power transmission grids using phasor measurement unit," *IEEE Trans. Power Del.*, vol. 25, no. 1, pp.270-278, 2010.
- [43]D.I. Jeerings and J.R. Linders, "Unique aspects of distribution system harmonics due to high impedance ground faults," *IEEE Trans. Power Del.*, vol. 5, no. 2, pp. 1086-1094, 1990.
- [44]M. Saito, T. Takeshita, and N. Matsui, "Modeling and harmonic suppression for power distribution systems," *IEEE Trans. Ind. Electron.*, vol. 50, no. 6, pp. 1148-1158, 2003.
- [45]H. Ukai, K. Nakamura, and N. Matsui, "DSP- and GPS-based synchronized measurement system of harmonics in wide-area distribution system," *IEEE Trans. Ind. Electron.*, vol. 50, no. 6, pp. 1159-1164, 2003.
- [46]J.F. Fuller, E.F. Fuchs, and D.J. Roesler, "Influence of harmonics on power distribution system protection," *IEEE Trans. Power Del.*, vol. 3, no. 2, pp. 549-557, 1988.
- [47]A. A. Eajal and M. E. El-Hawary, "Optimal capacitor placement and sizing in unbalanced distribution systems with harmonics consideration using particle swarm optimization," *IEEE Trans. Power Del.*, vol. 25, no. 3, pp. 1734-1741, 2010.
- [48]D. Yazdani, A. Bakhshai, G. Joos, and M. Mojiri, "A real-time extraction of harmonic and reactive current in a nonlinear load for grid-connected converters," *IEEE Trans. Ind. Electron.*, vol. 56, no. 6, pp. 2185-2189, 2009.
- [49]M. Mojiri, M. Karimi-Ghartemani, and A. Bakhshai, "Processing of harmonics and interharmonics using an adaptive notch filter," *IEEE Trans. Power Del.*, vol. 25, no. 2, pp. 534-542, 2010.
- [50]L. Hsu, R. Ortega, and G. Damm, "A globally convergent frequency estimator," *IEEE Trans. Autom. Control*, vol. 44, no. 4, pp. 698-713, 1999.

- [51]M. Karimi-Ghartemani, S.A. Khajehoddin, P. Jain, A. Bakhshai, and M. Mojiri, "Addressing DC component in PLL and notch filter algorithms," *IEEE Trans. Power Electron.*, pp. 1-16, 2011.
- [52]M. Karimi-Ghartemani and M. R. Iravani, "Robust and frequency-adaptive measurement of peak value," *IEEE Trans. Power Del.*, vol. 19, no. 2, pp. 481-489, 2004.
- [53]D. Jovcic, "Phase locked loop system for FACTS," *IEEE Trans. Power Syst.*, vol. 18, no. 3, pp. 1116-1124, 2003.
- [54]P. Rodriguez, J. Pou, J. Bergas, J.I. Candela, and R.P. Burgos, and D. Boroyevich, "Decoupled double synchronous reference frame PLL for power converters control," *IEEE Trans. Power Electron.*, vol. 22, no. 2, pp. 584-592, 2007.
- [55]P.K. Dash, D.P. Swain, A.C. Liew, and S. Rahman, "An adaptive linear combiner for on-line tracking of power system harmonics," *IEEE Trans. Power Syst.*, vol. 11, no. 4, pp. 1730-1735, 1996.
- [56]B. Singh and J. Solanki, "An implementation of an adaptive control algorithm for a three-phase shunt active filter," *IEEE Trans. Ind. Electron.*, vol. 56, no. 8, pp. 2811-2820, 2009.
- [57]*Electromagnetic compatibility (EMC)-Part 4-7: Testing and measurement techniques-General guide on harmonics and interharmonics measurements and instrumentation, for power supply systems and equipment connected thereto, IEC Standard 61000-4-7, 2002.*
- [58]H. Karimi, M. Karimi-Ghartemani, M.R. Iravani, and A.R. Bakhshai, "An adaptive filter for synchronous extraction of harmonics and distortions," *IEEE Trans. Power Del.*, vol. 18, no. 4, pp. 1350-1356, 2003.
- [59]M.I. Marei, E.F. El-Saadany, and M.M.A. Salama, "A processing unit for symmetrical components and harmonics estimation based on a new adaptive linear combiner structure," *IEEE Trans. Power Del.*, vol. 19, no. 3, pp. 1245-1252, 2004.
- [60]L. Hongxing and L. Bingzhang, "Adaptive control based on genetic algorithm and fuzzy tuning for unknown systems with time-delay," *Proc. World Congress on Intelligent Control and Automation*, 2008, pp. 8650-8655.

- [61]S.M. Brahma, P.L. De Leon, and R.G. Kavasseri, "Investigating the option of removing the antialiasing filter from digital relays," *IEEE Trans. Power Del.*, vol. 24, no. 4, pp. 1864-1868, 2009.
- [62]F.A.S. Neves, H.E.P. de Souza, F. Bradaschia, M.C. Cavalcanti, M. Rizo, and F.J. Rodriguez, "A space-vector discrete Fourier transform for unbalanced and distorted three-phase signals," *IEEE Trans. Ind. Electron.*, vol. 57, no. 8, pp. 2858-2867, 2010.
- [63]H.A. Darwish and M. Fikri, "Practical considerations for recursive DFT implementation in numerical relays," *IEEE Trans. Power Del.*, vol. 22, no. 1, pp. 42-49, 2007.
- [64]M. H. J. Bollen and I. Y. H. Gu, *Signal Processing of Power Quality Disturbances*. IEEE Press on Power Engineering, New York, John Wiley & Sons, 2006.
- [65]T. T. Nguyen, "Parametric harmonic analysis," *IEE Proc.-Gener. Transm. Distrib.*, vol. 144, no. 1, pp. 21-25, 1997.
- [66]R. K. Mai, L. Fu, Z. Y. Dong, B. Kirby, and Z. Q. Bo, "An adaptive dynamic phasor estimator considering dc offset for PMU applications," *IEEE Trans. Power Del.*, vol. 26, no. 3, pp. 1744-1754, 2011.
- [67]G. E. Mog and E. P. Ribeiro, "Total harmonic distortion calculation by filtering for power quality monitoring," *IEEE/PES Transmission and Distribution Conference and Exposition: Latin America*, 2004, pp. 629-632.
- [68]M. Wang and Y. Sun, "A practical method to improve phasor and power measurement accuracy of DFT algorithm," *IEEE Trans. Power Del.*, vol. 21, no. 3, pp. 1054-1062, 2006.
- [69]S. Mishra, "A hybrid least square-fuzzy bacterial foraging strategy for harmonic estimation," *IEEE Trans. Evol. Comput.*, vol. 9, no. 1, pp. 61-73, 2005.
- [70]M. Bettayeb and U. Qidwai, "A hybrid least squares-GA-based algorithm for harmonic estimation," *IEEE Trans. Power Del.*, vol. 18, no. 2, pp. 377-382, 2003.
- [71]P. Jafarian and M. Sanaye-Pasand, "Weighted least error squares based variable window phasor estimator for distance relaying application," *IET Gen. Trans. Dist.*, vol. 5, no. 3, pp. 298-306, 2011.

- [72]J.Z. Yang, C.W. Liu, and W.G. Wu; “A hybrid method for the estimation of power system low-frequency oscillation parameters,” *IEEE Trans. Power Syst.*, vol. 22, no. 4, pp. 2115-2123, 2007.
- [73]S. K. Jain and S.N. Singh, “Harmonics estimation in emerging power system: Key issues and challenges,” *Electric Power Systems Research*, vol. 81, no. 9, pp. 1754-1766, 2011.
- [74]A. A. Girgis, J. W. Stephens, and E. B. Makram, “Measurement and prediction of voltage flicker magnitude and frequency,” *IEEE Trans. Power Del.*, vol. 10, no. 3, pp. 1600-1605, 1995.
- [75]Z. Peroutka, V. Smidl, and D. Vosmik, “Challenges and limits of extended Kalman filter based sensorless control of permanent magnet synchronous machine drives,” *European Conference on Power Electronics and Applications*, 2009. pp. 1-11.
- [76]K. Kennedy, G. Lightbody, and R. Yacamini, “Power system harmonic analysis using the Kalman filter,” *IEEE Power Engineering Society General Meeting*, 2003, pp. 752-757.
- [77]P. K. Dash, R. K. Jena, G. Panda, and A. Routray, “An extended complex Kalman filter for frequency measurement of distorted signals,” *IEEE Trans. Instrum. Meas.*, vol. 49, pp. 746–753, 2000.
- [78]A. Routray, A.K. Pradhan, and K.P. Rao, “A novel Kalman filter for frequency estimation of distorted signals in power systems,” *IEEE Trans. Instrum. Meas.*, vol. 51, no. 3, pp. 469-479, 2002.
- [79]V.V. Terzija, “Improved recursive Newton-type algorithm for power system relaying and measurement,” *IEE Proc.Gen. Trans. Distrib.*, vol. 145, no. 1, pp. 15-20, 1998.
- [80]V.V. Terzija, “Improved recursive Newton-type algorithm for frequency and spectra estimation in power systems,” *IEEE Trans. Instrum. Meas.*, vol. 52, no. 5, pp. 1654-1659, 2003.
- [81]V.V. Terzija and V. Stanojevic, “Two-stage improved recursive Newton-type algorithm for power-quality indices estimation,” *IEEE Trans. Power Del.*, vol. 22, no. 3, pp. 1351-1359, 2007.

- [82]V.V. Terzija, M. B. Djuric, and N. Z. Jeremic, "A recursive Newton type algorithm for digital frequency relaying," *Elect. Power Syst. Res.*, vol. 36, no. 1, pp. 67-72, 1996.
- [83]M.S. Sachdev and M. Nagpal, "A recursive least error squares algorithm for power system relaying and measurement applications," *IEEE Trans. Power Del.*, vol. 6, no. 3, pp. 1008-1015, 1991.
- [84]B. Subudhi, P.K.Ray, A.M. Panda, and S.R. Mohanty, "Parameter estimation techniques applied to power networks," in *Proc. TENCON 2008*, 2008, pp.1-5.
- [85]I. Kamwa and R. Grondin, "Fast adaptive schemes for tracking voltage phasor and local frequency in power transmission and distribution systems," *IEEE Trans. Power Del.*, vol. 7, no. 2, pp. 789-795, 1992.
- [86]L.A.L. De Almeida and A.C. de C. Lima, "Covariance management based RLS algorithm for phasor estimation in severely noisy systems," *IEEE Trans. Power Del.*, vol. 13, no. 4, pp. 1067-1072, 1998.
- [87]A. Kuh, "Adaptive kernel methods for CDMA systems," *Proc. Int. Joint Conf. Neural Networks*, 2001, vol. 4, pp.2404-2409.
- [88]Y. Engel, S. Mannor, and R. Meir, "Sparse online greedy support vector regression," *Proc. 13th Eur. Conf. Machine Learning*, 2002, pp.84-96.
- [89]Y. Engel, S. Mannor, and R. Meir, "The kernel recursive least-squares algorithm," *IEEE Trans. Signal Process.*, vol. 52, no. 8, pp. 2275–2285, 2004.
- [90]S. V. Vaerenbergh, J. Via, and I. Santamaria, "A sliding-window kernel RLS algorithm and its application to nonlinear channel identification," *Proc. Int. Conf. Acoustics, Speech, Signal Processing*, 2006, pp. 789–792.
- [91]W. Liu, I. Park, Y. Wang, and J.C. Principe, "Extended Kernel Recursive Least Squares Algorithm," *IEEE Trans. Signal Process.*, vol. 57, no. 10, pp. 3801-3814, 2009.
- [92]M. Bettayeb and U. Qidwa, "Recursive estimation of power system harmonics," *Elect. Power Syst. Res.*, vol. 47, no. 2, pp. 143-152, 1998.
- [93]A.S. AlFuhaid and M.A. El-Sayed, "A recursive least-squares digital distance relaying algorithm," *IEEE Trans. Power Del.*, vol. 14, no. 4, pp. 1257-1262, 1999.

- [94] M.I. Marei, E.F. El-Saadany, and M.M.A. Salama, "Envelope tracking techniques for flicker mitigation and voltage regulation," *IEEE Trans. Power Del.*, vol. 19, no. 4, pp. 1854-1861, 2004.
- [95] M.I. Marei, E.F. El-Saadany, and M.M.A. Salam, "Estimation techniques for voltage flicker envelope tracking," *Elect. Power Syst. Res.*, vol. 70, no. 1, pp. 30-37, 2004.
- [96] M. Bongiorno, J. Svensson, and L. Angquist, "Online estimation of subsynchronous voltage components in power systems," *IEEE Trans. Power Del.*, vol. 23, no. 1, pp. 410-418, 2008.
- [97] H. Song and K. Nam, "Instantaneous phase-angle estimation algorithm under unbalanced voltage-sag conditions," *Proc. Inst. Elect. Eng.*, vol. 147, pp. 409-415, 2000.
- [98] D.A. Fernandes, S.R. Naidu, and C.A.E. Coura, "Instantaneous sequence-component resolution of 3-phase variables and its application to dynamic voltage restoration," *IEEE Trans. Instrum. Meas.*, vol. 58, no. 8, pp. 2580-2587, 2009.
- [99] F. Rahimi and A. Ipakchi, "Demand response as a market resource under the smart grid paradigm," *IEEE Trans. Smart Grid*, vol. 1, no. 1, pp. 82-88, 2010.
- [100] C. Bennett and S.B. Wicker, "Decreased time delay and security enhancement recommendations for AMI smart meter networks," *Innovative Smart Grid Technologies Conference*, 2010, pp. 1-6.
- [101] IEC Smart Grid Standardization Roadmap, SMB Smart Grid Strategic Group (SG3), Ed. 1.0 2010.
- [102] S. Drenker and A. Kader, "Nonintrusive monitoring of electric loads," *IEEE Comput. Appl. Power*, vol. 12, no. 4, pp. 47-51, 1999.
- [103] C. Laughman, K. Lee, R. Cox, S. Shaw, S. Leeb, L. Norford, and P. Armstrong, "Power signature analysis," *IEEE Power Energy Mag.*, vol. 1, no. 2, pp. 56-63, 2003.
- [104] J. Liang, S.K.K. Ng, G. Kendal, and J.W.M. Cheng, "Load signature study-Part I: Basic concept, structure, and methodology," *IEEE Trans. Power Del.*, vol. 25, no. 2, pp. 551-560, 2010.

- [105] J. Liang, S.K.K. Ng, G. Kendal, and J.W.M. Cheng, "Load signature study-Part II: Disaggregation framework, simulation and applications," *IEEE Trans. Power Del.*, vol. 25, no. 2, pp. 561-569, 2010.
- [106] G. W. Hart, "Nonintrusive appliance load monitoring," *Proc. IEEE*, vol. 80, no. 12, pp. 1870-1891, 1992.
- [107] A. Vojdani, "Smart integration," *IEEE Power Energy Mag.*, vol. 6, no. 6, pp. 71-79, 2008.
- [108] H. Tai and E.O. Hogain, "Behind the buzz," *IEEE Power Energy Mag.*, vol. 7, no. 2, pp. 96-92, 2009.
- [109] A. Armenia and J.H. Chow, "A flexible phasor data concentrator design leveraging existing software technologies," *IEEE Trans. Smart Grid*, vol. 1, no. 1, pp. 73-81, 2010.
- [110] L. Toivonen and J. Morsky, "Digital multirate algorithms for measurement of voltage, current, power and flicker," *IEEE Trans. Power Del.*, vol. 10, pp. 116-126, 1995.
- [111] H. Lev-Ari, A.M. Stankovic, and S. Lin, "Application of staggered undersampling to power quality monitoring," *IEEE Trans. Power Del.*, vol. 15, no. 3, pp. 864-869, 2000.
- [112] P. Petrovic, S. Marjanovic, and M.R. Stevanovic, "New algorithm for measuring 50/60 Hz AC values based on the usage of slow A/D converters," *IEEE Trans. Instrum. Meas.*, vol. 49, no. 1, pp. 166-171, 2000.
- [113] P. Petrovic and M. Stevanovic, "Measuring active power of synchronously sampled AC signals in presence of interharmonics and subharmonics," *IEE Proc.-Electr. Power Appl.*, vol. 153, no. 2, pp. 227-235, 2006.
- [114] J.R. de Carvalho, C.A. Duque, M.V. Ribeiro, A.S. Cerqueira, T.L. Baldwin, and P.F. Ribeiro, "A PLL-based multirate structure for time-varying power systems harmonic/interharmonic estimation," *IEEE Trans. Power Del.*, vol. 24, no. 4, pp. 1789-1800, 2009.
- [115] R. C. Dugan, M. F. McGranaghan, S. Santoso, and H. W. Beaty, *Electrical Power Systems Quality*. 2nd ed., McGraw-Hill, 2004.

- [116] A. A. Girgis and W. L. Peterson, "Adaptive estimation of power system frequency deviation and its rate of change for calculating sudden power system overloads," *IEEE Trans. Power Del.*, vol. 5, no. 22, pp. 585-594, 1990.
- [117] G.W. Chang, Y. J. Liu, V. Dinavahi, and H. J. Su, "On real-time simulation for harmonic and flicker assessment of an industrial system with bulk nonlinear loads," *IEEE Trans. Ind. Electron.*, vol. 57, no. 9, pp. 2998-3009, 2010.
- [118] P. G. V. Axelberg, M. H. J. Bollen, and I. Y. H. Gu, "Trace of flicker sources by using the quantity of flicker power," *IEEE Trans. Power Del.*, vol. 23, no. 1, pp. 465-471, 2008.
- [119] G. Wiczynski, "Analysis of voltage fluctuations in power networks," *IEEE Tran. Instrum. Meas.*, vol. 57, no. 11, pp. 2655-2664, 2008.
- [120] A. Elnady and M. M. A. Salama, "Unified approach for mitigating voltage sag and voltage flicker using the DSTATCOM," *IEEE Trans. Power Del.*, vol. 20, no. 2, pp. 992-000, 2005.
- [121] G. W. Chang, C. I. Chen, and Y. L. Huang, "A digital implementation of flicker meter in the hybrid time and frequency domains," *IEEE Trans. Power Del.*, vol. 24, no. 3, pp. 1475-1482, 2009.
- [122] R. Naidoo and P. Pillay, "A new method of voltage sag and swell detection," *IEEE Trans. Power Del.*, vol. 22, no. 2, pp. 1056-1063, 2007.
- [123] A.K. Pradhan and A. Routray, "Applying distance relay for voltage sag source detection," *IEEE Trans. Power Del.*, vol. 20, no. 1, pp. 529-531, 2005.
- [124] S. C. Vegunta and J. V. Milanovic, "Estimation of cost of downtime of industrial process due to voltage sags," *IEEE Trans. Power Del.*, vol. 26, no. 2, pp. 576-587, 2011.
- [125] S. Saleh, C. Moloney, and M. Rahman, "Analysis and development of wavelet modulation for three phase voltage source inverters," *IEEE Trans. Ind. Electron.*, vol. 58, no. 8, pp. 3330-3348, 2011.
- [126] A. Elmitwaly, S. Farhai, M. Kandil, S. Abdelkadar, and M. Elkateb, "Proposed wavelet-neurofuzzy combined system for power quality violations detection and diagnosis," *IEE Gen. Trans. Dist.*, vol. 148, no. 1, pp. 15-20, 2001.

- [127] P.K. Dash, B.K. Panigrahi, and G. Panda, "Power quality analysis using S-transform," *IEEE Trans. Power Del.*, vol. 18, no. 2, pp. 406-411, 2003.
- [128] B. Biswal, P. K. Dash, and B. K. Panigrahi, "Power quality disturbance classification using fuzzy C-means algorithm and adaptive particle swarm optimization," *IEEE Trans. Ind. Electron.*, vol. 56, no. 1, pp. 212-220, 2009.
- [129] B. Boashah, "Estimating and interpreting the instantaneous frequency of a signal. I. Fundamentals," *Proc. IEEE*, vol. 80, no. 4, pp. 520-538, Apr. 1992.
- [130] S. Shukla, S. Mishra, and B. Singh, "Empirical-mode decomposition with Hilbert transform for power-quality assessment," *IEEE Trans. Power Del.*, vol. 24, no. 4, pp. 2159-2165, 2009.
- [131] J. A. Sanders, F. Verhulst, and J. Murdock, *Averaging Methods in Nonlinear Dynamical Systems*. Springer, 2000.
- [132] J. Nocedal and S. J. Wright, *Numerical Optimization*. Springer Series in Operation Research and Financial Engineering, ed. 2, 2006.
- [133] K. Srinivasan, "Digital measurement of voltage flicker," *IEEE Trans. Power Del.*, vol. 6, no. 4, pp. 1593-1598, 1991.
- [134] X.X. Yang and M. Kratz, "Power system flicker analysis by RMS voltage values and numeric flicker meter emulation," *IEEE Trans. Power Del.*, vol. 24, no. 3, pp. 1310-1318, 2009.
- [135] *IEEE Recommended Practice for Measurement and Limits of Voltage Fluctuations and Associated Light Flicker on AC Power Systems*, IEEE Standard 1453, 2005.
- [136] DSPACE systems, <http://www.dspace.com>.
- [137] SCU/UPC-3 programmable power supply, Pacific Power Source, <http://www.pacificpower.com>.
- [138] LV 25-P voltage transducer, www.lem.com.
- [139] *IEEE Recommended Practice for Monitoring Electric Power Quality*, IEEE Standard 1159, 2009.

- [140] A. Florio, A. Mariscotti, and M. Mazzucchelli, "Voltage sag detection based on rectified voltage processing," *IEEE Trans. Power Del.*, vol. 19, no. 4, pp. 1962-1967, 2004.
- [141] H.C. Lin, "Fast tracking of time-varying power system frequency and harmonics using iterative-loop approaching algorithm," *IEEE Trans. Ind. Electron.*, vol. 54, no. 2, pp. 974-983, 2007.
- [142] J.A. Apolinario Jr., *QRD-RLS Adaptive Filtering*. Springer, 2009.
- [143] N. Zhou, J.W. Pierre, D.J. Trudnowski, and R.T. Guttromson, "Robust RLS methods for online estimation of power system electromechanical modes," *IEEE Trans. Power Syst.*, vol. 22, no. 3, pp. 1240-124, 2007.
- [144] T.A. Short, *Electric Power Distribution Handbook*. CRC Press, 2004.
- [145] *IEEE Standard for Synchrophasors for Power Systems*, IEEE Standard C37.118-2005, Mar. 2006.
- [146] *Electromagnetic compatibility (EMC)-Part 4-13: Testing and measurement techniques-Harmonics and interharmonics including mains signaling at ac power port, low frequency immunity test*, IEC Standard 61000-4-13, 2002.
- [147] LV 20-P voltage transducer, www.lem.com.
- [148] N.R. Chaudhuri and B. Chaudhuri, "Damping and relative mode-shape estimation in near real-time through phasor approach," *IEEE Trans. Power Syst.*, vol. 26, no. 1, pp. 364-37, 2011.
- [149] J. A. de la O Serna, and J. Rodriguez-Maldonado, "Instantaneous oscillating phasor estimates with Taylor-Kalman filters," *IEEE Trans. Power Syst.*, pp. 1-9, 2011.
- [150] K. Sun, S.T. Lee, and P. Zhang, "An adaptive power system equivalent for real-time estimation of stability margin using phase-plane trajectories," *IEEE Trans. Power Syst.*, vol. 26, no. 2, pp. 915-923, 2011.
- [151] E. Ghahremani and I. Kamwa, "Dynamic state estimation in power system by applying the extended Kalman filter with unknown inputs to phasor measurements," *IEEE Trans. Power Syst.*, pp. 1-11, 2011.

- [152] A. Borghetti, C.A. Nucci, M. Paolone, G. Ciappi, A. Solari, “Synchronized phasors monitoring during the islanding maneuver of an active distribution network,” *IEEE Trans. Smart Grid*, vol. 2, no. 1, pp. 82-91, 2011.
- [153] M. Abdel-Akher and K.M. Nor, “Fault analysis of multiphase distribution systems using symmetrical components,” *IEEE Trans. Power Del.*, vol. 25, no. 4, pp. 2931–2939, 2010.
- [154] S. Orts-Grau, F.J. Gimeno-Sales, A. Abellan-Garcia, S. Segui-Chilet, and J.C. Alfonso-Gil, “Improved shunt active power compensator for IEEE standard 1459 compliance,” *IEEE Trans. Power Del.*, vol. 25, no. 4, pp. 2692-2701, 2010.
- [155] M. Castilla, J. Miret, J.L. Sosa, J. Matas, and L.G. de Vicua, “Grid-fault control scheme for three-phase photovoltaic inverters with adjustable power quality characteristics,” *IEEE Trans. Power Electron.*, vol. 25, no. 12, pp. 2930-2940, 2010.
- [156] A.A. Girgis, W. Chang, and E.B. Makram, “Analysis of high-impedance fault generated signals using a Kalman filtering approach,” *IEEE Trans. Power Del.*, vol. 5, no. 4, pp. 1714–1724, Oct. 1990.
- [157] F.D. Freijedo, J. Doval-Gandoy, O. Lopez, and E. Acha, “A generic open-loop algorithm for three-phase grid voltage/current synchronization with particular reference to phase, frequency, and amplitude estimation,” *IEEE Trans. Power Electron.*, vol. 24, no. 1, pp. 94-107, 2009.
- [158] M. Karimi-Ghartemani and H. Karimi, “Processing of symmetrical components in time-domain,” *IEEE Trans. Power Syst.*, vol. 22, no. 2, pp. 572-579, 2007.
- [159] *IEEE Guide for Protective Relay Applications to Distribution Lines*, IEEE Std C37.230-2007, 2007.
- [160] *IEEE Guide for automatic reclosing of line circuit breakers for ac distribution and transmission lines*, IEEE Std C37.104, 2003.
- [161] J.J. Tomic, M.D. Kusljevic, and V.V. Vujicic, “A new power system digital harmonic analyzer,” *IEEE Trans. Power Del.*, vol. 22, no. 2, pp.772-780,2007.
- [162] J. De La Ree, V. Centeno, J.S. Thorp, and A.G. Phadke, “Synchronized phasor measurement applications in power systems,” *IEEE Trans. Smart Grid*, vol. 1, no. 1, pp.20-27,2010.

- [163] S.R. Samantaray and P.K. Dash, "Transmission line distance relaying using a variable window short-time Fourier transform," *J. Elect. Power Syst. Res.*, vol. 78, no. 4, pp. 595-604, 2008.
- [164] T.S. Sidhu, J. Burnworth, A. Darlington, B. Kasztenny, Y. Liao, P.G. McLaren, M. Nagpal, M.S. Sachdev, M.M. Saha, M. Swanson, and P.B. Winston, "Bibliography of relay literature, 2006 IEEE committee report," *IEEE Trans. Power Del.*, vol. 23, no. 4, pp.1864-1875, 2008.
- [165] Y. Wang, W. Li, J. Lu, and H. Liu, "Evaluating multiple reliability indices of regional networks in wide area measurement system," *J. Elect. Power Syst. Res.*, vol. 79, no. 10, pp.1353-1359, 2009.
- [166] T.S. Bi, X.H. Qin, and Q.X. Yang, "A novel hybrid state estimator for including synchronized phasor measurements," *J. Elect. Power Syst. Res.*, vol. 78, no. 8, pp.1343-1352, 2008.
- [167] A. Elnady and M.M.A. Salama, "Mitigation of the voltage fluctuations using an efficient disturbance extraction technique," *J. Elect. Power Syst. Res.*, vol. 77, pp.266-275, 2007.
- [168] M. Karimi-Ghartemani, "A distortion-free phase-locked loop system for FACTS and power electronic controllers," *J. Elect. Power Syst. Res.*, vol. 77, no. 8, pp.1095-1100, 2007.
- [169] M. Joorabian, S.S. Mortazavi, and A.A. Khayyami, "Harmonic estimation in a power system using a novel hybrid least squares-Adaline algorithm," *J. Elect. Power Syst. Res.*, vol. 79, no. 1, pp. 107-116, 2009.
- [170] J. S. Hsu, "Instantaneous phasor method for obtaining instantaneous balanced fundamental components for power quality control and continuous diagnostics," *IEEE Trans. Power Del.*, vol. 13, no. 4, pp.1494-1500, 1998.
- [171] T.K. Abdel-Galil, E.F. El-Saadany, and M.M.A. Salama, "Power quality event detection using Adaline," *J. Elect. Power Syst. Res.*, vol. 64, no. 2, pp. 137-144, 2003.
- [172] D. Belega and D. Dallet, "Amplitude estimation by a multipoint interpolated DFT approach," *IEEE Trans. Instrum. Meas.*, vol. 58, no. 5, pp. 1316-1323, 2009.

- [173] I.-K. Yang, N.-J. Jung, Y.-I Kim, “Status of advanced metering infrastructure development in Korea,” *Transmission & Distribution Conference & Exposition, Asia and Pacific*, pp. 1-3, 2009.
- [174] S.-W. Luan; J.-H. Teng, S.-Y. Chan, and L.-C. Hwang, “Development of a smart power meter for AMI based on ZigBee communication,” *International Conference on Power Electronics and Drive Systems*, pp.661-665,2009.
- [175] Assessment of smart metering models: The case of Hungary, Energy Sector Management Assistance Program (ESMAP), available online at: <http://www.esmap.org/esmap>, 2011.
- [176] *Electromagnetic compatibility (EMC)–Part 4-30: Power quality measurement methods*, IEC Standard 61000-4-30, 2003.
- [177] MATLAB® 7.8, The MathWorks, www.mathworks.com/trademarks.
- [178] *Electricity metering equipment (ac)-General requirements, tests and test conditions - Tariff and load control equipment*, IEC Standard 62052-21, ed. 1.0, 2004.
- [179] <http://www.aemo.com.au>, 2011.
- [180] IEEE Task Force on Harmonics Modeling and Simulation, Interharmonics: Theory and modelling, *IEEE Trans. Power Del.*, vol. 22, no. 4, pp.2335-2348,2007.
- [181] MX30 power supply, California Instruments, <http://www.calinst.com>, 2011.
- [182] LA 55-P current transducer, www.lem.com, 2011.
- [183] Analog Devices, <http://www.analog.com/en/analog-to-digital-converters/energy-measurement/ade5166/products>, 2011.
- [184] I. Kamwa, A. K. Pradhan, and G. Joos, “Adaptive phasor and frequency-tracking schemes for wide-area protection and control,” *IEEE Trans. Power Del.*, vol. 26, no. 2, pp. 744-753, 2011.
- [185] T.L. Vandoorn, B. Renders, L. Degroote, B. Meersman, and L. Vandeveldel, “Active load control in islanded microgrids based on the grid voltage,” *IEEE Trans. Smart Grid*, vol. 2, no. 1, pp. 139-151, 2011.

- [186] O. Samuelsson, M. Hemmingsson, A.H. Nielsen, K.O.H. Pedersen, and J. Rasmussen, "Monitoring of power system events at transmission and distribution level," *IEEE Trans. Power Syst.*, vol. 21, no. 2, pp. 1007-1008, 2006.
- [187] A. Carta, N. Locci, and C. Muscas, "GPS-based system for the measurement of synchronized harmonic phasors," *IEEE Trans. Instrum. Meas.*, vol. 58, no. 3, pp. 586-593, 2009.
- [188] M. Powalko, K. Rudion, P. Komarnicki, and J. Blumschein, "Observability of the distribution system," *Proc. 20th Int. Conf. Exhib. Elect. Distrib.*, 2009, pp1-4.
- [189] W. Yao, L. Jiang, Q.H. Wu, J.Y. Wen, and S.J. Cheng, "Delay-dependent stability analysis of the power system with a wide-area damping controller embedded," *IEEE Trans. Power Syst.*, vol. 26, no. 1, pp. 233-240, 2011.
- [190] B. Naduvathuparambil, M. C. Valenti, and A. Feliachi, "Communication delays in wide area measurement systems," *Proc. 34th Southeastern Symp. System Theory*, 2002, pp. 118-122.
- [191] A.G. Phadke and R.M. de Moraes, "The wide world of wide-area measurement," *IEEE Power and Energy Mag.*, vol. 6, no. 5, pp. 52-65, 2008.
- [192] Y. Wang, W. Li, and J. Lu, "Reliability analysis of wide-area measurement system," *IEEE Trans. Power Del.*, vol. 25, no. 3, pp. 1483-1491, 2010.
- [193] C. W. Taylor, M. V. Venkatasubramanian, and Y. Chen, "Wide-area stability and voltage control," *Proc. VII Symp. Specialists in Electric Operational and Expansion Planning*, 2000, pp. 1-9.
- [194] D. Schneider, "Is this the moment for broadband over power lines?," *IEEE Spectr.*, vol. 46, no. 7, p. 17, 2009.
- [195] J. Y. Cai, H. Zhenyu, J. Hauer, and K. Martin, "Current status and experience of WAMS implementation in north America," *Proc. IEEE Power Eng. Soc. Transmission and Distribution Conf. Exhibit.: Asia and Pacific*, 2005, pp. 1-7.
- [196] N. R. Chaudhuri, S. Ray, R. Majumder, and B. Chaudhuri, "A new approach to continuous latency compensation with adaptive phasor power oscillation damping controller (pod)," *IEEE Trans. Power Syst.*, vol. 25, no. 2, pp. 939-946, May 2010.

- [197] D.N. Kosterev, C.W. Taylor, and W.A. Mittelstadt, "Model validation for the August 10, 1996 WSCC system outage," *IEEE Trans. Power Syst.*, vol. 14, no. 3, pp. 967-979, 1999.
- [198] B. Tianshu, H. Liu, X. Zhou, and Q. Yang, "Impact of transient response of instrument transformers on phasor measurements," *IEEE Power and Energy Society General Meeting*, 2010, pp. 1-6.
- [199] S. Bruno, M. De Benedictis, and M. La Scala, "Integrating dynamic optimization methodologies with WAMS technologies," *IEEE Power Engineering Society General Meeting*, 2007, pp. 1-8.
- [200] R. Malpani, Z. Abbas, and K.S. Swarup, "High precision frequency estimation using internet-based phasor measurement unit," *IEEE Trans. Power Syst.*, vol. 25, no. 2, pp. 607-614, 2010.
- [201] <http://www.nbn.gov.au>, 2011.
- [202] P.K. Iyambo and R. Tzoneva, "Transient stability analysis of the IEEE 14-bus electric power system," *AFRICON*, 2007, pp. 1-9.
- [203] S. Han, S. Han, and K. Sezaki, "Development of an optimal vehicle-to-grid aggregator for frequency regulation," *IEEE Trans. Smart Grid*, vol. 1, no. 1, pp. 65-72, 2010.
- [204] M. Kayikci and J.V. Milanovic, "Dynamic contribution of DFIG-based wind plants to system frequency disturbances," *IEEE Trans. Power Syst.*, vol. 24, no. 2, pp. 859-867, 2009.
- [205] A. Bose, "Smart transmission grid applications and their supporting infrastructure," *IEEE Trans. Smart Grid*, vol. 1, no. 1, pp. 11-19, 2010.
- [206] B. D. Russell and C. L. Benner, "Intelligent systems for improved reliability and failure diagnosis in distribution systems," *IEEE Trans. Smart Grid*, vol. 1, no. 1, pp. 48-56, 2010.
- [207] A. G. Phadke, J. S. Thorp, and M. G. Adamiak, "A new measurement technique for tracking voltage phasors, local system frequency, and rate of change of frequency," *IEEE Trans. Power App. Syst.*, vol. 102, no. 5, pp. 1025-1038, 1983.

- [208] S. M. Muyeen, R. Takahashi, T. Murata, and J. Tamura, "A variable speed wind turbine control strategy to meet wind farm grid code requirements," *IEEE Trans. Power Syst.*, vol. 25, no. 1, pp. 331-340, 2010.
- [209] A. Ipakchi and F. Albuyeh, "Grid of the future," *IEEE Power Energy*, vol. 7, no. 2, pp. 52-56, Mar./Apr. 2009.
- [210] C. M. Rader, "Recovery of undersampled periodic waveforms," *IEEE Trans. Acoust., Speech, Signal. Process.*, vol. 25, no. 3, pp. 242-249, Jun. 1977.
- [211] P. E. Pace, R. E. Leino, and D. Styer, "Use of the symmetrical number system in resolving single-frequency undersampling aliases," *IEEE Trans. Signal Process.*, vol. 45, no. 5, pp. 1153-1160, 1997.
- [212] S. Qiu, "The undersampled discrete Gabor transform," *IEEE Trans. Signal Process.*, vol. 46, no. 5, pp. 1221-1228, 1998.
- [213] I. Kamwa, M. Leclerc, and D. McNabb, "Performance of demodulation-based frequency measurement algorithms used in typical PMUs," *IEEE Trans. Power Del.*, vol. 19, no. 2, pp. 505-514, 2004.
- [214] D. Jovcic, "Phase locked loop system for FACTS," *IEEE Trans. Power Syst.*, vol. 18, no. 3, pp. 1116-1124, 2003.
- [215] D. Yazdani, M. Mojiri, A. Bakhshai, and G. Joos, "A fast and accurate synchronization technique for extraction of symmetrical components," *IEEE Trans. Power Electron.*, vol. 24, no. 3, pp. 674-684, 2009.
- [216] SimPowerSystems/Extra Library/Control Blocks/1-phase PLL, MATLAB® 7.8, MathWorks, www.mathworks.com/trademarks.
- [217] D.M. Brookes, "Coloured noise generation without filter startup transient," *IET Electronics Letters*, vol. 37, no. 4, pp. 255-256, 2001.
- [218] A. Gelb and P. Palosky, "Generating discrete colored noise from discrete white noise," *IEEE Trans. Autom. Control*, vol. 11, no. 1, pp. 148-149, 1966.
- [219] W. Gardner and L. Franks, "Characterization of cyclostationary random signal processes," *IEEE Trans. Inf. Theory*, vol. 21, no. 1, pp. 4-14, 1975.
- [220] M. Okumura, H. Tanimoto, T. Itakura, and T. Sugawara, "Numerical noise analysis for nonlinear circuits with a periodic large signal excitation including

cyclostationary noise sources,” *IEEE Trans. Circuits Syst. I, Fundam. Theory Appl.*, vol. 40, no. 9, pp. 581-590, 1993.

[221] PSS1 power system simulator, TecQuipment, www.tq.com.

[222] 2253IX programmable power supply, California Instruments, <http://www.calinst.com>.